

Nonlinear Integrated Photonics for Ranging Applications

Présentée le 6 avril 2023

Faculté des sciences et techniques de l'ingénieur
Laboratoire de photonique et mesures quantiques (STI/SB)
Programme doctoral en physique

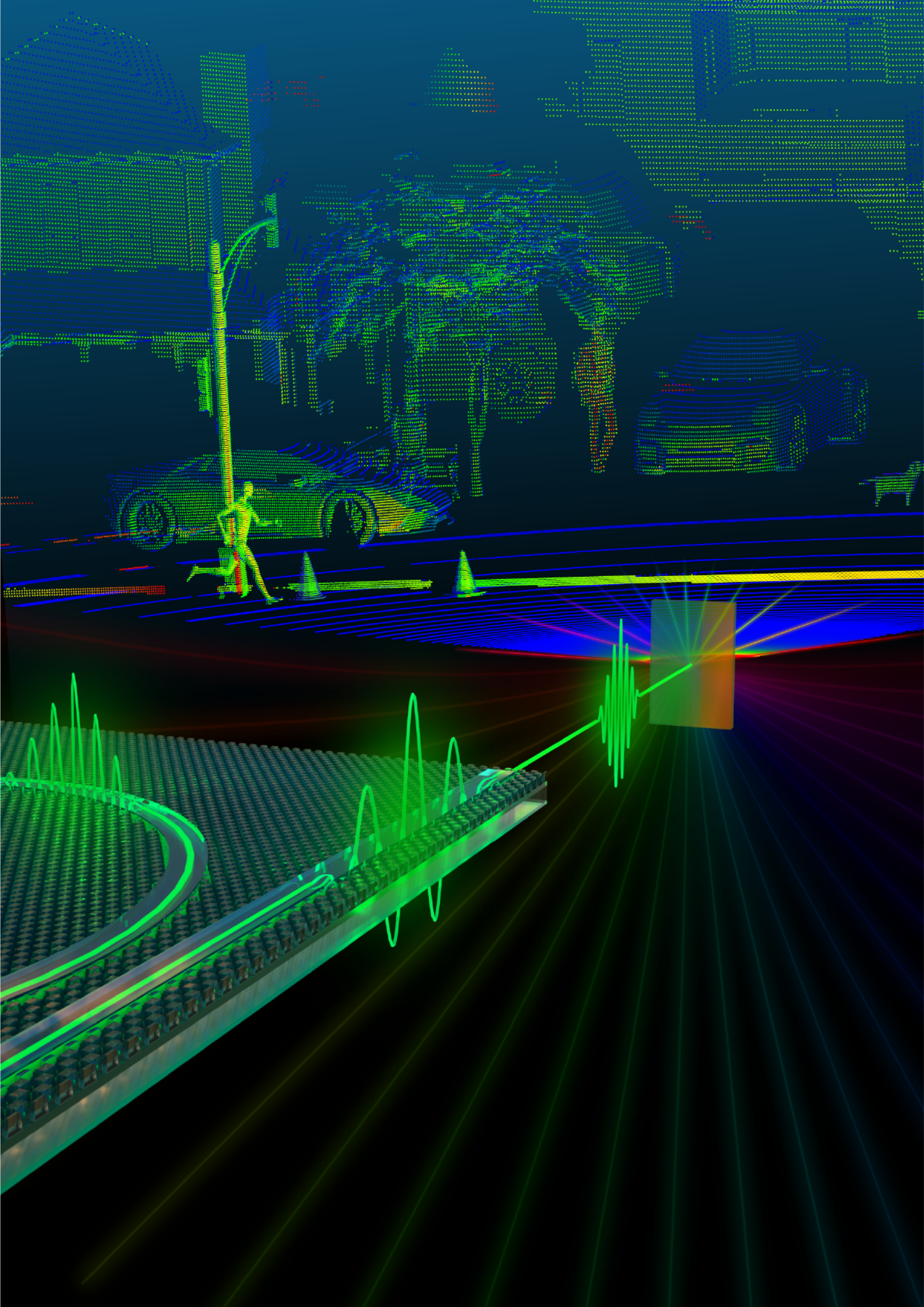
pour l'obtention du grade de Docteur ès Sciences

par

Anton LUKASHCHUK

Acceptée sur proposition du jury

Prof. L. Villard, président du jury
Prof. T. Kippenberg, directeur de thèse
Prof. V. Torres-Company, rapporteur
Prof. M. Heck, rapporteur
Prof. C. Moser, rapporteur



Acknowledgements

First, I would like to thank Prof. Tobias Kippenberg for the time I spent in LPQM. I greatly appreciate the opportunity to join K-Lab in 2017 and to become a part of big multicultural family. I thank Tobias for creating a collaborative environment that embraces young researchers and their passion to do science. I am grateful to Tobias for his trust and for supporting my pursue to do the projects that I liked. Throughout my PhD I could enjoy immense opportunities for research including state-of-the-art Lab facility and equipment, numerous conferences and workshops. It goes without saying that Tobias' drive, energy and constant push for excellence make our Lab stand out and be a special place.

I would like to express my gratitude to Antonella Ragnelli and Kathleen Vionnet. I can't imagine how difficult my life could be if not their support. They are the most essential part responsible for LPQM's successful operation and my own.

I am grateful to all of the group members, past and present, with whom I worked, had lunches, went out for beers, had small chats or shared a funny moment during weekly group meetings.

I thank Maxim Karpov, who took care of me once I joined the Lab. He was always eager to fully elaborate and educate me disregarding the silliness of my questions. Thank you for sharing experimental skills and giving me over all of the PHA frequency comb heritage. I enjoyed numerous discussions we had over lunches and starbucks coffees. I admire your approach to problem solving and your consistency in doing so. I value your friendship that went significantly beyond the Lab and I would still try to argue and challenge your point of view (though it becomes much harder).

I am thankful to Martin Pfeiffer for his support and absolute readiness to answer another part of silly questions despite writing his thesis.

I thank Johann Riemensberger with whom we spent summer 2019 carrying out our first LiDAR experiments. Johann played a key role in my personal development as a researcher. He is the person I learned the most from during my time in LPQM. Throughout my PhD I tried to replicate Johann's working ethics and attitude. The majority of the ideas, techniques and experimental implementations in this thesis were born during discussions with Johann.

I thank Junqiu Liu, who fabricated the famous '2nd golden batch' D44, which is a backbone of the thesis and a foundation of LiDAR journey in K-Lab. I thank Erwan 'mon

lapin' Lucas for organizing regular bouldering nights and for giving me memorable french lessons. I would like to thank Clément Javerzac-Galy, Philippe Rölli, Itay Shomroni, Liu Qiu, Martin Pfeiffer, Maxim Karpov - the 'old' PHA team - who always made my experimental work funny and joyful in the beginning of my PhD. I am thankful to Nick Sauerwein and Alberto Beccari with whom we hanged out during our first days in the lab. I also thank Nick for the sailing lessons and the memory when we were stuck in the middle of Lac Lemman during the storm. I thank Arslan Raja for mutual support while writing our theses and for our frequent gossip talks. I thank Miles Anderson for his outstanding COMSOL tutorial, K-Lab PowerPoint templates, and his engaging way of expressing his ideas, whether it be during a group presentation or a casual conversation at the bar. I thank Anat Siddharth for taking over the legacy in PHA and for bringing Indian flavor to K-Lab multicultural family. I really enjoyed working with Yang Liu. You have a very attractive duality: Chinese wisdom and approach to tackle problems and absolutely non-Chinese sense of humour. I thank our 'theoretician' team, Aleksandr Tusnin and Alexey Tikan, for fundamental understanding of the physics we do in the lab and for educating me on multiple occasions. I would like to thank Deeplight team – Andrey Voloshin, Andrea Bancora, Vladimir Shadymov – for further pushing the LiDAR work into the new realms and for kindly sharing your office when I am kicked out of the quiet office. I, in particular, thank Andrey for his friendliness and for sharing his valuable life experience.

I also would like to thank other team members, with whom I had a chance to interact and work with: Hairun Guo, Wenle Weng, Jia-Jung 'Jj' Ho, Nathan Bernier, Daniel Toth, Alexey Feofanov, Romain Bouchand, Jordan Wachs, Connor Skehan, Jijun He, Xinru Ji, Zheru Qiu, Alisa Davydova, Nikolai Kuznetsov, Viacheslav Snigirev, Zihan Li, Amir Youssefi, Rui Ning Wang, Yujia Yang. I am thankful to Nils Engelsen for being my link to BM and optomechanics worlds. Thanks for enriching my beers experience and for multiple delicious dinners organized by you and Deborah. I thank our optomechanics and circuits teams, who have been a good counterpart to the comb team: Sergey Fedorov, Alberto Beccari, Mohammad Bereyhi, Amir Youssefi, Guanhao Huang, Amirali Arabmoheghi, Evgenii Guzovski, Terence Blésin, Wil Kao, Mahdi Chegnizadeh, Jiahe Pan, Alessio Zicoschi, Shingo Kono, Marco Scigliuzzo and others. I appreciate all the good times we've had together, from the fun lunches to our inside jokes. And I really appreciate all the help and advice you're always willing to give. I thank Marta Divall for managing our laboratory activities and helping me during PHA reconstruction despite my Asana experience. I thank Andrea Triscari for sharing same 'waves' and 'resonances'. Nikolai and Nils deserve a special 'thanks' for regularly posting on K-Lab MEMEs channel.

I thank Mikhail Churaev for taking 7 AM trains over the weekends with me, your samogon, 3 years of Martinet, guitar lessons, 'katalka' playlist and the backpack I borrowed for 1 year. My life became much richer once you joined the Lab.

I thank Aleksandr Tusnin for always keeping a pack of gummies for the most important

moments. Thank you for finding Grisha's phone in the powder and for tamedog sessions. I always appreciate your strong involvement in the discussions and your straightforward position when conveying your thoughts.

I thank Grigorii Likhachev for seamless driving allowing me to sleep on the way back to Lausanne. I am also thankful to Grigorii for bridging the cultural gap in K-Lab and actively teaching other group members the Russian language. Thanks for taking probably the most pictures of me than anyone else combined. I value your broad life experience and the deep conversations we have on the route.

Misha, Sasha, and Grisha, all together, deserve a special 'thank you' for being the foundation of the legendary 'bande de ski'. I hope you enjoyed those weekends as much as I did. I would like to thank Dmitrii 'Pidgos' Pidgaiko – who recently joined the band and recognized the importance of the proper 'pop' like no one else – for Leysin and, in particular, montagnard appreciation.

I would like to thank Tanya Buriakova for organizing Graubunden weekend and letting me be 'your new best friend' multiple times. Thanks to Anton Stroganov for offering Ligentec chips and joining volleyball sessions. Thanks to Nikolai Pavlov for bringing a special atmosphere to any party. I would love to play 'mafia' with you again. I thank Kerim Yildirim for an opportunity to work together and educating me on integrated circuits. I would like to thank Florence Hagen for the regular IT support and Anh Eymann for the kind help with EDPY despite me often missing the deadlines. Je remercie mes Profs de français Anna et Vincent pour les meilleurs cours. Grâce à vous, je peux commander du vin chaud sans soucis tous les week-ends de ski. I would like to thank Eamonn Murphy for the great opportunity to visit ESTEC. I really enjoyed getting first-hand insights about the technologies applied to space during probably the best lunches throughout my PhD studies in ESTEC cafeteria.

Je remercie mes coachs JJB Joao et Catalin, ainsi que tous ceux avec qui j'ai roulé. Les séances de Jiu-Jitsu ont été un vrai dé foulement mental et physique après une journée passée au Labo. Merci aux supers équipes de 'THEJUMPSHOT' où j'ai pu m'amuser sur les trampas.

I thank 'Diable Rabattable'/'shekolda' collective for all of the cringe and funny moments as well as for your great music. I thank Lauriane Mollier for introduction to the authentic french culture in all its shades. I would like to thank my MIPT friends: Ramzil, Vlad, Emil', Anton, Yulya, Igor', Il'ya, Damir, Dima. I enjoyed seeing you here in Europe or during my brief visits to Russia. You are a link to some of the best memories of my past, and I value a lot both our friendship and those memories. I thank my school friends Damdin and Roma for our Baikal trip and for the unforgettable experience at the Buryat wedding. I thank Dmitrii Gusak for our friendship lasting far beyond 15 years and for remembering all of the great moments from our Gymnasium #1 days.

I would like to express my gratitude to Maxim Kuznetsov. There are only two people who care about me more than you do, my parents. Thank you for your unwavering support and wise advice (dating back to our Skoltech days) no matter what issues I face.

I admire your positive attitude and appreciate you always sharing it with me. Thank you also for sharing your adventures with An'ka and for being one of my friends who made it to Nakhodka.

I ended up here in Lausanne in big part thanks to Daniil Domaretskiy. I appreciate your readiness to help me anytime and anywhere and your responsiveness to my spontaneous ideas like a call in the morning to go to Annemasse or to buy bikes in France and ride back to Geneva. You are the person I would call to discuss some problems from general physics class and thank you for always helping me to get to the answer. Thanks for often visiting me in Lausanne, for the countless photo sessions and for our chats recalling the most funny moments from MIPT.

I would like to thank Albert Podusenko. I appreciate that we both have strong opinions on different matters allowing us to have elaborate discussions and, at the end of the day, agreeing that ultimately what matters is the ability to commit. You have a great skill to surround yourself with amazing people and I was fortunate to be a part of that group on some occasions. I took over different preferences and skills from you - let it be my spotify playlist or some other habits - but all enriching my life experiences.

I would like to thank Khurram Pirov. Thank you for always understanding and supporting me. Thanks for pushing me in different directions and being able to provide that momentum when it is needed the most. I admire your skill to find solutions in hopeless situations and your will to go till the end no matter what. Thanks for our numerous adventures and New Years in different parts of the world, and for your friendship.

Finally, I want to thank my family. Olga and Yury, Mom and Dad, thank you for bringing me up and giving me all the qualities that I carry with me throughout my life and that have brought me up to this point. All of my accomplishments, small and slightly bigger, are your merit. I thank my brother, Misha, for letting me educate him on every occasion. I'll soon stop doing so, I promise.

Lausanne, April 2023

Anton Lukashchuk

Abstract

This thesis explores the application of recent advances in integrated photonics to the field of light detection and ranging (LiDAR). The progress in photonic integration allows for unprecedented levels of light manipulation on micrometer scales through the fabrication of high-confinement, low-loss optical waveguides. In combination with medium nonlinearity, these waveguides enable a plethora of phenomena, one of which is frequency combs. Since their discovery in 2007, microcombs have been used in a wide range of applications, including astronomical spectrometer calibration, chip-scale atomic clocks, optical telecommunications, and microwave synthesis. In this thesis, I investigate new approaches to optical ranging with Si_3N_4 microresonator frequency combs and novel photonic integrated laser sources.

First, I report on the demonstration of massively parallel coherent ranging enabled by a newly discovered frequency-modulated microcomb. This study solves a longstanding bottleneck of parallel acquisition in frequency-modulated continuous-wave (FMCW) LiDAR community. Owing to a single high coherence frequency agile laser, ranging with 40 parallel independent channels was achieved. The subsequent result highlights the possibilities attained by the convergence of microresonator combs, metrology and optical telecommunications fields. The dual chirped comb implementation, in conjunction with a high-bandwidth telecommunication receiver, resulted in 6 MPix/s imaging rates, which were the fastest demonstrated at that time for coherent LiDAR. Next, by revisiting the foundations of the complex dynamics of nonlinear systems, the chaotic frequency combs were studied in the context of optical ranging. For the first time, it was shown that incoherent combs can be harnessed to utilize their unique chaotic properties, which so far had not been considered before, and to implement random modulation LiDAR. Counter-intuitively, the wide band amplitude and frequency noise allowed the performance comparable to FM microcombs while alleviating the transmitter requirements for modulators and high-speed electronics. Based on the previous discoveries, parallel and inertia-free 3D ranging was presented. The combination of 2D optical disperses with broadband tuning of a noisy microcomb, enabled by integrated microheaters, resulted in fully passive scanning, which had never been demonstrated with frequency combs and is widely required for future LiDAR. Lastly, photonic-electronic integrated LiDAR engine was developed. This result truly highlights the late progress in photonic integration at EPFL and in general. The engine includes: low-noise frequency agile Vernier laser based on Si_3N_4 waveguides with integrated piezo actuators and hybrid integrated III-V

gain media, Erbium-doped chip-scale optical amplifier, and a high-voltage arbitrary waveform generation circuit using standard CMOS foundry process. Coherent ranging demonstrated with this source paves the way to fully integrated LiDAR in conjunction with solid state scanning approaches.

What was hard to imagine few years ago, now becomes routinely accessible.

Keywords: LiDAR, integrated photonics, nonlinear photonics, optical frequency combs, optical microresonators, Kerr combs, dissipative Kerr solitons.

Résumé

Cette thèse explore l'application des avancées récentes de la photonique intégrée au domaine de la détection de la lumière et de la télémétrie (LiDAR). Les progrès de l'intégration photonique permettent des niveaux de manipulation de la lumière sans précédent, atteignant l'échelle du micromètre grâce à la fabrication de guides d'ondes optiques à haut confinement et faible perte. Ces guides d'ondes, s'ils sont fabriqués dans un matériau non linéaire sont capables de produire une pléthore de phénomènes, notamment des peignes de fréquence. Depuis leur découverte en 2007, les micropeignes ont été utilisés dans un large éventail d'applications, notamment l'étalonnage de spectromètres astronomiques, les horloges atomiques à l'échelle de la puce, les télécommunications optiques et la synthèse de micro-ondes. Dans cette thèse, j'étudie de nouvelles approches de télémétrie optique avec des peignes de fréquence produits par des microrésonateurs en Si_3N_4 , ainsi que de nouvelles sources laser photoniques intégrées.

Tout d'abord, je démontre de la télémétrie cohérente massivement parallèle rendue possible par un micro-peigne fin de fréquences modulé en fréquence récemment découvert. Cette étude résout un obstacle de longue date de l'acquisition parallèle dans la communauté LiDAR à onde continue modulée en fréquence (FMCW). Grâce à un seul laser agile à fréquence de cohérence élevée, une télémétrie avec 40 canaux parallèles indépendants a été obtenue. Le résultat qui en découle met en évidence les possibilités atteintes par la convergence des domaines des peignes fins de fréquences de microrésonateurs, de la métrologie et des télécommunications optiques. La mise en œuvre du double peigne fin de fréquences chirpé, en conjonction avec un récepteur de télécommunications à large bande passante, a abouti à des taux d'imagerie d'environ 6 MPix/s, les plus rapides démontrés à l'époque pour un LiDAR cohérent. Ensuite, en revisitant les fondements de la dynamique complexe des systèmes non linéaires, les peignes fins de fréquences chaotiques ont été étudiés dans le cadre de la télémétrie optique. Pour la première fois, il a été démontré que les peignes incohérents peuvent être exploités pour utiliser leurs propriétés chaotiques uniques, ce qui n'avaient jusqu'à présent pas été envisagées, ainsi que pour mettre en œuvre le LiDAR à modulation aléatoire. Contre toute attente, l'amplitude large bande et le bruit de fréquence ont permis des performances comparables aux microcombes FM tout en diminuant les exigences d'émetteur pour les modulateurs et l'électronique à grande vitesse. Sur la base des découvertes précédentes, une télémétrie 3D parallèle et sans inertie a été présentée. La combinaison de dispersions optiques 2D avec le réglage à large bande d'un microcomb bruyant, activée par des micro-chauffeurs

intégrés, a abouti à un balayage entièrement passif, qui n'avait jamais été démontré avec des peignes de fréquence, bien qu'essentiel pour le futur LiDAR. Enfin, un engin LiDAR intégré photonique-électronique a été développé. Ce résultat met véritablement en évidence les progrès récents de l'intégration photonique, à l'EPFL et ailleurs. L'engin LiDAR comprend : un laser de type Vernier à fréquence modulable et à faible bruit basé sur des guides d'ondes en Si_3N_4 avec des actionneurs piézoélectriques intégrés et un support à gain III-V intégré hybride, un amplificateur optique à l'échelle de la puce dopé à l'erbium et un circuit de génération de formes d'onde arbitraires haute tension ne recourant qu'aux procédés de fonderie standards CMOS. La télémétrie cohérente démontrée avec cette source ouvre la voie à un LiDAR entièrement intégré en conjonction avec des approches de balayage à l'état solide.

Ce qui était difficile à imaginer il y a quelques années, devient désormais systématiquement accessible.

Mots clés : LiDAR, photonique intégrée, photonique non linéaire, peignes de fréquence optique, microrésonateurs optiques, peignes de Kerr, solitons dissipatifs de Kerr.

Publication List

Main publications

- J. Riemensberger, **A. Lukashchuk**, M. Karpov, W. Weng, E. Lucas, J. Liu and T. J. Kippenberg, "Massively parallel coherent laser ranging using a soliton microcomb", *Nature*, 581, p.164, (2020).
- **A. Lukashchuk**, J. Riemensberger, M. Karpov, J. Liu and T. J. Kippenberg, "Dual chirped microcomb based parallel ranging at megapixel-line rates", *Nature Communications*, 13, p. 3280, (2022).
- **A. Lukashchuk**, J. Riemensberger, A. Tusnin, J. Liu and T. J. Kippenberg, "Chaotic micro-comb based parallel ranging", *arXiv*, (Oct. 2021; accepted to NatPhot).
- **A. Lukashchuk**, J. Riemensberger, A. Stroganov, G. Navickaite and T. J. Kippenberg, "Chaotic microcomb inertia-free parallel ranging", *arXiv*, (2022).
- **A. Lukashchuk***, K. Yildirim*, A. Bancora, G. Lihachev, Y. Liu, A. Voloshin and T. J. Kippenberg, "Photonic-electronic integrated circuit-based coherent LiDAR source", (2023)

*These authors contributed equally to the work

Additional contributions

- M Karpov, MHP Pfeiffer, J Liu, **A Lukashchuk**, T J Kippenberg, "Photonic chip-based soliton frequency combs covering the biological imaging window", *Nature communications*, 9 (1), 1-8, (2018)
- J Hu, J He, J Liu, AS Raja, M Karpov, **A Lukashchuk**, T J Kippenberg, C Brès, "Reconfigurable radiofrequency filters based on versatile soliton microcombs", *Nature communications*, 11 (1), 1-9, (2020)
- J Feldmann, N Youngblood, M Karpov, H Gehring, X Li, M Stappers, M Gallo, X Fu, **A Lukashchuk**, A Raja, J Liu, D Wright, A Sebastian, T J Kippenberg, W Pernice, H Bhaskaran, "Parallel convolutional processing using an integrated photonic tensor core", *Nature*, 589 (7840), 52-58, (2021)
- A Youssefi, I Shomroni, YJ Joshi, NR Bernier, **A Lukashchuk**, P Urich, L Qiu and T J Kippenberg, "A cryogenic electro-optic interconnect for superconducting devices", *Nature Electronics* 4 (5), 326-332, (2021)
- AS Raja, S Lange, M Karpov, K Shi, X Fu, R Behrendt, D Cletheroe, **A Lukashchuk**, I Haller, F Karinou, B Thomsen, K Jozwik, J Liu, P Costa, T J Kippenberg, H Ballani, "Ultrafast optical circuit switching for data centers using integrated soliton microcombs" , *Nature communications*, 12 (1), 1-7, (2021)
- Y. Liu, Z. Qiu, X. Ji, **A. Lukashchuk**, J. He, J. Riemensberger, M. Hafermann, R. Wang, J. Liu, C. Ronning and T. J. Kippenberg, "A photonic integrated circuit-based erbium-doped amplifier", *Science*, 376 (6599), 1309-1313, (2022)

Contents

Acknowledgements	iii
Abstract (English/Français)	vii
Publication List	xi
1 Light detection and ranging	1
1.1 Why LiDAR?	1
1.2 Coherent ranging	4
2 Microresonator-based frequency combs and integrated lasers	7
2.1 Optical microresonators	7
2.2 Kerr frequency combs	11
2.3 Si ₃ N ₄ sample details and fabrication	17
2.4 DKS applications	18
2.5 Microresonator-based laser sources	22
3 Massively parallel coherent laser ranging using soliton microcombs	25
3.1 Introduction	25
3.2 Frequency-modulated soliton	26
3.3 Concept of soliton-based parallel FMCW ranging	28
3.4 Frequency modulated DKS dynamics and Raman nonlinearity	29
3.5 Pump chirp linearization and calibration	31
3.6 Characterization of parallel FMCW LiDAR source	35
3.7 Parallel ranging, velocimetry and 3D imaging	38
3.8 Conclusion	42
4 Dual chirped microcomb based parallel ranging	45
4.1 Introduction	45
4.2 Multiheterodyne detection and its application to ranging	47
4.3 Characterization of a dual chirped LiDAR source	50
4.4 Massively parallel coherent ranging	52
4.5 Dense megapixel per second coherent ranging	54
4.6 Discussion	57

5	Chaotic microcomb based parallel ranging	59
5.1	Introduction	59
5.2	Historical outlook and overview of Random LiDAR	60
5.3	Concept of chaotic modulation instability coherent LiDAR	61
5.4	Chaotic modulation instability characterization	63
5.5	Ranging with chaotic microcomb	66
5.6	Velocimetry with chaotic microcomb	67
5.7	Summary	69
6	Chaotic microcomb inertia-free parallel ranging	71
6.1	Introduction	71
6.2	Concept of chaotic inertia-free LiDAR	72
6.3	Chaotic microcomb inertia-free ranging	77
6.4	Discussion	78
7	Photonic-electronic integrated circuit-based coherent LiDAR source	81
7.1	Introduction	81
7.2	Vernier laser	84
7.3	High-voltage Arbitrary Waveform Generator ASIC	86
7.4	Electro-optic transduction and linearity	88
7.5	Coherent ranging	90
7.6	Discussion	92
8	Conclusion and Outlook	95
A	Appendix to chapter 4 - Dual chirped microcomb based parallel ranging	99
A.1	Parallel velocimetry and ranging details	99
A.2	Coherent detection and post-processing	100
A.3	Calibration of channel-dependent frequency excursion	102
A.4	Impact of nonlinear chirp transduction	104
A.5	Signal-to-noise ratio of multiheterodyne FMCW LiDAR	108
B	Appendix to chapter 5 - Chaotic microcomb based parallel ranging	111
B.1	Post-processing	111
B.2	Numerical simulations	112
B.3	Direct detection RMCW LiDAR	117
B.4	Comparison with ASE noise LiDAR	119
B.5	SNR, resolution and precision of coherent RMCW LiDAR	121
C	Experimental methods	129
C.1	IQ modulation/demodulation for coherent telecommunication experiment	129
C.2	Post-processing and BER estimation in telecommunication experiment .	134
C.3	Delay line distance measurement via VNA response	138

Bibliography	160
Curriculum Vitae	161

1 Light detection and ranging

"Anyone relying on LiDAR is doomed."

Elon Musk, 2019

Light Detection and Ranging (LiDAR) technology has come a long way since its first introduction in the 1960s. The technology, which uses laser to measure distances, has been widely adopted in a variety of fields, including autonomous vehicles, robotics, and spatial mapping. However, it wasn't until the early 2000s that LiDAR began to attract significant attention from the research community. This was due in large part to the series of autonomous vehicle challenges - DARPA Grand Challenges. These competitions, aimed at innovation in self-driving cars [1], sparked a renewed interest in the technology as a key enabler for autonomous navigation.

At the time, LiDAR was a bulky and expensive apparatus, primarily used in research and industrial settings. However, the DARPA Grand Challenges served as a catalyst for the development of smaller, more affordable LiDAR systems. In the years that followed, LiDAR technology continued to evolve and improve, with a particular focus on reducing size and cost. Its ability to quickly and accurately capture detailed, high-resolution 3D images of the environment makes it a powerful tool in various applications. The ongoing development of LiDAR, particularly its chip-scale integration (allowing for new architectures so far), promises to bring even more capabilities, making it an exciting field to watch.

1.1 Why LiDAR?

Fig. 1.1 illustrates functional comparison among main imaging sensors: radar, camera and LiDAR. Cameras provide semantic information easily perceived by humans and modern machine learning algorithms. Radars, operating at 1° angular resolution, are

Chapter 1. Light detection and ranging

resilient to adverse weather conditions. The main advantage of LiDAR is the high spatial resolution and centimeter level ranging precision (at ~ 100 m ranging).

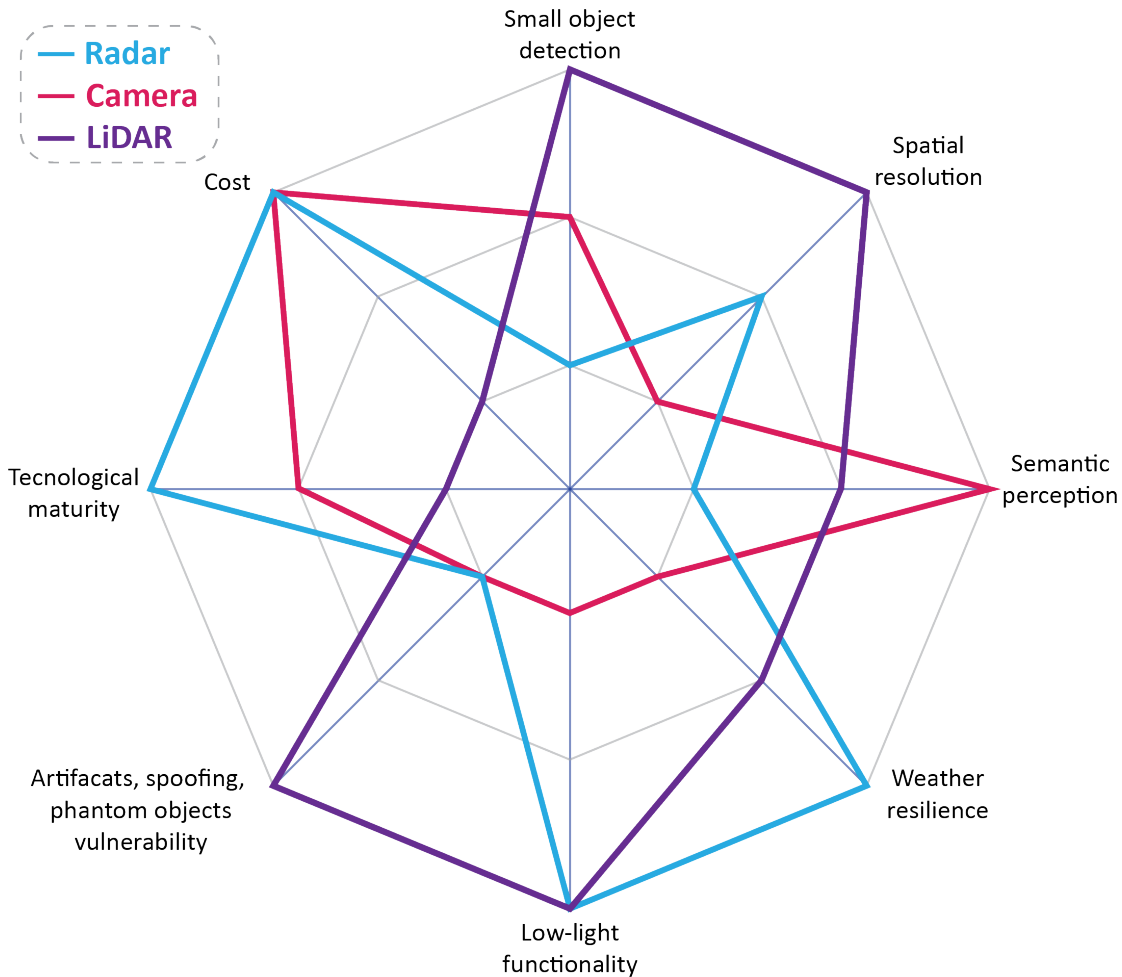


Figure 1.1: Functional comparison of the imaging sensors: Radar, camera, LiDAR.

The choice of the sensor depends on the application and the required functionality. For autonomous vehicles, it is widely regarded [1] that the combination of all these sensors is the way to go. For example, in 2007 Urban Challenge 5 out of 6 finishers utilized LiDAR. While nowadays, all of the major car manufacturers adopt laser sensors for advanced driving assistance.

The field of autonomous driving is interesting to consider not because of the hype around or large amount of investments ($\sim 5B\$$) over the last years. It is the biggest LiDAR battleground of scientific ideas and approaches. Immaturity of the field resulted in ~ 100 companies on the market that supply their unique solutions. And it is still unclear who wins or whose approach will dominate in the future.

Why are there so many different options for LiDAR technology? There are plenty

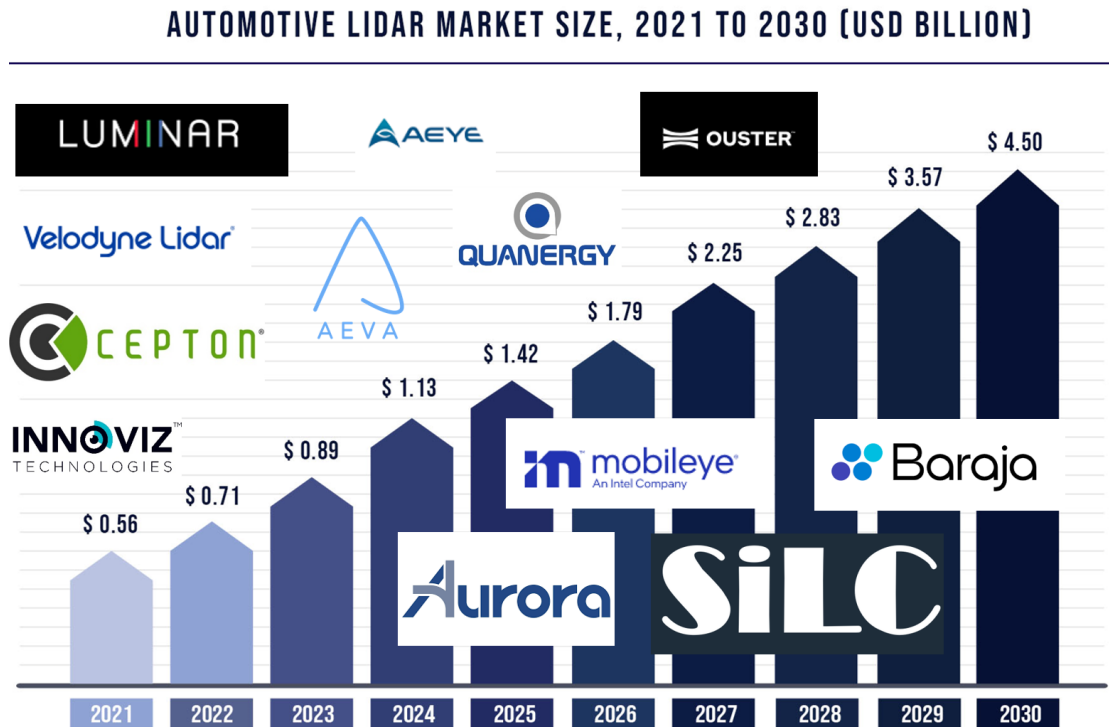


Figure 1.2: LiDAR market projections [2] and some of the companies.

of degrees of freedom to vary. For example, the wavelength of the laser emission can be 900 nm, 1550 nm, or even 1300 nm in the case of MobilEye. The operation principle can also differ: time-of-flight, frequency modulation continuous-wave, or random modulation continuous-wave. Additionally, the method of beam scanning ranges from fully mechanical rotating mirrors to metasurfaces, dispersive optics, MEMS mirrors, optical phased array (OPA), focal plane array, or flash LiDAR. The transceiver architecture can also support high levels of parallelization or use a single unit. The light source can be a fiber laser, pulsed diode, distributed feedback laser, distributed bragg reflector laser, vertical cavity surface emitting laser, or heterogeneously integrated III-V material. Optical detectors can include linear time-of-flight, single photon, or avalanche detectors, as well as heterodyne receivers. Furthermore, all of these components can be integrated onto the same or multiple chips. On top of that, custom digital signal processing and artificial intelligence recognition algorithms are combined in different flavors.

This thesis employs approaches that are similar to those used in commercial LiDARs. For example, companies like Santec, Insight LiDAR, and Baraja use dispersive optics to steer the beam in the fast axis and a galvo mirror to perform slow axis scanning. Similarly, this thesis describes passive 1D scanning using a diffraction grating to spread the frequency comb horizontally and a mirror to scan it vertically (chapters 3, 4, 5, 6).

Aurora employs a random phase modulation CW ranging principle, which is the basis of the LiDAR described in chapter 5 but using the phase noise of a chaotic frequency comb state. Additionally, Baraja uses amplitude modulation CW, which is also employed in chapter 6.

1.2 Coherent ranging

To date most LiDAR implementations are based on ToF sensors that send out laser pulses. The distance of an object is determined based on the reflection delay - time of flight (cf. Fig. 1.3). To increase the speed of image acquisition, modern systems employ an array of individual lasers (as many as 256) to replace slow mechanical scanning [3]. Legacy 900 nm diode lasers and silicon detectors are relatively cheap; this fact contributed to the early success of Velodyne. The velocity information in ToF LiDAR can only be inferred by comparing subsequent images, which is prone to errors due to vehicle motion.

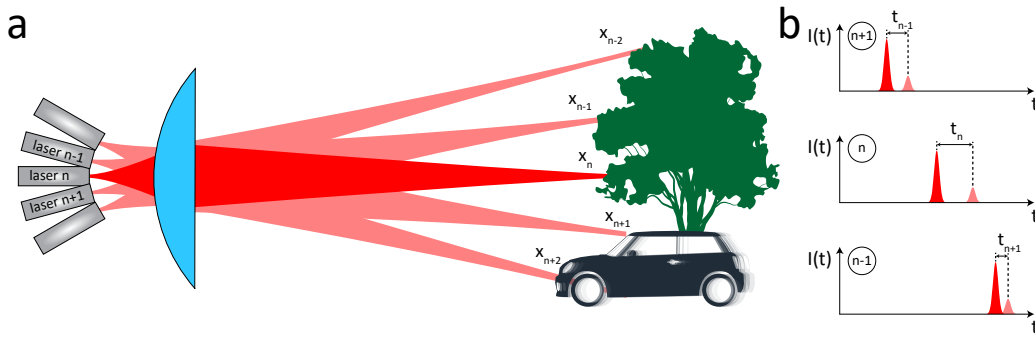


Figure 1.3: Time-of-flight LiDAR (a) and its operation principle (b).

A different principle is that of frequency-modulated continuous-wave (FMCW) LiDAR [4, 5, 6]. In this case a laser that is linearly chirped is sent to an object, and the time-frequency information of the return signal is determined by delayed homodyne (heterodyne) detection. The maximum range is therefore limited not only by the available laser power but also the coherence length of the laser [6]. Assuming a triangular laser scan (over an excursion bandwidth B with period T , cf. Fig. 1.4), the distance information (i.e. time-of-flight Δt) is mapped to a beat note frequency [5], i.e. $\bar{f} = \Delta t \cdot 2B/T$ for a static object. Due to the relative velocity (v) of an object, the returning laser light is detected with a Doppler shift $\Delta f_D = \vec{k} \cdot \vec{v} / \pi$, where \vec{k} is the wavevector and \vec{v} the velocity of the illuminated object. As a result, the homodyne return signal for a moving object is composed of two frequencies for the upwards and downwards laser scan, i.e. $f_u = \bar{f} + \Delta f_D$ and $f_d = |-\bar{f} + \Delta f_D|$.

From the measured beat notes during one period of the scan, one can therefore determine both distance and relative velocity of an object. The latter greatly facilitates image processing and object classification, particularly relevant to traffic. Moreover, FMCW

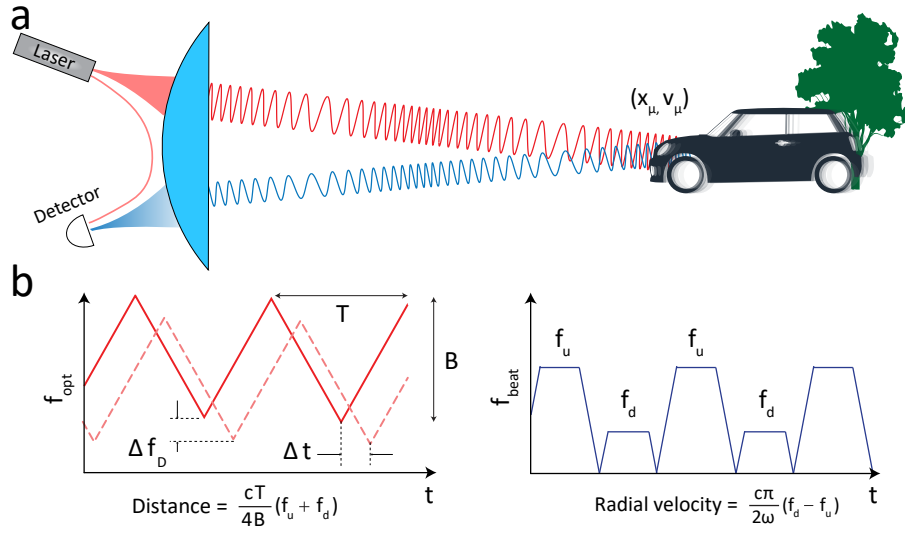


Figure 1.4: Frequency-modulated continuous-wave LiDAR (a) and its operation principle (b).

LiDAR allows for higher average powers and photon flux due to CW operation, as opposed to pulsed operation. Coherent LiDAR is widely considered to be superior to ToF implementations in high background light conditions and presence of another LiDAR sources or crosstalk [7], as delayed homodyne detection makes it almost impervious to interference and malicious remote attacks [8]. Furthermore, it can achieve high depth resolution increasing the chirp excursion without the need for high-bandwidth photodetectors and digitizers. For example, a LiDAR with a frequency excursion of a few THz can still provide a beatnote in ~ 100 MHz band [9].

FMCW challenges

Despite aforementioned advantages, coherent ranging suffers from the stringent requirement of narrow linewidth [6], as well as fast and linear frequency chirping [10]. The accessibility of such laser sources and their costs make massively parallel coherent implementations, as used in ToF LiDAR, challenging. In fact, this bottleneck is imposed by diode laser sources that trade-off tunability versus linewidth. The subject of chapter 7 will address this issue employing novel photonic integrated circuit design.

Furthermore, FMCW is more vulnerable to vibrations and when employing fast mechanical scanning, it leads to artificial Doppler broadening due to the mirror tilt motion. One of the limitations on FMCW acquisition speeds is the pixel dwell time, that is widely regarded to range from 10 to 100 μs for autonomous driving applications to collect enough reflected photons for reliable detection. Going beyond megapixel per second acquisition rates inevitably requires parallelization. In chapters 3, 4, 5 we suggest a solution to this problem employing microresonator frequency combs and using a single legacy FM laser.

2 Microresonator-based frequency combs and integrated lasers

This chapter focuses on the basics of microresonator-based integrated photonics. It describes the remarkable transition that took place in K-Lab at EPFL. The author notes that in 2018, the lab was primarily a frequency comb group, but now the focus has shifted to integrated photonics that goes beyond exploring soliton dynamics in microresonators. The chapter traces this evolution and covers the fundamentals of optical microresonators, frequency combs, and photonic integrated light sources developed in the lab in recent years. It follows the author's own journey of research, starting from soliton-based LiDAR and ending with an integrated LiDAR engine.

2.1 Optical microresonators

The foundation of this thesis is built upon optical resonators. Similar to the 1899 invention of Fabry and Perot, optical resonators consist of two bulk mirrors that guide light in a closed path at specific frequencies, known as optical resonances. This fact allowed, for example, study of closely spaced spectral lines observed in Zeeman effect or narrow atomic transitions. With the advent of optical masers in the 1960s, optical resonators became widespread and played a crucial role in the development of lasers, spectroscopy, nonlinear optics, optical feedback and stabilization, and optical telecommunications.

Tremendous progress in laser science and semiconductor technology with more than 20 Nobel prizes over the last six decades (triggered by 1956 transistor and 1964 laser Nobel prizes) in turn drives microfabrication techniques. In addition to miniaturization, robust operation and reliability required by consumer market, the shift towards microscale¹ opened a plethora of new scientific research in the field of optical microcavities [11]. Cavity optomechanics, cavity quantum electrodynamics, nanophotonics, nonlinear photonics including microcombs are novel areas that emerged with the introduction of

¹Though not all optical resonators are made equal and some of them require particularly large sizes. For example, LIGO experiment employs optical cavities with 4 km length.

optical microresonators.

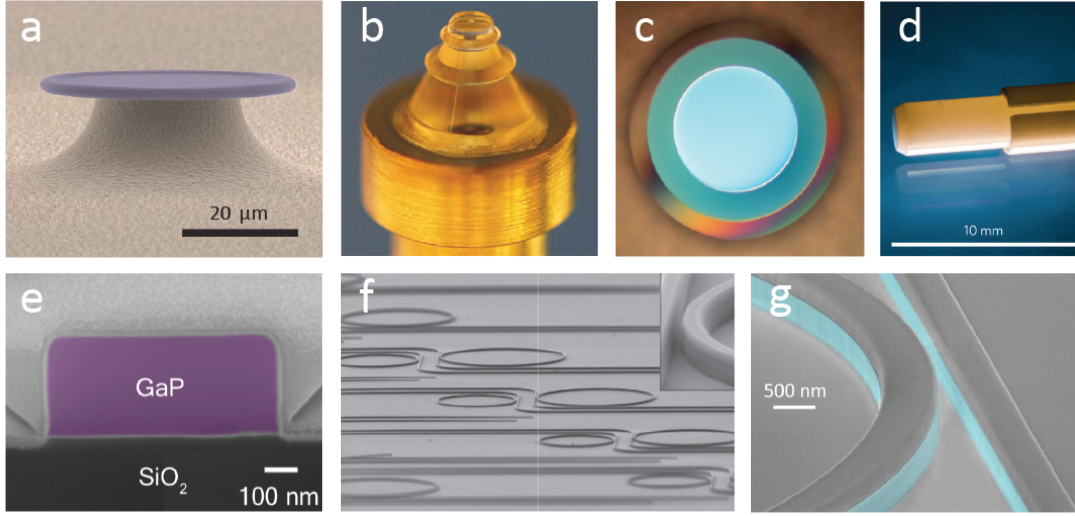


Figure 2.1: **Various microresonator platforms (all images are adapted from the corresponding cited sources).** a) Fused silica (SiO_2) microtoroid [12]. b) Magnesium fluoride (MgF_2) crystalline resonator [13]. c) Silica wedge-shaped microresonator [14] (top view). d) Fiber-based microcavity [15]. e) Cross-section of gallium phosphide microring [16]. f) Diamond microresonators [17]. g) Aluminum gallium arsenide ($\text{Al}_x\text{Ga}_{1-x}\text{As}$) microring resonator [18].

The key feature of a microresonator is to keep the light confined and circulating. Historically, the first optical microresonators studied for nonlinear properties are whispering-gallery mode resonators (WGMR) [19]. The guiding principle in WGMR is based on total internal reflection and it requires resonators to have circular symmetry². Fig. 2.1a,b,c depict typical WGMR. They can achieve quality factors of few billions due to mature polishing techniques reducing surface scattering - the main loss source, thus approaching quality factors of commercial silica fibers - 0.2 dB/km.

Fig. 2.1e,f,g show another type of microresonators, waveguide-based microresonators. The refraction index contrast between the waveguide dielectric material and the surrounding confines the transverse mode of the light allowing for small mode volumes ($\sim \lambda^2$). Such microresonators are formed by patterning a waveguide on a substrate (usually silica) and they can be integrated with other components (modulators, detectors) on the same chip. Integrated optical waveguides benefit from the progress in microelectronic semiconductor technology and this is partially referred to what is known as ‘Silicon Photonics’ [20].

Si_3N_4 optical microresonators

Silicon nitride has been used to make optical waveguides since the 1980s. One major challenge in using this material was the high tensile stress of silicon nitride thin films,

²Lord Raleigh introduced the term whispering-gallery mode explaining the phenomenon of whisper waves observed in the dome of St Paul’s Cathedral

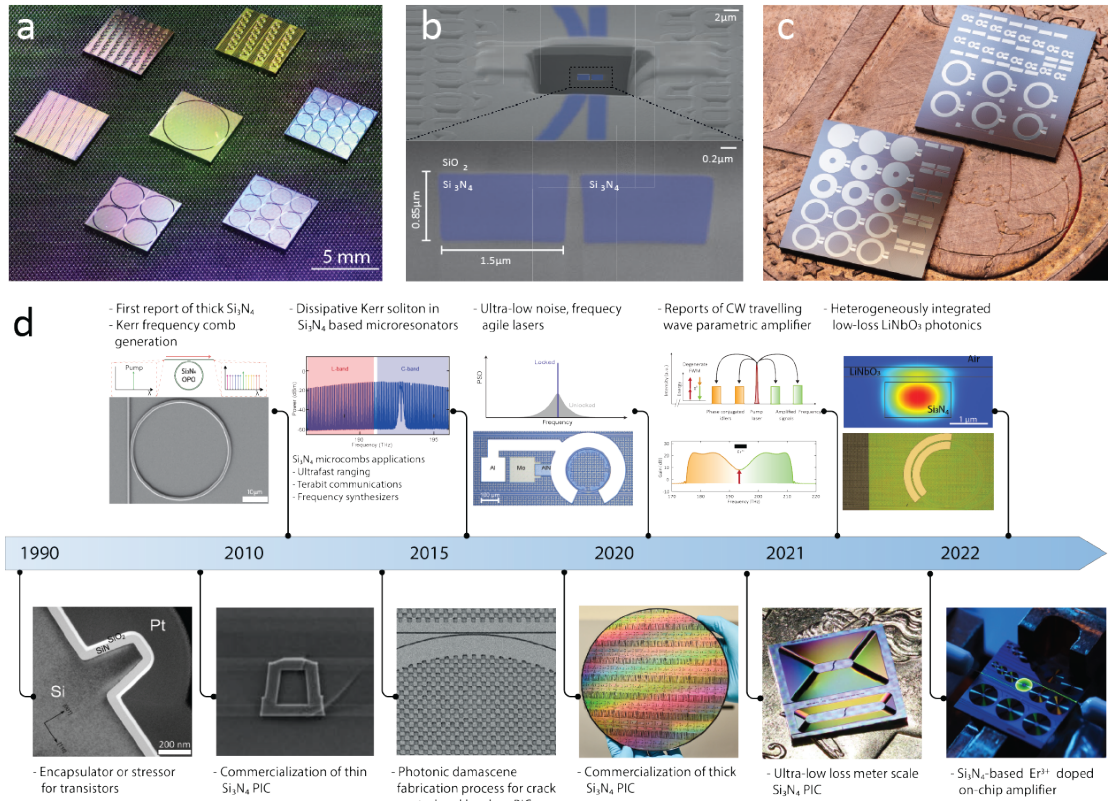


Figure 2.2: Si₃N₄ **photonic integrated circuits**. a) Si₃N₄ microresonators with various FSRs ranging from 10 GHz to 1 THz (photo by J.He). b) Si₃N₄ microresonator coupled to a bus waveguide [21]. c) Si₃N₄ microrings with integrated piezoactuators (photo by A.Bancora). d) Historical outlook of Si₃N₄ integrated photonics development (image assembly by A.Raja)

which made it difficult to deposit films thicker than 400 nm. However, this limitation was overcome through the use of multistep deposition and thermal cycling, allowing the production of anomalous dispersion waveguides [22]. In 2014, the Photonic Damascene process was developed as an alternative method for reducing the stress in silicon nitride [21].

Silicon nitride is an attractive material for integrated photonics because it has several attractive properties. It has a large electronic bandgap, a wide optical transparency window, and strong third-order nonlinearity without two-photon absorption, making it suitable for use in the visible wavelength range. Additionally, silicon nitride allows for the fabrication of waveguides with very low loss, meter-scale, high aspect ratio, tight confinement and, more importantly, the fabrication process implements standard commercial CMOS foundry techniques.

Si₃N₄ fabrication process

The standard processing technique for silicon nitride, known as the subtractive process, involves depositing a uniform film of silicon nitride on an oxidized substrate and defining waveguides through lithography and etching. However, this method has the drawback of causing waveguide cracking due to the tensile stress of the film and being unable to produce high aspect ratio structures due to non-uniform oxide top cladding deposition. The photonic Damascene process, developed at EPFL by K-Lab fabrication team (Martin Pfeiffer, Junqiu Liu, Arne Kordts, Rui Wang and others) solves these problems by inverting the waveguide fabrication process (cf. Fig. 2.3). Instead of etching the silicon nitride film, a preform is etched into the silicon oxide substrate. Depositing silicon nitride into the pre-structured substrate minimizes the formation of cracks, and excess nitride is removed through reactive ion etching and chemical mechanical polishing. The stress release patterns surrounding the waveguide are optimized to prevent the formation and propagation of cracks.

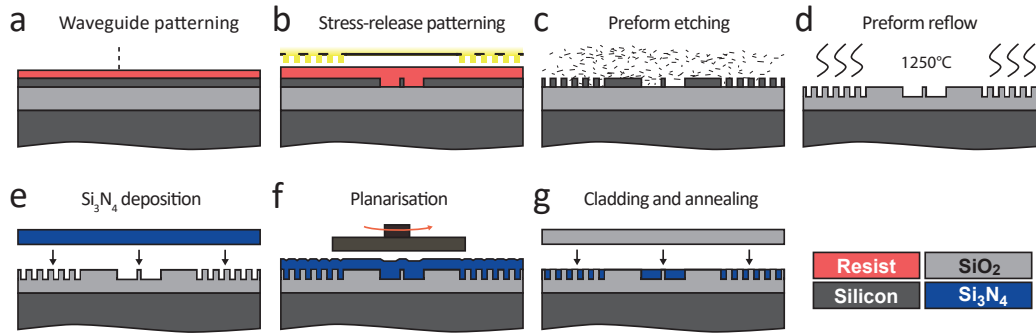


Figure 2.3: **Photonic Damascene fabrication process (adapted from [23]).** a) Waveguide patterning in the resist layer. b) Stress-release patterning. c) Pattern transfer to the silica via etching. d) Reflow to decrease sidewall roughness. e) Si₃N₄ chemical vapor deposition. f) Excess layer removal via planarization. g) Silica cladding chemical vapor deposition.

In the past, silica microspheres were able to achieve Q-factors of over 100 million thanks to their atomically smooth sidewalls and the glass transition process, as reported in Braginsky's 1989 study [19]. However, silicon nitride lacks a glass transition and cannot replicate this process. Nevertheless, the photonic Damascene process, which involves the use of thermal reflow, has been able to attain Q-factors of 30 million in silicon nitride.

Ultimately, the fundamental limit of Si₃N₄ microresonators quality factor is governed by absorption losses [24] potentially allowing for 200×10^6 Q factors. Currently achieved resonator linewidths of few tens of MHz is due to the scattering loss and it could be further improved with more advanced fabrication techniques.

2.2 Kerr frequency combs

The most exciting thing about a microresonator is the rich variety of physical phenomena it enables due to the strong light-matter interaction. The latter is enabled by high **quality factors** and **nonlinearity** of the dielectric waveguide material. In case of Kerr nonlinearity, the light coupled to such a microresonator effectively exhibits an intensity dependent local refractive index modulation. This in turn allows for **modulation instability** and **parametric oscillations** at offset microresonator modes from the pump where the **parametric gain**, determined by microresonator **dispersion** and **losses**, pump detuning and power, is maximized. This process can repeat itself in cascade via four-wave mixing and ultimately lead to the formation of microresonator Kerr combs and dissipative Kerr solitons (DKS).

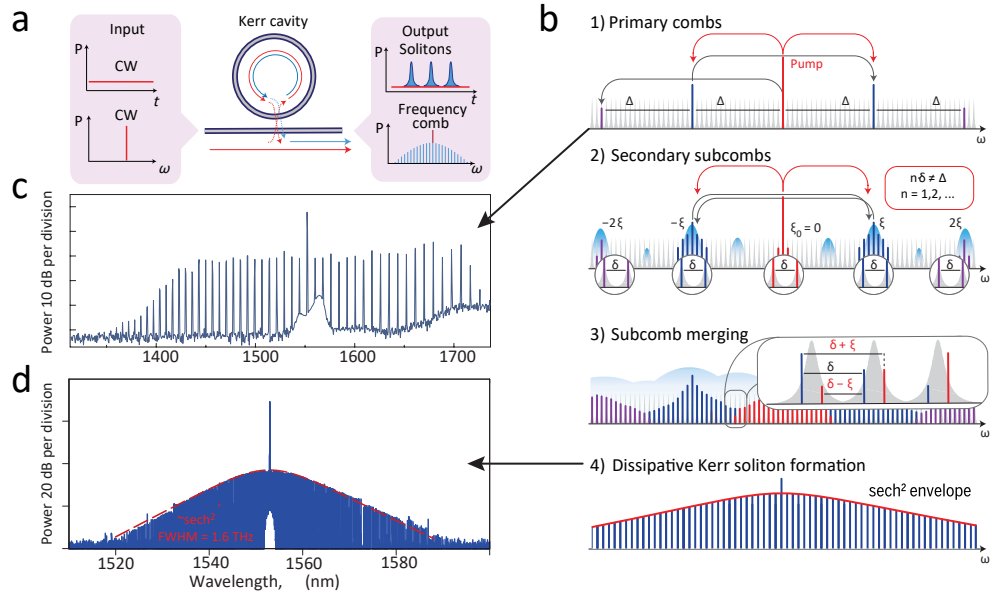


Figure 2.4: **Frequency comb and dissipative Kerr soliton.** a) Time and frequency domain profiles of a pumped microresonator generating soliton state. b) Spectral evolution of the intra cavity profile with the pump being tuned into the resonance. c) First reported microresonator Kerr comb generated by P. Del'hay in 2007 [12]. d) First reported dissipative Kerr soliton generated by T. Herr in 2013 [13].

Kerr frequency comb represents a ruler in a frequency domain with equidistant line spacing. It is parametrized by two parameters: repetition rate and offset frequency - $f_n = f_{\text{ceo}} + n \times f_{\text{rep}}$. It is important to note that the frequency of the pump laser is included within the comb, which is distinct from mode-locked combs where the gain material is pumped incoherently. Coherent Kerr combs or dissipative Kerr solitons (DKS) have a fixed phase relationship between the comb lines and in time domain represent a train of pulses. Due to their micrometer scale, the repetition rates of these resonators can range from a few GHz to THz frequencies. The comb spacings achievable with microresonators are not attainable with bulk mode-locked combs, and have enabled a

wide range of applications, which will be discussed further below.

The description of the aforementioned phenomena requires the formalism of **waveguide-resonator coupling**, microresonator **intracavity build-up** and **coupled mode equations**. I will omit the elucidation of these important concepts and cite the relevant literature - PhD theses of my colleagues who pioneered microresonator Kerr solitons and gave extensive explanations of the underlying physics: Tobias Herr [25], Victor Brasch [26], Erwan Lucas [27], Maxim Karpov [28]. Below, I will mention some basics and key features of Kerr combs relevant to the physics employed in LiDAR demonstrations throughout the thesis.

Excitation of Kerr combs

To routinely access soliton states in optical microresonators one needs to tune the CW pump through the resonance starting from the blue detuned side [29]. I used a python based Lugiato-Lefever equation solver (developed by A. Tikan and A. Tuskunov [30]) to simulate the dynamics. The evolution of the intracavity power and slow-fast time dynamics are illustrated in Fig. 2.5. Starting with a CW regime, we tune into the resonance, where as at some point we observe appearance of background modulation (cf. Fig. 2.5c -left). The creation of additional spectral frequencies or sidebands from an initial constant-frequency field is a common occurrence in various fields. This process is known as modulation instability (MI) or Turing rolls [31], and it refers to a state in which the system does not suppress random spectral fluctuations, but rather amplifies them, resulting in strong oscillations in the sidebands. In the context of Kerr combs, the term MI is used for different operating regimes where the pump is on the blue-detuned side of the driven resonance and the microresonator is above the threshold for four-wave mixing (FWM). Tuning further, we observe chaotic MI state (cf. Fig. 2.5c - middle). It corresponds to further formation of modulation instability, but for the primary combs and subsequent subcombs [32]. High-order combs can thus fill the resonances and fully develop into a chaotic state. The spacing between subcombs generally differs from the one of initial combs. Non-degenerate four-wave mixing further enhances the variation in spacing. It leads to the presence of multiple sidebands within one resonance. This state is also termed noisy frequency comb, as the optical signal detected on a low-bandwidth photodiode will result in a broad-band noise ($> 10\times$ resonance linewidth [33]). In the time domain, it corresponds to spatiotemporal chaotic waveform (cf. Fig. 2.5b). We study noise properties of chaotic frequency comb and utilize it to demonstrate random modulation LiDAR in chapters 5, 6.

Once the pump frequency goes through the resonance, the system enters the so-called bistability region where a soliton state can be accessed (cf. Fig. 2.5 inset) [29]. The characteristic feature of the soliton state is a step in intracavity power which can gradually increase upon further detuning away from the cavity. It is important to note, that

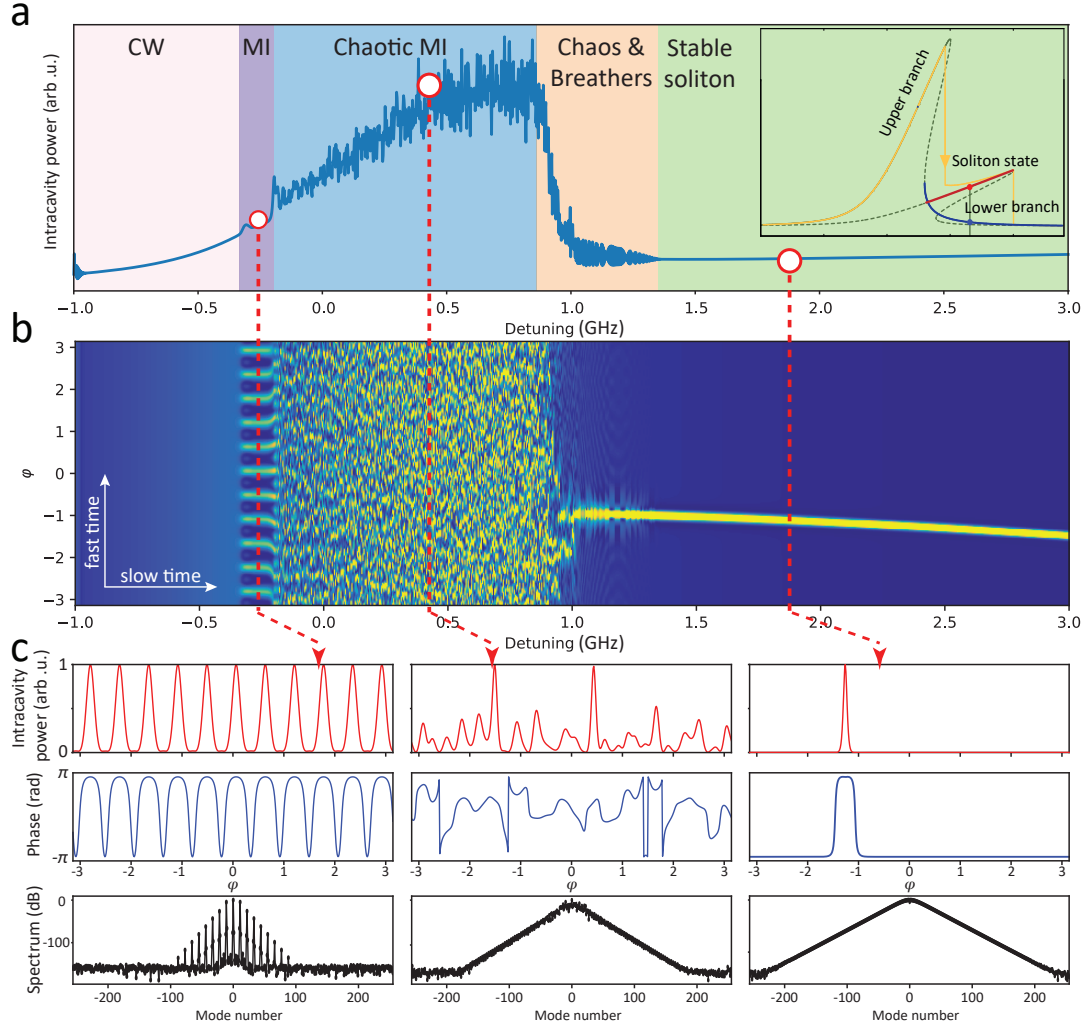


Figure 2.5: **Cavity optical waveform evolution via pump laser tuning.** a) Intracavity power vs cavity detuning. Inset - Kerr nonlinearity mediated resonance bistability. b) Slow and fast time dynamics highlighting spatio-temporal formation (colormap in dB scale). c) Amplitude and phase fast time profiles and spectra for selected regimes: modulation instability or Turing rolls, chaotic modulation instability, DKS. Simulated with PyCORE solver [30].

spatiotemporal instabilities of DKS and breathers precede stable soliton state. The stable soliton profile is reminiscent to fiber solitons derived from nonlinear Schroedinger equation. The light propagation in optical microresonator is described by Lugiato-Lefever equation (LLE) [34] where the same formalism as in case of optical fibers is applied, but adding pump and loss terms as well as pump-resonance detuning. In dimensionless form LLE equation reads as

$$\frac{\partial \Psi(\theta, t)}{\partial \tau} = \left(-1 - i\zeta_0 + i\frac{\partial^2}{\partial \theta^2} + i|\Psi(\theta, t)|^2 \right) \Psi(\theta, t) + f \quad (2.1)$$

where $\Psi(\theta, t)$ is a slowly varying intracavity waveform in fast (renormalized to periodic phase) and slow time coordinates. The only two independent parameters that can be varied are ζ_0 and f - dimensionless detuning and pump correspondingly. M. Gorodetky was first to derive DKS as an analytical solution of LLE - $\Psi(\theta, t) \simeq \Psi_c + \sqrt{2\zeta_0}e^{i\varphi_0} \text{sech}(\sqrt{2\zeta_0} \cdot \theta)$ (written with a CW background). It was experimentally confirmed in 2013 by T. Herr et al. [13].

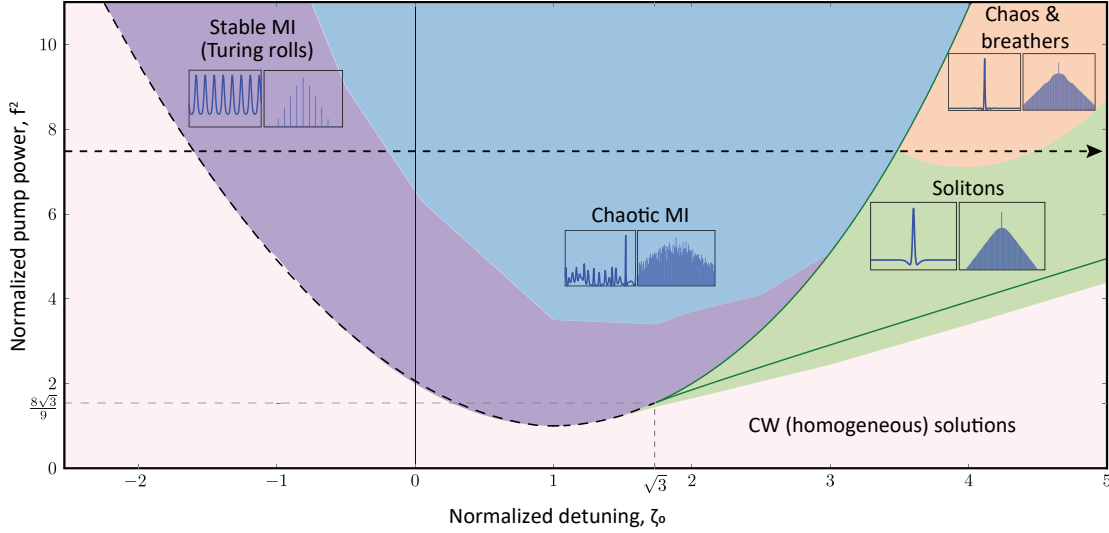


Figure 2.6: **Dimensionless LLE stability chart.** (adapted from [27]) Various stability regimes color-coded similar to Fig. 2.5. Black line shows pump tuning implemented in Fig. 2.5.

The numerical analysis of LLE equation for convergence of various stable solutions with varying pump power and detuning results in stability chart [32, 35]. Stable DKS region (colored as green) exists only on the red detuned side from the cold cavity resonance (detuning $\zeta_0 = 0$). The key feature that we will employ in chapters 3, 4 is that for a fixed pump power, the detuning can be varied within a certain range, while keeping the soliton state alive, though slightly changing its properties [36]. Another region of interest is modulation instability and, particularly, chaotic MI. It is accessible starting from the blue-detuned side even before the cavity resonance and up to the bistability region (green straight lines). As we will show in chapter 5, to leverage the broadband noise of chaotic combs the pre-soliton switching state with maximum detuning is desired (blue - red border).

VNA response of a CW driven cavity

Recalling the stability chart, we know that the DKS state is supported within a certain detuning range. Hence, the knowledge of the detuning appears to be handy to ensure that the DKS will stay alive, given constant laser frequency drift or external perturbations. M. Karpov developed a nondestructive technique to probe a pumped cavity for DKS

existence and monitoring [29]. This method operates by phase modulating the pump and analyzing the cavity transfer function via vector network analyzer (VNA). The setup schematics is presented in Fig. 2.7a. VNA applies a frequency sweep on the electro-optic modulator, where as the current response is analyzed after direct photodetection.

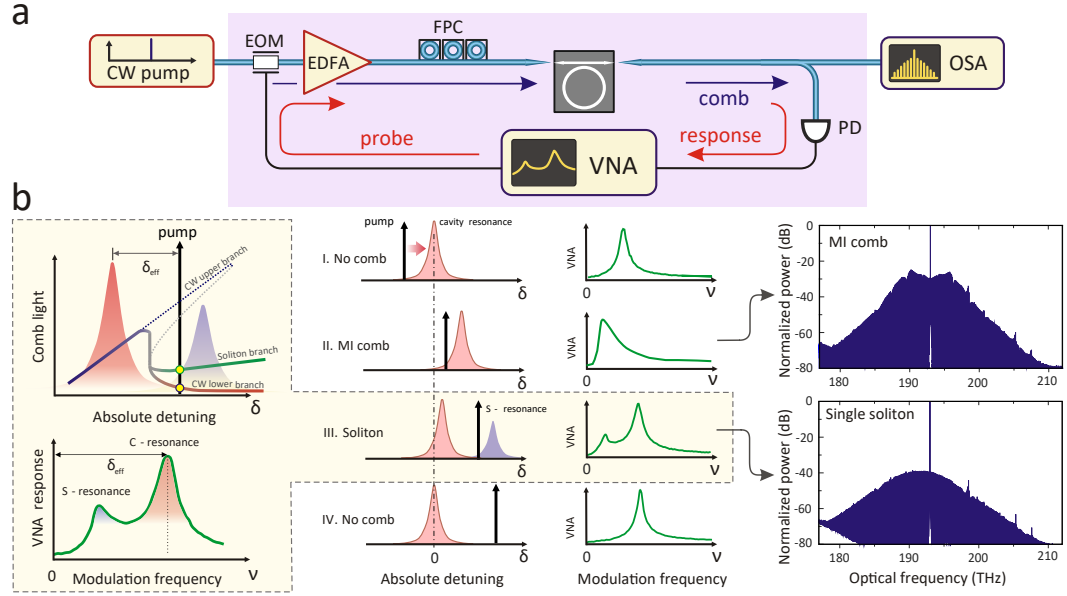


Figure 2.7: Cavity probing via VNA. (adapted from [29]) (a) Experimental setup highlighting the VNA actuating the electro-optic modulator (EOM) and measuring the photocurrent response after detection (PD). (b) (Left,top) Panel shows a schematic of the double-resonance cavity transfer function in the soliton state, with the green line indicating the power trace of the soliton component and the blue and red lines indicating the high- and low-intensity branches of the bistability. (Left, down) Panel shows the double-resonance cavity transfer function measured with VNA, with the high-frequency peak indicating the cavity resonance and the low-frequency peak indicating the soliton resonance. (Middle) The middle panel shows four stages of the microresonator frequency comb formation and corresponding cavity transfer function measured with a VNA as the pump laser is tuned over the resonance. The right panel shows the frequency comb spectra corresponding to the chaotic MI operation regime and the single soliton state.

If there is a resonance in the system, the phase modulated signal whose sideband is swept through this resonance, will result in amplitude response upon photodetection (cf. Fig. 2.7b - I). Thus tuning into the resonance can be easily visualized by the VNA. When the pump laser is tuned into the soliton existence range, the transfer function shows a double-resonance feature and when the pump frequency is tuned out of the soliton existence range, the transfer function shows again a single, Lorentzian-like resonance. The double-resonance feature corresponds to a CW background solution and a soliton solution. It can be intuitively understood by considering that the photons trying to couple into the cavity in presence of the soliton, feel a shifted resonance due to the higher refractive index mediated by the local Kerr effect of the soliton intensity.

By probing the cavity via VNA we ensure wide excursion (of few GHz) of the soliton

sweep in chapter 3, minimize the relative detuning of two solitons in chapter 4, and maximize the noise bandwidth of the chaotic comb by tuning further into the resonance (but not switching into the soliton state).

DKS Raman shift

The Raman scattering is a nonlinear optical process responsible for interaction of the optical field with the vibrational modes of the resonator material leading to the transfer of energy between different optical frequencies [37]. In case of a soliton Kerr comb, the Raman effect leads to a frequency shift of the comb teeth to lower frequencies [38]. It will play a crucial role in understanding the physics of frequency-modulated soliton in chapters 3, 4.

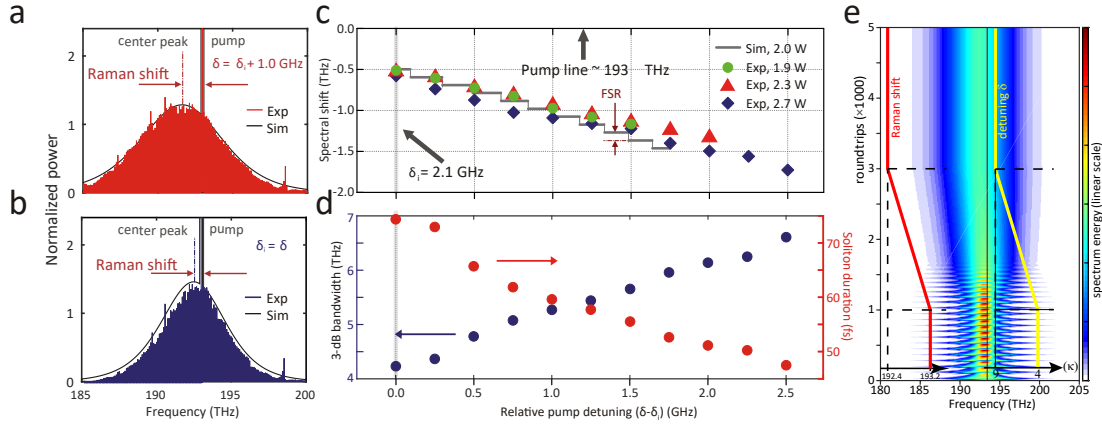


Figure 2.8: **Raman shift of DKS.** (adapted from [38]) a,b) Experimental and simulated soliton spectra at two different detunings. c) DKS frequency shift as a function of detuning $\delta - \delta_i$. d) Soliton duration and its spectral 3-dB bandwidth as a function of detuning $\delta - \delta_i$ e) Simulated evolution of the spectral envelope and its Raman shift with a varied detuning (yellow). Black line shows pump tuning implemented in Fig. 2.5.

Importantly, the Raman shift can be as high as few THz and it depends on the pump-cavity detuning. Figs. 2.8a,b illustrate the shift of the soliton central peak relative to its pump for two distinct detunings. If the detuning is gradually increased, the Raman shift follows the same trend (cf. Figs. 2.8c,d,e). In fact, it can reach several THz until the detuning crosses the soliton existence range, which is only few GHz (though dependent on the pump power). Such a dramatic shift of the soliton center will ultimately change its properties, for example, repetition rate. This change is due to the frequency dependent microresonator dispersion or group velocity dispersion. As we will show in the next chapter, a 2 GHz variation in detuning causes ~25 MHz variation in soliton repetition rate, purely caused by Raman induced nonlinearity.

2.3 Si₃N₄ sample details and fabrication

I was fortunate to have worked with essentially one batch of chips (famous D44 - cf. Fig. 2.9d) throughout my PhD that I designed back in 2018. It was fabricated by Junqiu Liu at EPFL clean room facility. The design comprised microrings targeted for 100 GHz free spectral range (FSR) with variation from 500 MHz to 10 GHz for the possible dual comb applications. High microresonator dispersion D_2 allows for easier soliton generation and higher comb power (for the lines next to the pump) but the power roll-off is steeper [39]. To target C-L band operation, 1 MHz D_2 value was selected (cf. Fig. 2.9b). I further swept the bus waveguide microresonator coupling distance from 450 nm to 1 μm to cover overcoupled and critically coupled regimes of operation. While critical coupling regime facilitates the soliton generation requiring least pump power [40], operation in the strongly overcoupled regime bears the advantage of suppressing thermal nonlinearities during tuning as well as increasing the power per comb line before and optical signal to noise ratio after post-amplification [39]. Samples with external coupling $10\times$ higher than intrinsic linewidth (cf. Fig. 2.9c) were used in chapter 5 to above all leverage the noise properties of the chaotic modulation instability, which of course was not considered back in 2018.

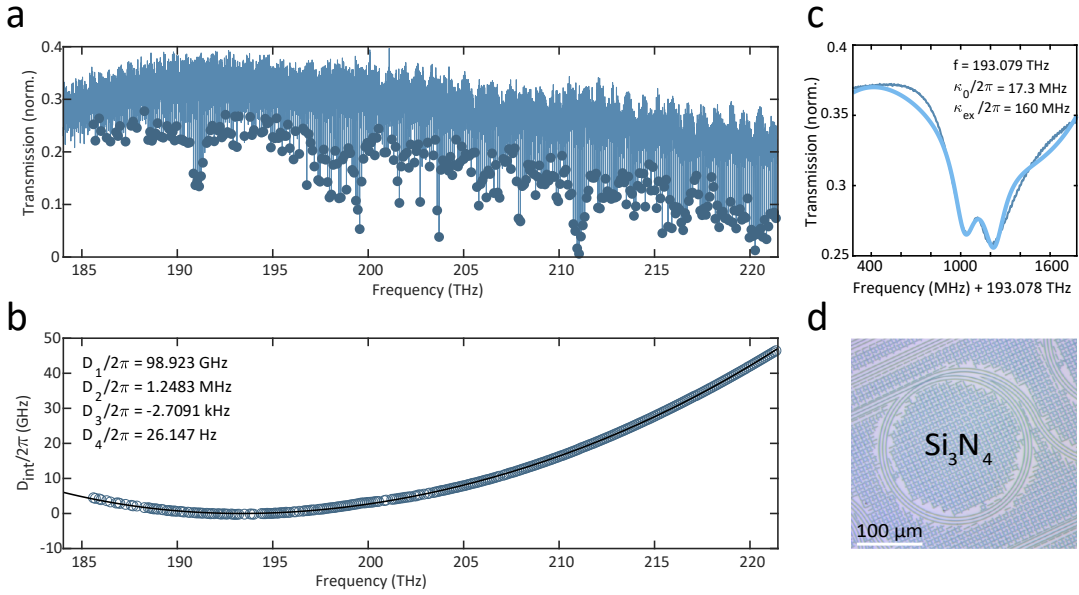


Figure 2.9: **D44 Si₃N₄ resonator characterization.** a) Transmission scan of the resonator featuring TE mode resonances spaced 99 GHz apart. b) Integrated dispersion of TE mode. c) Zoom in of the resonance used as pumping resonance in ch. 5. The resonance is highly overcoupled. d) Electron microscope picture of 228.43 μm Si₃N₄ microring resonator.

Integrated Si₃N₄ microresonators were fabricated with the photonic Damascene process [41], deep-ultraviolet (DUV) stepper lithography and silica preform reflow [23]. The progress of K-Lab fabrication team over the last years [42, 24] enabled wafer-scale fabrication of high-Q Si₃N₄ microresonators. The statistics measured over 8 samples is

depicted in Figs. 2.10c,d with the mean intrinsic loss of 15 MHz. Such losses allow for soliton generation at sub 10 mW optical powers.

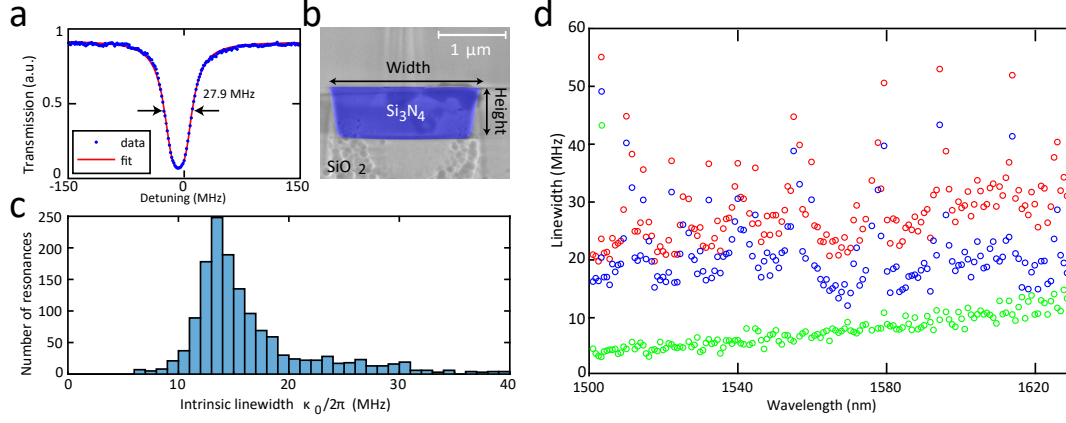


Figure 2.10: **Linewidth characterization of D44 batch.** (adapted from [42]) a) Critically coupled resonance fitted with a Lorentzian profile. The loaded and intrinsic linewidth are 27.9 MHz and 13.7 MHz correspondingly. b) Electron microscope image of a Si_3N_4 waveguide buried in oxide cladding. c) Histogram depicting intrinsic linewidth statistics measured over 8 samples. d) Loaded, intrinsic and external coupling linewidths measured over C-L bands for a TE mode of an undercoupled microresonator.

The waveguide cross-section is $1.5 \mu\text{m}$ wide and $0.82 \mu\text{m}$ high (cf. Fig. 2.10b), with anomalous second order dispersion of $D_2/2\pi = 1.2 \text{ MHz}$ and third-order dispersion parameter of $D_3/2\pi = -2 \text{ kHz}$, where the positions of the resonance frequencies close to the pumped resonance are expressed with the series $\omega_\mu = \omega_0 + \sum_{i \geq 1} D_i \mu_i / i!$. The ring radius is $228.39 \mu\text{m}$ and results in a resonator free-spectral-range of $D_1/2\pi = 98.9 \text{ GHz}$, which was chosen to match the 100 GHz telecom ITU grid. In chapters 3, 4, 5 the resonators were operated in the strongly overcoupled regime with an intrinsic loss rate $\kappa_0/2\pi \sim 15 \text{ MHz}$ and bus waveguide coupling rate $\kappa_{\text{ex}}/2\pi$ ranging from 100 MHz to 160 MHz. Input and output coupling of light to and from the photonic chip is facilitated with double inverse tapers [43] and lensed fibres.

2.4 DKS applications

The pursuit of measuring optical frequencies led to the invention of mode-locked lasers and the 2005 Nobel prize being awarded to John Hall and Theodor Hänsch. This marked a new era in frequency metrology, allowing for the first time atomic clocks to be referenced to optical transitions. Kerr frequency combs enable similar functionality [44], but they can go substantially beyond due to their key features: they support three orders of magnitude of free spectral ranges, from GHz to THz level, and importantly, they can be integrated into photonic systems on chip. While the first aspect opens a window for new applications, potential for photonic integration is driving research towards practical, real-world uses for Kerr frequency combs. In the following paragraphs, I will provide a

brief overview of some of the key applications of DKS that have been demonstrated in recent years (cf. Fig. 2.11).

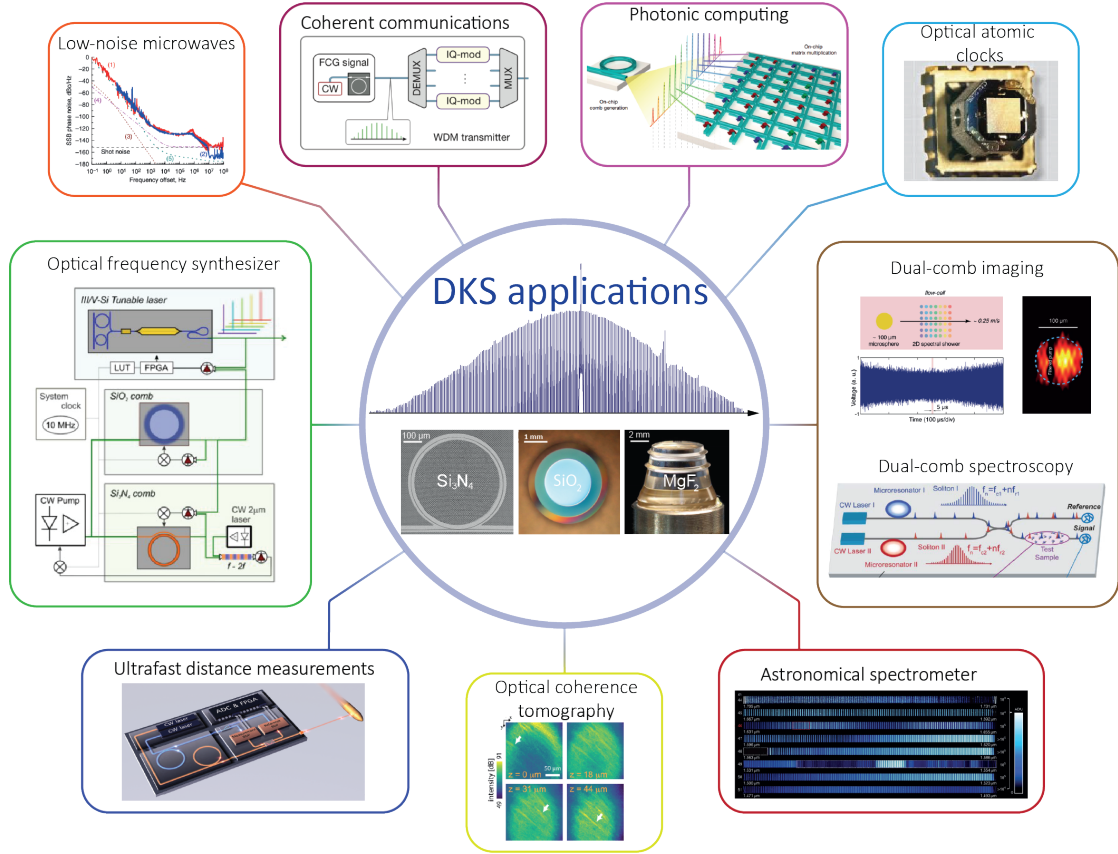


Figure 2.11: Application areas of microresonator-based DKS combs. The scheme was initially prepared by the author for [45], and adapted for the present work using images from [39, 46, 47, 48, 49, 50, 51, 52].

Microwave-to-optical link

As mentioned in the previous paragraph, integrated DKS have been demonstrated in optical-to-RF link for optical atomic clockworks [44]. Leveraging 5 orders of magnitude difference in absolute frequency, optical frequency division technique allows for low-noise microwave generation [53, 54, 48]. Absolute optical frequency synthesizer was demonstrated by Spencer et al. [55] utilizing self-referenced Si_3N_4 comb as a ruler.

Spectroscopy

Kerr frequency combs are an effective tool for spectroscopy measurements due to their broadband spectral coverage. Studies such as those in references [56, 49] have demonstrated a dual-comb approach, in which one comb is used to interrogate a target, while a second comb with a slightly different repetition rate is used to sample the first comb, allowing for the measurement of amplitude and phase changes due to the interaction. This technique builds on dual-comb spectroscopy using mode-locked lasers

[57], which gained popularity by offering the advantage of fast measurement time, high resolution, high sensitivity, and broadband coverage over traditional Fourier transform spectroscopy.

Telecommunications

Kerr combs are particularly well-suited for optical telecommunications. The 50 or 100 GHz ITU grid spacing and the ~ 70 nm spectral coverage of the C and L optical bands make them an excellent choice for a parallel laser source. In addition to showing impressive communication speeds [58, 39], Kerr combs have also demonstrated energy efficiency, being more cost-effective than an array of separate lasers [39, 59].

It is worth mentioning that the so called dark pulses - coherent solutions of LLE with normal dispersion (though it is more subtle according to M. Anderson [60]) - has been also repeatedly employed in coherent telecommunications demonstrations [61, 62], including recent petabit experiments [63]

Microwave (RF) photonics

Photonics is widely used in microwave waveform generation and signal processing. The generation of arbitrary RF waveforms has been demonstrated by accessing each comb line individually and manipulating its phase and amplitude with pulse shapers or spatial light modulators [64]. DKS can also be used for all-optical reconfiguration of microwave filters [65]. As for the RF signal detection, optical analog-to-digital conversion enables either usage of low-bandwidth electronics through the spectral slicing technique [66, 67], or record high acquisition bandwidths beyond 300 GHz [68]. The ultimate goal of microwave photonics is to develop a fully photonic-based radar, which has so far been demonstrated with mode-locked lasers [69].

Optical coherence tomography

Optical coherence tomography can benefit from the broadband spectral coverage of Kerr combs. Both coherent and incoherent combs have been demonstrated as a source for spectral domain OCT. [47, 70].

Astronomical spectrometer calibration

Kerr combs can be utilized to calibrate astronomical spectrometers for the detection of small Doppler shifts caused by the movements of distant stars due to the orbit of their planets. The measurement of these fine spectral changes is crucial in the search for exoplanets [71, 46]. Si_3N_4 microcomb was successfully employed to calibrate GIANO-B spectrograph at the Telescopio Nazionale Galileo (TNG), La Palma, Spain [71].

Photonic computing

The recent rise of photonic computing is supported by several advantages over its electronic counterparts. These advantages include the ability to perform massively parallel data transfer through wavelength division multiplexing and the use of multichannel sources like optical frequency combs. The extremely high data modulation speeds are

only limited by the bandwidth of on-chip optical modulators and photodetectors (Ref. [72]). Additionally, once the network is trained, the computations can be performed in a fully passive manner, without requiring extra power for multiply-accumulate operations (Ref. [73]). A study by Feldmann et al. (Ref. [51]) utilized dissipative Kerr solitons (DKS) for parallel vector matrix multiplication and demonstrated a photonic tensor core capable of performing convolution operations and image classification.

Novel theoretical concepts

The potential of frequency combs extends beyond the previously mentioned applications. There is also a vast array of new and exciting theoretical phenomena that have been observed or predicted to be possible with frequency combs. For instance, when frequency combs are generated in coupled microresonators or microresonator chains, they can be used to study novel physics, such as frequency combs as topological edge states [74], complex dynamics featuring exceptional points and parity-time symmetry systems [75, 76], synthetic frequency dimensions [77], and emerging nonlinear phenomena in photonic dimers [78].

Frequency comb based LiDAR demonstrations

The use of frequency combs for distance measurements has a long history. This stems from the pioneering work by Dankler [79], who first proposed the concept of multi-wavelength interferometry. This technique involves performing an interferometric measurement with a synthetic wavelength, $\Lambda = \lambda_1 * \lambda_2 / |\lambda_1 - \lambda_2|$, which extends the unambiguity range to millimeter or even meter range while maintaining precision.

Frequency combs, as multi-savelength sources, are well-suited for this type of application [80]. J. Ye took this idea further by combining time-of-flight and interferometric techniques in a single measurement using a dual-comb approach [81]. This was successfully demonstrated by Coddington et al. [82] using two mode-locked lasers, achieving 3 μm precision with time-of-flight measurements and 5 nm precision with the interferometric phase.

More recently, Trocha et al. [52] used Si_3N_4 microresonators and 100 GHz combs to achieve similar results, while Suh et al. [83] used two DKS generated in a single microresonator (co- and counter-propagation) for time-of-flight measurements only.

While dual-comb approaches have been successful in delivering high precision and ultra-fast measurements [82, 52], they are limited by an ambiguity range equal to the pulse repetition rate and by the fact that all optical pulses interrogate a single target. Additionally, they are prone to non-effectiveness due to deliberately mismatched repetition rates and subsequent deadtime, although this issue was addressed in Ref. [84] via time-programmable frequency comb.

2.5 Microresonator-based laser sources

The following section outlines the recent advancements in K-Lab at EPFL for creating photonic integrated lasers. Photonic integration not only brings benefits in terms of SWaP - size, weight, and power consumption, but it also allows for the performance *on par* with legacy lasers. The lab has made progress in developing ultra-low loss Si_3N_4 optical microresonators, which have found use in hybrid integrated narrow-linewidth lasers utilizing self-injection locking effect [85, 86]. Further efforts on integrating MEMS piezoelectric materials [53] added frequency agility functionality that makes such lasers useful in coherent ranging, OCT, and frequency domain reflectometry. These novel

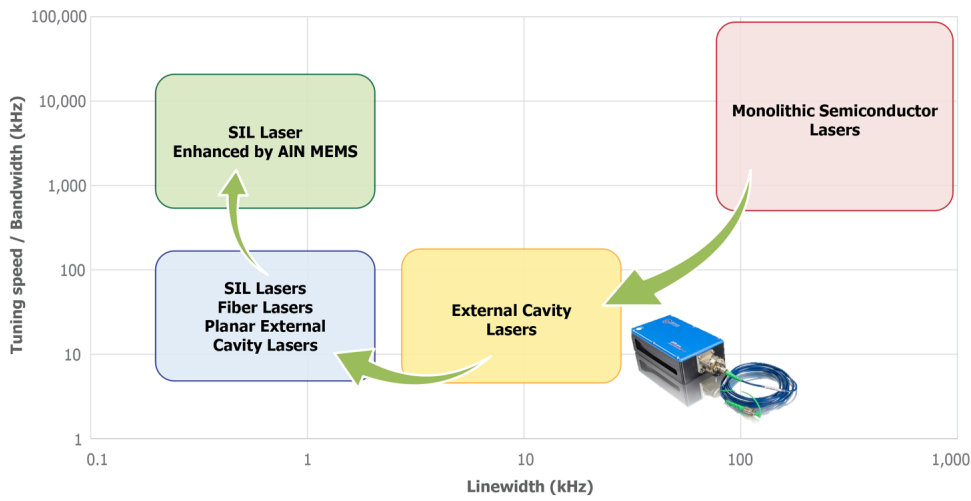


Figure 2.12: Different lasers on tunability vs. linewidth chart. Assembled by A. Voloshin.

photonic integrated lasers possess linewidths comparable to those of fiber lasers and the tuning abilities of distributed feedback (DFB) lasers. It is important to note that the photonic integration addressed the bottleneck of the laser technology where the laser cavity trades off tunability versus low noise operation (cf. Fig. 2.12).

Low-noise frequency-agile integrated laser

The study by G. Lihachev et al. [87] aimed to produce high coherence frequency-agile lasers for use in coherent sensing applications. They succeeded in creating a hybrid integrated laser that is low in phase noise and capable of petahertz chirp rates, using aluminum nitride and PZT actuators. The laser demonstrated a linewidth of a few kHz at millisecond integration times, with piezoelectric actuators providing a flat response of up to 10 MHz tuning frequencies and frequency excursions exceeding 1 GHz. The frequency sweeps were free of hysteresis and exhibited pre-calibration linearity of around 0.1%. The results were made possible by combining piezoelectric actuators

with apodization to suppress the mechanical modes of the chip. The processes used to produce the laser are accessible in semiconductor foundries and include photonic integrated circuits made of Si_3N_4 , AlN, and PZT MEMS processing, making them suitable for large-scale production.

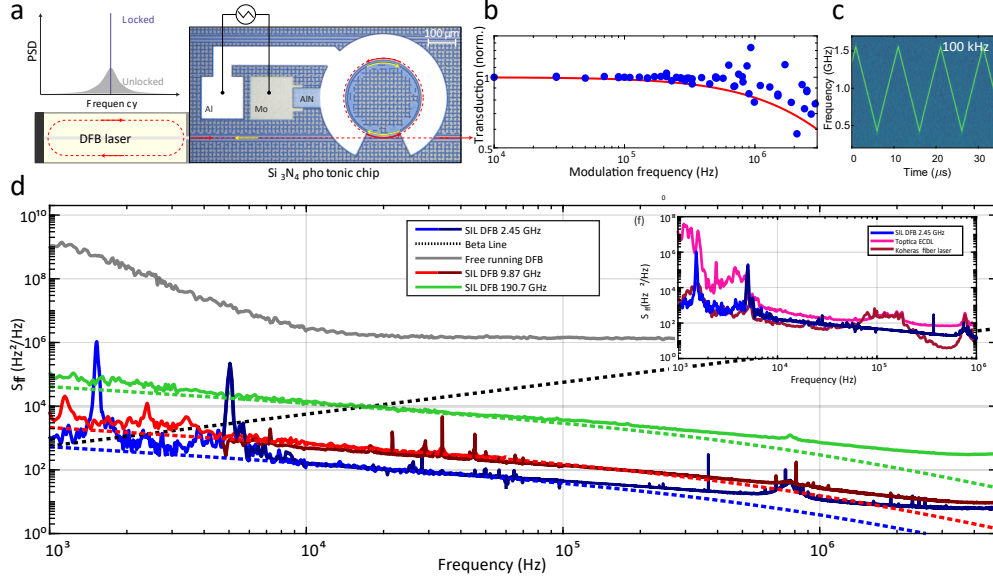


Figure 2.13: **Frequency-agile laser.** Figure adapted from [87]. a) The concept of self-injection locking. b) Frequency transduction by piezo actuators. c) Time-frequency spectrogram of the linear laser chirp. d) Single-sided PSD of frequency noise of the different hybrid integrated laser systems.

The frequency sweeps are hysteresis free and achieve pre-calibration linearity on the order of 0.1%.

Lasers based on integration with novel platforms

Further research is focused on exploring novel platforms and architectures. One such platform is lithium niobate, a material well-known in the telecommunication industry due to its widespread use in optical modulators, thanks to its electro-optic properties. Lithium niobate-based modulators are compatible with low-voltage CMOS electronics, providing an advantage over previous approaches that rely on piezoelectric actuators (AlN and PZT), which require tens to hundreds of volts for 1 GHz excursion tuning. Our team has successfully fabricated photonic circuits with thin film lithium niobate on a Si_3N_4 platform [88] and monolithic lithium niobate [89]. Both platforms demonstrated low-noise hybrid integrated lasers with petahertz-level frequency agility.

Other research directions include photonic hybrid integrated solutions at various wavelengths [90], the study of distributed bragg reflector laser architectures in combination

with piezoelectric actuators, Erbium doped Si_3N_4 waveguide lasers [91], and novel prospective materials compatible with silicon photonics such as barium titanate.

3 Massively parallel coherent laser ranging using soliton microcombs

This chapter reports on the study of frequency modulated dissipative Kerr soliton and its application to parallel coherent ranging. The results are partially adapted from J. Riemensberger, **A. Lukashchuk**, *et al.*, "Massively parallel coherent laser ranging using a soliton microcomb", *Nature*, 581, p.164, (2020).

The methods and procedures to implement a LiDAR device based on a frequency modulated soliton are also patented: **A. Lukashchuk**, J. Riemensberger, T.J. Kippenberg, "Optical frequency comb based parallel fm lidar", EU Patent №: EP4062192A1



Figure 3.1: Nature Journal cover. May 2020. Rendered by the author and Ryan Allen.

3.1 Introduction

We talked about main challenges of coherent LiDAR in chapter 1. Here, we tackle the parallelization problem of FMCW LiDAR. The new method described in the current chapter presents and investigates a new state of the dissipative Kerr soliton - frequency-modulated DKS, and also shows generation of tens to hundreds highly-coherent frequency chirped laser lines, thereby allowing massively parallel FMCW ranging.

First of all, we showed that, surprisingly and counter-intuitively, we can maintain dissipative Kerr soliton states in photonic chip based micro-resonators, despite very rapid, non-adiabatic changes of the pump laser, that encompass the entire soliton existence range (several GHz; *compare with cavity linewidth of 15 MHz*). This finding *per se* is remarkable, as one expects the soliton to be lost if the external excitation parameters are varied in such perturbative fashion ¹. We demonstrated that we can attain 2.5 GHz scan

¹Back in the days, my colleagues working in BM lab were asking their opto-mechanics fellows to close the exit door in a very gentle manner. We needed our solitons to be 'alive' and avoided any unnecessary perturbation

amplitudes at up to 10 MHz scan rates. We experimentally studied chirp transduction, its linearity properties as well as soliton dynamics effects on the chirp. In a proof-of-concept experiment, employing simple off-the-shelf telecommunication equipment, we performed distance and velocity measurements in a parallel fashion.

This approach allowed for the first time a massively parallel coherent LIDAR, whose distinct comb teeth, could be readily dispersed and used for individual detection. We increased the volumetric scan rates of coherent ranging by more than an order of magnitude utilizing a single narrow linewidth and frequency agile laser source only. We employed >30 distinct channels, demonstrating both parallel distance and velocity measurements at an equivalent rate of >3 Mpixel/s, with potential to improve sampling rates beyond 150 Mpixel/s and increase the image refresh rate of FMCW LiDAR up to two orders of magnitude without deterioration of eye safety.

The approach is based on and compatible with current generation photonics integrated circuits, and if combined with phased arrays [92] based on nanophotonic gratings [93], can provide a technological basis for compact, massively parallel and ultra-high frame rate coherent LiDAR systems.

3.2 Frequency-modulated soliton

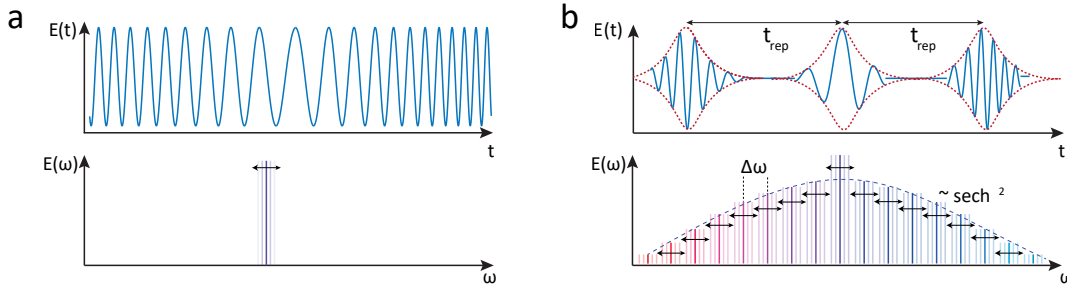


Figure 3.2: Frequency-modulated soliton. Principle of dissipative Kerr soliton (DKS) generation in a microresonator with a frequency agile laser. By chirping the continuous wave pump laser (a), the soliton pulse stream (b) exhibits a change in the underlying carrier, while the pulse to pulse repetition rate remains unchanged. In the frequency domain this corresponds to scanning each individual comb tooth, i.e. a change of the carrier envelope frequency only.

First, I would like to draw a comparison between Kerr solitons and mode-locked lasers. One of the key differences is the pump mode. In a Kerr soliton, the laser pump is the exact mode of the generated microcomb, while in the case of mode-locked lasers, the gain bandwidth and cavity dispersion determine the overall mode distribution. This fact, in the former case, allows for independent access to the global offset frequency of the comb. Recall that the frequency comb is parameterized by $f_n = f_{\text{microceo}} + n \times f_{\text{rep}}$, where $f_{\text{pump}} = f_{\text{ceo}}$ for microcombs. It is possible to achieve a frequency-modulated (FM) coherent comb if the comb can be preserved while the pump is swept.

In the time domain (see Fig. 3.2), the underlying soliton carrier frequency is modulated, while changes to the pulse envelope and repetition rate are kept to a minimum. In the frequency domain, this corresponds to concurrent modulation of the optical frequency of each comb tooth around its average value, i.e., a modulation of the frequency comb's carrier-envelope frequency.

Fig. 3.3 describes a basic setup for FM soliton generation. We set up a frequency-agile pump laser using a CW external cavity diode laser (ECDL) coupled into an electro-optical phase modulator (EOM) for measurement of the relative laser cavity detuning, and dual Mach-Zehnder modulator (SSB) biased to single sideband modulation, which was driven by a frequency-agile voltage controlled oscillator (VCO, 5-10 GHz) and an arbitrary function generator (AFG).

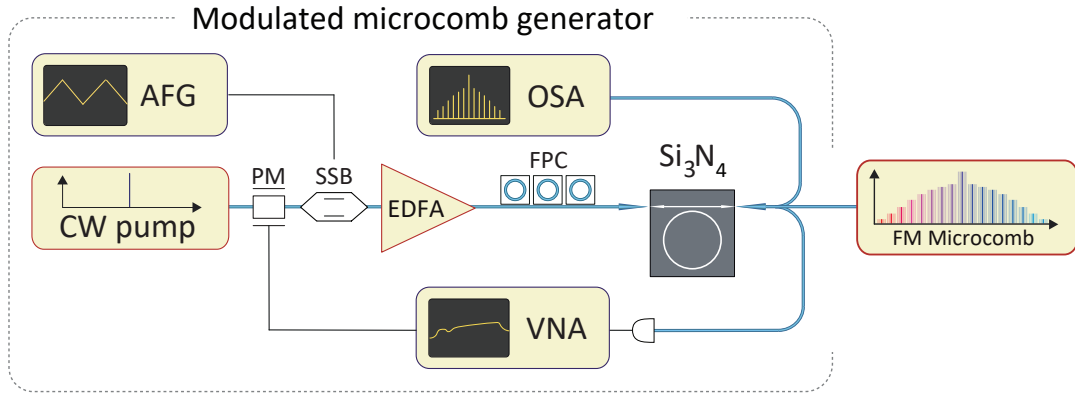


Figure 3.3: **Frequency-modulated soliton generation setup.** An amplified external cavity diode laser (ECDL) laser at 193 THz generates a soliton microcomb on the photonic chip. Frequency modulation is applied with a single sideband modulator (SSB). Optical spectrum analyzer (OSA) and vector network analyzer (VNA) are used for soliton state characterization.

The cw laser was amplified to 1.7 W and 1 mW is split off in a separate imbalanced Mach-Zehnder fibre interferometer for chirp linearization purposes outlined below. We generated a DKS by coupling the FM pump laser onto the photonic chip and tuning of the laser into resonance and single soliton state using the established piezo tuning scheme [29]. We monitored the detuning with respect to the Kerr shifted cavity resonance and the bistable soliton response using a VNA driving a weak phase modulation via an inline electro-optical-modulator and an optical spectrum analyzer. The generated soliton was coupled back into optical fiber, the residual pump light was filtered and the soliton pulse train was amplified with a gain-flattening erbium-doped fiber amplifier (EDFA). We aligned the cavity pump resonance to the ITU telecom channel C30 at a wavelength of 1553.3 nm using a thermo-electric cooling (TEC) device located below the active chip. The neighboring resonances overlapped with the standard ITU grid (192 THz + $n \cdot 100$ GHz) owing to the comb FSR of 99 GHz.

While it is possible to directly modulate all comb teeth post DKS generation, this method

suffers from excess insertion loss of the SSB modulation and leads to the generation of unwanted RF modulation sidebands at all the comb teeth. Moreover, we want to highlight the feasibility of our scheme irrespective of the choice of laser and microresonator actuation schemes.

3.3 Concept of soliton-based parallel FMCW ranging

The path to massively parallel coherent LiDAR is straightforward, given the ability to generate a FM soliton. Fig. 3.4 illustrates the principle. The underlying idea is to transfer the chirp of a narrow linewidth pump laser (which could be used as a standalone LiDAR source) to multiple comb sidebands by using it to generate a FM DKS. This in turn will result in a massively parallel array of *independent* FMCW lasers.

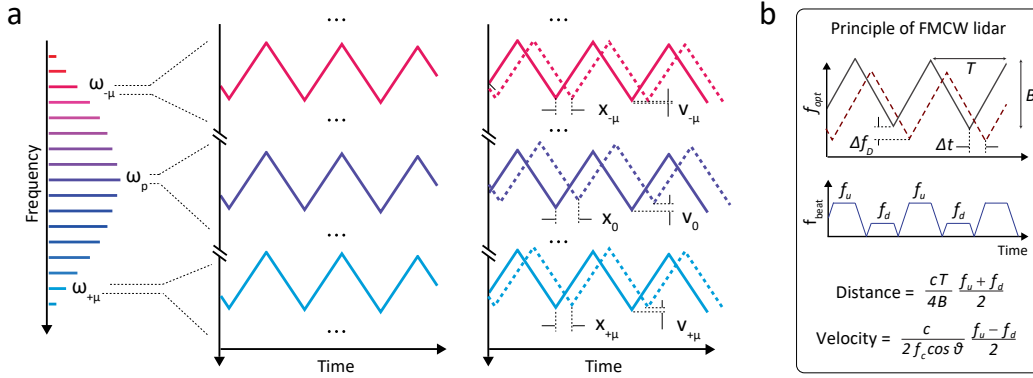


Figure 3.4: **Concept of massively parallel FMCW LiDAR using soliton microcombs.** a) Principle of coherent velocimetry and ranging with multiple optical carriers isolated from a soliton microcomb. Interleaved upwards and downwards frequency slopes map the distance and radial velocity of target objects onto the mean and the separation of two intermediate frequency beat tones in a delayed homodyne detection scheme. b) Schematic of the detected beat notes arising in coherent LiDAR ranging of a moving object outlined in 1. Every optical channel after photodetection will result in two homodyne beat notes during one scan period of the laser.

The novel scheme leverages three key properties of DKS; the large (i.e. GHz) existence range of the soliton, the fact that repetition rate changes associated with laser scanning are small, and the possibility, as detailed below, to very rapidly sweep between stable operating points without destroying the soliton state or deterioration of the chirp linearity.

Fig. 3.5 illustrates the LiDAR implementation using a FM DKS. Wide spectral bandwidth occupied by the comb lines suggests usage of diffractive optics. This fact eases the requirements on scanning optics, mainly galvo mirrors, as one dimension can be scanned simultaneously in a parallel and passive fashion. We homodyne detected the reflected signals with their original replicas channel-by-channel using low bandwidth detectors and digitizers. The reconstructed RF signals for *each comb line* μ , yielded velocity and

distance (x_μ, v_μ) for each target pixel. The presented scheme thus enables true parallel detection of dozens and potentially hundreds of pixels simultaneously.

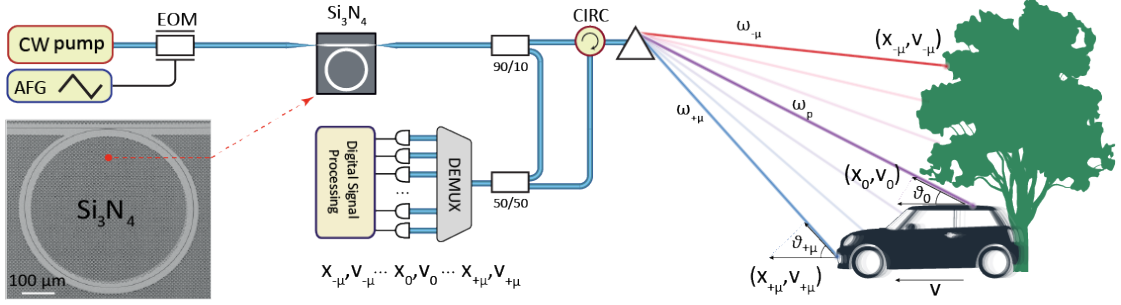


Figure 3.5: **Experimental schematics of soliton based FMCW LiDAR.** Schematic outline of the proposed system design. A frequency modulated pump laser drives a photonic integrated Si_3N_4 microresonator. Each individual sideband, spatially dispersed with diffractive optics, serves as source of FM modulated laser light in a parallel detection scheme. Bottom left - Electron microscope picture of $228.43 \mu\text{m}$ Si_3N_4 microring resonator.

It is important to mention, that our approach contrasts from dual-frequency comb based coherent time-of-flight systems [83, 52], which on the other hand achieve best distance precision and acquisition speeds, yet exhibit a limited ambiguity range dictated by the pulse repetition rate, and are challenging to parallelize as the whole frequency comb must illuminate a single pixel. In a similar fashion, coherent stitching of multiple channels from an electro-optical frequency comb generator can be used to improve the distance measurement accuracy of FMCW [94], yet demands the spectral overlap of adjacent comb modes and concurrent illumination of a single pixel.

3.4 Frequency modulated DKS dynamics and Raman nonlinearity

Fig. 3.6a shows the optical spectra of the 99 GHz DKS at the extrema of the soliton existence range with relative laser-cavity detuning $\Delta_1 = 1.2$ GHz and $\Delta_2 = 2.9$ GHz. Increasing the detuning, we observed well known temporal compression (58 fs to 45 fs) [36] and Raman self-frequency shift ($\Omega_R/2\pi = 2$ THz) [38] of the DKS. Interestingly, despite the frequency excursion strongly exceeding the overcoupled cavity linewidth ($\kappa_0/2\pi = 15$ MHz, $\kappa_{\text{ex}}/2\pi = 100$ MHz) the power of comb teeth between 190 THz and 200 THz did not change by more than 3 dB, providing therefore more than 90 channels suitable for coherent LiDAR. The relative laser detuning can be inferred from the phase modulation response spectrum (cf. Fig. 3.6b), wherein the C -resonance peak directly

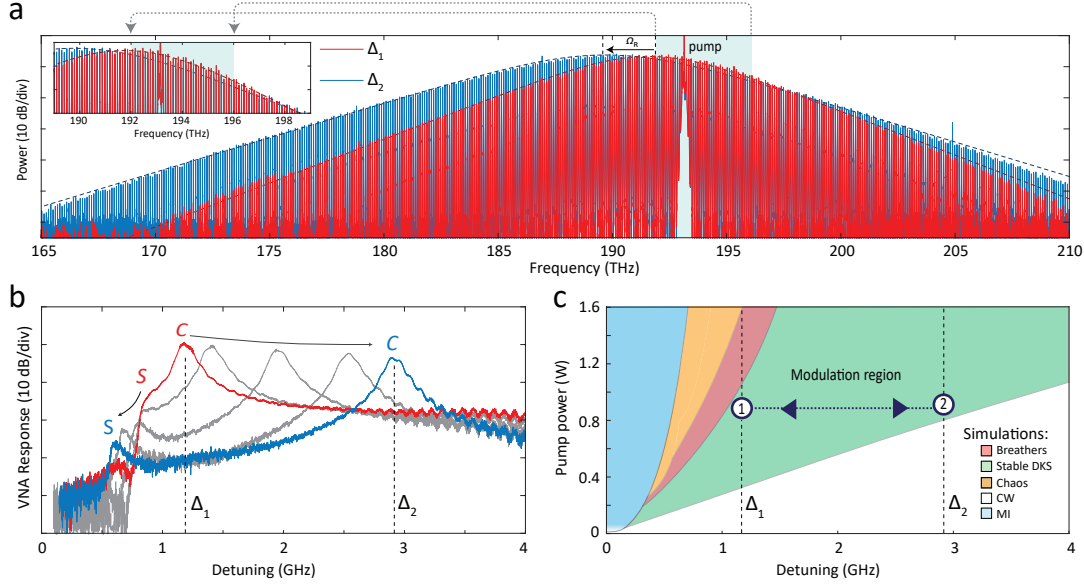


Figure 3.6: Dynamics of frequency-modulated soliton microcombs a) Optical spectra of a 99 GHz dissipative Kerr soliton (DKS) at relative laser cavity detuning $\Delta_1 = 1.2$ GHz and $\Delta_2 = 2.9$ GHz, respectively. The Raman self-frequency shift $\Omega_R/2\pi$ of the soliton is highlighted. Inset: Spectral region of FM LiDAR operation showcasing individual line flatness better than 3 dB over the full pump laser frequency excursion range. b) Phase modulation response of DKS measured with vector network analyzer. c) Simulated stability chart of the soliton microcomb for the device used in the LiDAR experiments. The soliton existence range is highlighted in green and confined by the stability of the soliton solution.

reveals the relative detuning between the cavity resonance and the CW pump laser [29].

We next performed numerical simulations based on the Lugiato-Lefever equation (LLE) [34, 95], which demonstrate the ability of the DKS state to transfer the chirp from the pump to all comb teeth (cf. Fig. 3.7). The numerical laser scan started at $\Delta = -0.4$ GHz and the detuning was subsequently increased with a linear chirp rate of $|\frac{d\Delta}{dt}| = 4 \cdot 10^{15}$ Hz², tuning past the modulation instability region (MI) exciting a single soliton. Hereafter, the linear laser scan was inflected and a symmetric triangular FM with equal chirp rate was continued. If stimulated Raman effects [38, 96] and higher order dispersion were neglected, the repetition rate remained almost perfectly constant and the frequency chirp was faithfully transduced to each comb line. Even more surprisingly, the inclusion of stimulated Raman scattering and third order dispersion effects, only induced a small repetition rate mismatch Δf_{rep} of 20.6 MHz per 1.7 GHz of laser tuning (cf. Fig. 3.7b), which was observed as acceleration and deceleration of the soliton in the cavity (cf. Fig. 3.7a). This phenomena can be intuitively understood, if one considers soliton propagation in the cavity. Higher detuning results in higher Raman shift. Raman shift effectively shifts the ‘center of mass’ of the soliton (cf Fig. 3.6a) and thus its group velocity changes (which is dependent on the center frequency of the pulse due to the dispersion). Faster

group velocity corresponds to the lower repetition rate and lower group velocity - to the higher f_{rep} .

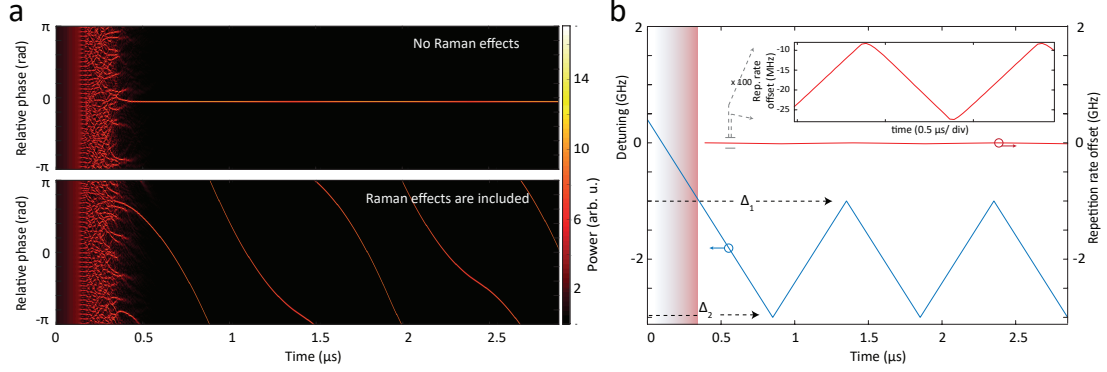


Figure 3.7: **Dynamics of frequency-modulated soliton microcombs** a) Numerical simulation results of FM DKS. Intracavity phase profile in the presence of the pump frequency modulation at 1 MHz rate with and without Raman effects. b) The laser is tuned through the modulation instability region (blue shaded area) and the breathing region (red shaded area) into the soliton state and triangular FM is imprinted at a chirp rate of $(d\omega_L/dt)/2\pi \approx 4 \cdot 10^{15} \text{ Hz}^2$. The inclusion of stimulated Raman scattering into the simulation reveals a modulation of the repetition rate of up to 15 MHz during the FM cycle.

The fundamental limit for the tuning speed is set by the cavity photon decay rate $\frac{d\Delta}{dt} < (\kappa)^2/2\pi$. In our case this would result in $\sim 10^{17} \text{ Hz/Hz}$ tuning rates or 10 GHz excursion at 10 MHz modulation. Counter-intuitively, a 'bad' cavity with low quality factor could attain much higher rates. However, soliton generation might be quite challenging in such cavities and would require high pump power for soliton generation and even higher powers for accessing modulation region with excursions of few GHz.

The linear (in the leading order) dependence $\frac{df_{\text{rep}}}{d\Delta} \approx \frac{\Omega_R}{2\pi} \frac{D_2}{D_1}$ results in a spectral channel-dependent bandwidth. Hence, a the measured LiDAR distance would require a constant rescaling factor, which we can determine during calibration. Only nonlinear dependencies of the pulse repetition rate f_{rep} on the detuning Δ , from either the Raman shift [97] or multimodal interactions [96] actually degrades the linearity of the transduced chirp. The maximum detuning, which still supports stable DKS generation is determined by the input pump power [36], which in turn is fundamentally limited by a Raman instability [98].

3.5 Pump chirp linearization and calibration

FM LiDAR requires highly linear chirp ramps in order to achieve precise and accurate distance measurements [10]. We implemented a digital pre-distortion circuit in order to minimize the chirp nonlinearity of the pump frequency sweep, similar to prior implementations [99]. The optimization procedure was applied in two configurations to

measure the pump frequency chirp, either via **heterodyne** with a reference laser, or via delayed **homodyne** detection in an imbalanced Mach-Zehnder interferometer (MZI).

Two techniques are almost identical and give similar results. However, the heterodyne technique is simpler for linearity analysis, since the whole waveform is detected directly, while in case of homodyne detection, the waveform should be numerically retrieved and it appears to be undetermined in the regions of extremal points. The beat frequency zeros down in those points and the phase becomes ambiguous, which necessitates exclusion of extremal regions.

Heterodyne characterization technique

The setup and optimization results for this method are detailed in Fig. 3.8. The chirp

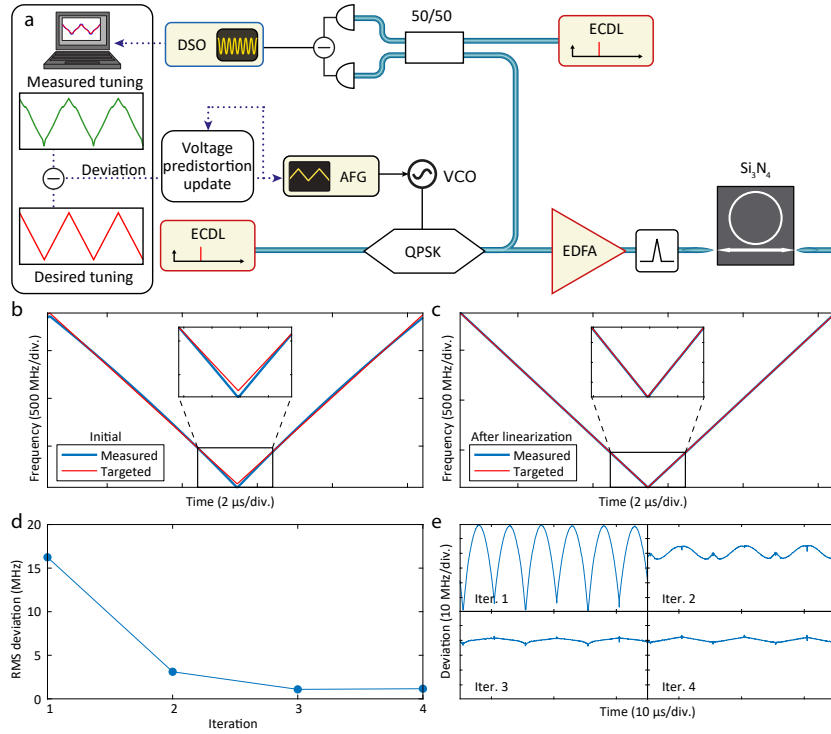


Figure 3.8: **Pump frequency sweep linearization via the heterodyne method** a) Setup for pump laser frequency measurement via heterodyne beat note and chirp linearization feedback. b) Initial frequency modulation, when the VCO is driven with a triangular ramp. The measured frequency is compared with the targeted ideal modulation. The ramp frequency is 100 kHz. c) Final triangular frequency modulation pattern, after 4 iterations. d) Evolution of the RMS frequency deviation during the optimization loop. e) Evolution of the deviation between measurement and target sweep, at each iteration of the loop.

was applied to the CW laser with a VCO-driven single sideband modulator. The VCO was initially driven by a simple triangular function generated with the AFG. The driving voltage was then iteratively corrected to improve the chirp linearity. After

modulation, a fraction of the light was picked up to generate a beat note with a reference external cavity diode laser. The downmixed laser frequency was sampled on a real-time oscilloscope (20 GSa/s) and digitally processed to perform a short-term Fourier transform followed by peak detection. The resolution bandwidth Δf of the transform window is adjusted to minimize the effective linewidth of the chirped signal $\Delta f = \sqrt{\frac{2B}{T}}$. The measured frequency evolution was fitted with a perfect triangular function having a fixed target frequency excursion. This allowed the deviation from the desired frequency chirp to be assessed. The frequency deviation was then converted to voltage – after computing the average voltage-to-frequency coefficient of the VCO – and then added to the current tuning function of the AFG. This procedure effectively addresses the nonlinear response of the VCO, as shown in Fig. 3.8b-e. The optimization procedure was applied successfully at different tuning speeds (10 kHz – 10 MHz), as shown in Fig. 3.9. However, with increasing tuning speed, the residual RMS deviation increases, which we attribute to the limited tuning bandwidth of the VCO.

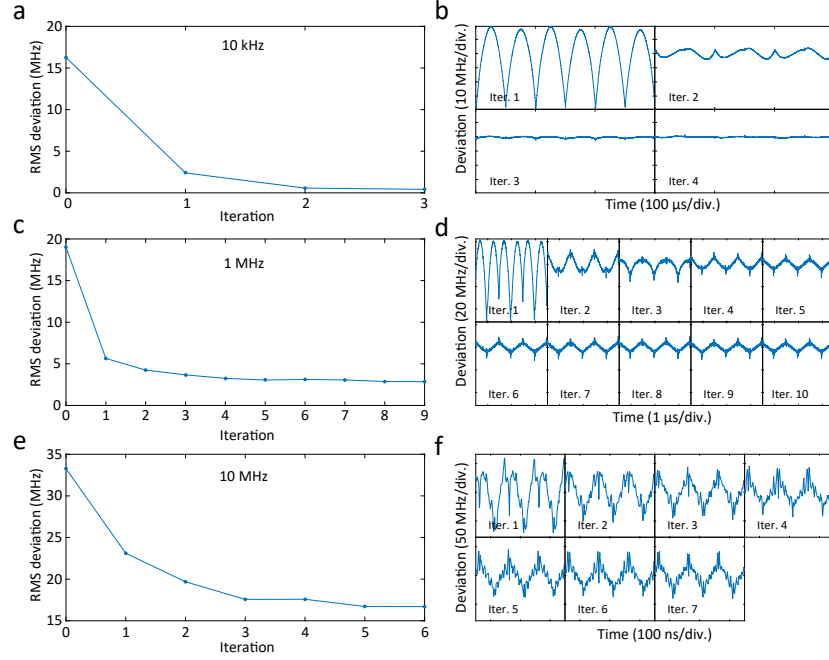


Figure 3.9: **Linearization results at different modulation frequencies** a) c) e) Show the evolution of the RMS frequency deviation during the optimization loop for modulation frequencies of 10 kHz, 1 MHz and 10 MHz, respectively. b) d) f) Corresponding evolution of the deviation between the measurement and the target sweep, at each iteration of the loop.

Homodyne characterization technique

Homodyne linearization technique requires only a frequency discriminator such as MZI interferometer without the need for auxiliary laser and is widely employed in real LiDAR systems [100, 101]. Its implementation is rather simple and straightforward

(cf. Fig. 3.10), and in terms of post-processing it requires calculation of the Hilbert transform only [102, 103]. The key underlying idea is that the phase of the selfhomodyne detected RF current is proportional to the optical instantaneous frequency, while the proportionality coefficient is the optical path length in a delay line. Thus the Hilbert transformation of the current directly results in the chirped frequency of the FM source.

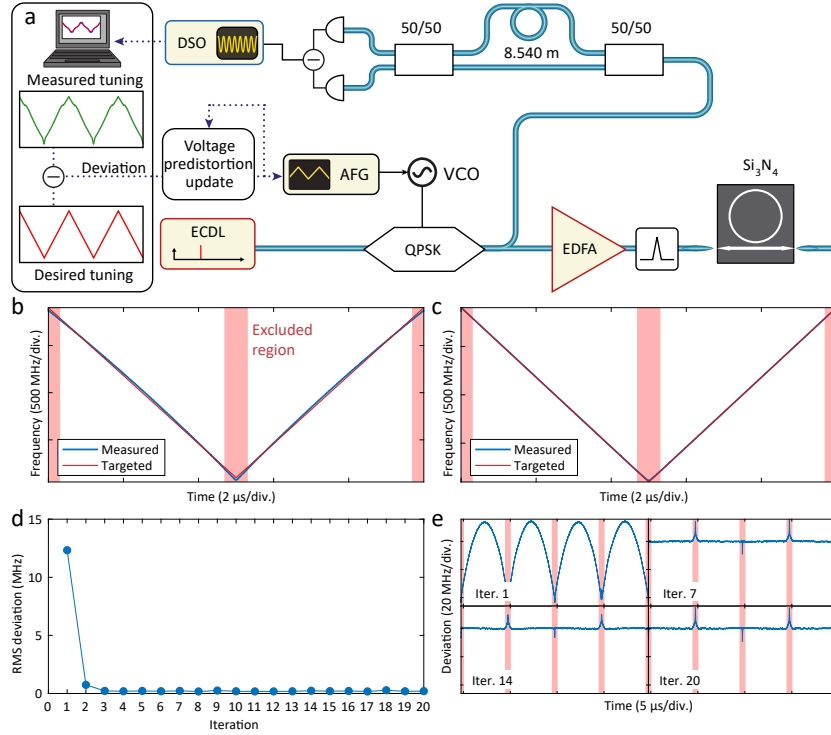


Figure 3.10: Pump frequency sweep linearization via the delayed homodyne method a) Setup for pump-laser frequency measurement via delayed homodyne detection and chirp linearization feedback. Calibration of the MZI is performed by fitting the frequency-dependent phase modulation response of the MZI. b) Initial frequency modulation, when the VCO is driven with a triangular ramp, determined using a Hilbert transform. The measured frequency is compared with the targeted ideal modulation. The ramp frequency is 100 kHz. The red-shaded regions around the extremal points are excluded from the linearization update. c) Final triangular frequency modulation pattern, after 20 iterations. Convergence achieved after four iterations. d) Evolution of the root-mean-square frequency deviation during the optimization loop. e) Evolution of the deviation between measurement and target sweep, at each iteration of the loop.

Like in the previous implementation, we iteratively updated the AFG waveform by calculating the residual frequencies between instantaneous frequency chirps and ideal triangular waveform. The length difference of the calibration MZI arms (12.246 m) was determined by fitting the \sin^2 function to the VNA spectral response function of the MZI (technique described in Appendix).

3.6 Characterization of parallel FMCW LiDAR source

Next, we experimentally demonstrated the ability to faithfully transfer the pump laser chirp to the soliton microcomb sidebands. In our analysis, we employed heterodyne and homodyne techniques in similar to the upper section fashion. The former gave access to the true down-converted waveform and was used to demonstrate time-frequency maps and analyze linearity. While for the channel dependent excursion calibration we employed both techniques with similar results.

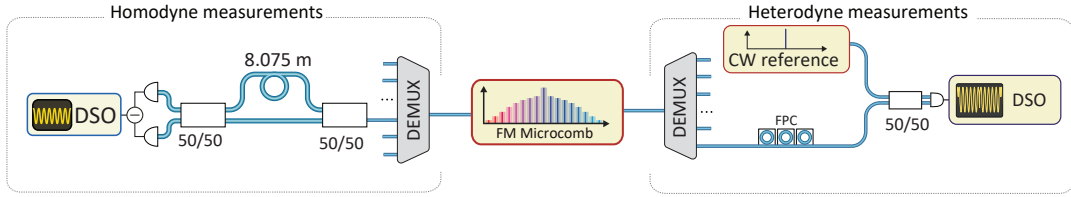


Figure 3.11: **Frequency-modulated soliton.** Setup for parallel FMCW LiDAR source characterization. Similarly to the upper section, we employed both homodyne and heterodyne detection techniques.

In general, heterodyne characterization of the transduced modulation avoids possible ambiguities of delayed homodyne detection and catches high frequency noise components obscured in low bandwidth detection. Fig. 3.11 depicts the experimental schematics. The spectral channels were isolated using a commercial telecom WDM demultiplexer based on planar arrayed waveguide gratings and superimposed on a high-bandwidth (10 GHz) balanced photoreceiver. The fast realtime sampling oscilloscope (40 GS/s) recorded the data.

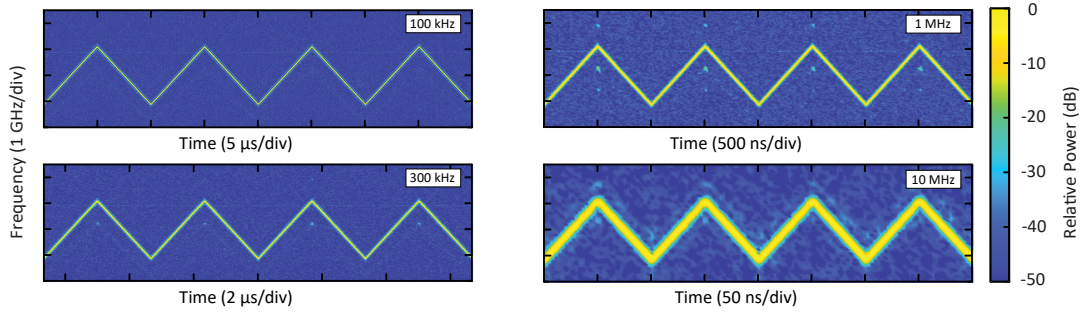


Figure 3.12: **Time-frequency analysis of the transduced chirps.** Time-frequency maps of 1.6 GHz pump laser chirps at modulation frequencies from 10 kHz to 10 MHz, detected at the $\mu = +20$ comb sideband (195 THz).

Results for the comb tooth at 195 THz ($\mu = +20$) and modulation frequencies $1/T$ from 100 kHz to 10 MHz are depicted in Fig. 3.12. We calculated the instantaneous frequency via short-time Fourier transform using a 4th-order Nuttall window. The optimal resolution bandwidth Δf of the transform window was again (similar to the

heterodyne pump linearization above) selected to minimize the effective linewidth of the chirped signal $\Delta f = \sqrt{\frac{2B}{T}}$. By tuning the second ECDL close to the individual comb sidebands, we could separately measure the transduced frequency modulation patterns for each comb sideband within the bandwidth of the demultiplexer. The resulting time frequency maps for modulation frequencies 100 kHz and 10 MHz across 4 modulation periods are depicted in Fig. 3.13.

Note that the frequency excursion bandwidth B_μ increases linearly with the channel number μ (or increasing frequency, cf Fig. 3.14a). The chirp amplitudes or excursions are depicted in Fig. 3.14c. The increase rate of $\frac{dB_\mu}{d\mu} = 22.15$ MHz is in agreement with the predictions from numerical simulations including stimulated Raman scattering (cf. Fig. 3.7).

Almost linear change of the frequency excursion is the manifestation of the Raman effect. Despite solely varying f_{ceo} , the FM DKS experiences a slight change in f_{rep} . The comb lines further away from the pump undergo $\mu \cdot f_{\text{rep}}$ variation. The soliton self-frequency shift varies nonlinearly with detuning [97, 104]. That's why the comb lines with larger $|\mu|$ oscillate in a less linear fashion (cf. Fig. 3.14d). However the excursion amplitude is lower for the frequencies below the pump, that is why the RMS nonlinearity (normalized to the amplitude) still decreases. We define the chirp nonlinearity as the deviation of the measured instantaneous frequency from a perfectly symmetric triangular FM scan, estimated with least-squares fitting as shown in Fig. 3.14b. The channel dependent RMS nonlinearity remains below 1/500 of the full frequency excursion for all channels at 100 kHz modulation frequency. Narrow peaks of the chirp nonlinearity (194 THz channel in Fig. 3.14b) are attributed to single-mode dispersive waves [96]. We do not observe intermode breathing of the soliton [105] in the present system.

Next, we study the chirp transduction by analyzing Fourier components of the FM comb chirps. Recall that the Fourier representation of a triangular wave is $x_{\text{triangle}}(t) = \frac{8}{\pi^2} \sum_{i=0}^{N-1} (-1)^i n^{-2} \sin(2\pi nt/T)$, where T is the modulation period. We determine frequency-dependent transduction from the intensities of the 1st to 9th harmonic of the triangular FM spectrum, which we normalize with respect to the corresponding pump modulation amplitude. Figs. 3.15c,d show the transduction of channel $\mu = +20$ at 100 kHz and 10 MHz modulation frequencies. One can clearly observe the response degradation at Fourier frequencies higher than 100 MHz.

We analyzed different comb channels with modulation frequencies from 10 kHz to 10 MHz (cf. Fig. 3.15). The total measurement duration was between 0.5 ms (10 kHz) and 30 μs (10 MHz). We found a lower bound for the 3 dB modulation frequency cutoff of 40 MHz, which corresponds to a maximum per-channel chirp rate of $1.6 \cdot 10^{17} \text{ Hz}^2$. The estimated accumulated chirp rate of all channels thus rivals state-of-the-art swept source lasers, which achieve chirp rates of $10^{18} - 10^{19} \text{ Hz}^2$ [106].

3.6 Characterization of parallel FMCW LiDAR source

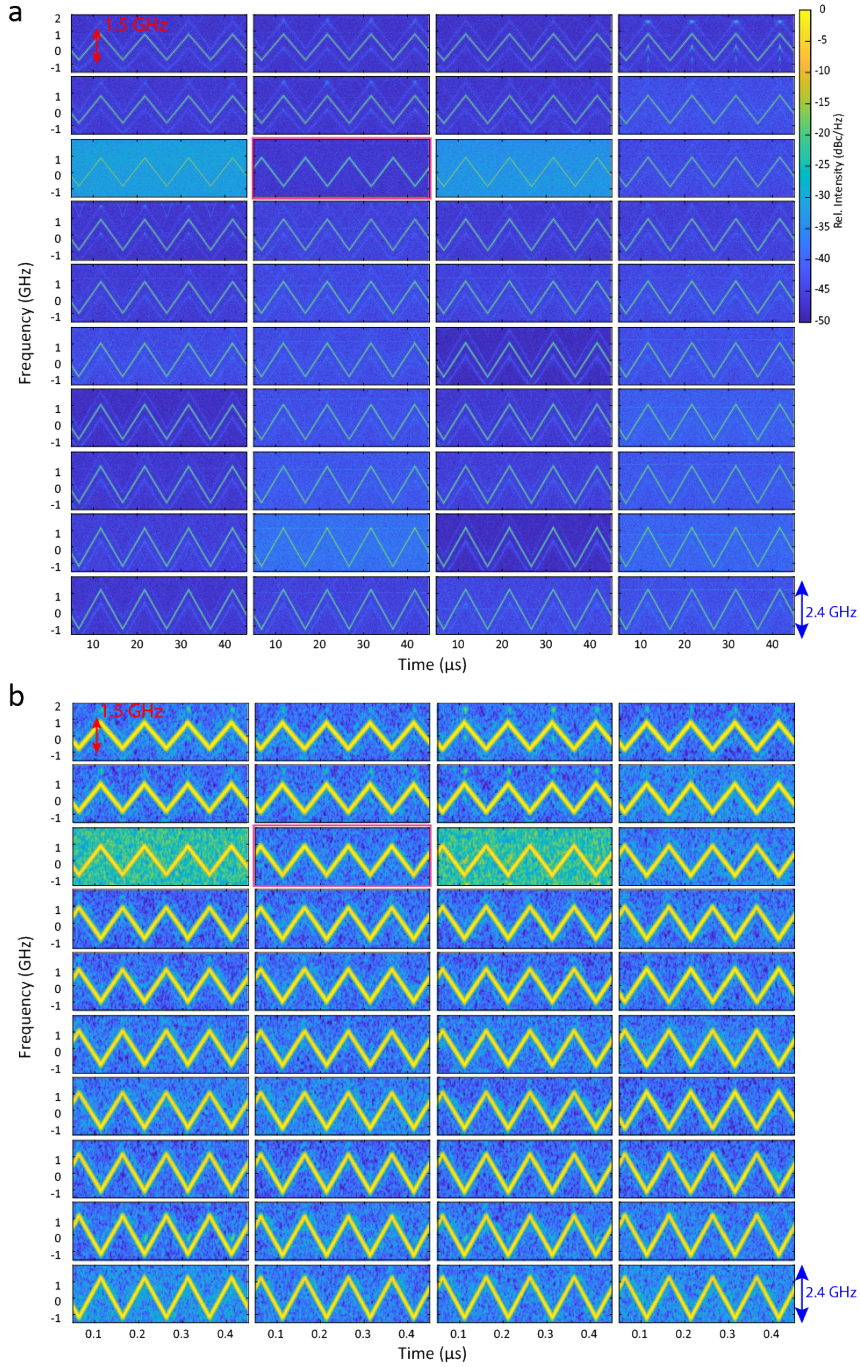


Figure 3.13: **Channel-by-channel analysis of heterodyne chirp characterization** a) Time-frequency maps obtained via short-time Fourier transform of the heterodyne beat detection of the individual FMCW channels. Top left to bottom right panels denote optical carriers between 192.1 THz and 196 THz. Modulation frequency 100 kHz. The pump channel at 193 THz is indicated in purple. b) Same as a) but for modulation frequency 10 MHz.

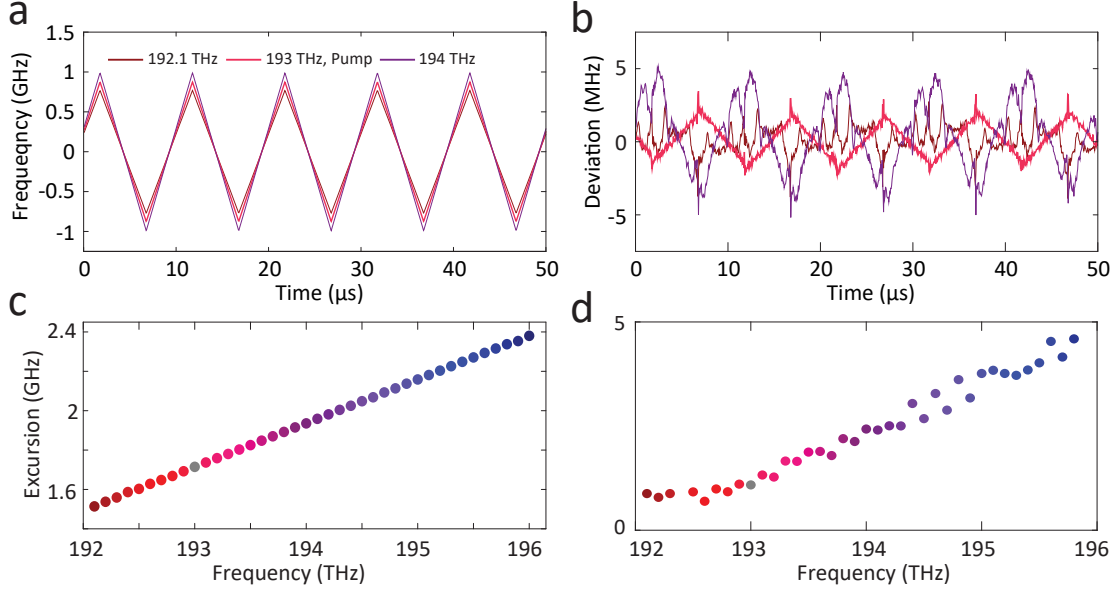


Figure 3.14: **Frequency excursion of FM comb lines** a) Instantaneous frequency of the heterodyne beat note determined by short-time Fourier transform at 100 kHz modulation frequency. b) Deviation from a perfect triangular scan calculated by least-squares fitting. c) Channel-dependent frequency excursion at 100 kHz modulation frequency. d) RMS deviation from perfectly triangular modulation pattern.

A fine analysis further reveals that for low modulation frequencies, weak even order sidebands arise. We attribute it to the hysteresis effect, which accompanies the generation of single mode dispersive waves [96, 105] essentially introducing a small asymmetry in the transduced chirp.

An experimentally observed tuning rate transduction limit of $\sim 10^{17}$ Hz matches the theoretical prediction arising from the cavity response time. However, it could be also limited by the actuation bandwidth of the AFG (100 MHz bandwidth) and VCO.

3.7 Parallel ranging, velocimetry and 3D imaging

Next, we performed a proof-of-concept demonstration of the massively parallel LiDAR system. The experimental setup is illustrated in Fig. 3.16a. The calibrated FM microcomb was amplified up to ~ 500 mW and split (90/10) into a signal and a local oscillator paths. A total power of 350 mW was emitted from the collimator, which equated between 5 mW and 20 mW per comb line. A transmission grating (966 lines/mm) spectrally dispersed the individual signal comb lines along the circumference of the small flywheel (radius 20 mm) mounted on a DC toy-motor. We used separate collimators for the transmit and receive path in a bistatic scheme to minimize spurious backreflection in the fiber components. Two commercial DEMUX units spectrally separated signal and LO comb lines. We employed two 1x40 mechanical optical switches to allow

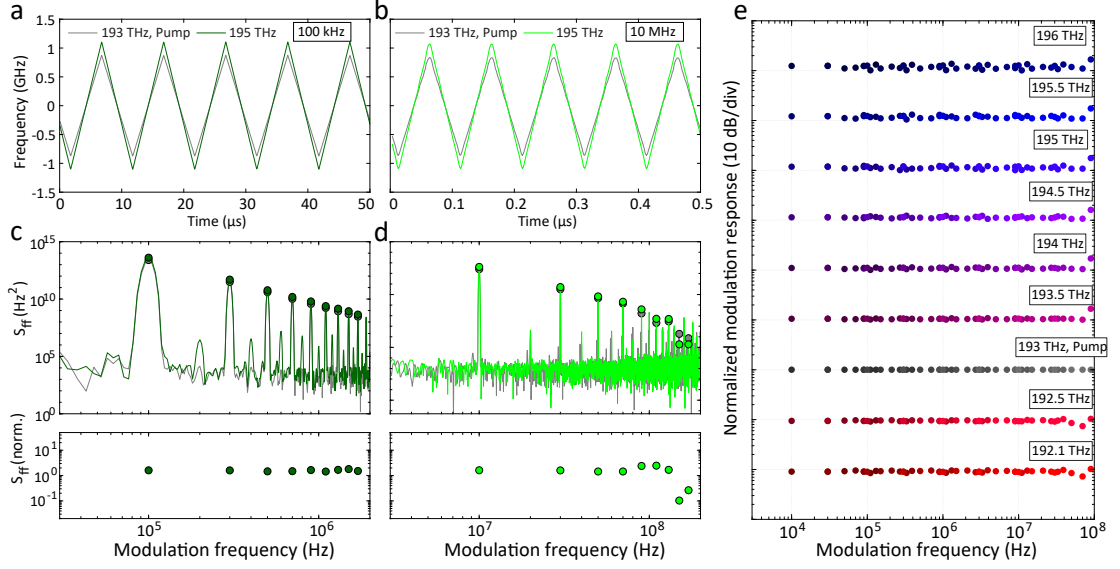


Figure 3.15: Frequency-dependent transduction of carrier modulation from pump to comb sidebands a) Time dependent frequency of pump laser at 193 THz (grey) and 195 THz comb sideband ($\mu = 20$, dark green) and modulation frequency 100 kHz. b) Same as a), but for modulation frequency 10 MHz. c) Power spectral density of frequency modulation S_{ff} for pump (grey) and sideband (dark green). The Markers denote the positions of harmonics, which are used in the transduction analysis. Bottom: Power spectral density of sideband frequency modulation harmonics normalized to the corresponding modulation power spectral density of the pump. d) Same as c), but for modulation frequency 10 MHz. e) Pump to sideband FM transduction determined from the FM amplitude of the first 9 harmonics of the modulation frequency of linearized FM traces between 10 kHz (dark shading) and 10 MHz (light shading). Sideband values are offset by 10 dB and normalized with respect to the modulation amplitudes of the pump.

individual channels to be measured sequentially, alleviating the requirement to provide >30 balanced photodetectors and analog-to-digital converters. The total optical loss budget of the demultiplexing network is around 5 dB per channel and could be reduced by co-integration on the photonic chip. We stress that all measurements are done illuminating and receiving light and demultiplexing all the pixels simultaneously. Hence any additional noise and crosstalk between the channels would be detected in our setup. Yet, our system is impervious to crosstalk and interference between the channels, because of the spectral channel separation, in contrast to simple spatial channel separation [107, 108, 109].

The results of parallel distance and velocity measurement including standard deviations over 100 FM periods for the static wheel are displayed in Fig. 3.17a,c. We adjusted the modulation $1/T$ and excursion B of the microcomb pump to 100 kHz and 1.7 GHz, respectively. Channels beyond 195.2 THz were not observed with sufficient signal-to-noise ratio (SNR), because of limited amplification bandwidth. The measurement imprecision over 25 spectral channels is below 1 cm, comparable with state-of-the-art

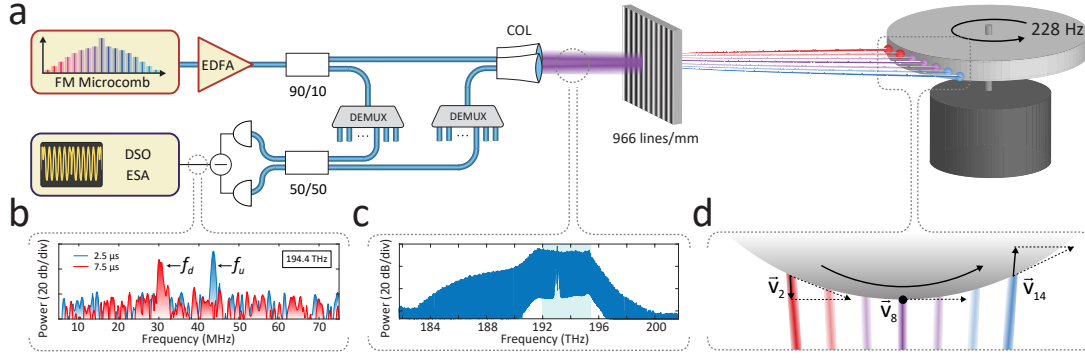


Figure 3.16: Setup for parallel velocity measurement using a soliton microcomb. a) Experimental setup. The amplified FM LiDAR microcomb source is split into signal and local oscillator (LO) pathways. The signal is dispersed with a transmission grating (966 lines/mm) over the horizontal circumference of a flywheel mounted on a small DC motor. The reflected signals are spectrally isolated before detection. b) RF spectrum of LiDAR backreflection mixed with the LO (sampling length $3.75 \mu\text{s}$) around $2.5 \mu\text{s}$ (upward ramp) and $7.5 \mu\text{s}$ (downward ramp). c) Optical spectrum of comb lines after amplification. Blue shading highlights 30 comb lines with sufficient power ($> 0 \text{ dBm}$) for LiDAR detection. d) Schematic illustration of the flywheel section irradiated by the FM soliton microcomb lines indicating the projection of the angular velocity of the wheel onto the comb lines.

TOF LiDAR systems and can be improved by using more broadband chirps. Small systematic offsets on the level of 1 cm are associated to the lengths of fibre pigtailed in the demultiplexers and switches. The results for the wheel spinning at 228 Hz are depicted in Fig. 3.17b,d, resolving the position dependency of the projected velocity around the circumference of the wheel. Normal incidence reflection of the wheel is obtained by the FM microcomb sideband at 193.8 THz, whereas the comb lines with higher frequencies detected receding pixels and lower frequencies – approaching.

The data analysis was performed with simple Fourier transform accounting for a constant 535 ns delay between the AFG and the LiDAR lasers, which was predominantly obtained from the optical fibre lengths of the EDFAs. We applied a 4th-order Blackmann-Harris type window function with effective resolution bandwidth of 530 kHz. This resolution bandwidth corresponds to a range bin width of 7.9 cm (192.1 THz) to 5.9 cm (194.9 THz) in accordance with the FMCW fundamental range resolution $\Delta x = \frac{c}{2B}$. Two spectra corresponding to the upwards and downwards slopes of the frequency chirp were separately transformed within each FMCW period and we applied Gaussian peak fitting to determine the peak frequency in each spectrum. We determined the statistical distance error by calculating the standard deviation of 100 consecutive distance measurements, which deviate by less than 1 cm from the mean.

We performed the calibration of the channel-dependent frequency excursion bandwidth using a second MZI before the start of the measurements and assumed it constant throughout.

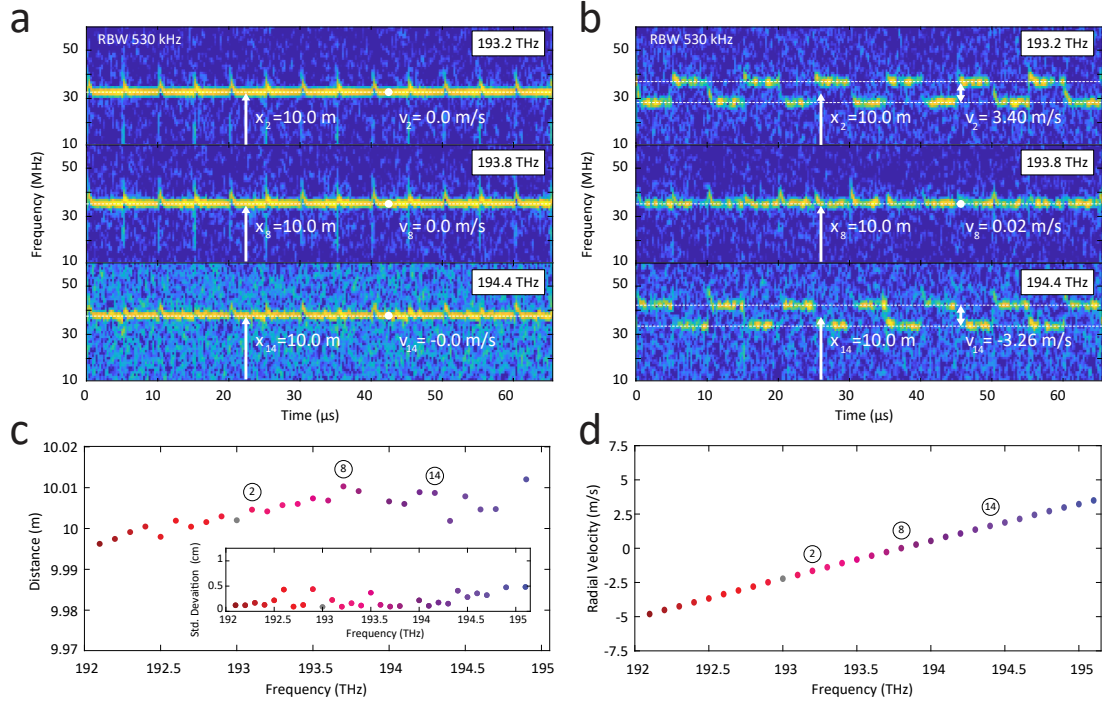


Figure 3.17: Velocity and range measurement of a flywheel. a) Time-frequency maps of selected microcomb FMCW LiDAR channels (sampling length 0.5μ s) for the static flywheel. b) Same as e) but for flywheel rotating at 228 Hz. c) Multichannel distance measurement results for the static flywheel. Distance measurement not corrected for fiber path difference between signal and LO path. d) Multichannel velocity measurement for the flywheel rotating at 228 Hz. The accuracy of distance and velocity measurements in case of the rotating flywheel is limited by vibrations.

Last, we demonstrated parallel 3D imaging concurrently illuminating a target composed of two sheets of white paper spaced by 11 cm with the "EPFL" logo cutout in the front plane (cf. Fig. 3.18). While in the previous section we effectively presented 1D line imaging, here we utilize extra galvo mirror to access full 2D scene scanning. We employed monostatic detection setup and co-observed backreflection from the collimation lens, which served as the zero-distance plane in the measurement. Target points detected in the back plane were clearly separated due to the cm-level distance precision and accuracy observed on all 30 FMCW channels (cf. Fig. 3.18,d) and highlighted as filled points. We increased the detector aperture by placing a 75 cm focal length lens 1 m away from the 4 mm collimator and behind the grating.

We note that the equivalent distance and velocity sampling rate of the 30 independent channels is 3 Mpixel/s.

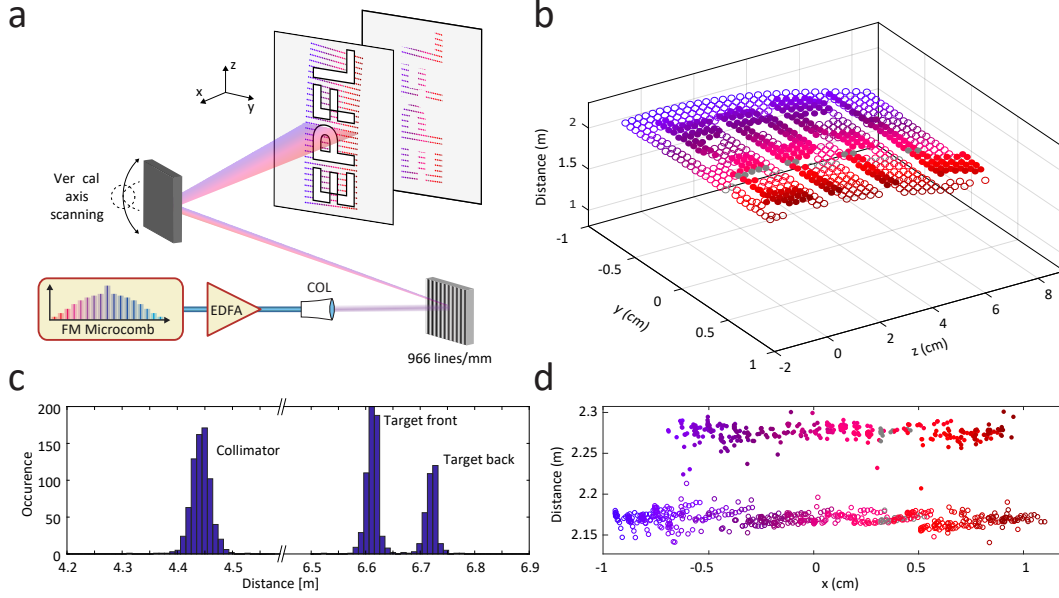


Figure 3.18: **Parallel distance measurement and imaging** a) Experimental setup. 30 channels of the soliton microcomb are spectrally dispersed with a transmission grating in the horizontal axis (y). Vertical translation is performed by a planar mirror placed behind the grating. The target is formed by two vertical sheets of paper placed at a distance of 11.5 cm. The EPFL logo is cut out from the first sheet. The colored dots mark the approximate positions of the individual beams during the scan and denote the individual spectral channels according to Fig. 3.14a. b) Obtained 3D image by scanning the beam array in the vertical direction. Filled circles denote pixels detected in the target back plane. c) Histogram of successful detections for the collimator (zero distance plane), front and back planes. d) Projection of b) along the z-axis reveals the cm level distance measurement accuracy and precision for the 30 FM LiDAR channels.

3.8 Conclusion

In summary, we have reported a novel method for massively parallel coherent LiDAR utilizing photonic chip-based soliton microcombs. It enables to reproduce arbitrary frequency chirps of the narrow linewidth pump laser onto all comb teeth that compose the soliton at speeds beyond 10^{17} Hz², and has the potential to significantly increase the frame rate of imaging coherent LiDAR systems via parallelization. In contrast to earlier works in frequency comb-based LiDAR [83, 52, 94], the comb teeth in parallel FMCW LiDAR are spatially dispersed with diffractive optics and separately measure distances and velocities in a *truly parallel* fashion. Assuming a similar setup as [39], i.e. 179 carriers with 50 GHz spacing in the C+L telecom wavelength bands, we expect aggregate pixel measurement rates of 17.9 Mpixel/s for 100 kHz modulation frequency and 179 Mpixel/s for 1 MHz modulation frequency, well beyond current technologies of long range TOF and FMCW LiDAR systems. Although, the slow power modulation of the comb sidebands during the frequency chirp only weakly influences the distance and velocity evaluation, we emphasize that it can be avoided entirely if both the laser and cavity are modulated in unison. Promising actuation technologies include recently

developed high-bandwidth and energy-efficient integrated electro-optical [103] and piezoelectrical actuators [110]. The work of Liu et al.[53], published later, demonstrated feed-forward scheme where the Raman shift was completely eliminated. Similarly, the laser can be self-injection locked to the modulated cavity, which can furthermore extend the laser coherence length significantly [48, 85].

Our current setup utilizes discrete telecom fiber components and optical switches for the detection. However we emphasize that high-performance integrated photonic solutions for many-channel DWDM communications have been demonstrated [111] and can be integrated on the Si_3N_4 photonic chip with comparable performance as the commercial telecom components employed here [112, 113].

Moreover, by virtue of the laser line separations, our concept is compatible with nanophotonic based gratings for beam separation and could significantly simplify optical phased array systems [93], wherein one axis of beam separation is provided by the nanophotonic grating and a second axis is provided by integrated phase shifters. Furthermore, this concept alleviates problems with eye safety, as the light is dispersed over multiple detection pixels at all times, similar to time-of-flight flash systems, yet avoids the problems associated with the excessive peak powers of high-energy pulsed light sources.

It should be noted that (resonant) electro-optical frequency combs [114, 103] based on LiNbO_3 also provide a platform in which the presented approach can be realized. Hence, we conclude that, combined with concurrent advances in chip-scale lasers, optical beamforming structures, and hybrid electro-optical integration, our approach provides a path towards rapid, precise and simultaneously long-range coherent LiDAR modules suitable for industrial, automotive and airborne applications demanding high-speed 3d imaging in excess of 10 Mpixel/s.

4 Dual chirped microcomb based parallel ranging

This chapter reports on the Dual-comb implementation of parallel ranging with microcombs. It is a logical continuation step of the previous chapter. The results are partially adapted from A. Lukashchuk *et al.*, "Dual chirped microcomb based parallel ranging at megapixel-line rates", *Nature Communications*, 13, p. 3280, (2022).

4.1 Introduction

Let's consider a depth imaging sensor with reasonable update rates (25 Hz) and standard definition video quality (700x500 pixels). These requirements translate into measurement rates greater than 5 million pixels per second (MPix/s). To date, these measurement speeds have not been achieved for coherent LiDAR.

In the previous chapter, we provided a clear path to parallelize the FMCW LiDAR using DKS, but this is not a straightforward task as it requires large banks of photodetectors and digitizers that must operate in parallel. Although we speculated about aggregate sampling rates of up to 3 MPix/s, with the potential to increase it beyond 10 MPix/s, all of the measurements were performed sequentially and not simultaneously.

Recent state-of-the-art coherent ranging demonstrations used broadband laser sources and spectral scanning approaches (similar to what we performed with a diffraction grating) and reported rates below 1 MPix/s [9]. The work by Qian et al. [115] presented video rates greater than 7 megapixels, but it was an optical coherence tomography (OCT) demonstration rather than LiDAR, as the coherence length of the laser was limited to less than 1 meter. Furthermore, LiDAR operating at rates greater than 1 MPix/s with only one laser source (i.e., no parallelization) has a stringent constraint on integration time, which would be less than 1 microsecond. This time is likely insufficient for the coherent averaging of the reflected signal at 100 meters, given a time of flight of 670 nanoseconds, and thus obtaining a reliable signal-to-noise ratio (SNR). Typically, the FMCW LiDAR in the automotive industry employs chirps with sweeps ranging from 10

to 100 kilohertz and integration times of 10 to 100 microseconds.

Megapixel frame rates are currently only achieved in time-of-flight (ToF) systems that use a bank of parallel laser sources, such as Ouster's systems with 128 laser channels or Velodyne's systems with 256 lasers. In contrast, megapixel measurement rates have never been reported for coherent ranging to the best of our knowledge (as of 2020, not for aggregate rates), due to the complexity of both the laser and heterodyne detection. Therefore, we believe that such a demonstration is critical to the future success of the FMCW technology.

Coherent LiDAR signals are generally low bandwidth (10's MHz) and therefore do not take full advantage of silicon photonics data center transceiver technology comprising coherent receivers, that operate and detect signals with 10s GHz modulation. We bridge the technological gap by harvesting the excess bandwidth of optical telecommunication technology applying it to FMCW LiDAR. In this chapter, we demonstrated a hardware efficient, single laser and single detector coherent LiDAR that operates at megapixel per second rates achieving >5 MPix/s. This represents – to the best of our knowledge – the fastest frame rate ever demonstrated for coherent LiDAR, putting it on par with ToF. The key idea is to leverage the frequency dimension, distributing and detecting all of the channels on the same high-bandwidth receiver. It originates from the early works on dual-comb spectroscopy, where two pulsed sources with a slight offset in repetition rate were used. Two synchronously frequency modulated solitons generated in similar Si_3N_4 integrated microresonators from a single laser serve as signal and local oscillator in multi-heterodyne detection. Due to the offset, baseband frequency will be different for distinct channels, allowing distance and velocity information of multiple channels to be retrieved from a single interferogram recorded over one period of the chirp.

Viewed broadly, the demonstration of a hardware efficient megapixel per second coherent LiDAR via frequency multiplexing and using telecommunication coherent detection, shows the major potential that the combination of *detection and ranging*, *optical telecommunications* and *metrology* can offer. The wide deployment of silicon photonics based phase-diversity receivers in data center interconnects and telecommunications makes this tool easily accessible in semiconductor foundries, where all the key LiDAR components can be integrated on chip.

In combination with injection-locked electrically driven DKS microcombs [116, 117], integrated piezoactuators [53] and heterogeneously integrated semiconductor optical amplifiers [118], this approach could meet and excel SWAP (size, weight and power) requirements for a future photonic LiDAR engine, while inherently providing eye-safe operation, parallel acquisition, high frame rates, centimeter-level resolution. Of course, this is speculation. As Reviewer #5 (of the relevant manuscript; peer review file available) mentioned: "This result is a tour-de-force, it is technically very impressive, but I question if it will really have any practical impact." Indeed, it might not have any

practical impact, albeit demonstrating for the first time coherent LiDAR with >5 MPix/s line scan rates.

4.2 Multiheterodyne detection and its application to ranging

Our approach is a swept frequency version of multiheterodyne detection [119] of optical frequency combs, commonly referred to as dual-comb spectroscopy. This technique has attained widespread attention and application in (nonlinear) optical and THz spectroscopy [120, 57, 121], optical microscopy [122, 123], distance measurement [82, 52, 83], two-way time-frequency transfer [124], microwave photonics [125], multi-dimensional spectroscopy [126], coherent anti-Stokes Raman imaging [127] and sub-noise detection of a random event [128].

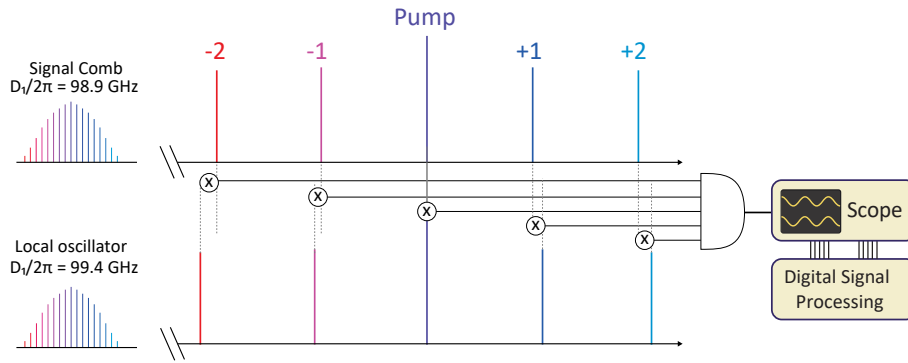


Figure 4.1: **Multiheterodyne detection.** Signal (carrying some modulation information) and LO combs have offset repetition rate difference of 500 MHz. The beatnotes between relevant channels μ are spaced apart by 500 MHz. Neither demultiplexer nor photodiode arrays are required when superimposing all channels on a single high bandwidth photodetector.

While in conventional dual-comb approach the actual signal is encoded on the signal comb as amplitude and phase change, here we consider every signal comb tooth to carry a frequency modulation. The multiheterodyne method decodes all individual low frequency (MHz bandwidth) channels using a single high speed (GHz) coherent ‘intradyne’ (also referred to as phase diversity) receiver [129] by radio-frequency multiplexing. The beatnote between signal-LO comb lines μ should be lower than the half of the repetition offset difference Δf_{rep} , otherwise the beatnotes overlap and corrupt the total signal.

To mitigate the degeneracy in optical detection between $+\mu$ and $-\mu$ comb lines located symmetric about the pump ($\mu = 0$), we employ a phase diversity receiver architecture [130, 131] and measure both the in-phase (I) and quadrature (Q) components of the multiheterodyne beat note (cf. Fig. 4.2). These receivers are nowadays widespread in data centers [132]; for example, a recently introduced silicon photonics-based coherent optical pluggable transceiver 400ZR supports 64 GBaud/s modulation speeds [133], which would constitute an off-the-shelf component solution for a chip-scale FMCW

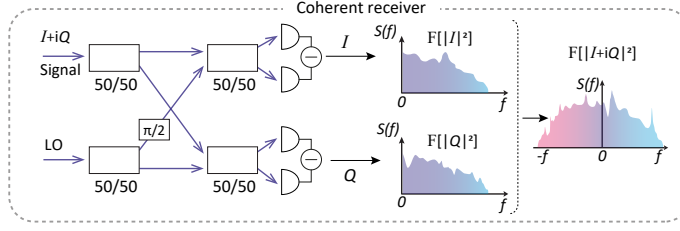


Figure 4.2: **Phase-diversity receiver.** The complex RF spectrum is retrieved by phase diversity detection and Fourier transform.

LiDAR.

In the frequency domain, we obtain two soliton microcombs with slightly different comb line spacing Δf_{rep} where each comb line inherits the pump laser frequency modulation. Multiheterodyne mixing of the reflected signal comb with the local oscillator (LO) comb on a single coherent photoreceiver enables the reconstruction of the entire complex RF spectrum, which contains the distance x_μ and velocity v_μ information for each comb line μ simultaneously.

In comparison to conventional FMCW LiDAR [134], multiheterodyne detection modifies the formulas to calculate (x_μ, v_μ) from the beat notes f_μ^u, f_μ^d measured during the up- and down-chirping of the FMCW laser because the intermediate frequency is no longer at the baseband. Instead, consecutive channels in the radio-frequency (RF) domain are separated by the difference in comb line spacing Δf_{rep} . The Fourier transform of the complex field amplitude $I + iQ$ distinguishes positive and negative frequencies in the multiheterodyne beat spectrum [129]. The deviation of the beat note pattern from $\mu \cdot \Delta f_{\text{rep}}$ determines the Doppler shift and non-zero detection distance translates into a splitting of the RF beat note

$$\begin{aligned} x_\mu &= \frac{cT}{4B_\mu} \cdot \frac{f_\mu^u - f_\mu^d}{2} \\ v_\mu &= \frac{c}{2\nu_\mu \cos\theta_\mu} \cdot \left[\frac{f_\mu^u + f_\mu^d}{2} - \mu \Delta f_{\text{rep}} \right], \end{aligned} \quad (4.1)$$

where $\nu_\mu \cos\theta_\mu$ is a projection of the target velocity along the optical path and ν_μ is the optical frequency of the μ -th comb line.

In our experiments (cf. Fig. 4.4), we utilized a single highly coherent FMCW laser that was amplified, split and coupled into two size-mismatched photonic chip-based integrated Si_3N_4 microring resonators driving two DKS. Similarly to the previous chapter, the pump laser frequency was modulated by dual Mach-Zehnder biased to single-sideband modulation. The voltage-controlled oscillator drove the modulator with a triangular waveform that we digitally predistorted and linearized. We simultane-

4.2 Multiheterodyne detection and its application to ranging

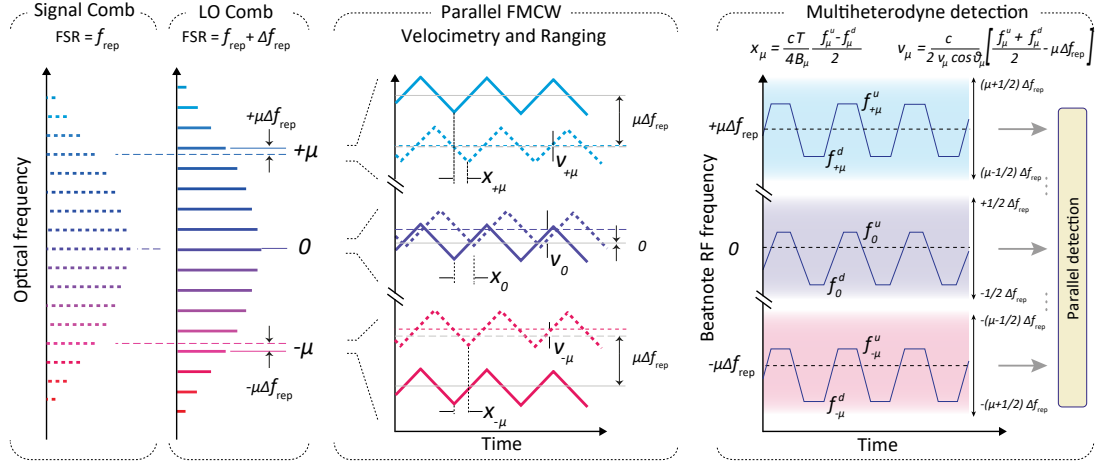


Figure 4.3: **Principle of multiheterodyne ranging and velocimetry.** The Signal and LO combs have repetition rates f_{rep} of 98.90 GHz and 99.39 GHz, respectively. The reflected signal comb light is both time delayed, and frequency shifted due to the Doppler effect. Beat notes of consecutive comb tooth pairs are spaced 490 MHz in the RF spectrum. Triangular frequency modulation maps the distance of target objects to two RF beat notes, f_μ^d and f_μ^u , spaced around the center frequency of the multiheterodyne channel $\mu \cdot f_{\text{rep}}$ offset by the Doppler shift caused by the relative velocity of LiDAR transmitter and target.

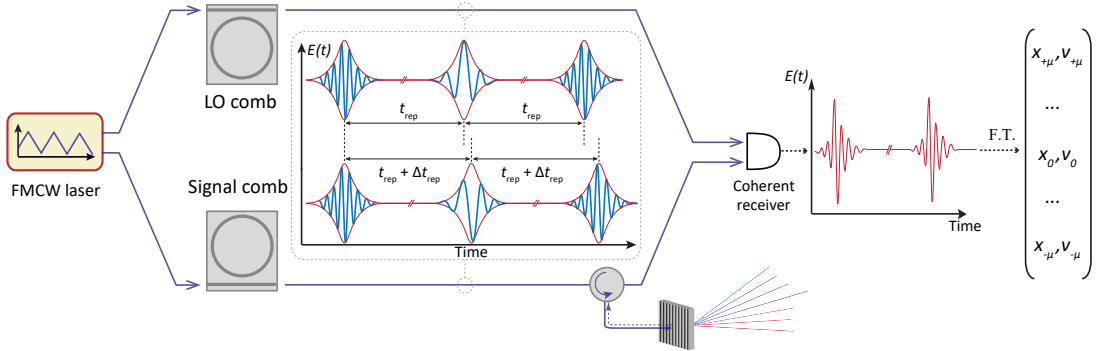


Figure 4.4: **Architecture of the multiheterodyne parallel FMCW LiDAR.** A single pump laser with triangular frequency modulation is split, and drives two distinct optical microresonators with slightly different radii, which serve as signal and local oscillator (LO) in the experiment. The signal comb is spatially dispersed over the target area using diffractive optics. Each signal comb tooth μ represents an independent FMCW ranging channel measuring distance x_μ and velocity v_μ .

ously generated two DKS from a single triangularly chirped laser with an amplitude $B = 1.5$ GHz and a period $T = 10 \mu\text{s}$. We monitored the laser detunings using the phase modulation response technique (VNA) and temperatures of the samples were adjusted during the dual soliton switching process, if necessary using a thermal tuner. In this way, dual single soliton states could be obtained routinely and quickly. We subsequently optimized the laser-cavity detunings $\delta^{\text{sig,LO}}$ of signal and LO combs by thermal tuning

to minimize the differential Raman shift and hence optimize linearity (outlined below in more detail).

4.3 Characterization of a dual chirped LiDAR source

We again employed heterodyne detection to built time-frequency maps and individually analyze chirps' linearity of the signal and LO combs, as well as delayed homodyne detection for excursion calibration.

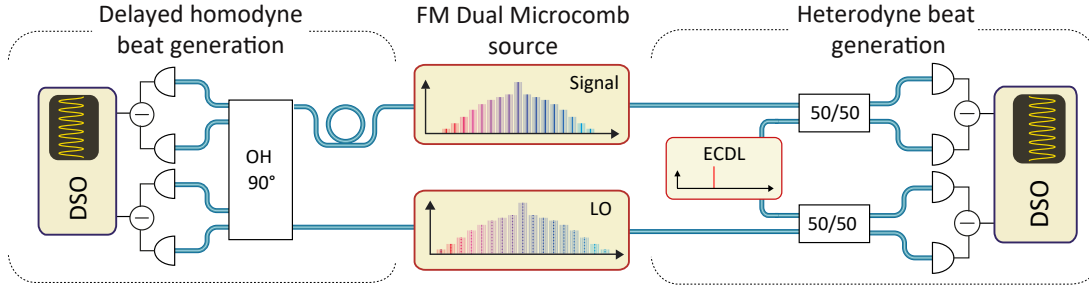


Figure 4.5: **Optical setup for heterodyne and delayed homodyne beat note measurement.**

a) The signal microcomb is delayed and mixed in a 90° optical hybrid and superimposed with the local oscillator (LO) microcomb on a pair of balanced photoreceivers for delayed homodyne beat frequency generation. Alternatively, the tuning of individual comb line pairs are characterized by heterodyne mixing with an external cavity diode laser (ECDL).

In the experiments, we used frequency combs with 99.39 GHz and 98.9 GHz repetition rates, i.e. a 490 MHz difference (cf. Fig. 4.6a). First, we obtained a heterodyne beatnote by superimposing the frequency combs individually with an external-cavity diode laser onto two balanced photoreceivers (BPD). The resulting signals were analyzed by short-time Fourier transform. Fig. 4.6b shows the laser frequency of the two simultaneously chirped local oscillator and signal microcomb for channels $\mu = \pm 3, \pm 11$, highlighting the similarity and relative spacing of the frequency modulation pattern. The delayed homodyne beat note spectrum for the same channels is depicted in Fig. 4.6b where the delay line distance corresponds to the frequency splitting.

The maximum number of LiDAR channels is limited by the optical amplification and coherent receiver bandwidths B_{pd} . The latter limitation reads as $\mu \Delta f_{rep} < B_{pd}$ and can be overcome by reducing the repetition rate difference Δf_{rep} with the trade-off of a reduced distance ambiguity range. The channel-dependent frequency excursion B_μ (cf. Fig. 2f) due to the soliton self-frequency shift induced by intrapulse Raman scattering ranges from 1.3 GHz to 1.8 GHz, which corresponds to a native axial distance resolution $\Delta x_\mu = c/2B_\mu$ of 12 cm to 8 cm.

The performance of dual-comb FMCW heterodyne detection relies not only on the

4.3 Characterization of a dual chirped LiDAR source

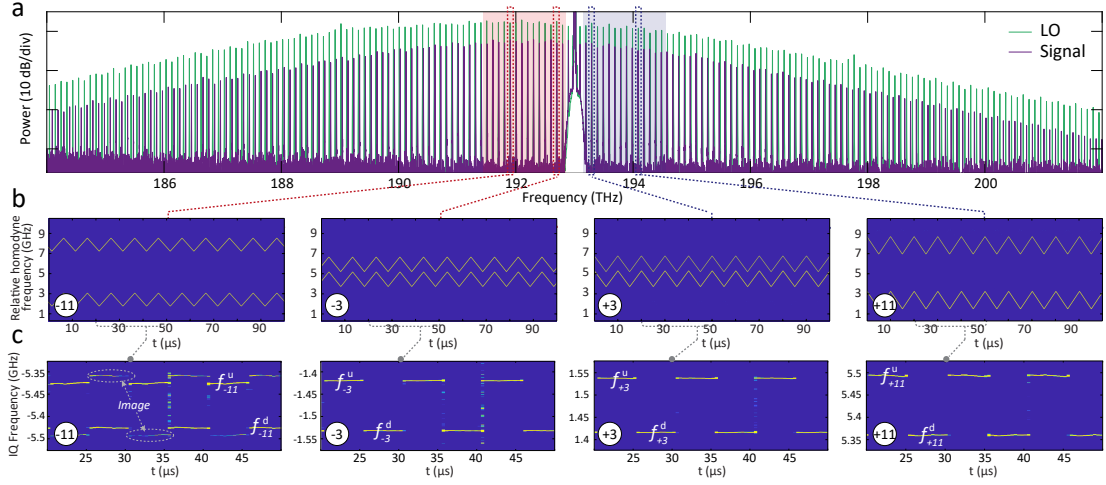


Figure 4.6: **Coherent detection of multiple FMCW laser channels.** a) Optical spectra of signal and LO combs featuring a slight offset in repetition rate. The blue(red) shading highlights positive(negative) channels ($\mu = 0$ denotes the pump laser) used in LiDAR experiments limited by the available amplifier bandwidth and amplified spontaneous emission noise. b) Time-frequency map of heterodyne beat spectroscopy at the ± 3 and ± 11 channels. ENBW 2.45 MHz. c) Time-frequency map of delayed homodyne beat spectroscopy. ENBW 2.45 MHz.

mutual coherence of the Signal and LO combs (ensured by degenerate pumping scheme), but also on the equality (cf. Fig. 4.7b) and low nonlinearity (cf. Fig. 4.7c,d) of the chirp transduction from the pump laser in both nonlinear microresonators.

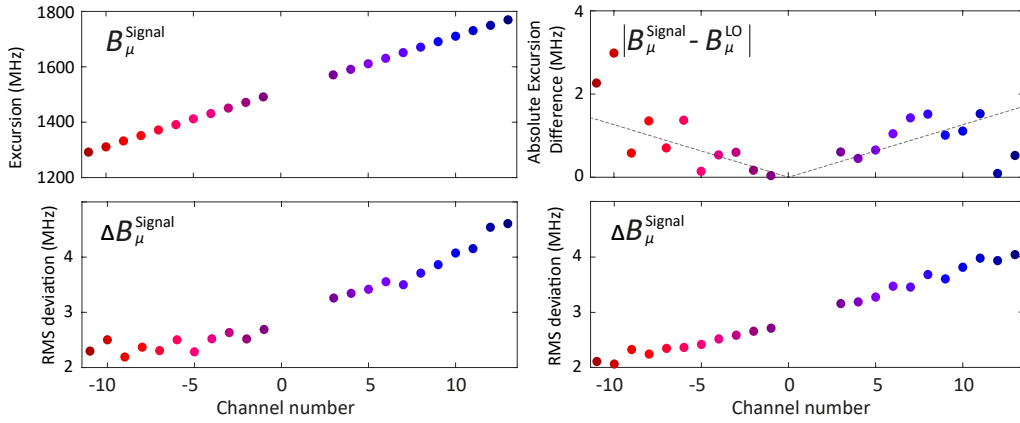


Figure 4.7: **Dual chirped microcomb excursion and nonlinearity.** a) Channel-dependent frequency excursion bandwidth at 100-kHz modulation frequency. b) Channel-dependent absolute excursion difference of signal and LO combs. c,d) Channel-dependent RMS deviation from a perfect triangular frequency chirp for LO and signal (similar to Fig. 3.14).

In the previous chapter we had one resonator to consider. In the dual comb case, we have to look at the interplay of both Raman shifts in distinct resonators. The varying Raman shifts would result in different channel-dependent excursions for signal and LO and thus triangular sweeps with different amplitudes (cf. Fig), ultimately resulting in a

tilted beatnote (observed in Fig. ch. +11), leading to broadening and SNR deterioration. I analyzed in Appendix the relative phase deviation between the corresponding Signal and LO comb lines and show how to minimize it. It appears that one needs to take into account, for example, differential detuning $\Delta\delta = \delta^{\text{sig}} - \delta^{\text{LO}}$, which equates excursion dependences of the signal and LO when minimized. Eventually, a feed-forward scan scheme [53] or phase-locking the comb to a tuned resonator [135] would be favorable to avoid detuning-dependent changes of the microcomb repetition rates and to eliminate Raman nonlinearities. Co-integration of both microcomb resonators on a single chip to avoid differential frequency drift is equally straightforward.

4.4 Massively parallel coherent ranging

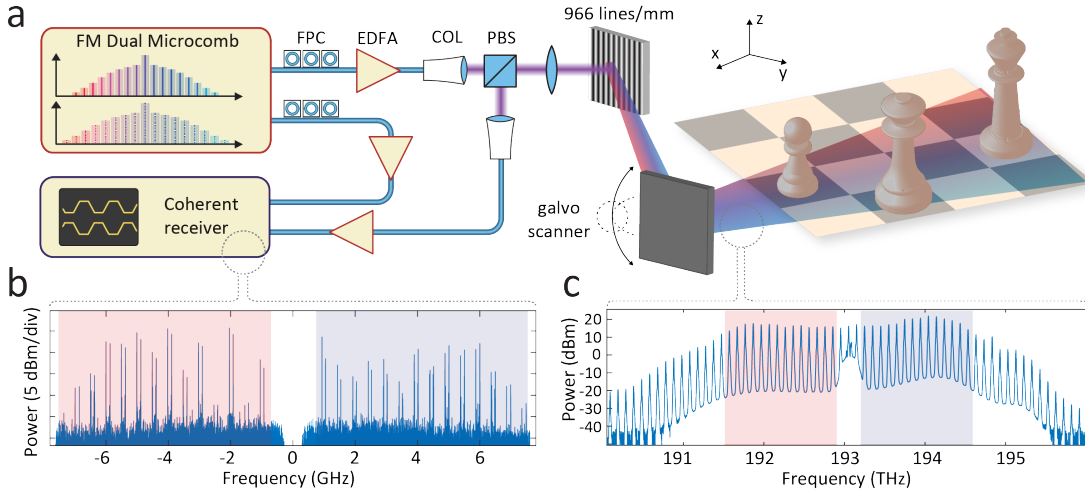


Figure 4.8: Dual comb imaging setup. a) The amplified signal comb is dispersed in free-space by a 966 lines/mm transmission grating and vertical scanning is provided by a mirror galvanometer. FPC: Fiber polarization controller; COL: collimator; PBS: Polarizing beamsplitter. b) Power spectral density of the electrical signal obtained at the coherent receiver highlighting 28 FMCW channels. The red and blue shading highlights signals obtained from negative and positive channel numbers, respectively. The resolution bandwidth equals to 100 kHz. SNR ranges in between 5-20 dB with polarization dependent variations. c) Optical spectrum used for 3D imaging. The red and blue shaded regions correspond to the signal plotted in panel b).

To demonstrate the capabilities of dual-comb massively parallel coherent imaging, we performed proof-of-principle parallel ranging experiments. The setup is depicted in Fig. 4.9a. The amplified signal comb (cf. Fig. 4.9c) illuminated the target comprised of three chess figures (queen, king and pawn) placed approximately ~ 1 m in front of the beam-splitter and optical transmission grating. A single-axis galvanometric mirror was used for beam scanning in the vertical direction. The Fourier transform of the complex signal $I + iQ$, photodetected on the coherent receiver during $10 \mu\text{s}$, represents a two-sided spectrum containing information about all 28 channels (cf. Fig. 4.9b). Blue and red shadings highlight positive $\mu > 0$ and negative $\mu < 0$ frequency comb teeth

with respect to the pump laser frequency.

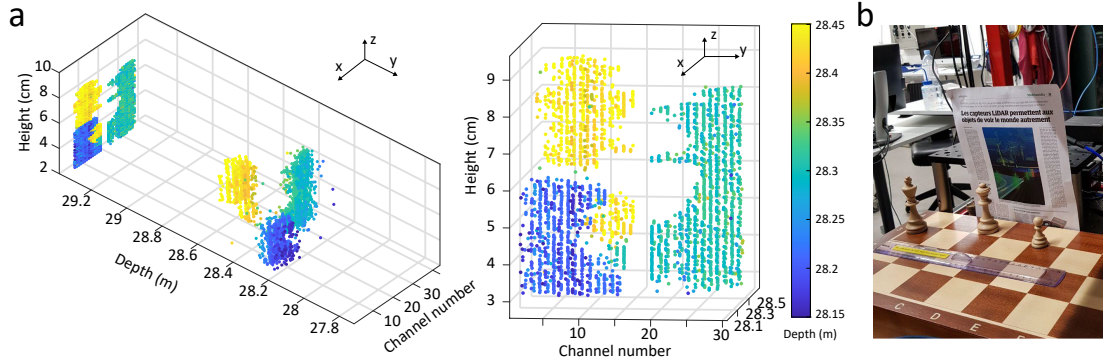


Figure 4.9: **Dual comb parallel 3D imaging.** a) Point clouds of the three chess figures obtained during a scan (28×136 points) of the mirror galvanometer. b) Photograph of the target scene.

Two different projections of the 3D-imaging results for a scan of 136 vertical angles across the set of chess figures are depicted in Fig. 3d,e. A line of 28 pixels is recorded during a single $10 \mu\text{s}$ triangular laser chirp, which equates to a true, i.e., bona fide 2.8 MPix/s coherent distance sampling rate at the sampling oscilloscope. The full scene measurement time was less than 1.5 s, and was limited by the response of the galvo. **We emphasize that this operation differs from experiments, which detect, digitize, and process each de-multiplexed channel successively and thus report aggregated data or sampling rates [136].** The details of the multichannel data segmentation filtering, IQ phase and amplitude imbalance compensation, computational complexity of the required signal processing are outlined in Appendix.

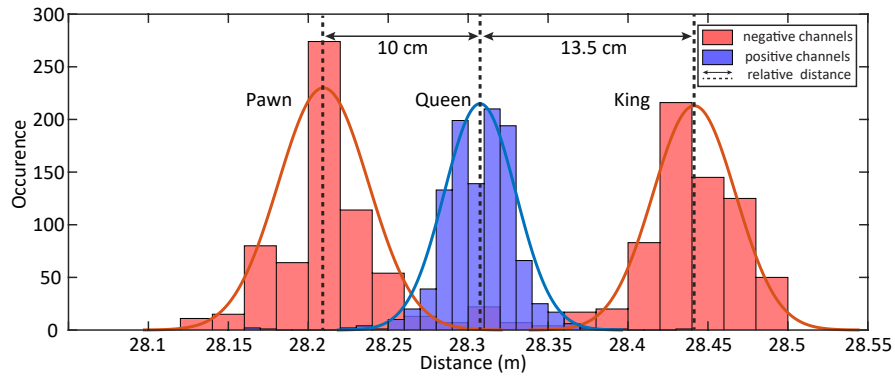


Figure 4.10: **Chess ranging measurement relative accuracy.** Measured relative distance for chess figures ranging experiment. Red histogram corresponds to the pixels in negative channels that illuminated Pawn and King, while blue histogram corresponds to Queen illuminated by positive channels. Histograms depict 136×28 measured pixels, where one line of 28 pixels was acquired during $10 \mu\text{s}$ time.

The space between Pawn and Queen, and Queen and King figurines was 10.5 cm and 13.5 cm correspondingly (the differential delay between signal and LO combs in optical

fiber was around 27 m). Fig. 4.10 depicts the relative distance accuracy by plotting histograms of detected pixels for both positive and negative channels.

To estimate the overall distance precision of the dual comb LiDAR, we performed ranging experiment of a static object by measuring 49 chirp periods ($490 \mu\text{s}$) and calculating the standard deviation. Precision of our system ranges from 1 to 5.5 cm (cf. Fig. 4.11). The precision value is governed by how precisely one can define the RF frequency beatnote. It depends on the frequency bin spacing determined by the target interrogation time, SNR, and nonlinearities in the system that broaden the beatnote. In our system, Raman nonlinearity degrades the comb line precision towards higher $|\mu|$ since its impact is proportional to the relative comb number.

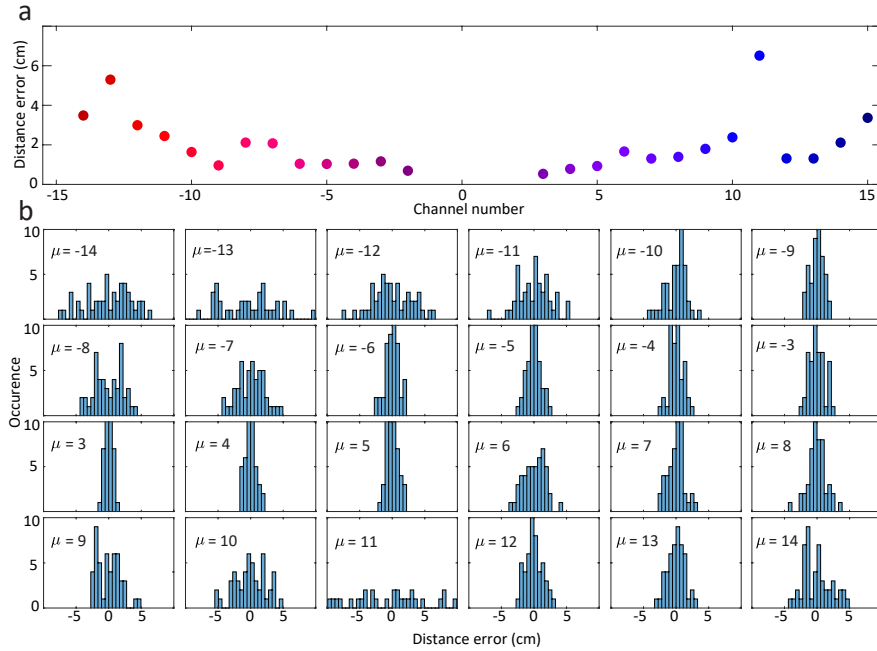


Figure 4.11: **Distance precision of the Dual-Comb LiDAR.** a) Channel-dependent distance precision. b) Histograms obtained during 49 distance measurements of the static object.

4.5 Dense megapixel per second coherent ranging

In a second proof-of-principle experiment, we demonstrated dense coherent hardware-efficient parallel velocimetry with our dual frequency-modulated soliton microcomb platform at even higher rates of 6.4 megapixel per second. Lowering the repetition rate to 35 GHz illustrates the advantage of the dual-comb approach, which alleviates the need to operate at large line spacings compatible with wavelength division multiplexers and facilitates mode spacing related limitations of channel isolation. To this end, we employed two low repetition rate soliton microcombs operating at f_{rep} of 35 GHz

allowing us to have more than 60 channels within the Erbium-doped fiber amplifier (EDFA) gain window.

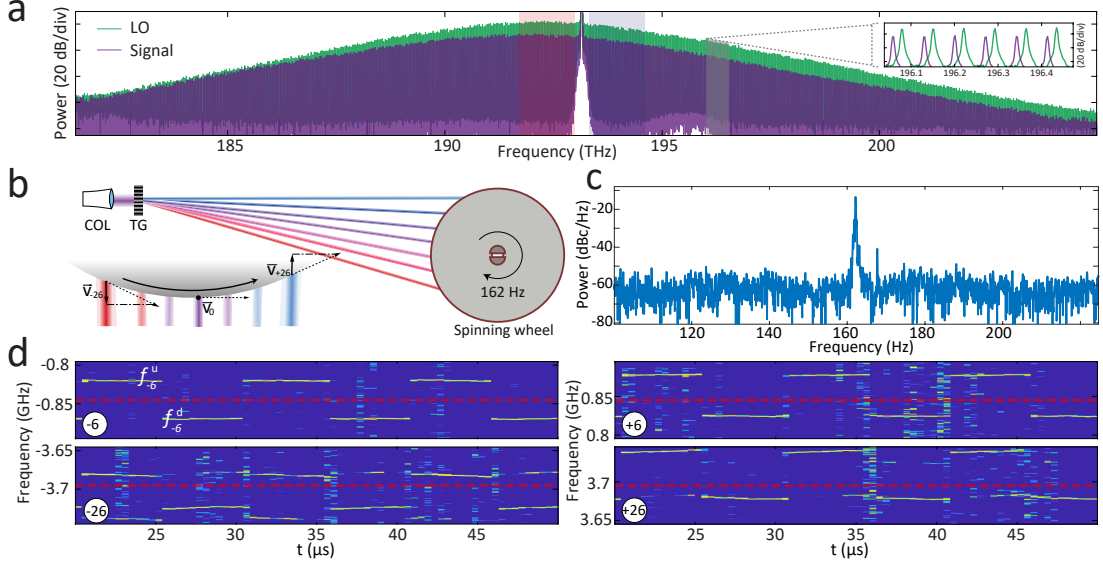


Figure 4.12: Dense dual comb at 35 GHz repetition rates. a) Optical spectra of the 35 GHz dual FMCW combs. b) Schematic illustration of the flywheel section irradiated by the signal comb lines. (Left) COL: Collimator; TG: transmission grating. (Right) The projections of the velocity v_μ of the wheel onto the comb lines. c) Periodogram of the spinning flywheel sound recorded on a cellphone microphone depicting a peak corresponding to the rotation frequency. d) Time-frequency map featuring an offset of the mean beat frequency from the $\mu\Delta f_{\text{rep}}$ due to the Doppler shift. ENBW 2.45 MHz.

While spectral compression of the microcomb from 99 GHz to 35 GHz does limit the triangular chirp frequency excursion to 700 MHz at the same pump power (500 to 900 MHz excursion variation for 60 channels), this does not limit the accuracy of Doppler velocimetry and we can retain the 100 kHz modulation frequency. The optical spectra of the signal and LO solitons are shown in Fig. 4.12a. The inset highlights the repetition rate offset Δf_{rep} of ~ 140 MHz. The signal comb was dispersed by the same transmission grating along the circumference of a 20 mm flywheel rotating at 162 Hz (cf. Fig. 4.12b,c). The pump channel was approximately aligned at the center of the flywheel such that negative channels (negative RF frequencies) recorded an approaching target and positive channels (positive RF frequencies) a receding target. The time-frequency maps of the complex spectrum for the $\mu = \pm 6, \pm 26$ channels are plotted in Fig. 4.12d, and the dashed red lines highlight the baseband frequencies of multiheterodyne detection equal to $\mu\Delta f_{\text{rep}}$.

We calculated the velocities by computing the mean deviation of the beat notes from the equivalent baseband and depict the results in Fig. 4.13. Open circles correspond to the results after analyzing a single scan period, while the filled circles correspond to the averaging over five chirp periods. We also demonstrate a velocity profile of the

static wheel (gray circles) for comparison. On average, we attained 56 pixel detections over one period resulting in 5.6 MPix/s, i.e., actually detected, velocity and distance information acquisition speed. The velocity measurement uncertainty (Fig. 4.13d) grows with higher $|\mu|$ as the beatnote linewidth increases. We attribute extra variations to the mechanical vibrations of the flywheel. The distance measurement is depicted in Fig. 4.13e and is less accurate compared with ranging utilizing 100 GHz combs due to the reduced frequency excursion and, consequently, resolution and accuracy.

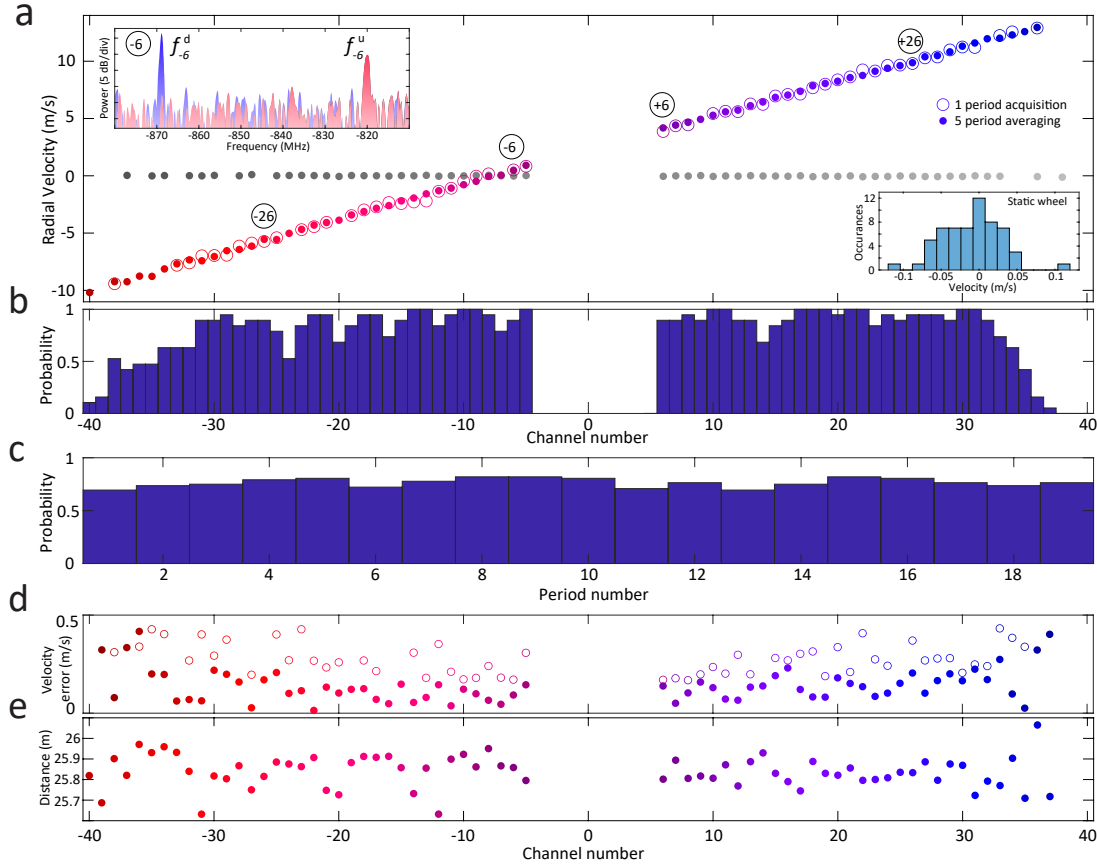


Figure 4.13: Dense dual comb parallel velocimetry measurement at 6.4 megapixel/second rates. a) Multichannel velocity measurement for the flywheel rotating at around 200 Hz for a single $10 \mu\text{s}$ scan (open circles) and five frame stacking (filled circles). Grey data points show velocimetry results for the static wheel. b) Probability of a pixel to be detected in channel μ . Statistics are obtained over 19 periods measurement time ($190 \mu\text{s}$). The roll-off at large distance from the pump laser originates from the limited optical amplifier bandwidth. c) Probability of detection over a given time frame ($10 \mu\text{s}$). The probability is calculated as number of total pixels detected in that time frame divided by 81 ($\mu = -40, +40$). d) Error of velocimetry for single scan and 5 frame stack. e) Ranging results for five frame stacking. Higher deviation and lower precision are due to the significantly lower excursion of 700 MHz with native resolution of 22 cm

With recent demonstrations of DKS in low-repetition rate microresonators [137] the approach could readily exceed 10 MPix/s.

4.6 Discussion

In summary, we have demonstrated a megapixel-rate parallel coherent laser ranging based on multiheterodyne detection of chirped carriers on a single coherent receiver. Two integrated soliton microcombs driven by the same chirped pump laser provide a minimalist implementation of the dual chirped-comb system. The approach is free of channel separation, photo-detection and processing of individual channels.

Utilization of arbitrary, particularly very dense, frequency comb channel spacing is possible since multiplexers are not required. When combined with phased arrays, or other compact non-inertial scanning solutions, our approach provides a route to field-deployable MPix/s LiDAR systems that enable sufficient frame rate for video rate 3D imaging. Moreover, high-bandwidth silicon photonics-based IQ detectors are already offered commercially - making our method fully compatible with photonic integration. A recently demonstrated full heterogeneous integration combining InP/Si semiconductor lasers and ultralow-loss silicon nitride microresonators for DKS generation [138] is feasible as a path to chip-scale parallel FMCW LiDAR. Such photonic integration does not only bring another degree of miniaturization and possibility of wafer-scale production but also reduces optical loss, increases noise performance of the laser, and achievable scanning rates [87]. Erbium-doped fiber amplifiers could be replaced by waveguide amplifiers [91] or broadband semiconductor optical amplifiers (SOA) co-integrated on the silicon substrate [118, 139]. The broadband amplification would increase comb repetition rate while maintaining high channel count, which leads to improved soliton comb line power and relaxes the requirements on the grating line density.

While the approach comes at the expense of reduced Signal-to-Noise ratio due to the multiheterodyne detection penalty [140] scaling with the number of channels N utilized (outlined in Appendix), it benefits from the absence of multiplexers or photonic integrated solutions for detection of individual channels, which typically exhibit significant insertion loss.

Synchronous tuning of the pump laser and the microresonator, i.e., using monolithically integrated piezoelectrical frequency tuners [53] or frequency comb generation in electro-optical materials [103], serves to eliminate the residual nonlinearities of tuning that arise from the Raman self-frequency shift of the soliton and remove the requirement of high-power pumping while possibly extending the soliton existence range.

Finally, this architecture enables simultaneous acquisition of more than 64 pixels on a single receiver during a scan of 10 μ s resulting in greater than 5 MPix/s measurement rates. It demonstrates the significant advantages of acquisition speed afforded by the convergence of optical telecommunication and metrology technologies.

5 Chaotic microcomb based parallel ranging

This chapter reports on the first application of chaotic modulation instability in frequency combs where we specifically leverage the properties of optical chaos, unattainable in DKS. The results are partially adapted from A. Lukashchuk *et al.*, "Chaotic micro-comb based parallel ranging", *arXiv*, (In review, Oct. 2021).

5.1 Introduction

The transition to chaos is ubiquitous in nonlinear systems ranging from fluid dynamics and superconducting circuits to biological organisms [141]. Optical systems driven out of equilibrium such as lasers [142] and supercontinuum generation [143] exhibit chaotic states of light with fluctuations of both amplitude and phase and can give rise to Levy statistics, turbulence, and rogue waves [144, 145]. Spatio-temporal chaos also occurs in continuous-wave driven photonic chip based Kerr micro-resonators [146], where it is referred to as chaotic modulation instability. Such modulation instability states have generally been considered impractical for applications, in contrast to their coherent light state counterparts, which include soliton [13] or dark-pulse states [147]. Indeed, vast amount of applications in metrology, sensing and communications rely on coherent frequency combs with low noise and narrow linewidth. The focus has been on ever more robust control and deterministic operation, which remains challenging given the stochastic nature of multi-soliton generation. Even though studied in context of nonlinear dynamical systems, noisy frequency combs based on modulation instability have not received much attention and their large linewidth and low coherence is rather regarded as a flaw.

In this chapter, we demonstrate that incoherent and chaotic states of light in an optical microresonator can be harnessed to implement unambiguous [148] and interference-immune [149] massively parallel coherent laser ranging by using the intrinsic random amplitude and phase modulation of the chaotic comb lines. We utilized 40 distinct lines

of a microresonator frequency comb operated in the modulation instability regime. Each line carried >1 GHz noise bandwidth, which greatly surpassed the cavity linewidth [33], and enabled to retrieve the distance of objects with cm-scale precision. Our approach utilizes one of the most widely accessible microcomb states, and offers - in contrast to dissipative Kerr soliton states - high conversion efficiency, as well as flat optical spectra, and alleviates the need for complex laser initiation routines. Moreover the approach generates wideband signal modulation without requiring any electro-optical modulator or microwave synthesizer. Viewed more broadly, similar optical systems capable of chaotic dynamics could be applied to random modulation optical ranging [150] as well as spread spectrum communication [151], optical cryptography [152] and random number generation [153].

5.2 Historical outlook and overview of Random LiDAR

The term Random Modulation Continuous Wave (RMCW) denotes a number of microwave and optical techniques for ranging and velocimetry, where random amplitude or phase modulation of a carrier is used to interrogate a target. A noise-modulated measuring system was first proposed in 1959 [148], highlighting unambiguous ranging as an important advantage over periodically modulated continuous-wave (CW) range finders. It was later realized that a randomly modulated signal occupying wide bandwidth can also be applied in electronic warfare supporting low probability of intercept and effectiveness against electronic counter-countermeasures [149]. Indeed, the security and robust immunity to jamming and interference led to development of spread spectrum communications [154] where a broadband transmitted signal resembles naturally occurring noise.

RMCW light detection and ranging (LiDAR) was first demonstrated in 1983 by Takeuchi et al. [155] and like its microwave counterpart [156, 157] relies on cross-correlation between the received signal (or decoded modulation data) and the reference (code) for time delay estimation [158]. RMCW systems, similar to other continuous wave LiDARs, can operate with higher average optical powers than pulsed laser systems and allow for coherent averaging, i.e. the signal-to-noise ratio (SNR) increases in linear fashion with the measurement time. However, in contrast to frequency modulated continuous-wave (FMCW) LiDAR [159, 134], it does not require stringent conditions on frequency agility and linearity of the lasers that trade-off tuning range (i.e. distance resolution) versus coherence length (i.e. detection range) [160]. Furthermore, RMCW is capable of dynamically updating the measurement integration time without the need to adjust the emitted waveform [102].

Similarly to FMCW, the bandwidth of the source determines the resolution [161] and coherent RMCW, employing heterodyne detection to recover the phase of the signal yields range and velocity information simultaneously. In the foreseen epoch of unmanned

vehicles the immunity to mutual interference with other LiDARs and ambient light sources makes this advantage of RMCW significant. Indeed, LiDAR based on random noise modulation achieves lower false alarm rate and decreased SNR reduction penalty compared to other implementations when subjected to interference of other sensors [7].

RMCW LiDAR found its application in atmospheric sensing and aerosol detection [162, 163, 164] as well as in time domain reflectometry [165, 166]. Furthermore, well-established commercial LiDAR manufacturers employ either random amplitude [167] or random phase [168] modulation CW approaches. Conventionally, the modulation is encoded in the form of a random bit sequence [169, 170] or broadband noise [7] with an external phase or amplitude modulator. Otherwise, so-called chaotic LiDAR [171, 150] leverages the nonlinear dynamics of a semiconductor laser with optical injection or feedback [172]. Recently, researchers demonstrated chaotic LiDAR operated in pulsed regime capable of 3D long-range imaging with cm-level precision [173] and 100 kPix/s acquisition rates obtained in field experiments [174].

5.3 Concept of chaotic modulation instability coherent LiDAR

Here, we focus on chaotic frequency combs [33, 32] possessing complex nonlinear dynamics that we leverage to implement a novel type of parallel random LiDAR. We emphasize that in contrast to previous applications of frequency combs, the technology described in this letter uniquely requires the use of incoherent microcomb states.

Recent works on the application of microresonator frequency combs have largely focused on dissipative Kerr solitons [175, 13, 45], i.e highly coherent low noise states of the driven nonlinear microresonator that have proven to be promising in many applications discussed in chapter 2. Indeed, nearly all applications of photonic chip based microcombs to date have used dissipative coherent structures of light with the exception of optical coherence tomography [70] where the added intensity noise of the MI state is shown to be detrimental [47].

Combining conventional coherent RMCW techniques and the chaotic nature of modulation instability (MI) microresonator frequency combs, we demonstrated a modulator-free massively parallel RMCW LiDAR that provides unambiguous distance and velocity information, attains ~ 10 cm resolution enabled by its characteristic ~ 1 GHz noise bandwidth. Moreover MI microcombs are power efficient and provide a flat-top optical spectrum and support both parallel direct detection for distance and parallel coherent detection for simultaneous distance and velocity measurement with a suitable local oscillator. Lastly, individual comb teeth can be spatially dispersed using low-cost diffractive elements [136] for rapid 3D imaging.

The principle of random modulation microcomb coherent LiDAR is illustrated in Fig.

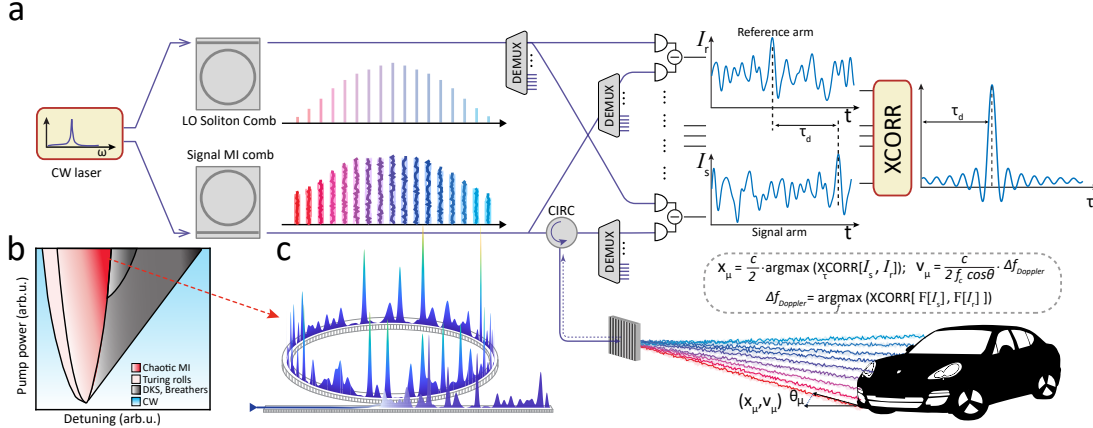


Figure 5.1: Concept of chaotic microcomb coherent LiDAR. a) Schematic of experimental setup. A single pump laser drives two distinct optical microresonators, generating a chaotic microcomb (signal) and a soliton microcomb (local oscillator, LO) with nearly identical mode spacing. The chaotic signal comb is spatially dispersed over the target area using a diffraction grating. Each signal comb tooth μ represents an independent RMCW channel measuring distance x_μ and velocity v_μ of objects along its beam path. A small portion of the chaotic comb is tapped for the reference measurement. The signal, reference and LO comb teeth are filtered with wavelength division multiplexers (DEMUX), superimposed on two balanced photodetectors, and analyzed for time delay estimation. Maximum peak in the cross-correlation trace corresponds to the travel time from which the distance is inferred. The velocity is calculated by measuring Doppler shift via cross-spectrum correlation. b) Microcomb stability chart illustration. Chaotic modulation instability (MI) area represents the microcomb state of interest. Gradient fill towards top right highlights the preferred region of operation. c) Simulation of chaotic MI waveform in the microresonator.

5.1a. Its operation follows prior works on RMCW systems [157, 7] but exploits multiple independent optical carriers for line illumination and facilitates parallel detection. Similarly to the implementations in the previous chapters, we utilized a CW laser that pumped two integrated Si_3N_4 microring resonators with similar mode spacing of 99 GHz. Chaotic MI (cf. Fig. 5.1b,c) generated in one resonator served as an array of signals and a dissipative Kerr soliton generated in the second resonator served as an array of local oscillators (LOs). While we used a DKS as an array of parallel LOs, we note that this is not required. An array of integrated receivers [133, 176] - developed and commercialized for datacenters - can equally address the signals individually.

Part of the signal was dispersed by an optical grating to scan the scene. The reflected light was demultiplexed and beat with the corresponding LO to produce the signal current. Another part of the signal generated the reference current with a second part of the LO. The currents were digitized and cross-correlated to infer distance and velocity of the target. To individually access the optical lines three units of commercial dense wavelength division (DWDM) demultiplexers covering the range between 192-196 THz (20-60 ITU channels) were used. The system requires $2 \times N$ balanced photodiodes and analog-to-digital converters where N is the number of channels detected in parallel. Unlike conventional dual-comb implementations where signal and LO combs are detected on a single receiver [57, 177], high noise bandwidth of MI precludes this implementation.

However, any parallel architecture requires \sim linear scaling. This is the case in telecommunications where for distinct wavelengths one has transmitter/receiver modules. This is the case for digital cameras with megapixels definitions. This is the case in ToF sensors (Velodyne, Ouster). This is the case in FMCW imagers, where researches develop parallel acquisition with subsequent parallel detection, let it be switching tree scheme [107] or a focal plane array architecture [108]. Scientist saying it to be a complexity increase (and it is exactly that) and on ground of that claiming the work to be redundant, just do not know what they are talking about (peer review file to be published upon publication of the current work).

The distance information can be inferred from the peak location estimate of the correlation trace [158]. Cross-spectrum correlation of the signal and reference currents results in a Doppler shift. The two combs operate in a free-running regime and do not require any stabilization. Unlike FMCW-soliton based implementations of massively parallel coherent laser ranging [136, 177], this approach does not depend on either linearization via phase-locked loop, predistortion of the pump waveform, nor channel calibration. MI state is obtained deterministically, does not require complex tuning [29] and is thermally self-locked.

We note that Chaotic MI is not limited to coherent (heterodyne) ranging only. Direct-detection or incoherent LiDAR that captures amplitude information of the field can be equally implemented with MI frequency combs (also shown below). Random amplitude CW LiDAR (commercially available [167]) does not require any LO, rather sensitive photon counting detectors.

5.4 Chaotic modulation instability characterization

A key advantage of the present implementation of massively parallel coherent laser ranging is the use of chaotic microcombs to directly generate a large number of broadband optical noise states in the optical microresonator with high power conversion efficiency. The optical spectrum of the chaotic microcomb after filtering out the residual pump laser is depicted in Fig. 5.2.

It reaches high power per comb line of up to -5 dB m with a flat-top spectral shape spanning ~ 8 THz in 3 dB, which significantly exceeds the nonlinear conversion performance of soliton microcomb generation in the same resonator.

We attained $>20\%$ power transfer efficiency while typical microresonator soliton state reaches less $<1\%$ [178] and is theoretically limited to $\sim 2\%$ [179]. We have deliberately chosen an overcoupled resonance with a total linewidth of 180 MHz to increase the power per comb line and to attain chaotic MI states with higher noise bandwidth (outlined below).

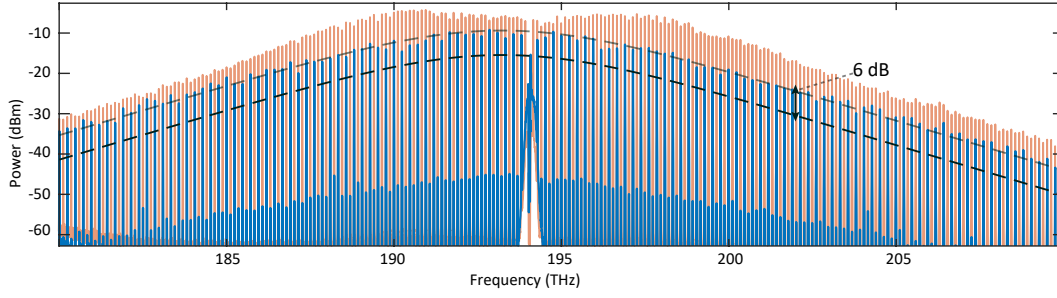


Figure 5.2: **Optical spectra of MI and soliton state** MI (red) and two-soliton state (blue) spectra obtained in the same resonance and the same pump power. Gray dashed line is a two-soliton sech fit, while black dashed line shows how a single soliton state would look like (-6dB compared with a single soliton). The reader is referred to differences in power levels between the soliton and MI.

The dynamics of the Kerr combs in monostable regime (i.e. on the blue-detuned side of the resonance) was studied in [146]. Furthermore, it was shown that gradual increase in the pump power leads to transition from the modulation instability state to the spatiotemporal chaos [180]. The resulting noise bandwidth of the waveform increases with the pump power which can be evidenced from the narrowing auto-correlation trace of the temporal intracavity field profile. In our experiments, we slowly tune the pump towards the resonance keeping the input power constant. As we show experimentally and computationally (see Appendix), the noise bandwidth of every single chaotic MI comb line increases when the pump is further tuned in to the resonance resulting in narrower distance auto-correlation traces and smaller distance resolution. It also leads to the largest bandwidth, spectral flatness and power conversion efficiency. Furthermore, RF noise bandwidth of the chaotic MI state comb lines depends on the microresonator Kerr frequency shift that is maximized for the overcoupled resonances. Counter-intuitively, the characteristic noise bandwidth of a given comb line can reach more than 3 GHz with increasing pump power significantly exceeding the cavity linewidth [33].

We utilized a single sideband modulator prior to soliton generation to offset it by 5 GHz from the signal MI. It enables us to unambiguously measure Doppler shifts without employing phase diversity detection [168], allows AC coupling of the photoreceivers (our RF amplifier has highpass cut-off at 550 MHz), and current phase calculation via Hilbert transformation [181] (the carrier frequency should be larger than the modulation frequency window) thus estimating the effective power spectral bandwidth of the equivalent frequency noise (estimating the bandwidth of frequency variation, we want to bring the analogy with FMCW and frequency excursion B).

Figure 5.3b illustrates heterodyne spectra of MI combs with corresponding LOs. Similar to conventional RMCW or FMCW LiDAR implementations, the distance resolution is directly related to the total noise bandwidth (RMCW) or chirp bandwidth (FMCW) as $\Delta R_\mu = c/2B_\mu$. Due to the irregular spectra of the chaotic light, it is not straightforward

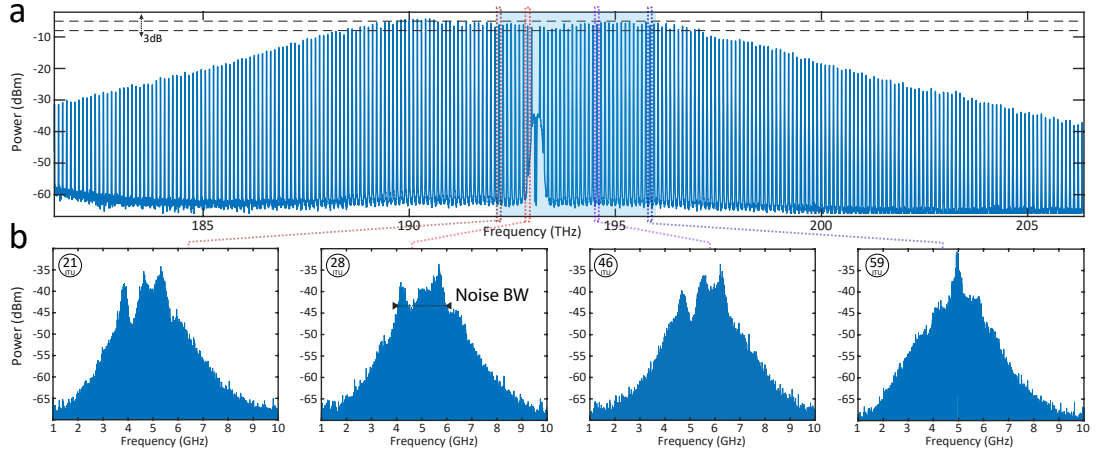


Figure 5.3: **Chaotic modulation instability noise properties.** a) Optical spectra of MI comb coupled out of the chip. The residual pump at 193 THz is filtered out. The blue shaded region covers the ITU DWDM channels 20-60 employed in our experiments. Two black dashed lines indicate 3 dB power variation and highlight ≈ 80 comb lines having small power variation. b) Heterodyne beatnote spectra for ITU channels 21, 28, 46, 59 correspondingly.

to estimate its noise bandwidth. Reference [182] studies chaos from optically injected semiconductor lasers and suggests a definition based on frequency segments containing the most power spectrum. However, we analyzed the instantaneous frequency [181] using a Hilbert transform of the beat with coherent soliton comb line to estimate the effective frequency noise bandwidth B_μ (cf. Fig 5.4a,b). We find that instantaneous frequency distribution is best fitted with a Cauchy distribution of power ~ 2.4 and the estimated noise bandwidth well matches the resolution obtained from cross-correlation corresponding to $\Delta R_\mu = c/2\sqrt{2}B_\mu$.

The cross-correlation between the digitized beat notes of the signal and reference arms, where the signal is delayed in 107 m of optical path length is depicted in Fig. 5.4c (delay divided by 2 to take into account time to distance scaling in ranging systems with back-and-forth propagation). The line-by-line dependence of the effective frequency noise bandwidth and the FWHM of the cross-correlation, which determines the smallest distance to distinguish between two semitransparent objects along the beam path, is depicted in Fig. 5.4e,f. As expected the two quantities are inversely proportional.

The dynamics in out-of-equilibrium nonlinear optical systems can exhibit non-Gaussian behavior, and give rise to Levy Statistics, i.e. heavy-tailed distributions, which lead to the appearance of rogue waves [183, 184]. Such rare events were observed in high power regime for the blue-detuned Kerr cavity [180]. In a practical system, rogue waves might lead to power spikes in the amplifiers and detectors. We did not observe any penalty on LiDAR operation in our lab experiments and line-by-line heterodyne detection with a strong local oscillator does mitigate the effects of rogue waves on the photoreceivers. We found that the amplitude of any particular comb line is well described by Rice's

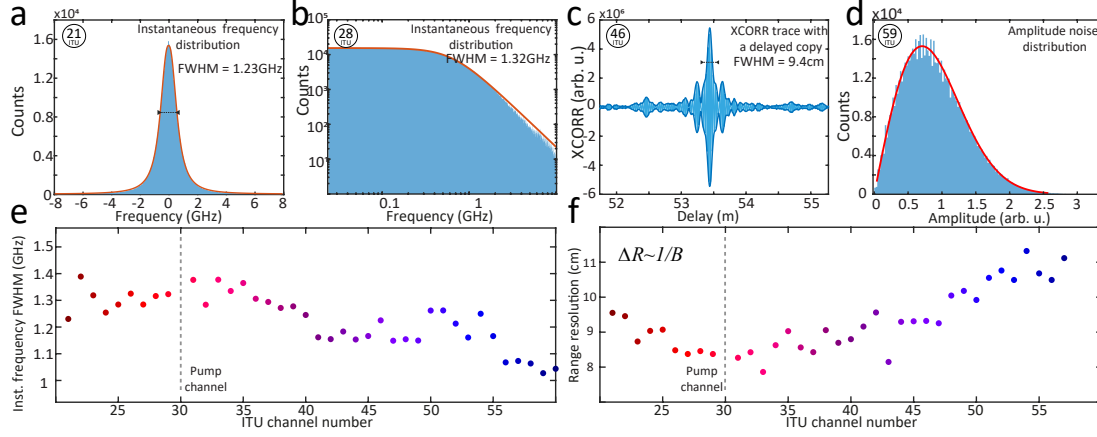


Figure 5.4: **Chaotic modulation instability noise properties.** a,b) Distribution of the instantaneous frequency with subtracted mean for ITU channel 21, 28 fitted by Cauchy distribution with ~ 2.4 power law. c) Cross-correlation of the signal and the reference for channel 46. d) Amplitude distribution for ITU channel 59 fitted by Rice distribution. e) FWHM of instantaneous frequency as a metrics characterizing frequency noise bandwidth vs ITU channel number. f) Channel-dependent distance resolution retrieved from cross-correlation. The distance resolution is consistent with the inverse proportionality to the characteristic noise bandwidth.

distribution [185] as expected for Gaussian white noise in both field quadratures and its effective noise bandwidth corresponds to the instantaneous frequency bandwidth. That means that each chaotic MI channel could also readily be applied for direct detection RMCW LiDAR systems at no resolution penalty and without the soliton LO. We employ parallel direct detection of a chaotic MI in chapter 6.

5.5 Ranging with chaotic microcomb

We performed proof-of-principle ranging experiments in similar fashion to the prior ranging experiments. A slightly different set of chess figures – Rook, Queen, Pawn, King – was placed approximately ~ 1 m in front of the beam-splitter and galvo mirror. Major part of the distance delay (105 m) comes from the fiber path difference between reference and signal arms. A point cloud of 40×100 pixels (cf Fig. 5.5b) was obtained sequentially from 40 acquisitions corresponding to every optical channel. Sampling oscilloscope operating at 40 GS/s recorded signals of distinct pixels for 10 μ s. The full pixel histogram of the scene is depicted in Fig. 5.5c. Resolvable distances of individual chess figurines demonstrate relative accuracy of the ranging.

To verify distance measurement accuracy of the chaotic frequency comb for different comb lines, we performed a fiber chromatic dispersion measurement. The specified dispersion < 18 ps/nm/km of a single-mode optical fiber [186] corresponds to ~ 0.7 ns propagation delay in 1.6 km optical fiber between 192 and 196 THz. The fitted slope for 35 channels on a delay-wavelength axis (cf. Fig. 5.5d) yields a value of 17.2 ps/nm/km.

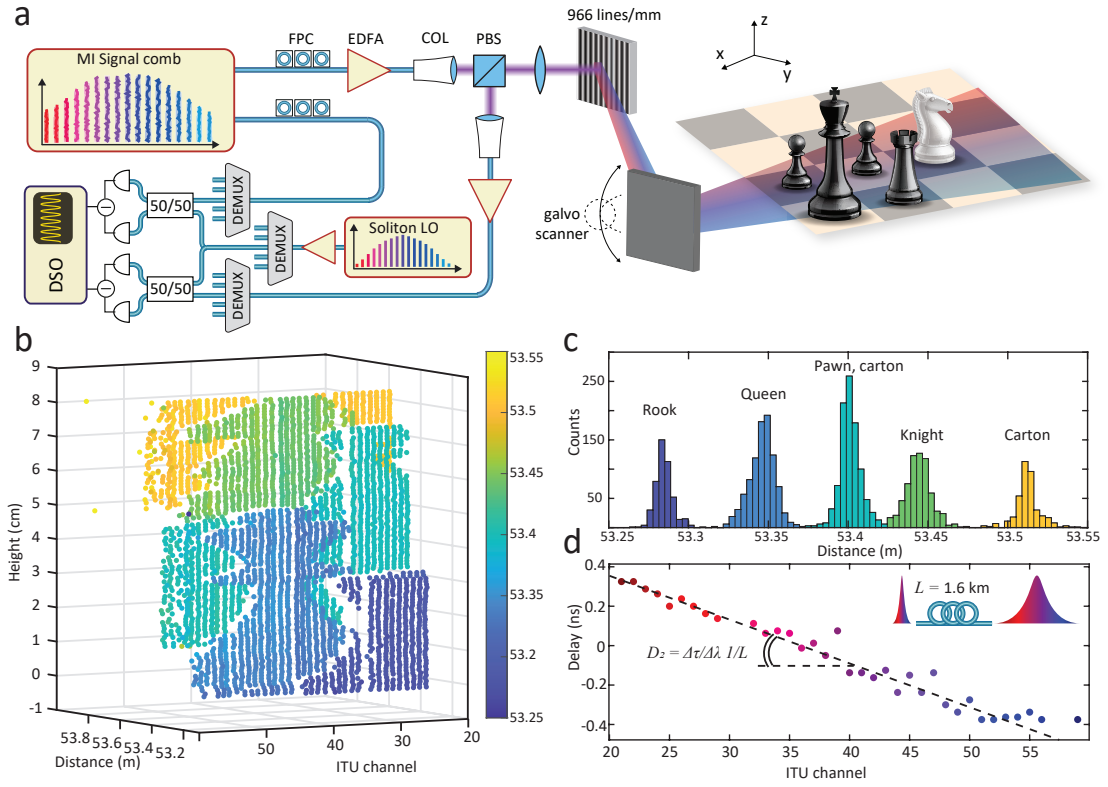


Figure 5.5: Chaotic modulation instability micro-comb based 3D imaging. a) Experimental setup. The amplified signal comb is dispersed in free-space by a 966 lines/mm transmission grating and vertical scanning is provided by a mirror galvanometer. FPC: Fiber polarization controller; COL: collimator; PBS: Polarizing beamsplitter. b) Point cloud of the four chess figures and a carton background obtained during a scan (40×100 points) of the mirror galvanometer. c) Detection histogram of panel b). The results demonstrate high relative accuracy of the measurements. d) Chromatic dispersion (D_2) measurement of 1.6 km Corning fiber patch cord. The inferred dispersion of 17.2 ps/nm/km shows high channel-to-channel accuracy.

This shows that channel-to-channel accurate and precise distance measurements are possible for every channel without any need for prior system calibration.

5.6 Velocimetry with chaotic microcomb

In the second set of experiments, we performed distance and velocity imaging of a small aluminum flywheel (on top of the same DC toy motor as before) that was covered with a lambertian reflector (cf. Fig. 5.6a,b). The motor rotation frequency was 41 Hz and the radius of the wheel was 2 cm. Direct cross-correlation of the signal and reference heterodyne beat notes (Fig. 5.6c(left)) resulted in a obscured trace with decreased SNR and shifted time delay. The problem of cross-correlation degradation in presence of Doppler shift is known from analog noise radar, where it imposes an upper limit on number of samples or the measurement integration time [161]. However, this issue

can be easily solved in digital domain via Doppler correction [168]. The Doppler shift was determined by taking a cross-spectrum correlation between signal and reference currents. The peak at ~ 5.2 MHz on Fig. 5.6c(middle) corresponds to a Doppler shift of ITU channel 21 detecting a pixel moving at ~ 4 m/s towards the beam. The signal current was downshifted by a Doppler frequency to result in a true delay estimation when cross-correlated with the reference (Fig. 5.6c(right)). The SNR is also substantially improved compared to correlation with the uncorrected trace. The velocity resolution depends on interrogation time and equates to the Fourier transform limited linewidth, which results in 16 cm/s velocity resolution for 10 μ s pixel integration time. Figure 5.6d presents the measured horizontal velocity profile of the flywheel. The ± 1 channels relative to the pump give false detection due to the excess of ASE noise in the soliton LO spectrum. Small variations of the velocity are attributed to mechanical vibrations during the line-by-line measurement.

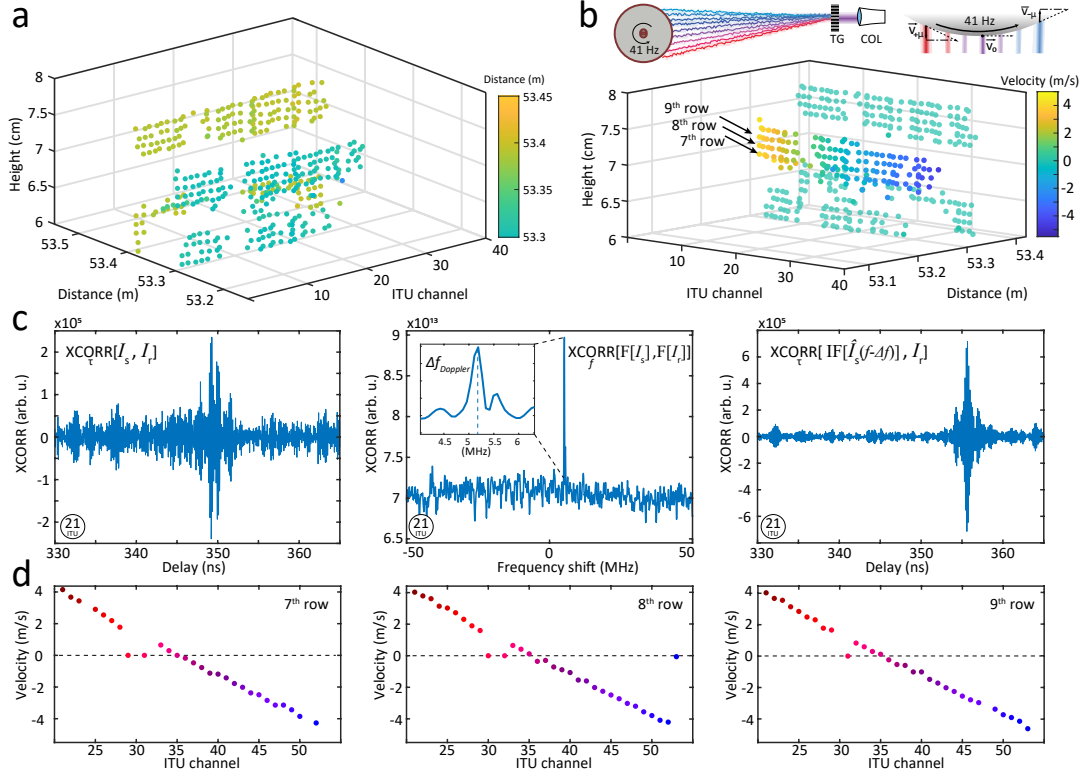


Figure 5.6: Chaotic modulation instability micro-comb based 3D velocimetry. a) Point cloud of a flywheel. Colormap represents distance information. b) Point cloud of a flywheel with a different perspective. Colormap represents radial velocity information. c) Distance and velocity inference procedure. (Left) Direct cross-correlation of signal and reference currents. (Middle) Cross-spectrum correlation highlighting the Doppler shift. Inset corresponds to the beatnote zoom-in with a Fourier transform limited resolution of 100 kHz. (Right) Cross-correlation of frequency downshifted signal and reference currents resulting in a true time delay estimation. d) Velocity profile cross-sections of the flywheel obtained from panel b).

The precision of the LiDAR is directly linked to its resolution (cf. Appendix eq. B.20) but also improves with higher SNR and measurement time (i.e. sampling points). While the measurement time in case of FMCW is hard-set by the chirp period, in case of RMCW it can be freely varied (dynamically or adaptively) to achieve sufficient SNR/precision. To highlight the achievable precision in our experiments, we demonstrate rotating flywheel circumference distance profiles (similar to Fig. 5.6d but for distances). The radius of the flywheel is 2 cm and the comb illuminates almost the whole circumference (41 Hz rotation corresponds to 5.15 m/s radial velocity, while the measured velocities span from 4 to -5 m/s). One can clearly observe the circumference with sub-centimeter level precision.

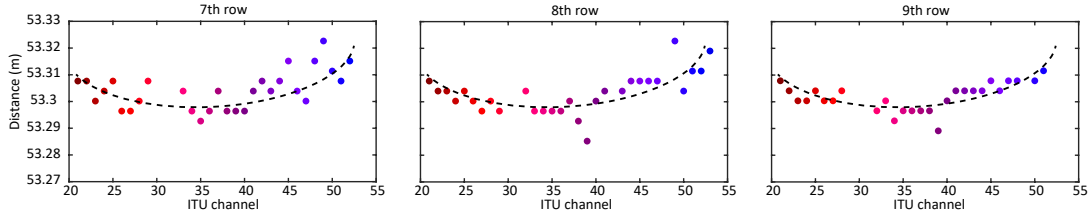


Figure 5.7: **Rotating flywheel circumference imaging** Rotating (41Hz) flywheel circumference with 2cm radius highlighting sub-centimeter precision measured by chaotic microcomb LiDAR with pixel acquisition time of 10 μ s.

5.7 Summary

In summary, we demonstrated a novel architecture for massively parallel chaotic microcomb coherent LiDAR. Unlike other applications of microresonator frequency combs, which are generally based on dissipative Kerr solitons, we focused on incoherent MI combs. We actively employed the complex dynamics in a driven Kerr nonlinear photonic microresonator that enables chaotic states of light. Spatio-temporal chaos replaces external modulators that imprint a broadband noise on each of the comb lines.

In our experiments, we utilized 40 comb lines with wideband GHz amplitude and phase modulation, which allowed for interference free and unambiguous implementation of massively parallel coherent 3D imaging. In contrast to our earlier work on parallel FMCW LiDAR [136, 177], the desired operational state of broadband chaotic MI has much greater optical efficiency, is obtained deterministically, does not require soliton switching and is free from sweeping the laser once the desired operation state is reached. Another big advantage is that depending on the operating conditions the measurement time can be dynamically updated a posteriori on a per channel basis to increase or decrease measurement sensitivity (range) and ensure the detection of faint objects or reduce computational complexity. Full heterogeneous integration of InP/Si semiconductor lasers and ultralow-loss silicon nitride microresonators for DKS/MI generation [138] is straightforward and feasible. Integrated erbium doped waveguide amplifiers [91] or

semiconductor optical amplifiers co-integrated on the silicon substrate [118, 139] could potentially replace Er-doped fiber amplifiers. Nonlinear impairment of the signal does not penalize the ranging performance as long as the reference arm is split from the signal arm after the amplification step and the noisy output waveform is the same in both arms.

The drawback of the architecture is that it requires $2 \times N$ balanced photodetectors and three wavelength division demultiplexer arrays. However, integration of demultiplexers is straightforward via arrayed waveguide gratings and chip-scale integration of large banks of balanced photodetectors has been recently demonstrated [108]. The sampling requirement of our system is on the order of 3 GS/s and compatible with silicon photoreceivers.

The random modulation and cross-correlation based ranging approach does not mandate the use of frequency-agile low noise lasers that would trade of tunability versus linewidth, nor a high degree of coherence between the signal and local oscillator. Waveform monitoring, linearization and predistortion are not required. Moreover, our system is able to parallelize detection in spectral scanning architectures for 3D imaging [187, 167], which allows to greatly increase the photon budget without raising eye safety concerns.

Lastly, we would like to highlight further potential applications of MI microcombs where the notion of chaos is actively utilized. First, optical spread spectrum communication would be possible if the data is encoded on noisy MI carriers and securely transmitted over a wide bandwidth [151]. Spatiotemporal chaos synchronization [188, 189] of MI states in remote optical microresonators could directly benefit the encoding and decoding of information on multiple carriers in such applications. Finally, cryptography based algorithms share a lot with chaotic systems [190] and chaotic maps have already been successfully applied to image encryption and decryption [152] for example.

6 Chaotic microcomb inertia-free parallel ranging

This chapter reports on the demonstration of fully solid state 2D parallel ranging. In comparison with the approaches described above, here I used two dispersive optical elements and a broadband scanning of the comb. The results are adapted from A. Lukashchuk *et al.*, "Chaotic microcomb inertia-free parallel ranging", *arXiv*, (2022).

6.1 Introduction

The ever-increasing pixel acquisition rates in the fields of augmented reality, autonomous driving and robotics has led to a growing interest in solid-state beam scanning solutions that do not rely on moving parts. This has driven modern photonics to push towards developing passive beam steering technology as a means of meeting these demands. Recently demonstrated imagers based on focal plane arrays, nanophotonic metasurfaces, and optical phased arrays enable unprecedented pixel resolution and measurement speed. However, parallelization of >100 lasers and detectors – successfully implemented in commercial time-of-flight sensors – has not been widely adopted for passive scanning approaches. Here, we show both inertia-free and parallel light detection and ranging (LiDAR) with microresonator frequency combs. We used 40 independent channels of a continuously scanned microresonator frequency comb operated in the chaotic regime in combination with optical dispersive elements to perform random modulation LiDAR with 2D passive beam steering.

Laser beam steering is one of the key challenges in the LiDAR field. The ongoing search for passive scanning solutions ranges from focal plane grating arrays [109, 108] and switching networks [107] to optical phased arrays [191] and nanophotonic metasurfaces [192]. Yet, conventional optical dispersive elements such as gratings and prisms offer mature and simple solutions for wavelength based beam steering. A combination of a virtually imaged phased array (VIPA) and a diffraction grating – also referred as 2D disperser – was demonstrated for 2D passive beam steering [50, 193] and frequency

mapping into a 2D array in the image plane of the spectrometer for molecular fingerprinting [194]. The VIPA (cf. Fig. 6.1) is a tilted etalon [195] that manifests angular dispersion by over an order of magnitude more than conventional diffraction gratings [196]. VIPA was first considered for an application of wavelength division multiplexing [195] where it could provide sufficient angular dispersion for few nm optical channels separation. The subsequent mounting of a VIPA and a grating allows for vertical and horizontal passive scanning if the source frequency bandwidth is much larger than the free spectral range (FSR) of the VIPA etalon. Recently, Li et al. [197] demonstrated VIPA-based inertia-free frequency-modulated continuous-wave (FMCW) LiDAR with a broadband swept source.

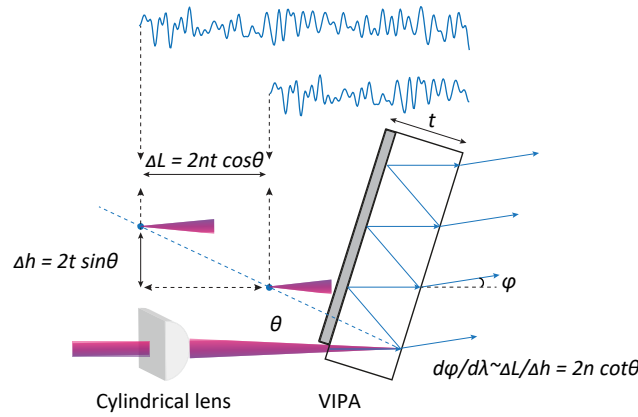


Figure 6.1: **Virtual imaged phased array (VIPA).** The VIPA etalon operates as an array of virtual images. The angular dispersion of $\sim 0.5^\circ/\text{nm}$ that is ~ 20 times higher than for the conventional grating is due to the spacing of virtual images [195].

We note that chip-scale optical microcombs can achieve 100s of nm of optical bandwidth and are suitable for massively parallel laser ranging as we demonstrated in previous chapters. Yet, true passive 2D beam steering with optical microcombs was not explored.

6.2 Concept of chaotic inertia-free LiDAR

Here, we investigate parallel and inertia-free microcomb based LiDAR. We employ the recently demonstrated chaotic random modulation LiDAR approach chapter 5, [198] where the photonic chip based microresonator is operated in chaotic modulation instability (MI) regime [33] to offer broadband noise, flat-top spectra, and high conversion efficiency. Based on the manifold of microcomb light and an optical disperser, we demonstrate passive and parallel 2D beam steering of a random modulation LiDAR system.

The principle of inertia-free LiDAR with chaotic microcombs is illustrated in Fig. 6.2a.

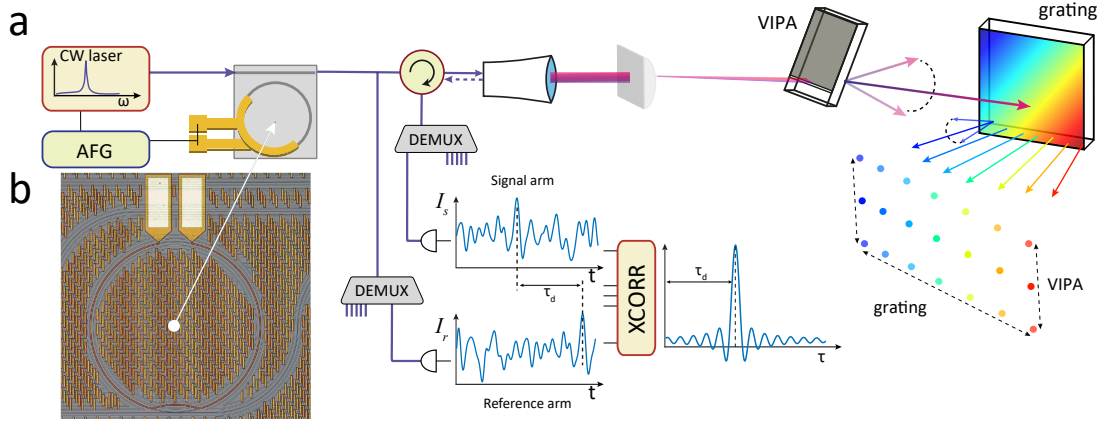


Figure 6.2: **Concept of chaotic microcomb based inertia-free ranging.** a) Schematic of the experimental setup. The chaotic comb is generated with a continuous wave pump laser and 2D-spatially dispersed with a VIPA (virtually imaged phased array) and a diffraction grating. Each signal comb tooth represents an independent random LiDAR channel and is individually accessed via wavelength division demultiplexers. Cross-correlation of the reflected signal and the reference arm is used for range inference. An arbitrary function generator (AFG) simultaneously drives the piezo controller of the laser and the chip heater to scan the comb. b) Microscope photo of the $\sim 227 \mu\text{m}$ radius Si_3N_4 microresonator with aluminum heater and contact pads.

We generated a chaotic modulation instability frequency comb where each comb line acted as an independent random LiDAR source [198, 150]. Two photoreceivers per each optical channel detected the random-like varying light intensity and the cross-correlation between the reflected signal and the reference resulted in time delay estimate or range of a given pixel. A commercial wavelength demultiplexer unit enabled individual comb line access and detection in parallel. We emphasize that here we employed direct detection approach detecting only amplitude noise of the MI comb, which is distinct from coherent detection requiring extra LOs.

Two optical diffraction elements, VIPA and grating, realize 2D inertia free scanning. While the 100 GHz microcomb free spectral range (FSR) allows for beam diffraction by the grating in horizontal dimension, the VIPA with 30 GHz FSR is responsible for vertical scanning. Thus, the 2D disperser subsequently maps every frequency to a point in space. To leverage the angular dispersion of the VIPA, the microcomb needs to be scanned for 30 GHz. To achieve broadband scanning, aluminum-based integrated heaters were implemented using additional lithographic and metal etching steps, with the spacing from the waveguide defined such that their presence does not introduce any considerable optical loss. The optical tuning range of the microheater exceeds the 100 GHz FSR of the microring resonator, which allows for full spectral coverage of the microcomb [135], though we targeted 30 GHz range to cover VIPA FSR. Simultaneous driving of the laser piezo controller and the microresonator heater attains the required frequency excursion (similar to broadband soliton scanning [135]) keeping the frequency detuning Δ between the pump and the cavity resonance locked (cf. Fig. 6.3b). A description of the optical

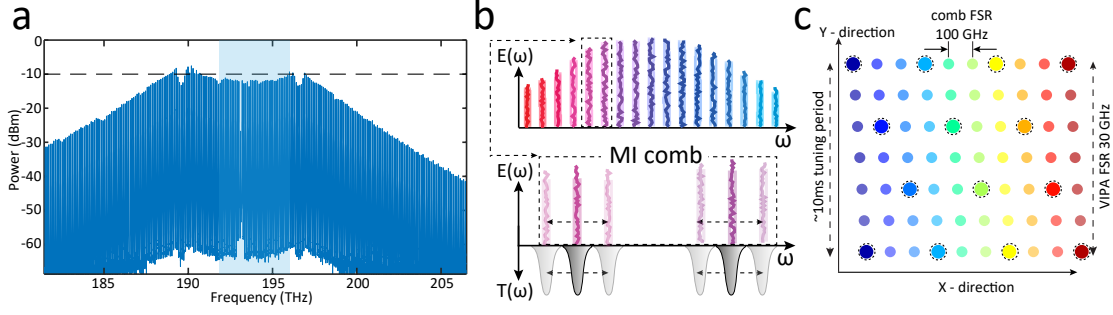


Figure 6.3: **Concept of chaotic microcomb based inertia-free ranging.** a) Optical spectrum of the chaotic comb with filtered out pump. The blue shaded region highlights comb channels (ITU 20-60) utilized for ranging experiments. The pump at 193 THz ($\mu = 0$, ITU 30) is filtered. b) Broadband scanning principle. The cavity resonances and comb lines are scanned in unison. Y-axis highlights the electric field amplitude $E(\omega)$ and transmission $T(\omega)$. c) 2D spectral shower principle. The black dashed circles highlight a 2D mapping of the comb for a given fixed frequency offset. The diffraction grating disperses the comb in the X-direction while the VIPA of 30 GHz FSR disperses in Y-direction. The full vertical scan is achieved by tuning the comb through the VIPA FSR. If the comb FSR is not an integer of VIPA FSR, ccomb channels have different output angles proportional to $\text{mod}(f_{\nu_0} + nFSR_{\text{comb}}, FSR_{\text{VIPA}})$.

configuration of VIPA and grating can be found in Ref.[199].

We pumped the Si_3N_4 microring with 900 mW of CW light at 1550 nm and achieved a 20% nonlinear conversion efficiency on-chip featuring up to -10 dBm comb line power (cf. Fig. 6.3a) and a flat-top spectrum (compared with a typical ‘sech’ profile of dissipative Kerr solitons [198]). We have 100 comb lines with the mean power of -11.5 dBm and a standard deviation of 2 dB in the spectral region covering 188-198 THz. Each comb line has a characteristic GHz-level amplitude noise bandwidth, compared with 50 MHz resonance linewidth, resulting in ~ 15 cm axial depth resolution and unambiguous ranging (due to the random-like waveform). The MI comb was generated blue-detuned from the optical resonance, i.e. it was thermally stable [200], and it followed a simple (compared with DKS) initiation routine. The blue shaded region on Fig. 6.3a highlights 40 comb channels (192-196 THz or ITU 20-60) utilized in the ranging experiments except for the filtered pump at 193 THz (ITU 30).

The novel LiDAR scheme relies on simple direct detection with cross-correlation range inference, without the need for high frequency electro-optics or precise control over the optical waveform. In our implementation, the microcomb scanning rate (shown up to 100 Hz) determines the overall frame rate of the proposed LiDAR since the field of view is covered twice during one scan.

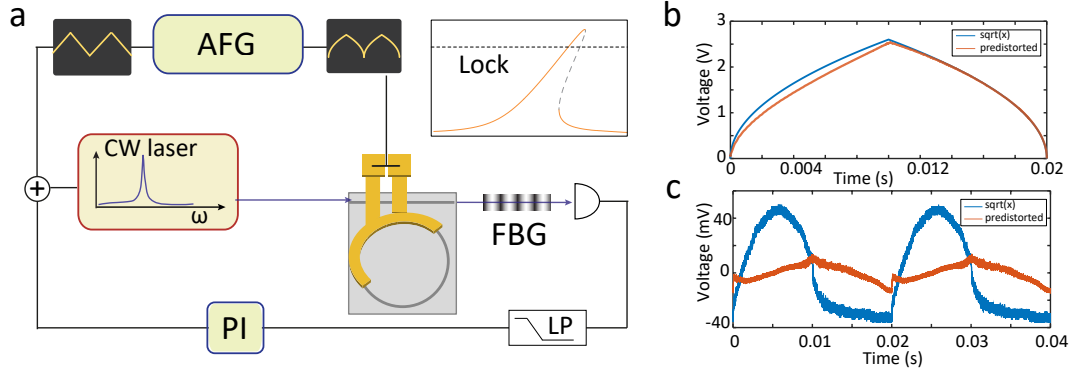


Figure 6.4: **Broadband chaotic microcomb scanning.** a) Scanning principle. Square root and linear electrical waveform signals drive microresonator heater and laser piezo correspondingly. The laser is furthermore locked to the pump resonance via side of fringe locking (cf. top right) with PI feedback applied to the laser piezo in combination with the triangular waveform. b) Initial square root-like (blue) and iteratively predistorted (red) waveforms applied to the heater. The error signal is derived from the photocurrent of the generated light (the pump is filtered). c) The feedback error signal recorded on the oscilloscope during two periods for the heater waveforms described in b). Predistorted driving corresponds to triangular-like scanning and facilitates the subsequent lock.

Chaotic microcomb tuning

Fig. 6.4a illustrates the MI microcomb scanning principle. We scanned both the pump laser and the optical microresonator to achieve a broadband frequency excursion covering the VIPA FSR of 30 GHz. The arbitrary function generator (AFG) drove the CW laser piezo controller with a triangular waveform and aluminum heater of the microresonator with a square root like waveform. The optical resonance shift is proportional to the temperature change (in the leading order) corresponding to the power dissipation or applied voltage squared. The broadband scanning of the microcomb also requires constant laser-resonance detuning Δ to maintain the MI state with uniform comb line power. We showed previously [198] that the MI operated in presoliton switching regime carries the most intracavity power resulting in highest power per comb line and effective noise bandwidth resulting in better ranging resolution and accuracy. To minimize the detuning Δ variation, we locked the pump to the slope of the resonance (side of fringe locking) via proportional-integral (PI) feedback control. We optimized the square root driving waveform of the integrated microheater by iterative predistortion to achieve linear (in the leading order) frequency chirping (cf. Fig. 6.4b,c). Similar tuning of the resonance and pump facilitated locking of the detuning and thus kept the MI uniform during the scan. It is important to keep the detuning constant to preserve noise properties, rather than have a particular tuning waveform (i.e. it should not be linear, as extra calibration would be required, since VIPA introduces nonlinearity in the vertical scan as well).

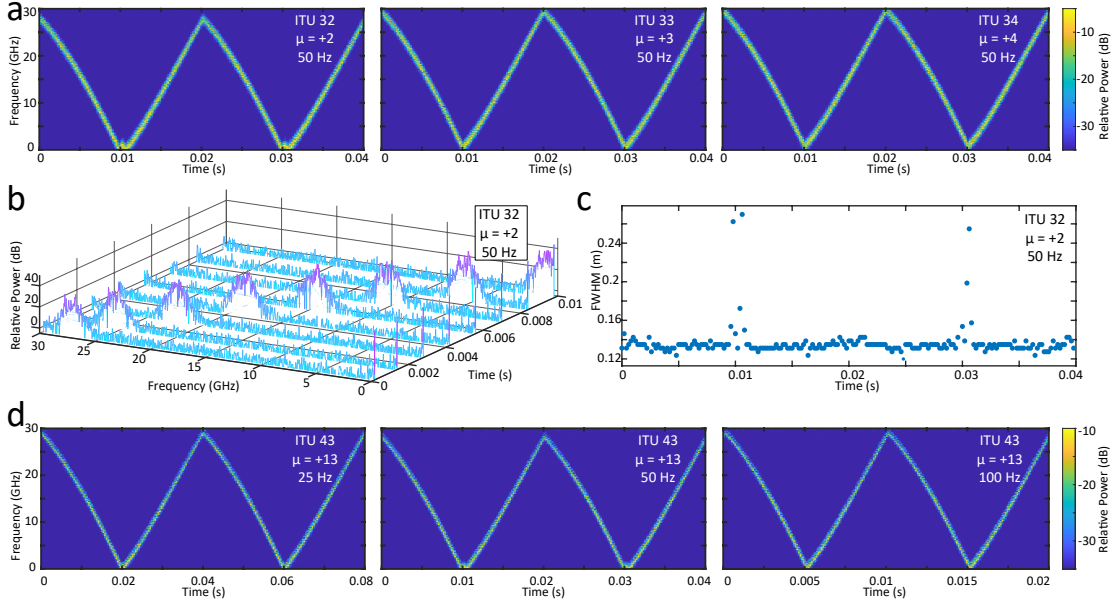


Figure 6.5: **Broadband chaotic microcomb scanning.** a) Spectrograms of heterodyne detected $\mu=2,3,4$ comb channels at 50 Hz scanning. RBW = 14.6 MHz. b) Power spectrum evolution over half of the scan period ($\mu = 2$). RBW = 29.1 MHz. Each spectra was recorded over 20 μ s while continuous scanning as in d). c) Full width half maximum of the auto-correlation traces ($\mu = 2$) recorded over 20 μ s per point while continuous scanning as in d). d) Heterodyne spectrograms for 25, 50, 100 Hz scan rates ($\mu=13$). RBW = 14.6 MHz

Fig. 6.5a depicts the heterodyne beat spectrograms of the $\mu=2,3,4$ comb lines (μ stands for the comb line number relative to the pump) recorded by superimposing the comb lines with an external cavity diode laser. We detected the beatnote with a 43 GHz balanced photodiode and digitized the photocurrent with a high-speed oscilloscope (80 Gs/s) in segmented acquisition mode at a 50 Hz comb scanning rate and 10 μ s segment length (overall 200 segments over 2 periods). The depicted spectrograms show the Fourier transforms of the individual segments. The drift of the local oscillator during the measurement was less than 1 MHz. The evolution of the MI comb line spectra for channel $\mu = 2$ is depicted in Fig. 6.4b. We observe a constant power and bandwidth of the chaotic beatnote. Fig. 6.4c depicts the full width at half maximum (FWHM) of the auto-correlation traces derived from the scanned MI comb channel $\mu = 2$. The 14 cm level determines resolution of the comb line at each step and confirms the locked detuning Δ (the reduced width around 0.01 and 0.03 s corresponds to the heterodyne spectrum folding around DC level).

In Fig. 6.5d, we show the chaotic microcomb tuning at different tuning rates on the example of channel $\mu = 13$. The fastest tuning rate that we could achieve is 100 Hz and it was limited by the response of the pump laser piezo controller. The aluminum heaters were reported to have response at kHz frequencies level [201], which could further increase the frame rate of the novel passive LiDAR.

6.3 Chaotic microcomb inertia-free ranging

Fig. 6.6a presents a point cloud of 39×20 pixels acquired during 0.01 s - full vertical swing or half of the scanning period (50 Hz). We sequentially detected 39 comb channels (ITU 20-60 excluding the filtered pump channel) while the detection can be performed in parallel requiring a number of photodetectors and digitizers equal to twice the number of channels (signal and reference for each channel). Every channel recording consisted of 40 segments ($20 \mu\text{s}$ each) corresponding to two vertical scans (up-swing and down swing, cf. Fig. 6.6b; recorded in the segmented acquisition mode of the oscilloscope similar to heterodyne analysis Fig. 6.5a). The demonstrated pixel measurement rate was limited by the available oscilloscope memory and the tuning rate of the external cavity diode laser. We used 1.5 GHz photoreceivers to record the chaotic intensity profiles and digitally computed cross-correlations for delay estimation. Cross-correlation trace comprises the target distance information and also the back-reflection from the collimator and circulator (cf. Fig. 6.6c). The dispersed comb illuminated carton blocks covered by retroreflecting tape at 2 to 3.6 m range away from the collimator. We achieve ~ 14 cm depth resolution as analyzed from the cross-correlation FWHM (cf. Fig. 6.6e and Fig. 6.5c). This is a direct consequence of a chaotic MI nature, where every comb line possesses >1 GHz effective noise bandwidth without the need for external modulation or control. Furthermore, the chaotic LiDAR is capable of unambiguous range detection [148] and has superior immunity to ambient light interference [7].

The 2D disperser scanning as depicted in Fig. 6.2a corresponds to the case when the comb FSR equals to the VIPA FSR times an integer number. In our case - the VIPA and microcomb had 30 GHz and 100 GHz FSR, respectively - every third comb line illuminated the target at a similar vertical angle since the accumulated frequency separation of three FSRs was ten times the VIPA FSR ($3 \times 100 \text{ GHz} = 10 \times 30 \text{ GHz}$), while every subsequent comb line had a vertical angular shift - $\sim 33\%$ of the vertical field of view (cf. Fig. 6.3c). Precise knowledge of the comb FSR and approximate VIPA FSR allowed us to calculate the relative vertical illumination angle shift for every comb line. The point cloud z-axis has arbitrary unit height value since we did not calibrate the absolute vertical angle corresponding to every segment of the linear sweep, though it is assumed to be linear in the leading order [196]. We used a high-density reflective diffraction grating with 1200 lines/mm to diffract the light in the horizontal direction.

Fig. 6.6d depicts a point cloud pixels histogram. The distance precision is on the order of the range resolution (~ 14 cm) due to the multiple beam round-trips in VIPA etalon, i.e. multiple reflections with different accumulated delays (cf. Fig. 6.6b) that can reach >10 cm with VIPA thickness of 3 mm and finesse \mathcal{F} of 100. Another potential drawback may come from the effective frequency noise bandwidth being comparable to the VIPA linewidth, i.e. ratio of VIPA FSR and its finesse \mathcal{F} , which results in extra angular divergence of a particular chaotic comb line, even when the comb is not scanned.

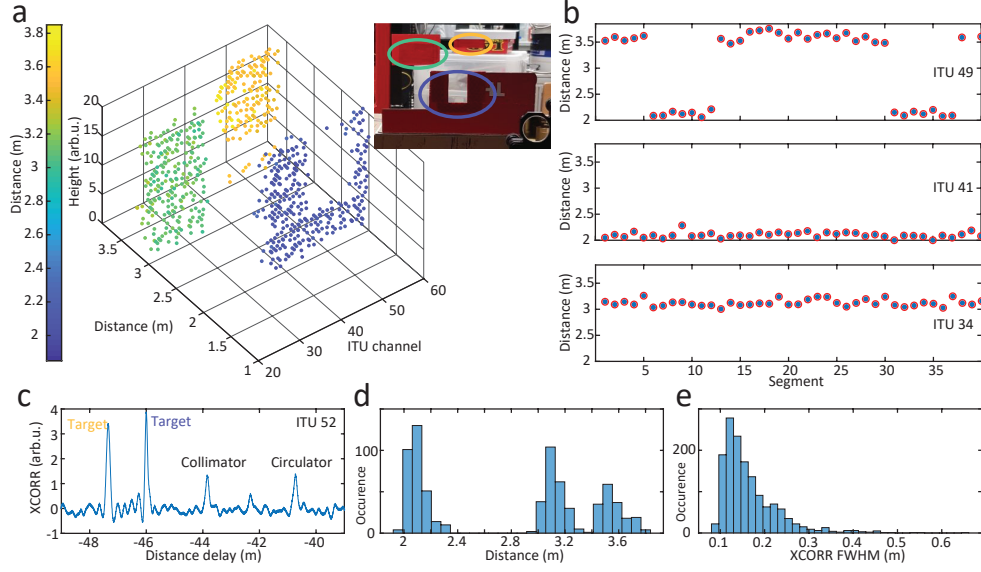


Figure 6.6: Chaotic microcomb inertia-free ranging. a) Point cloud of 39×20 pixels (top right: target photo). Height is depicted as 20 acquired segments corresponding to a full vertical VIPA swing over half of the scanning period. b) Ranging results for individual comb channels (ITU 49, 41, 34). 40 segments correspond to one scan period (0.02 s) with each segment recorded over $20 \mu\text{s}$. c) Cross-correlation trace of one segment ($20 \mu\text{s}$ acquisition) highlighting multiple targets. Two target reflections correspond to an edge case where VIPA operates in two orders. d) Detection histogram highlighting ~ 14 cm level precision. e) Statistics of the target cross-correlation FWHM depicting ~ 14 cm resolution.

The comb was amplified up to 500 mW prior to collimation. Since we used fiber coupled photoreceivers, the returned light was projected into a fiber mode resulting in significant intensity loss due to speckle, which necessitated the use of retroreflector and pre-amplifier to overcome the digitizer noise level (~ 5 mV) at the detection stage.

6.4 Discussion

We demonstrated chaotic microcomb based parallel inertia-free laser ranging. The proposed implementation requires minimum active components on the light transmitter side. Photonic integrated Si_3N_4 microresonator acts as a source of 40 and potentially >100 noisy comb channels for random LiDAR that are dispersed in 2D and can be detected in parallel. We showed that integrated aluminum micro-heaters enable agile frequency scanning of chaotic MI with 30 GHz excursion at 100 Hz rates (both limited by the laser piezo response) while Si_3N_4 microresonators were reported to achieve ~ 200 GHz excursion and up to kHz scanning rates [135, 201]. The higher excursion allows for VIPA with larger FSR and subsequently larger angular dispersion while higher scan rates translate into faster acquisition frame rates. The recently reported integration of aluminum nitride and lead zirconate titanate with Si_3N_4 photonic circuits [87] could

provide tuning with flat response and higher actuation bandwidth, but would require much higher voltage than aluminum heaters to cover several gigahertz range. We note that heterogeneous integration of Si_3N_4 frequency comb with InP/Si semiconductor laser [138] has been demonstrated as well as hybrid integrated solutions [117, 116] and on-chip optical amplifiers [91] paving the path to fully integrated LiDAR transmitter.

The combination of a VIPA and grating represents a simple yet mature 2D inertia-free scanning solution. It could provide $1.9 \times 7.7^\circ$ field of view [197], while the grating field of view could be easily extended by employing more comb lines or frequency combs with higher FSR. The VIPA tilt angle should be carefully chosen as it trades-off single order operation versus angular dispersion and tuning curvature [196]. Ultimately, any combination of passive optical dispersers can be considered. Non-etalon-based optical dispersers would eliminate the drawback of the multiple reflections and improve the ranging precision.

The sampling rate performance of the current scheme depends on the comb scanning period, pixel acquisition time and VIPA finesse. The total number of acquired pixels for one comb channel during one vertical scan should be less than the VIPA finesse $N < \mathcal{F}$. But also the total acquisition time should be less than the scanning period $N \times \Delta t < T/2$. For 100 Hz tuning rate and a VIPA finesse $\mathcal{F} = 100$, the achievable sampling rate per comb channel is 20 kS/s at 50 μs pixel acquisition time. Megapixel sampling rates are feasible when more than 50 comb lines employed, or 50×100 pixels at 200 frames per second rates.

Passive scanning is currently adopted as a commercial solution for true solid state LiDARs. Several LiDAR companies combine a 1D spectral scan approach based on optical dispersers with mechanical scanning for the second dimension [9, 167]. In addition, parallel illumination and acquisition - widely employed in time-of-flight LiDAR - may solve the long standing challenge of detecting megapixel rates required for real-time applications in robotics, unmanned driving and augmented reality. Finally, we have demonstrated parallel and inertia-free beam steering LiDAR based on chaotic microcombs.

7 Photonic-electronic integrated circuit-based coherent LiDAR source

This chapter covers the efforts towards integrated LiDAR engine. Here we combined fully integrated electronic circuit, hybrid integrated Si_3N_4 Vernier laser and erbium-doped waveguide amplifier to demonstrate coherent ranging with integrated LiDAR source. The results are adapted from **A. Lukashchuk***, K. Yildirim* *et al.*, "Photonic-electronic integrated circuit-based coherent LiDAR source", (*awaits submission, patent pending (ASIC)*), (2023)

7.1 Introduction

Chip-scale integration is one of the center pursuits for data center communication transceivers, imaging sensors, and consumer electronics. Photonic and electronic integrated chips benefit from miniaturization, large-volume production, and novel functionalities, and can outperform conventional bulk apparatus. To date, the compact, pluggable transceiver deployed in data centers is a paramount example demonstrating the advances brought by photonic and electronic integration [133]. The reduction in size, weight, power and the performance improvement of the miniaturized devices allows for the adoption of new photonic technologies unforeseen a decade ago. Photonic low-noise microwave generation [137] and reconfigurable RF filters [62, 65], integrated optical gyroscopes [202] and isolators [203], photonic computing [51, 73] and deep learning accelerators [72] are just a few examples of applications that have been made possible with integrated photonics.

In recent years, LiDAR technology has gained significant attention due to its potential applications in the rapidly growing self-driving market. However, despite its numerous advantages, the high costs associated with the manufacturing of individual LiDAR components and their assembly has hindered its widespread adoption. Photonic and electronic integration is widely regarded as a potential solution to address this challenge

*These authors contributed equally to the work

by reducing the costs associated with LiDAR systems and enabling mass-production.

Coherent LiDAR, in particular, requires multiple building blocks including a frequency agile laser, driving electronics, scanning optics, passive components (grating couplers, switching network), and detectors. A variety of recent work attempted to integrate LiDAR components on chip. Martin et al. demonstrated a silicon photonic circuit with integrated detectors, waveform calibration and switching network for passive beam scanning capable of 60 m coherent ranging at 5 mW output power [107]. Poulton et al. presented an optical phased array (OPA) based FMCW 3D ranging up to 10 m [191]. The same group demonstrated nearly centimeter scale OPA aperture with 8192 elements achieving $100^\circ \times 17^\circ$ field of view [204]. Rogers et al. developed a focal plane array (FPA) 3D LiDAR on a silicon chip with photonic-electronic monolithic integration of 512 pixel coherent receiver array [108].

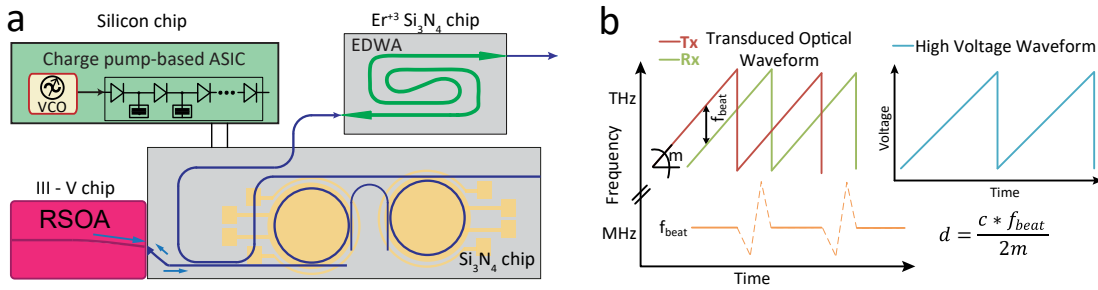


Figure 7.1: **Concept of photonic-electronic LiDAR source.** a) Schematics of photonic-electronic LiDAR structure comprising a hybrid integrated laser source, charge-pump based high-voltage arbitrary waveform generator ASIC, photonic integrated erbium-doped waveguide amplifier. b) Coherent ranging principle.

The aforementioned approaches are CMOS compatible, can be integrated with other passive or active optical components and are scalable, i.e., support further increase in number of pixels and field of view. However, these demonstrations used external lasers coupled via fiber, off-the-shelf driving electronics, erbium-doped fiber amplifiers for signal or reflection amplification and bulk modulators (Refs. [191, 108]). Importantly, all of these building blocks can be replaced with their integrated counterparts. Tackling the issue of discrete external components, Issac et al. fabricated an integrated transceiver module on InP platform [205], but no coherent ranging functionality was performed. Similarly, Ref. [206] showed a fully integrated coherent LiDAR on chip, though it is limited to single-pixel imaging and lacks scanning functionality. The combination of photonic and electronic circuits with existing integrated beam steering solutions [108, 109, 191] would constitute a fully integrated coherent LiDAR engine. Yet, such an engine that uses high coherence photonic integrated frequency agile laser, integrated electronic driving circuits and low noise amplification has so far remained challenging.

In this chapter, we report a photonic-electronic integrated circuits LiDAR source that combines an integrated laser, high-voltage (HV) arbitrary waveform generation (AWG)

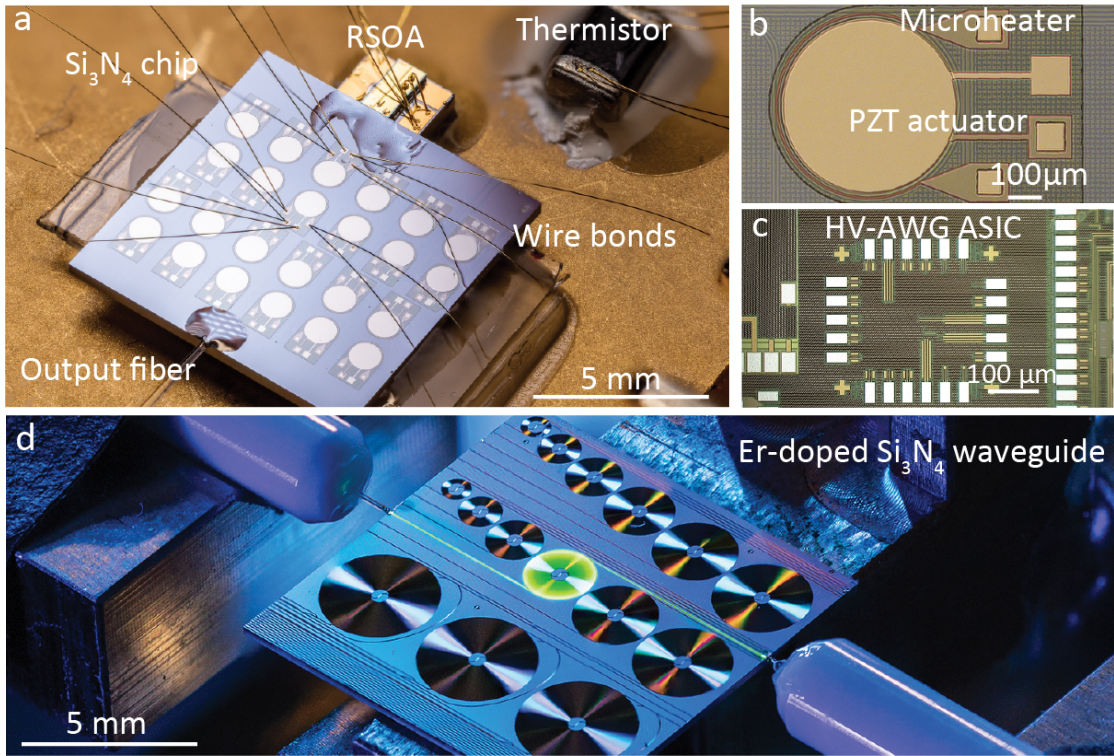


Figure 7.2: Integrated blocks of coherent LiDAR engine. a) Packaged laser source. RSOA is edge coupled to Si_3N_4 Vernier filter configuration waveguide, whereas the output is glued to the fiber port. PZT and microheater actuators are wirebonded as well as butterfly package thermistor. b) Zoom in view of c) highlighting a microring with actuators. c) Fully integrated high voltage arbitrary waveform generation ASIC. d) The Erbium-doped waveguide is optically excited by a 1480 nm pump showing green luminescence due to the transition from a higher lying energy level to the ground state.

ASIC, and chip-scale Erbium amplifier. The source contains building blocks compatible with prior LiDAR implementations and ready to substitute commercial bulk devices. First, we demonstrated a fully integrated high voltage arbitrary waveform generator (AWG) in standard 130-nm SiGe BiCMOS technology, which can be integrated with advanced electronics thanks to its small feature size while enabling tight assembly with photonic integrated circuits (PIC) technology for a miniaturized system. This application-specific integrated circuit (ASIC) utilizes a novel charge pump architecture, which generate arbitrary waveforms up to more than 20 volts with the need for no external high voltage supplies. Further, we used a hybrid integrated Vernier laser based on a low-loss Si_3N_4 platform with fast piezoelectric actuators that supports >100 kHz sweep rate and >2 GHz frequency excursion. Lastly, we employed an erbium-doped waveguide amplifier (EDWA) capable of providing 24 dB off-chip net gain [91] to meet the optical power budget requirement and compensate the losses caused by chip-to-chip coupling, switching network and local oscillator (LO) driving [107, 108]. The combination of integrated laser, AWG ASIC and chip-scale Erbium amplifier constitutes a

plug-and-play coherent LiDAR source, which can be applied to existing silicon imaging 3D sensors and pave a path towards a fully integrated coherent LiDAR engine.

7.2 Vernier laser

The photonic-electronic LiDAR structure consists of three main building blocks: laser, ASIC and on-chip amplifier Fig. 7.1a. The hybrid integrated laser (cf. Fig. 7.2a) operating at 1566 nm consists of a reflective semiconductor optical amplifier (RSOA) edge-coupled to a Si_3N_4 photonic chip with a microrsonator-based Vernier filter [207]. Two microresonators with loaded cavity linewidths of 200 MHz slightly differ in free spectral range (FSR), i.e., 96.7 and 97.9 GHz with Vernier frequency of 8.7 THz. Both rings have integrated microheaters realized in the bottom Pt electrode layer. The laser covers C band and can be tuned by the current injection, microheaters and PZT actuators (cf. Fig. 7.3c). We aligned the pair of resonances using a microheater to get up to 20% reflection back to the RSOA. Piezoelectric PZT actuators are integrated on top of the microrings to perform fast actuation via stress-optic effect for rapid laser frequency tuning. Platinum electrodes (cf. Fig. 7.2b) match the resonator radius to maximize the stress-optic tuning efficiency. The laser features $10^4 \text{ Hz}^2/\text{Hz}$ frequency noise at 10 kHz offset frequency reaching the white noise floor at $127 \text{ Hz}^2/\text{Hz}$ and 6 MHz offset (cf. Fig. 7.3d).

The hybrid assembly in the butterfly package includes a Si_3N_4 chip and an RSOA placed on the same Peltier element; the output of a cleaved SMF fiber is glued to the output Si_3N_4 waveguide. RSOA, Peltier element, thermistor, all microheaters, and PZT actuators are connected to butterfly pins using wirebonding. Hybrid packaging allows for turnkey laser operation and maintains the tuning performance after waveform predistortion and linearization.

The HV-AWG integrated circuit (cf. Fig. 7.2c) generates a 15 V sawtooth waveform driving the PZT actuators of the laser. The electrical waveform is further transduced to the optical domain, resulting in $>2 \text{ GHz}$ optical chirp excursion. Fig. 7.1b shows the coherent ranging principle. The detected range is proportional to the beatnote frequency inferred from the short-time Fourier transform of the recorded heterodyne signal. It is inversely proportional to the waveform chirp rate m - the ratio of the excursion and sweeping period.

In our experiments, the laser operated at a temperature of 26°C and RSOA current of 340 mA, resulting in 3 mW output optical power. We applied around 30 mW of electrical power to microheaters to align resonances of Si_3N_4 microrings. We do not have on-chip phase shifter section in our laser design, and the tuning range was empirically limited to 3 GHz while the RSOA current was fixed.

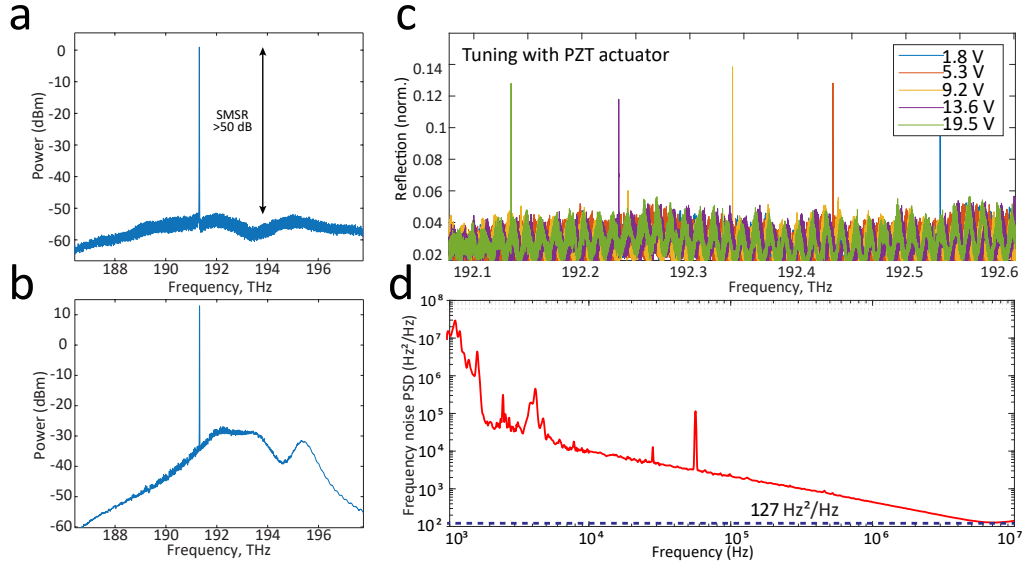


Figure 7.3: **LiDAR source electro-optical transduction and linearity.** a) Optical spectrum of Vernier laser output featuring 50 dB side mode suppression ratio. b) Optical spectrum after EDWA with >20 mW optical power. c) Normalized reflection of the Vernier filter at the different voltages applied to the integrated PZT actuator. Increasing voltage by 8 V shifts the cavity resonance by 1.2 GHz and allows to shift the reflection peak by 1 FSR (97 GHz) (adapted from [208]). d) Single-sided PSD of frequency noise of the hybrid integrated laser (adapted from [208]).

Erbium doped waveguide amplifier

We employed a chip-scale integrated EDWA [91] (cf. Fig. 7.1d) to amplify the laser to >20 mW optical power to meet the power requirements for robust and long-range coherent ranging [209]. Typically integrated LiDAR systems require >100 mW of optical power to compensate for coupling losses and be able to emit 10s mW at the aperture [107, 204]. The EDWA was implemented using an on-chip 21-cm-long Si_3N_4 spiral waveguide doped with high-concentration Erbium ions (3.25×10^{20} ions/cm) through a high-energy (up to 2 MeV) ion implantation process [210, 91]. The doped Erbium ions can be optically pumped to the excited state and allow for amplification stemming from the stimulated transition to the ground state. The EDWA provides linear and low noise optical amplification to the frequency modulated optical waveform due to the slow gain dynamics (millisecond lifetime) and the small emission cross section of Erbium ions [211].

Integrated Si_3N_4 spiral waveguides were fabricated with the photonic damascene process. The preform for waveguide structures and filler patterns for stress release was then defined by deep ultra-violet photolithography and transferred into the thermal oxide layer using reactive ion etching (RIE). Thermal treatment at 1250 °C was then applied to reflow the silicon oxide, reducing the roughness caused by the RIE etching [23], before

the preform recesses were filled with stoichiometric Si_3N_4 by LPCVD. An etchback process was performed to roughly planarize the wafer surface and remove the excess Si_3N_4 material. Chemical mechanical polishing (CMP) was then applied to reach the desired waveguide thickness, and create a top surface with sub-nanometer root-mean-square roughness. Using this process, 700 nm-thick Si_3N_4 waveguides buried in a wet oxide cladding but without top cladding were created, which allowed for direct Erbium implantation into the waveguide core. The Erbium ion beam energy of 0.955 MeV, 1.416 MeV and 2 MeV and the corresponding fluence of 2.34×10^{15} , 3.17×10^{15} and 4.5×10^{15} ions/cm², respectively, were consecutively applied to the separated passive Si_3N_4 photonic chips. This process can implant Erbium ions into the Si_3N_4 waveguides ($0.7 \times 2.1 \mu\text{m}^2$ cross-section) with a maximum doping depth of ca. 400 nm from the top surface and achieve an overlap factor of ca. 50 %. The doped Si_3N_4 was then annealed at 1000 °C in O_2 under atmosphere pressure for 1 hour to heal the implantation defects and optically activate the doped Erbium ions. The measured lifetime of the first excited state of doped Erbium ions is ca. 3.4 ms. Higher annealing temperature could lead to Erbium ion precipitations in the silica cladding [210]. The Erbium ion implantation of the Si_3N_4 photonic chips was performed at the University of Surrey Ion Beam Centre via commercial service.

7.3 High-voltage Arbitrary Waveform Generator ASIC

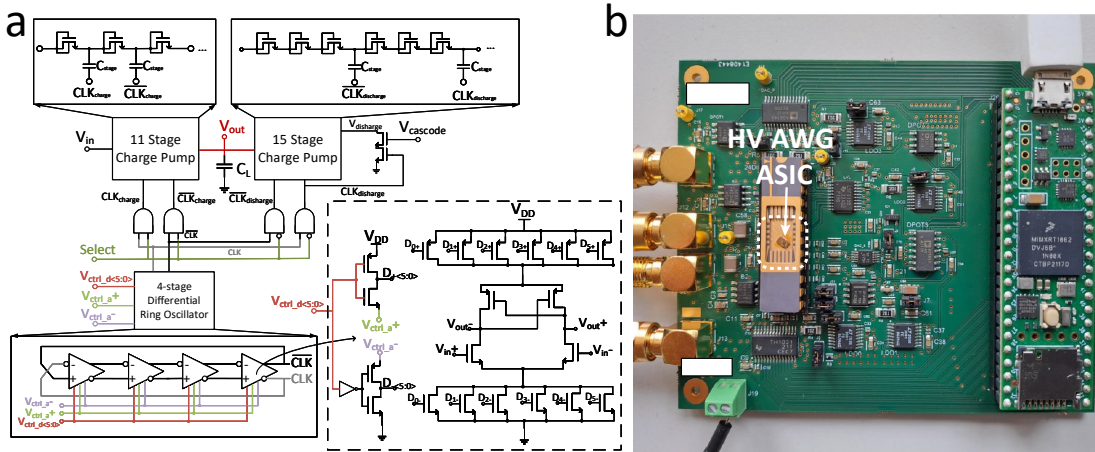


Figure 7.4: **High-voltage arbitrary waveform generator integrated circuit.** a) Schematics of the integrated circuit consisting of a 4-stage voltage-controlled differential ring oscillator which drives charge pump stages to generate high-voltage arbitrary waveforms. b) Testing board of the chip: the output voltage is connected to a unity-gain voltage buffer on the printed circuit board through the package, and the buffer output is used to drive an SMA connector that is used for the measurements.

Arbitrary waveform generation at high voltages is desired to drive various devices including ultrasound transducers [212, 213], piezoactuators [87], and neurostimulators

[214]. High-voltage AWGs (HV AWG) are usually provided as a single or even multiple discrete components [215, 87], which are generally challenging to be integrated due to their incompatibility with technologies supporting advanced electronics. We demonstrate a novel architecture which can generate HV arbitrary waveforms using a standard CMOS technology supplied at 3.3V. (Fig. 7.4). The ASIC consists of a ring oscillator, which drives the clocks of a charge pump. The oscillation frequency can be controlled externally. Fig. 7.4a shows the block diagram of the IC. It comprises a series of Dickson charge pump stages, whose clocks are driven by a 4-stage differential ring oscillator. The 11-stage charge pump generates the output waveform with rising edges, whereas the 15-stage charge pump generates falling edges. The two charge pump blocks operate in a complementary fashion, with the 'Select' signal controlling whether the output voltage increases or decreases. The clocks are applied only to the charging/discharging block during one half cycle when the output voltage rises/falls. The oscillator is designed to have a wide frequency range and a high frequency resolution, so as to achieve fine-tuning capability while controlling the waveform. The unit cell of the four-stage ring oscillator has six geometrically sized pairs of NMOS and PMOS (n-type/p-type metal-oxide-semiconductor) transistor loads to control the unit delay. The inputs, $V_{ctrlld<5:0>}$, can be digitally switched to turn on a pair of NMOS and PMOS loads each, where $V_{ctrlld<5>}$ corresponds to the load with the highest width per length. Using digital inputs, gate voltage of the PMOS loads is connected to V_{ctrla+} and the NMOS loads to V_{ctrla-} , respectively. These two gate voltages are controlled differentially in an analog fashion, where their sum equals to V_{DD} to fine tune the oscillation frequency. Operating at a supply of 1.2 V, the frequency of the designed oscillator can be set in the range of 6 MHz to 350 MHz, with a tuning control of 2% at lower frequencies and 0.5% at higher frequencies employing 10 mV steps for V_{ctrla+} and V_{ctrla-} .

Fig. 7.4a illustrates the principles of waveform generation. The rise time of a charge pump circuit depends on the frequency of the driving clocks, therefore enabling one to tune the time-domain waveform by changing the clock frequency at pre-determined time points. We can set a digital control input high to decrease the waveform rise time by increasing the charge pump clock oscillation frequency. To start the falling edge, we switch off 'Select' signal (cf. Fig. 7.5a) - middle panel), and the fall time is controlled in the same manner using the oscillator inputs. This allows the AWG ASIC to generate an output voltage more than 20 V. The output waveform has a period similar to 'Select'; the 'Select' duty cycle also sets the highest and lowest output voltage values. We can produce waveforms with different shapes, amplitudes, frequencies and offset values (cf. Fig. 7.5a) when operating the circuit with different oscillator control input sequences. Fig. 7.5b shows the generated 45 kHz sawtooth waveform used in our FMCW LiDAR experiments. The 6-bit digital frequency control input code is modulated in conjunction with the analog voltages to avoid sharp changes in the waveform.

The design was fabricated in standard 130-nm SiGe BiCMOS technology (cf. Fig. 7.2c), where only CMOS transistors were used. The chip measures 1.17-1.07 mm². The total

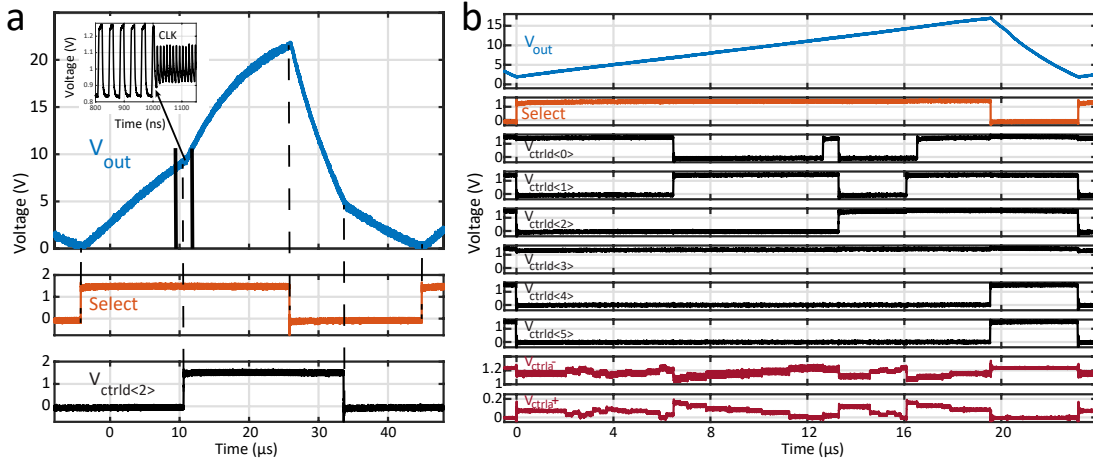


Figure 7.5: **High-voltage arbitrary waveform generation.** a) Principles of waveform generation demonstrated by the output response to the applied control signals in the time domain. Inset shows the change in oscillation frequency in response to a frequency control input, from 44 MHz to 91 MHz, which modifies the output waveform. b) Generation of the linearized sawtooth electrical waveform used in LiDAR measurements. Digital and analog control signals are modulated in the time domain to fine-tune the output.

active area of the design, i. e. excluding decoupling caps and IO pads, is approximately $35,000 \mu\text{m}^2$. The charge pump is implemented with diode connected isolated thick oxide NMOS transistors and metal-insulator-metal (MiM) capacitors. V_{in} and $V_{cascode}$ were biased at $V_{DD} = 3.3\text{V}$. The 15-stage charge pump has three diode-connected transistors in each stage, so as to set $V_{discharge}$ to $V_{out} - 45V_{th,n}$ as V_{out} rises during the charging phase. A cascode transistor is also introduced at $V_{discharge}$, so that a voltage up to $2V_{DD}$ can be tolerated at this node. This ensures that V_{out} can safely reach more than 20 volts without reaching breakdown of the discharge transistors, given that the capacitors and NMOS-to-bulk isolation are within breakdown limits as well. For the measurements presented, the output of the CMOS chip was fed to an external unity-gain voltage buffer whose output was measured and/or used to drive the actuators. Load capacitance at chip output was measured at 26 pF. The printed circuit board used for controlling the ASIC is shown in Fig. 7.4b.

7.4 Electro-optic transduction and linearity

Fig. 7.6a demonstrates the electrical waveform generated by the ASIC. The same sawtooth signal was applied to both piezoactuators of the Vernier laser. The heterodyne measurement carried out with an auxiliary laser shows the time-frequency map of the laser chirp (cf. Fig. 7.6b). The 15 V electrical signal resulted in $>2 \text{ GHz}$ optical frequency excursion over $23 \mu\text{s}$ period. The chirp m parameter of the up-swing used for the ranging equates to $\sim 110 \text{ THz/s}$. It ultimately determines the detected beatnote

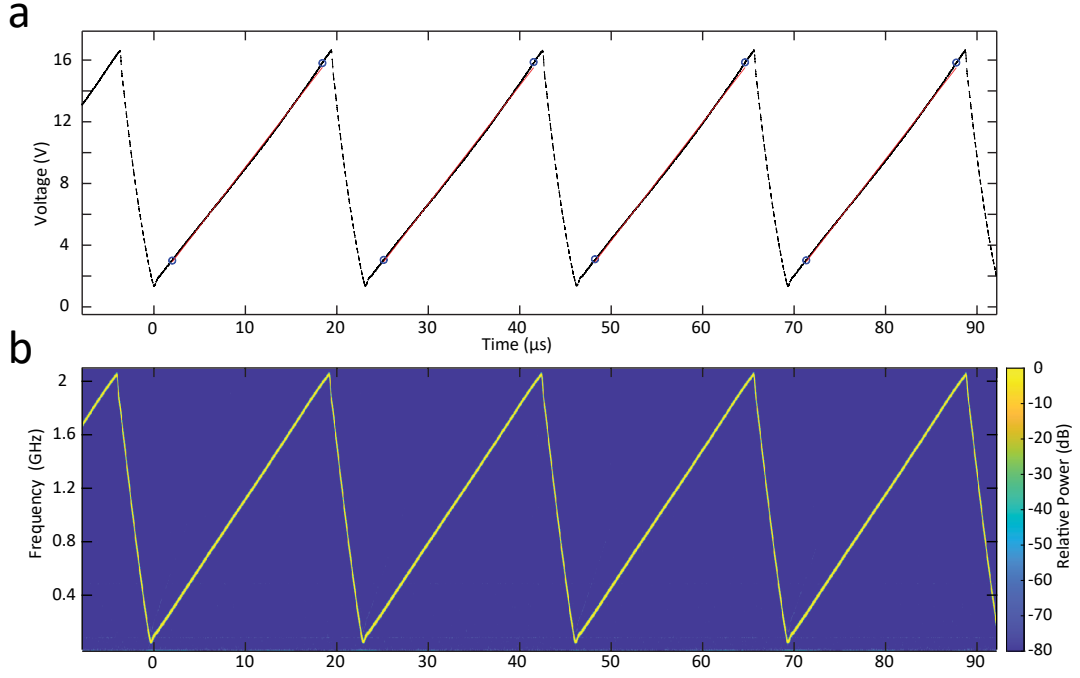


Figure 7.6: **LiDAR source electro-optical transduction and linearity.** a) Electrical waveform generated by ASIC. Blue circles highlight the segment of $\sim 16 \mu\text{s}$ used for ranging and linearity analysis. The red curve is a linear fit to the given segment. b) Time-frequency map of the laser chirp obtained via heterodyne detection with auxiliary laser. RBW = 10 MHz.

frequency f_{beat} to distance d mapping via $d = c/2m \times f_{beat}$ where c is the speed of light. In our experiment 1 m of range maps to ~ 1 MHz frequency beatnote for the laser sweep parameters described above.

For the long range and robust measurement, FMCW LiDAR requires high chirp linearity of the optical waveform [103]. We iteratively linearized the optical waveform employing a delayed homodyne detection method [102]. We employed similar procedure to linearize the pump for FM DKS generation in chapters 3,4. We calculated the instantaneous frequency of the chirp (cf. Fig. 7.7a) via Hilbert transformation of the beatnote electric signal. The ASIC architecture allows for the waveform fine tuning in an arbitrary fashion, therefore we optimized the frequency control inputs of the ASIC to minimize the root mean square error RMSE of the instantaneous frequency. In chapters 3,4 we fitted a perfect triangle to the instantaneous frequency and iteratively updated the AWG signal by adding the difference. Here, we used a $16 \mu\text{s}$ up-rise segment of the chirp for linearity analysis and afterwards updated the controls of the HV AWG.

Fig 7.7b depicts the chirp nonlinearity or instantaneous frequency deviation from the fitted linear line. The major part of the deviation lies within ± 2 MHz window and exhibits a total nonlinearity of $\approx 0.06\%$. While we optimized the optical waveform, the

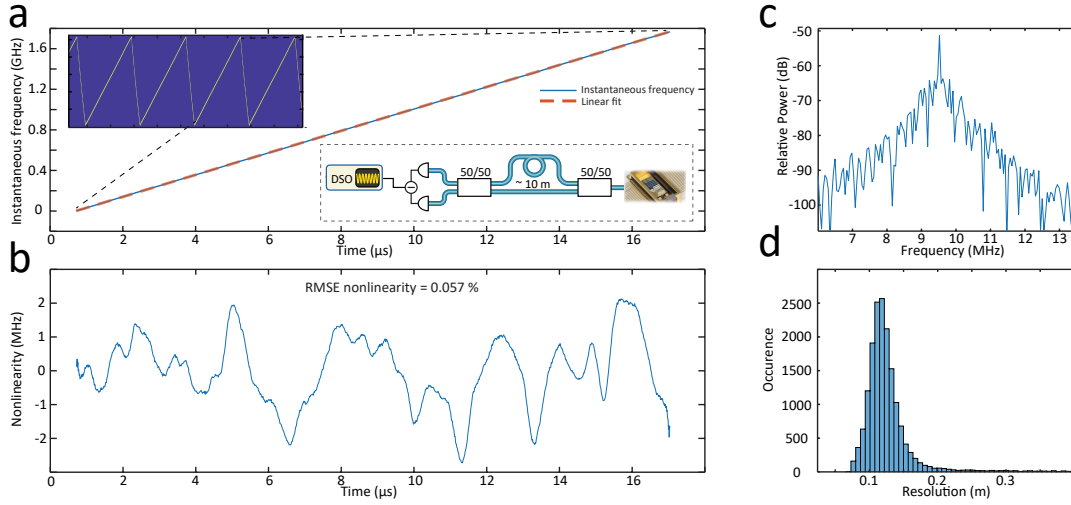


Figure 7.7: LiDAR source electro-optical transduction and linearity. a) Instantaneous frequency of the optical chirp obtained via delayed homodyne measurement (left bottom inset: experimental setup). Red dashed line corresponds to the linear fit. The excursion of the chirp equates to 1.78 GHz over 16 μs period. b) Nonlinearity of the laser chirp inferred from e). RMSE nonlinearity equates to 0.057% with the major chirp deviation from the linear fit lying in the window ± 2 MHz. c) The frequency beatnote in the delayed homodyne measurement corresponds to the reference MZI delay ~ 10 m. The 90% fraction of the beatnote signal is taken for the Fourier transformation. d) LiDAR resolution inferred from the FWHM of the MZI beatnotes over $> 2 \times 10^4$ realizations. Most probable resolution value is 11.5 cm while the native resolution is 9.3 cm corresponding to 1.61 GHz (90% of 1.78 GHz)

voltage ramp appeared to have 0.35% linearity and 0.05V RMSE at an overall 15 V voltage excursion due to the non-ideal electro-optic transduction. We note that precise linear chirp could be realized using a frequency discriminator and opto-electronic laser feedback in integrated fashion [101].

The Fourier transform of the delayed homodyne detection is shown in Fig. 7.7c. The full width at half maximum (FWHM) of the beatnote determines the resolution of the LiDAR. The beatnote linewidth is nearly Fourier transform limited featuring 60 kHz width. Fig. 7.7d presents statistics over 2×10^4 measurements. It indicates 11.5 cm resolution ΔR (most probable value) while the native resolution for the 1.6 GHz B (90% fraction of 1.78 GHz) excursion chirp equates to 9.3 cm following the equation $\Delta R = c/2B$.

7.5 Coherent ranging

Fig. 7.8a illustrates the FMCW photonic-electronic LiDAR experimental setup. The Vernier laser was turnkey initiated, and the ASIC pre-configured waveform was subsequently applied to the laser piezo-actuators. The output light was first split into the signal and local oscillator paths. The EDWA chip provided 13 dB gain and amplified the signal up to 22 mW. The optical spectra before and after the amplification stage

are depicted in Fig. 7.3a,b, respectively. Further amplification is possible with double side pumping of the EDWA chip or by matching the Vernier lasing frequency to the maximum of the gain profile; Liu et al. demonstrated 24 dB off-chip amplification [91]. We employed a mono-static imaging setup with the same collimator operating as a transmitter and a receiver. Two galvo mirrors scanned the laser beam at 2 Hz vertical and 63 Hz horizontal rates. An optical circulator separated the back-reflected light from the transmitted one, whereafter it was self-heterodyne mixed on a balanced photodetector. The digital oscilloscope sampled the photocurrent at 100 MS/s during 0.25 s acquisition time.

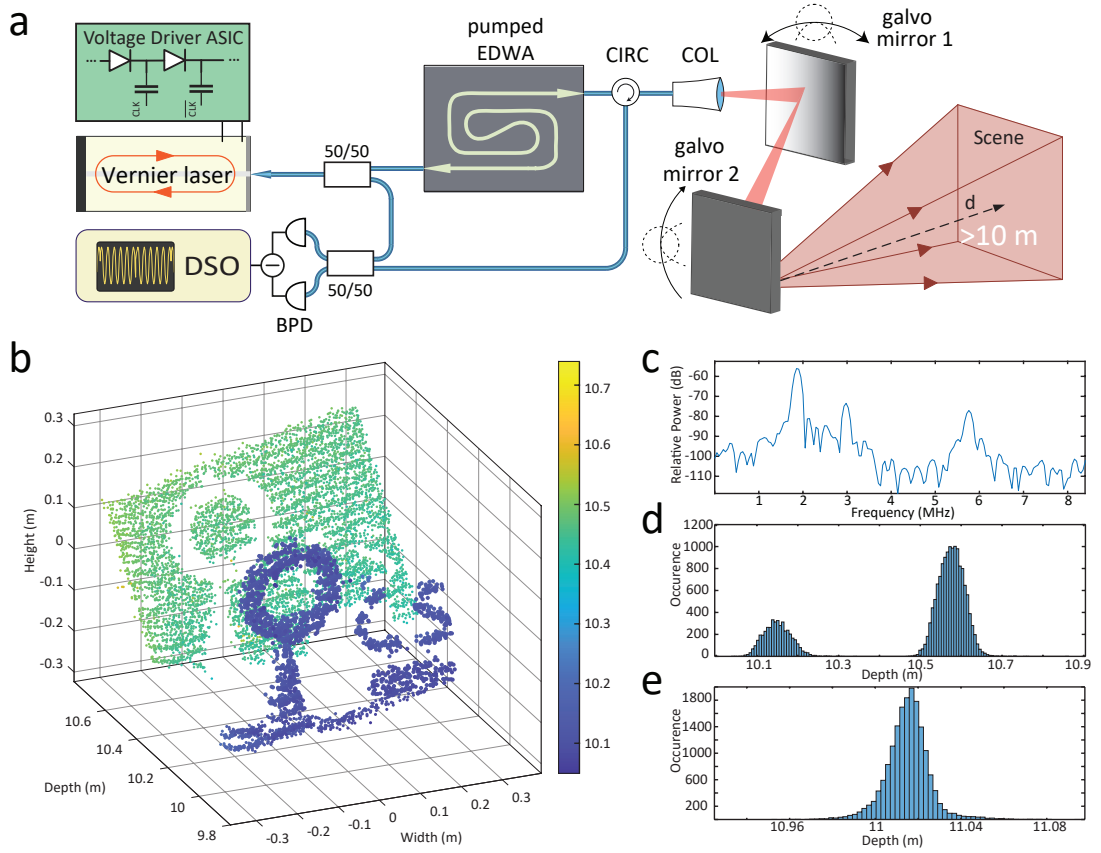


Figure 7.8: Ranging experiment. a) Schematics of the experimental setup for ranging experiments. The amplified laser chirp scans the target scene via a set of galvo mirrors. A digital sampling oscilloscope (DSO) records the balanced detected beating of the reflected and reference optical signals. CIRC - circulator, COL - collimator, BPD - balanced photodetector. b) Point cloud consisting of $\sim 10^4$ pixels featuring the doughnut on a cone and 'c', 's' letters as a target 10 m away from the collimator. c) The Fourier transform over one period, highlighting collimator, circulator and target reflection beatnotes. Blackman–Harris window function was applied to the time trace prior to the Fourier transformation. d) Detection histogram of b). e) Single point imaging depth histogram indicating 1.5 cm precision of the current setup.

Fig. 7.8b shows the resulting point cloud consisting of $\sim 10^4$ pixels. The target comprised a styrofoam doughnut and cone, 'c' and 's' paper letters, and a flat background placed

10 m away from the collimator. Every pixel was obtained by analyzing a single sawtooth period of $23 \mu\text{s}$. First, the signal was time-gated to the up-swing fraction of the chirp, and then Fourier transformed. Fig. 7.8c depicts a periodogram of the detected signal with the Blackman-Harris window applied. We performed the Gaussian fitting of the target beatnote to infer the range estimate. We estimated the precision of our setup to be $\sim 1.5 \text{ cm}$ derived from the statistics of a single point measurement over $\sim 2 \times 10^4$ realizations.

7.6 Discussion

In summary, we have demonstrated an integrated circuit-based coherent LiDAR source. The system-level architecture represents a plug-and-play high-power frequency-agile laser with arbitrary chirped waveforms on demand. We showed that a combination of a hybrid integrated Vernier ring laser with fast PZT actuators, a HV AWG ASIC and an EDWA Si_3N_4 chip attains $>2 \text{ GHz}$ frequency sweeps at 50 kHz rate with output power of more than 20 mW . Our LiDAR source achieves 12 cm lateral ranging resolution with chirp nonlinearity of less than 0.1% . Employing conventional 2D mechanical galvo mirror scanning, we demonstrated ranging at 10 m distance with 1.5 cm precision.

Recent advances in integrated photonics [216, 62] have led to the development of various LiDAR solutions. Low-loss photonic waveguide hybrid integration with distributed feedback laser or RSOA has enabled the creation of narrow-linewidth lasers [217]. Additionally, the use of piezo actuation [87] or electro-optic actuation of χ_2 materials, such as LiNbO_3 , LiTaO_3 , and BTO [218, 219, 89], has enabled even faster frequency chirps. Generally, lasers have a trade-off of tunability and low-phase noise operation [220]. Photonic integration successfully tackles this issue by combining high coherence native to fiber or external cavity lasers and fast frequency tuning of monolithic semiconductor lasers, thus enabling frequency-agility required for FMCW LiDAR.

The proposed ASIC architecture allows for high-voltage arbitrary waveform generation without using a high-voltage supply or RF power amplifier. The charge pump based design can generate output waveforms beyond the voltage rating of the transistors in the technology, therefore the driver can be implemented in advanced standard CMOS nodes. This is advantageous in terms of power consumption and computational processing capabilities of the system, but the manufacturing cost is typically higher. However, since the design has a small footprint with the possibility of having processing and high-voltage driver on a single CMOS chip, it supports further integration with PIC assembly, which is promising for the proposed LiDAR engine. The proposed design is capable of fine-tuning the waveform shape which allowed the generation of an only $\approx 0.06\%$ non-linear optical sawtooth waveform. The chirp rate can be further increased from 50 kHz by reducing the parasitic capacitance at the ASIC output by minimizing the packaging or co-integration with the PIC.

On-chip low-noise, high-power optical amplification has been recently made possible in Erbium-implanted Si_3N_4 photonic integrated circuits, showing competitive performance to widely-deployed electrically pumped semiconductor optical amplifiers (SOAs). In contrast to SOAs with picosecond scale carrier lifetime, the Erbium-based amplifiers enable optical amplification of modulated optical signals with negligible gain nonlinearity or channel cross talk, and lower spontaneous emission noise, benefiting from the millisecond scale long excited state lifetime and much smaller emission cross-section. Equally important, the EDWAs based on dielectric materials exhibit higher temperature stability than that of SOAs [211], which is critical to the amplification of FMCW LiDAR signals since the temperature-induced index change (phase shift) can lead to undesirable instantaneous frequency drift and thus corrupt frequency-time linearity.

Though, we have demonstrated separate integrated components, we note the Vernier laser and the EDWA are based on the same Si_3N_4 material. The laser source and the amplifier can be simultaneously integrated on the same photonic chip due to possibility of selective area Er implantation, providing improved signal-to-noise ratio and higher output and low fabrication complexity. We used a 1480 nm pump source for Er-ion excitation off-chip. However, it could be hybrid integrated via edge-coupling [221] or photonic-wire bonded [222].

8 Conclusion and Outlook

This thesis explores new techniques for light detection and ranging using microresonator frequency combs. In chapter 3, the concept of frequency-modulated solitons is introduced as a means of enabling parallel, coherent ranging. Chapter 4 utilizes dual-comb implementation of chirped solitons to demonstrate the fastest (as of 2020) FMCW line rates, with simultaneous detection of more than 60 channels on a single receiver. Chapter 5 goes against the widely held belief that incoherent combs are just a stepping stone to soliton states and leverages chaotic modulation instability in Si_3N_4 microresonators to demonstrate parallel, random noise LiDAR. Chapter 6 continues this theme by exploring parallel ranging with fully passive beam steering, achieved through microheater integration and agile control of a chaotic microcomb. Finally, chapter 7 presents a photonic-electronic integrated LiDAR source, showcasing the latest advances in integrated photonics (2022/23). By combining a low-loss Si_3N_4 -based, frequency-agile Vernier laser with integrated PZT actuators, a fully integrated high-voltage waveform generator in standard CMOS silicon technology, and an Erbium-doped waveguide amplifier, the chapter demonstrates high-performance FMCW ranging.

During the course of the thesis, both the frequency comb and integrated photonics fields underwent significant changes. The author was fortunate to witness this progress, including the transition of integrated photonics from a laboratory level to foundry-scale production. Photonic devices that were once designed in a lab and fabricated in a few locations around the world are now readily accessible through semiconductor foundries and are widely used in new commercial products.

Below, the author highlights future directions for development, addressing potential challenges and suggesting new ideas.

Generation, operation, and integration of microcombs. One of the significant challenges in operating microcombs is their power efficiency, which is currently limited to less than 1%. Recent studies such as ref. [223] have explored new solutions to this issue, which, if adopted, would address the main challenge facing Kerr combs. The

integration of piezoelectric actuators like AlN [53] and PZT [87] improved the control over microcomb states allowing for the feed-forward tuning. Complete elimination of Raman shift during pump frequency scans employing these actuators, will address the nonlinearity issues in FMCW ranging with microcombs.

There is still room to explore the rich nonlinear dynamics of coherent LLE solutions in microresonators [60]. A deeper understanding of dark pulse formation [63] could offer more flexibility over the spectral shape and power transfer of Kerr combs.

There has been a tremendous progress on microcomb integration including heterogeneous integration of III-V lasers with Si₃N₄ microresonators and turnkey soliton initiation [224] as well as novel trend in 3D integration [225]. Further option could be to integrate an Erbium-doped waveguide [91] for soliton booster-amplification and piezo actuators as discussed above. Essentially, all these steps have been demonstrated separately. Their combination would constitute a high level of technological readiness for applications in telecommunications.

Further development of parallel FM LiDAR For practical implementation in real-world applications, FMCW LiDAR systems will require parallelization. There are several promising passive beam steering architectures that support parallel operation, including the optical phased array (OPA) [204, 191] and the focal plane array (FPA) [108]. Both technologies are commercially available and are competing to establish their place in the market (Analog Photonics and PointCloud).

OPA offers 2D scanning through the use of both dispersion and phase shift. Frequency comb could be readily combined with an OPA (thus alleviating the need for a broadband laser scan) and integrated arrayed waveguide grating (AWG) for channel separation at the receiver. On the other hand, current FPA implementations operate using a switching network and illuminate the target sequentially. However, the FPA architecture does allow for routing of the different comb wavelengths to different transmission pixels, which can be detected individually in parallel using an integrated AWG at the receiver as well.

Chaotic combs applications: The demonstration in chapter 5 has already sparked new research in random LiDAR and chaotic comb based random number generation. However, there are few more fields that could be investigated. The 1990 paper by L. Pecora and T. Carroll [188] demonstrating chaotic circuits synchronization has received nearly 14000 citations. It would be interesting to study optical chaos synchronization in microresonators. This area of research could lead to new applications [226, 189] in cryptography [190] and spread spectrum communications [151]. Additionally, synchronization phenomena such as Arnold tongues have already been demonstrated in optical microresonators, albeit in the context of dissipative Kerr solitons [227], making this area ripe for further exploration.

Full scale integration of photonic devices: The integration of photonic devices into a single chip or a few closely connected chips holds the promise to transform the field of photonics in the same way that electronic integrated circuits did. Our group has recently made progress in this area by developing new platforms, such as heterogeneously integrated lithium niobate on Si_3N_4 circuits [88] and monolithic lithium niobate [89] enabling high-speed optical modulators. The next step would be to integrate these platforms with microresonator Kerr combs and laser solutions based on III-V materials or Erbium-doped waveguides. Such an integration would allow for a massively parallel coherent transmitter modules envisioned for data centers.

A Appendix to chapter 4 - Dual chirped microcomb based parallel ranging

This addendum contains some technical details, which I decided to avoid mentioning in the main body to keep the flow essential and simple.

A.1 Parallel velocimetry and ranging details

The full experimental ranging setup is illustrated in Fig. A.1a. We used an auxiliary balanced photodiode to calibrate Δf_{rep} and the channel-dependent frequency excursion B . The in-phase (I) and quadrature (Q) signals from the coherent photoreceiver were

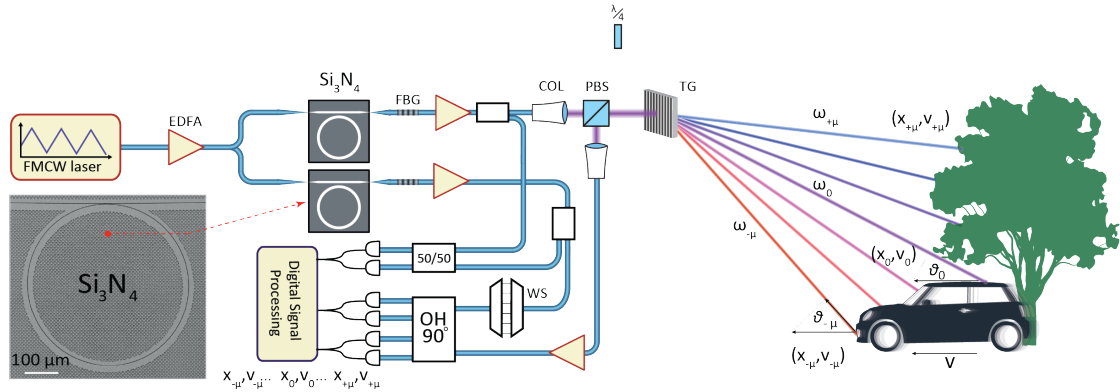


Figure A.1: **Full setup for dual chirped comb ranging experiment.** In addition to the description in the main body, we employed a waveshaper (WS) to filter out excess ASE noise around the pump of the LO and an extra reference balanced photodiode to measure frequency excursion and Δf_{rep} .

recorded on a fast oscilloscope and processed offline. For experiments with 100 GHz microrings, we utilized comb channels between $\mu = -15, +15$, where $\mu = 0$ denotes the pump frequency, while $\mu = 0, \pm 1$ were filtered out by the waveshaper (WS) due to the excess of the ASE, resulting in 28 independent channels. The required coherent

Appendix A. Appendix to chapter 4 - Dual chirped microcomb based parallel ranging

receiver bandwidth for this configuration is determined as $\mu\Delta f_{\text{rep}} \approx 7.5$ GHz. All the data points were collected from a single trace covering 136 vertical lines. The galvo-scanner was set on a linear scan mode, while the oscilloscope was triggered in segmental acquisition mode with 10 μs segment scan time and 10 ms idle time between segments to allow the Galvanometer enough time to rotate and capture the full scene. Overall, the measurement time was less than 1.5 seconds and was limited by the galvanometer response bandwidth, not the pixel sampling rate. The 3D point cloud of 136×28 pixels was obtained after post-processing.

For the velocity measurements, we employed channels $\mu = \pm 5, \pm 40$ of 35 GHz combs. Channels $\mu = -4, +4$ were filtered out by the WS due to the excess ASE. The velocity error (in Fig. 4.13) of a single measurement was defined by calculating a variance of the Gaussian fitted to the beatnote. For five consecutive measurements a standard deviation of $N \leq 5$ detected velocity values was calculated for every channel.

A.2 Coherent detection and post-processing

The frequency of the complex heterodyne beat note for the channel μ and a photon time-of-flight τ follows as the difference between the instantaneous optical frequencies of signal and LO comb teeth $\nu_{\mu}^{\text{sig,LO}}$

$$\begin{aligned} f_{\mu}^{\text{IQ}}(t) &= \nu_{\mu}^{\text{LO}} - \nu_{\mu}^{\text{sig}} \\ &= \delta(t) + \mu f_{\text{rep}}^{\text{LO}}(t) - \delta(t + \tau) - \mu f_{\text{rep}}^{\text{sig}}(t + \tau). \end{aligned} \quad (\text{A.1})$$

The first and third terms are similar to the case of single frequency coherent photoreceiver FMCW LiDAR [130]. In our case that frequency is offset by the repetition rate difference of the soliton microcombs multiplied by the channel number and adding the Doppler shift due to the relative target velocity v , we arrive at the following expressions:

$$\begin{aligned} f_{\mu}^{\text{u}} &= \mu \cdot \left(f_{\text{rep}}^{\text{sig}} - f_{\text{rep}}^{\text{LO}} \right) + \frac{B}{2T} \cdot \tau + \nu_{\mu} \cdot \frac{v}{c} \\ f_{\mu}^{\text{d}} &= \mu \cdot \left(f_{\text{rep}}^{\text{sig}} - f_{\text{rep}}^{\text{LO}} \right) - \frac{B}{2T} \cdot \tau + \nu_{\mu} \cdot \frac{v}{c}. \end{aligned} \quad (\text{A.2})$$

The linewidth of beatnote f_{μ}^{IQ} depends on the relative phase deviations between the Signal and LO comb lines (Figs. A.6, A.7) that inherent the chirp from single FMCW pump laser. This places additional requirements on linearity and uniformity of chirp transduction during DKS generation compared with the single comb case.

According to our notation, positive frequencies in the complex RF spectrum correspond to optical carrier frequencies larger than the pump, negative frequencies to channels with smaller optical carrier frequencies than the pump. The distance and velocity can be

inferred from these expressions and are depicted in the inset of Fig. 4.3.

Our coherent receiver consisted of 90° optical hybrid coupler, two balanced photodetectors and subsequent RF amplifiers. This type of receiver is commonly referred as "phase-diversity homodyne receiver" [228, 229] or "intradyne receiver" [131]. It is similar to established receivers used in quadrature-amplitude modulation schemes that are employed in long haul optical communication systems. It allows full reconstruction of the amplitude and phase of the RF beat note between the signal and the LO and reveals distinct spectral information both in positive and negative RF frequencies. Due to the differential delays of discrete components and the response of the balanced photoreceivers and amplifiers, the in-phase (I) and quadrature (Q) signals are not perfectly orthogonal. We performed IQ imbalance correction [230], which substantially improved orthogonality (cf. Fig. A.2).

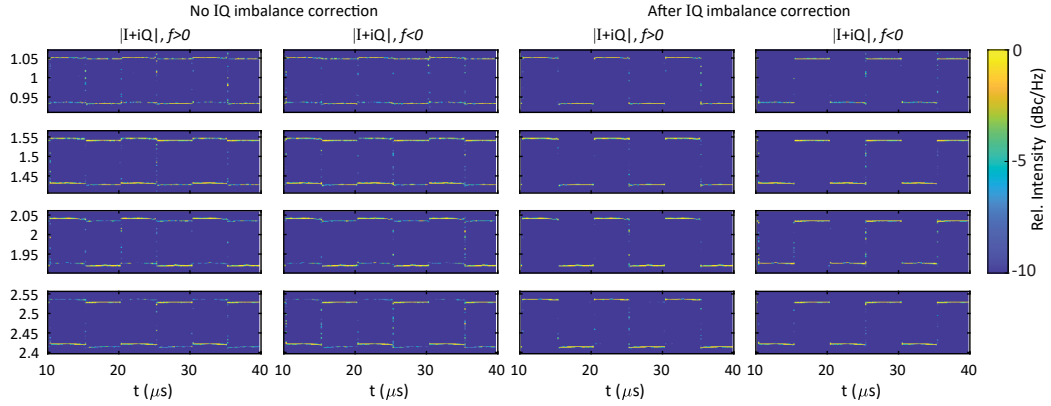


Figure A.2: **IQ imbalance correction.** Time-frequency map of delayed heterodyne beat spectroscopy for $\mu = \pm 2, \pm 5$. The first two columns correspond to positive and negative channels without IQ imbalance correction, while the second two columns are with IQ imbalance correction. ENBW 2.45 MHz.

The post-processing relies on short time Fourier transform over the half of the period to retrieve f_{μ}^u, f_{μ}^d RF frequencies. In this regard, the 'image' peaks due to imperfect IQ correction/mismatch do not pose a problem, since we know that the positive frequencies will give a higher frequency beat note first while for the negative ones it would be the lower one. Distance information is obtained as a difference between f_{μ}^u, f_{μ}^d , while the mean offset of $f_{\mu}^u + f_{\mu}^d$ from $\mu \Delta f_{\text{rep}}$ is proportional to the velocity. Calculation of the Δf_{rep} is outlined below. The problem of distance ambiguity at ranges that exceed the channel spacing in the complex multiheterodyne spectrum can be mitigated either by a more sophisticated peak sorting and matching algorithms and multiple up-chirping and down-chirping ramps [231].

A.3 Calibration of channel-dependent frequency excursion

In general, the soliton repetition rate f_{rep} depends on the laser cavity detuning, because of intrapulse stimulated Raman scattering [38, 97] and the soliton recoil effect associated with dispersive wave emission [232, 96]. During chirped soliton generation, this induces a change of the soliton repetition rate during each chirp cycle, which is observed in the form of a channel-dependent frequency excursion B_μ and chirp nonlinearity described in chapter 3. We observed that it did not depend strongly on the pump laser detuning and was independent of the pump power.

We measured the time-dependent chirp on both signal and LO combs and all channels by recording a heterodyne beat note with a second laser simultaneously on a pair of balanced photodetectors and a fast sampling oscilloscope (cf. Fig. 4.5). For direct comparison of signal and LO chirps, we added the two beat note signals prior to short-time Fourier transform and depict both beat notes on a single panel. The full dataset corresponding to the subset of heterodyne beat signals presented in Fig. 4.6b is depicted in A.3. The amplitude of the triangular ramps decreases from positive to negative

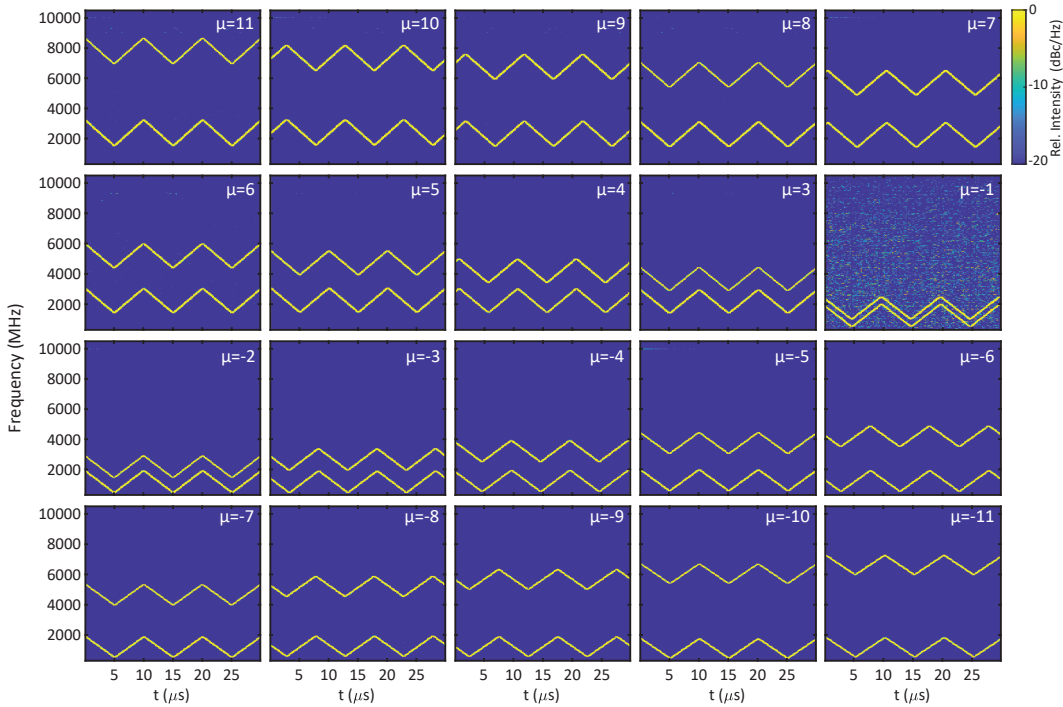


Figure A.3: **Heterodyne beat spectroscopy of signal and LO microcombs.** Time-frequency map of signal and LO comb channels obtained by short-time Fourier transform with resolution bandwidth 2.45 MHz. Depicted here is the full data set corresponding to Fig. 2d of the main manuscript.

A.3 Calibration of channel-dependent frequency excursion

channels both for LO and signal. We retrieved the frequency excursion by fitting a symmetric triangular ramp to the time-dependent frequency of the heterodyne beat notes. The result of this analysis is plotted in Fig. 4.7c,d.

Heterodyne beat spectroscopy is well suited to characterize the chirp waveforms, but not practical for ranging and velocimetry, as it requires an independent reference laser. Hence, during the experiments presented in Fig. 4.8,4.12 we utilized a reference optical fiber MZI that was derived by tapping a fraction of signal and LO and beating them together on a second balanced photodiode (cf. Fig. A.4a). Inphase detection sufficed, because Doppler-shifts were negligible in the reference MZI and all channels μ observed the same distance x_μ but different frequency excursions B_μ , which simplified interpretation of the signal plotted in Fig. A.4b.

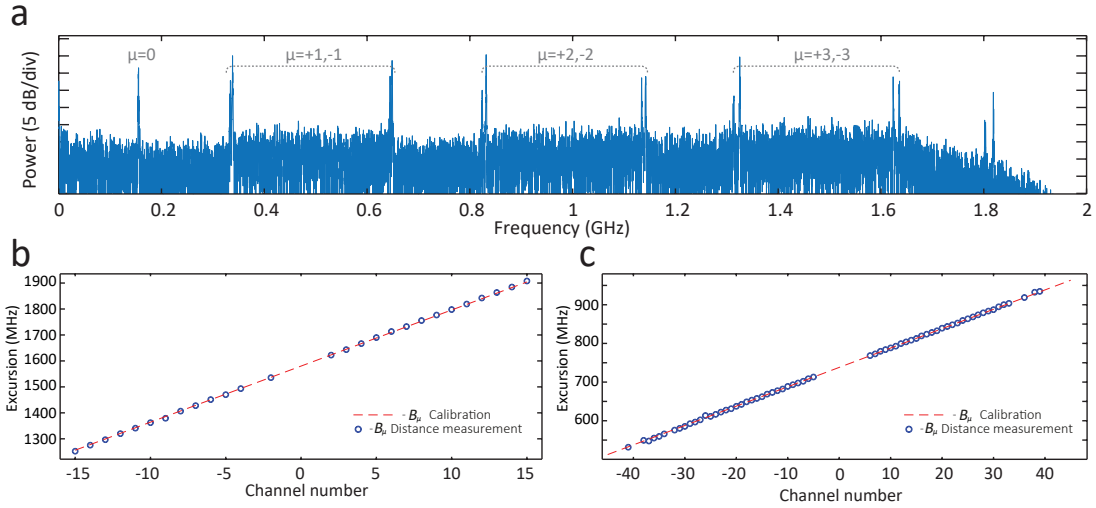


Figure A.4: **Repetition rate and excursion calibration with auxiliary photodiode.** a) Interferogram of a LO and signal combs beating recorded over one period ($10\mu s$) on the reference photodiode with 1.6GHz bandwidth. Beatings of 6 channels ($\mu = \pm 1, \pm 3$) allow Δf_{rep} and B_μ to be retrieved and used for the processing of the measured data. b) Two frequency excursion measurements with 100 GHz chips. Red dashed line is an extrapolation of excursion obtained from the reference delayed heterodyne measurement. Blue circles correspond to an excursion obtained from a lidar distance measurement of a carton block, where all the distances are the same for distinct channels. c) Same as b), but with 35 GHz chips

For every set of measurement we used excursion calibration measured in parallel. Channel-dependent excursion varies with soliton detuning, and since we used two microresonators, we had 3 variables to consider: 2 laser-cavity detunings and a differential detuning, which all determine the excursion dependence and linearity.

Every $\pm\mu$ channel would give a beat note consisting of four lines (cf Fig. A.4a), where two outer lines correspond to positive frequencies with higher excursion and two inner lines correspond to negative frequencies with lower excursion. Thus, we performed

Appendix A. Appendix to chapter 4 - Dual chirped microcomb based parallel ranging

excursion inference for the 6 channels $\mu = \pm 1, \pm 3$ (that is allowed by 1.6 GHz bandwidth) and further extrapolated it considering linear dependence (cf. Fig. 4.7c,d). For the 35 GHz chips we utilized channels $\mu = \pm 2, \pm 10$ for calibration. Knowledge of the pump excursion enabled us to calculate the distance of MZI, while given the distance, one can obtain excursion for channel μ from time-frequency analysis. The same way one can infer channel-dependent excursion from real distance measurement if the distance to the target is the same for all of the channels (e.g. carton block). Furthermore, we could also calculate Δf_{rep} from the same calibration measurement. Since there is no Doppler shift, Δf_{rep} is equal to the mean of two beat notes divided by $|\mu|$. Hence, we were able to conduct the experiments with free-running soliton microcombs. Figs. A.4b,c present comparison of the excursion inferred from the calibration measurement, which was further extrapolated, and from a real distance measurement with a carton block. In the experiments described in the main body we utilized excursion and Δf_{rep} for velocity and distance calculations inferred from the calibration measurements.

A.4 Impact of nonlinear chirp transduction

Multiheterodyne mixing of dual-chirped soliton microcombs necessitates not only soliton generation to preserve chirp linearity from the pump to the comb teeth, but also requires that chirps are transduced equally, so as to avoid a difference in the frequency excursion B_μ between the signal and LO comb teeth that would broaden the ranging beatnote and penalize detection precision and sensitivity. We have two contributions effecting soliton repetition rate given change in pump frequency: the chromatic dispersion of the cavity D_2 , i.e. frequency dependency of the free-spectral-range D_1 , and Raman shift Ω [38, 97]. The overall change in repetition rate as a function of the detuning δ (frequency difference between the pump and ‘cold’ cavity resonance) can be written as

$$f_{\text{rep}}(\delta) = f_{\text{rep}}(0) + (\delta + \Omega(\delta)) \frac{D_2}{D_1}. \quad (\text{A.3})$$

For dielectric integrated microresonators it is generally found that $\delta \ll \Omega(\delta)$ and hence the first term in the round brackets can be omitted. We also neglect the weak dependence of the free-spectral range and dispersion on the laser-cavity detuning that can be derived as $D_n(\delta) - D_n(0) \approx \delta \cdot D_{n+1}/D_1 \ll D_n(0)$. The linear dependence of the instantaneous f_{rep} on the laser-cavity detuning δ induces a channel-dependent frequency excursion B_μ without introducing nonlinearity into the triangular chirp [136]. Non-linear coupling between f_{rep} and f_{ceo} during the detuning sweep due to the soliton self-frequency shift leads to distortions of the triangular chirp. The nonlinear relation between the laser cavity detuning and the Raman soliton shift was derived in Ref. [97]:

$$\delta = \sqrt{\frac{15c\beta_2\omega_0}{32nQ} \frac{\Omega}{\tau_R}} - \frac{c\beta_2}{2n} \Omega^2, \quad (\text{A.4})$$

where τ_R is Raman shock time and $\beta_2 = -\frac{n}{c}D_2/D_1^2$ is the chromatic dispersion term. Figs. A.5 a,b depict the time-varying detuning $\delta(t)$ of a triangular chirp sequence of the pump laser and the Raman induced soliton self-frequency shift $\Omega/2\pi$ caused by the variation of the detuning. Fig. A.5 c depicts the induced variation of f_{rep} (blue) and Δf_{rep} component (red). We investigated the degradation of chirp linearity and similarity between the signal and LO combs due to the Raman effect as function of their respective and in general dissimilar detunings $\delta^{\text{sig,LO}}$ by inserting the Raman induced periodic change of f_{rep} into equations A.1 and A.2.

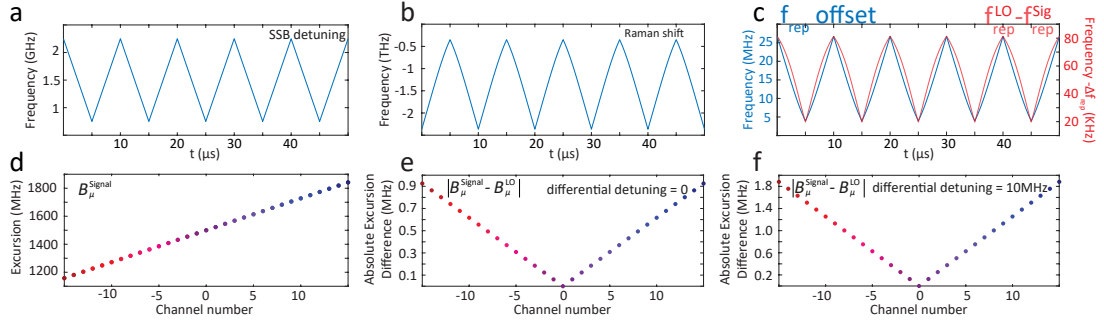


Figure A.5: Raman nonlinearity impact on tuning in 100 GHz resonators. a) Simulation of a pump cavity detuning representing a triangular ramp. b) Simulation of a Raman shift experienced by a Soliton while being frequency swept. c) Blue - f_{rep} offset from a 100GHz caused by Raman nonlinearities. Red - Δf_{rep} offset from a 500 MHz (100 and 100.5 GHz free spectral ranges were used in this simulation) for the two solitons while being frequency swept due to Raman nonlinearities. d) Simulated frequency excursion for 100 and 100.5 GHz resonators due to Raman effect. e,f) Simulated absolute frequency excursion difference considering soliton-cavity detuning to be the same for two resonators and have 10 MHz difference correspondingly.

We distinguish the cases of vanishing and modest differential detunings $\Delta\delta = \delta^{\text{sig}} - \delta^{\text{LO}} = 10\text{MHz}$ (cf. Fig. A.5 d,e,f).

The small difference in f_{rep} between signal and LO microcombs results in different Raman shifts, which causes frequency excursions to differ between the signal and LO combs on the scale of 1 MHz, which is comparable to the induced chirp nonlinearities of pump to sideband chirp transduction (Fig. A.5 c,e,f). According to the equations A.2 Raman nonlinearity scales with the relative mode number from the pump. This can be directly seen from Figs. A.6,A.7, where relative phase deviation between corresponding Signal and LO comb lines and their phase noise power spectral densities (PSD) $S_{\phi\phi}(f)$ increase for higher $|\mu|$.

We utilized heterodyne beat spectroscopy dataset (Fig. A.3) to infer relative phase deviation. We calculated signal and LO phases via Hilbert transformation. Afterwards we subtracted quadratic fit taking into account the frequency chirp. The differential phase variation was obtained by taking the difference. This value determines the beatnote broadening.

Appendix A. Appendix to chapter 4 - Dual chirped microcomb based parallel ranging

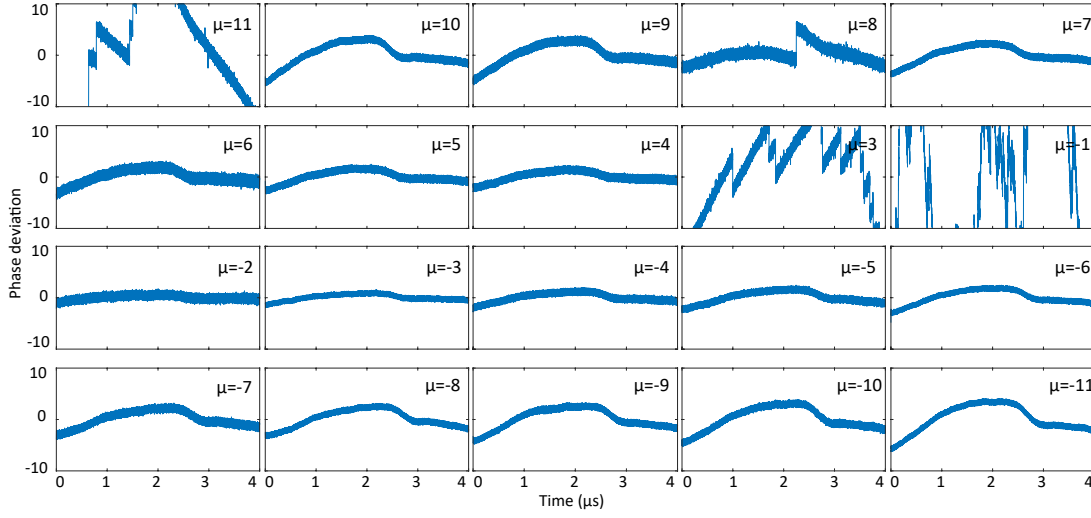


Figure A.6: **Differential phase deviation of the chirped comb lines.** The phase deviation is obtained by subtracting the phase of the Signal comb from the phase of the LO comb for a given channel with prior subtraction of quadratic fit.

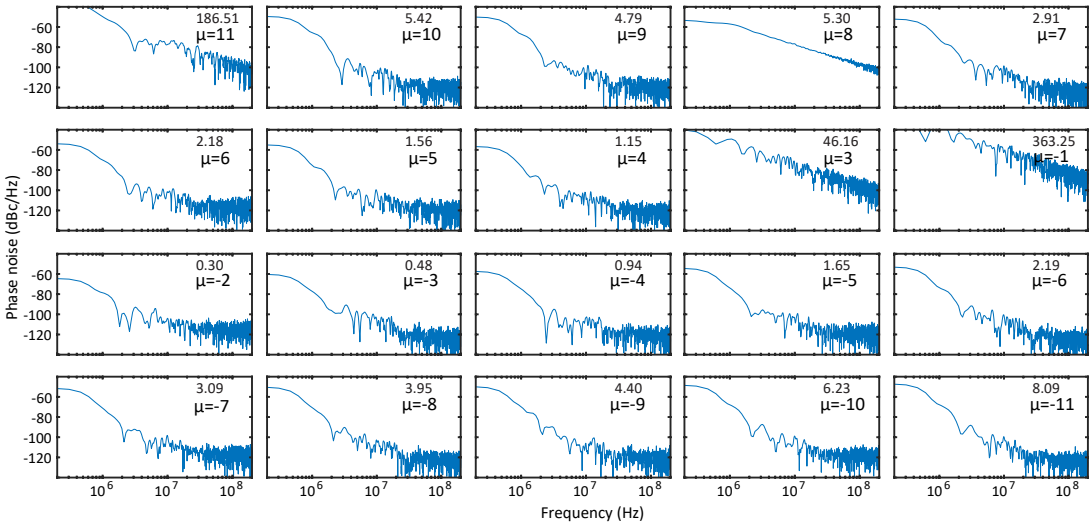


Figure A.7: **Phase noise of the beatnote signal between Signal and LO.** The number in the top right of every plot corresponds to the integral of the PSD. Heuristically, the value less than $2/\pi$ corresponds to the Fourier-limited beatnote linewidth.

Values in the top right corners of Supplementary Figure A.7 denote integral of the PSD. A value less than $2/\pi$ heuristically corresponds to the Fourier transform limited linewidth, since $\int_{-\frac{\Delta\nu}{2}}^{\infty} S_{\phi\phi}(f) df = 2/\pi$ [233]. Increased linewidth of the detected beatnotes results in the reduced resolution and degraded SNR, as well as impaired distance precision (Supplementary Figure 4.11). Substantially higher phase deviations in channels +11, +3 are attributed to the presence of mode crossings in the microresonator spectra [96]. Similarly, phase deviations in channel -1 do originate from unfiltered ASE noise.

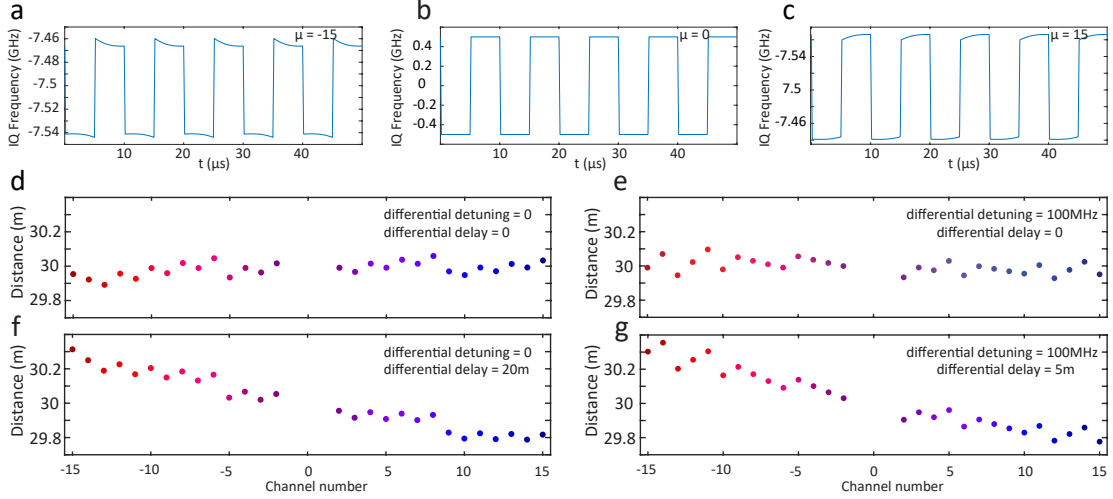


Figure A.8: Raman nonlinearity impact on ranging with 100 GHz resonators. g,h,i) Simulated time-frequency maps obtained from a beating of signal and LO combs. Difference in excursion due to Raman effect results in deformed trapezoidal traces. Channels $\mu = -15, 0, +15$ correspondingly. j,k,l,m) Simulated distance measurements calculated from time-frequency maps above. The term differential delay stands for the difference between optical delay of signal and LO for the real measurement on one side and optical delay of signal and LO for the reference calibration measurement on the other side.

To determine the distance inference degradation due to the soliton induced Raman self-frequency shift, we simulate the full signal generation and coherent detection chain at a distance of 30 m with a custom MATLAB script and apply the same data analysis techniques to the artificial (i.e. numerically generated) multiheterodyne LiDAR trace as for the real data. The resulting time frequency traces are depicted in Figs. A.8 a,b,c for the pump and the 15th low and high frequency comb teeth. The overall manifestation of the soliton Raman self-frequency shift induced nonlinearity can be seen in the tilt and curvature of the time dependent complex RF beat note frequency. The effects of the nonlinearities are exacerbated for channels further away from the pump. The curvature that is imposed by the nonlinear component of the Raman frequency shift leads to a bias of the measured distances that increases with length difference between the target and the calibration MZI, differential detuning $\Delta\delta$ and channel number (cf. Supplementary Figure A.5 d,e,f,g). In the ranging experiments presented here, we calibrate the bias by measuring the static target with the same distance for all the channels and apply

this correction for further ranging experiments. A feed-forward scan scheme [53] or phase-locking the comb to a tuned resonator [135] to avoid detuning-dependent changes of the microcomb repetition rates would be favorable, and are possible to avoid Raman effect.

A.5 Signal-to-noise ratio of multiheterodyne FMCW LiDAR

A significant advantage of heterodyne detection is that it can approach the photon shot noise limit of detection and attain single photon sensitivities for low signal powers on a conventional semiconductor photodiode, if sufficient LO power is supplied for amplification. In the multiheterodyne case all individual channel LO are impinging on a small number of photodiodes (4 in case of a phase diversity receiver with balanced photodiodes). Generally, for a heterodyne LiDAR detection $P^{LO} > P^{sig}$ and the shot noise (mainly contributed by the LO) is a dominating source of noise (i.e., higher than the thermal noise) if sufficient LO power is supplied to the photodiode.

$$SNR = \frac{\langle I^2 \rangle}{\langle \Delta I^2 \rangle} = \frac{P^{sig}}{\hbar\omega B_{RF}} \quad (A.5)$$

Where B_{RF} is the resolution bandwidth of the analysis FFT. For simplicity, we consider quantum efficiency of the photodiode to be 100%, thus the electric current is $I = RP = \frac{e}{\hbar\omega}P$. If an optical amplifier is used, than for the shot noise limited detection the total SNR would be at least 3dB lower:

$$SNR = \frac{P^{sig}}{2\hbar\omega B_{RF}} \quad (A.6)$$

Below we elaborate a more detailed analyzes for the case of multiple channels detected on a single balanced photodiode. Consider N distinct signal-LO channels distributed over the photodiode bandwidth with equal powers of the signal channels $P_{\mu}^{sig} = P^{sig}$ and LO channels $P_{\mu}^{LO} = P^{LO}$ for $\mu \in [1, N]$. For heterodyne detection the photodiode current of channel μ is $2R^2 P^{LO} P^{sig}$, while the total noise $\langle \Delta I^2 \rangle$ effecting channel μ would consist of shot noise, thermal noise, spontaneous-spontaneous beating noise, and signal/LO-spontaneous beating noise [234].

The photon shot noise is proportional to the mean current impinging on the photodiodes

$$\begin{aligned} \sigma_{sh}^2 &= 2q\langle I \rangle B_{RF} \\ &= 2qR(NGP^{LO} + NGP^{sig} + P_{ase}^{LO} + P_{ase}^{sig})B_{RF} \\ &\approx 2qRNGP^{LO} B_{RF} \end{aligned} \quad (A.7)$$

mainly contributed by N LOs. Where P_{ase} is spontaneous emission noise and it equals $\rho_{ase}\Delta\nu_{amp} = n_{sp}\hbar\omega(G-1)\Delta\nu_{amp}$ with the amplification bandwidth $\Delta\nu_{amp}$ (4 THz for

EDFA) and the spontaneous emission factor $n_{\text{sp}} = 1$ for the amplifier with complete inversion, q is the electron charge. Additionally, we consider equal gains for the detector pre-amplifiers of the signal and local oscillator microcombs $G^{\text{LO}} = G^{\text{sig}} = G$.

We consider the thermal noise of the photodiodes at room temperature

$$\sigma_{\text{th}}^2 = 4 \frac{kT}{Z} B_{\text{RF}} \quad (\text{A.8})$$

where kT is a thermal energy and the impedance Z of the load is 50 Ohm. Spontaneous-spontaneous and signal/LO-spontaneous beating noises include cross terms only, because we employ balanced photodetection,

$$\sigma_{\text{sp-sp}}^2 = 4R^2 \rho_{\text{ase}}^{\text{sig}} \rho_{\text{ase}}^{\text{LO}} \Delta\nu_{\text{amp}} B_{\text{RF}}, \quad (\text{A.9})$$

$$\sigma_{\text{sig/LO-sp}}^2 = 4R^2 (NGP^{\text{LO}}) \rho_{\text{ase}}^{\text{sig}} B_{\text{RF}} \quad (\text{A.10})$$

$$+ 4R^2 (NGP^{\text{sig}}) \rho_{\text{ase}}^{\text{LO}} B_{\text{RF}}. \quad (\text{A.11})$$

In the experiment, we use two optical amplifiers for the signal comb: a booster-amplifier before free-space emission and a detection pre-amplifier after light collection. In the above equations, P^{sig} denotes the optical power of the signal comb line at the input of the 90° optical hybrid. The ASE noise of the booster amplification stage is irrelevant in the coherent ranging application, as the optical loss in free space (> 60 dB) generally surpasses the single stage amplification gain. Thus the photon shot noise would be dominating at the post-amplification stage. Combining all noise terms and neglecting minor contributions, we determine the SNR for a given channel:

$$\text{SNR}_{\mu} = \frac{\langle I_{\mu}^2 \rangle}{\sigma_{\text{sh}}^2 + \sigma_{\text{th}}^2 + \sigma_{\text{sp-sp}}^2 + \sigma_{\text{sig/LO-sp}}^2} \quad (\text{A.12})$$

$$\approx \frac{2R^2 P^{\text{sig}} G P^{\text{LO}}}{4R^2 (NGP^{\text{LO}}) \rho_{\text{ase}}^{\text{sig}} B_{\text{RF}}} \approx \frac{P^{\text{sig}}}{2N\hbar\omega B_{\text{RF}}} \quad (\text{A.13})$$

Thus, in the case of shot-noise limited operation, the SNR of a channel μ is reduced by the shot noise of the additional local oscillators and N times lower than in case of its detection on N separate photodetectors. This multiheterodyne penalty is well known in the realm of dual comb spectroscopy [140] and amounts to 17 dB for 50 channels. It can be reduced by spectral slicing or interleaving. While the approach comes at the expense of reduced SNR due to the multiheterodyne detection penalty, the latter is compensated for by the absence of multiplexers or photonic integrated solutions for detection of individual channels, which typically exhibit significant insertion loss.

B Appendix to chapter 5 - Chaotic microcomb based parallel ranging

This addendum contains some technical details, which I decided to avoid mentioning in the main body to keep the flow essential and simple.

B.1 Post-processing

In RMCW ranging, distance to the target object d is inferred from the time delay estimation of cross-correlation between signal and reference currents:

$$d = \frac{c}{2} \operatorname{argmax}_{\tau} (\text{XCORR}[I_s, I_r]). \quad (\text{B.1})$$

However, if the object is moving, the signal current experiences a Doppler shift and straightforward cross-correlation does not retrieve the true time delay. As described in the Velocimetry section of the main manuscript, we calculate first the Doppler shift by cross-spectrum correlation and peak estimation [168].

$$\Delta f_D = \operatorname{argmax}_f (\text{XCORR}[\mathcal{F}[I_s], \mathcal{F}[I_r]]), \quad (\text{B.2})$$

where $\mathcal{F}[\cdot]$ and $\mathcal{F}^{-1}[\cdot]$ stand for the Fourier and the inverse Fourier transforms, Δf_D is a Doppler shift, f_c is an optical carrier frequency. The Doppler shift yields the target velocity via

$$v = \frac{c}{2f_c} \Delta f_D. \quad (\text{B.3})$$

The true time delay is then easily obtained via cross-correlation of the frequency-shifted signal current with the reference current

$$\tilde{I}_s = \mathcal{F}^{-1}[\mathcal{F}[I_s](f - \Delta f_D)], \quad (\text{B.4})$$

$$d = \frac{c}{2} \operatorname{argmax}_{\tau} (\text{XCORR}[\tilde{I}_s, I_r]). \quad (\text{B.5})$$

All cross-correlations and Fourier transforms are calculated digitally in batch processing via MATLAB. However, we note that analog processing of cross-correlations would also be feasible [235].

Next, we estimate the computational complexity of massively parallel RMCW optical ranging. Straightforward computation of the cross-correlation yields $O(N^2)$ with the number of samples N . Recalling that convolution operation can be calculated by the means of the Fourier transforms, i.e. the inverse Fourier transform of the multiplication of the Fourier transforms, the complexity can be estimated as $\approx 3 \times 4N \log_2(N)$ [236]. However, taking into account prior information from the preceding step or a neighboring pixel and restricting ourselves to a limited search range around the previous value, we assume that the cross correlation complexity can be estimated as $O(M \times N)$ if calculated directly, where $M \ll N$ and potentially $M < 3 \times 4 \log_2(N)$.

B.2 Numerical simulations

To verify the experimental results, we performed numerical simulations of the Lugiato-Lefever equation using two distinct numerical schemes: pseudo-spectral 1st order Split-Step method [237] and the step-adaptative Dormand-Prince Runge-Kutta method of Order 8(5,3) [238] with the second-order finite difference scheme for the dispersion operator. Laser power and cavity parameters were chosen to match the experimental settings and results. Similar to the experiment, we fixed the pump power and scanned the laser across the cavity resonance from the red to the blue detuned region as shown in Fig. B.5(b). Then, we fixed the laser-cavity detuning in the unstable region and investigated temporal dynamics of the optical field at several laser-cavity detunings. We computed heterodyne beatnote power spectral densities for several chaotic MI comb lines (see Fig. B.3) and found them in very good agreement with the experiment shown in Fig. B.1 for both numerical schemes. Before computing the corresponding auto-correlation traces, we added a 5 GHz frequency offset to the signal similar to the experiment. The obtained auto-correlation traces shown in Fig. B.4 along with range resolution in Fig. B.5 show qualitative and quantitative agreement with the experimental results.

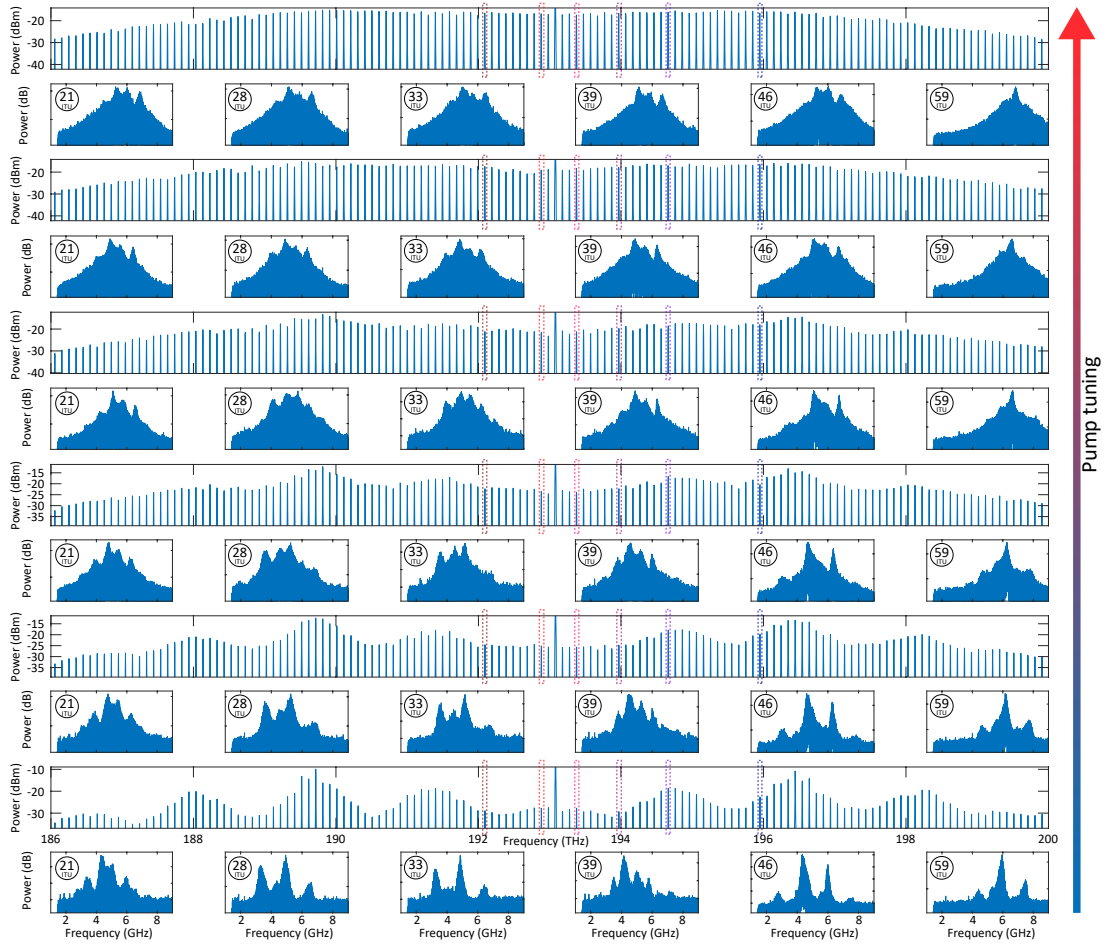


Figure B.1: Experimental observation of chaotic MI comb state. Experimentally measured optical spectra and heterodyne beatnote power spectral densities (PSD) of selected comb chaotic MI comb lines (ITU: 21, 28, 33, 39, 46, 59) at different laser cavity detuning. The PSD develops from discrete noise features that are derived from the initial frequency comb lines to a broadband continuous spectrum.

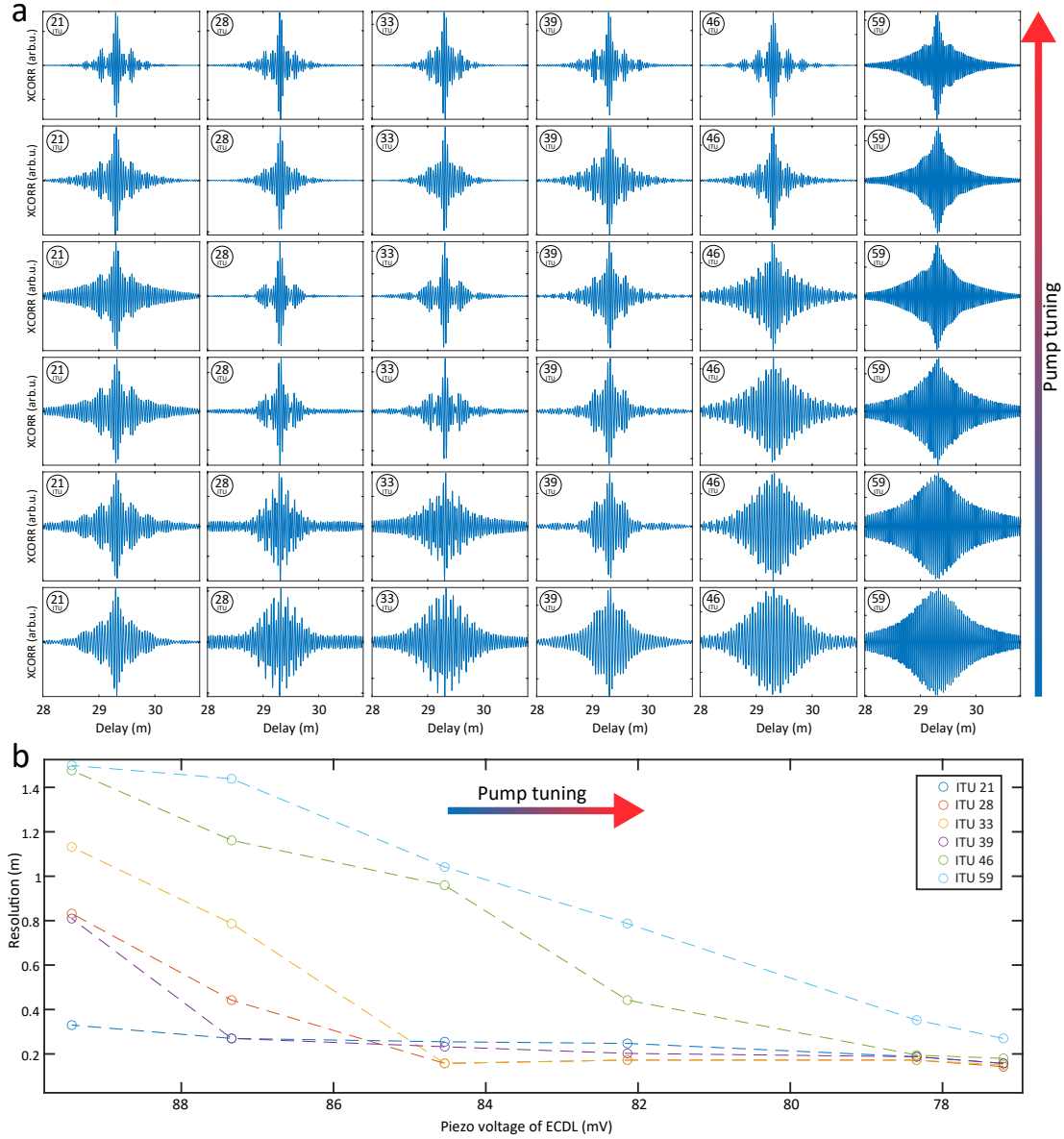


Figure B.2: **Experimental observation of chaotic MI comb state.** a) Auto-correlation of heterodyne beat note signals of chaotic MI comb lines with signal soliton microcomb lines shown in Extended Data Fig. B.1. The decreasing width of the autocorrelation peak does indicate increased range resolution for chaotic MI with small detuning. b) Range resolution evolution of selected comb lines inferred as full width at half maximum (FWHM) of auto-correlation traces.

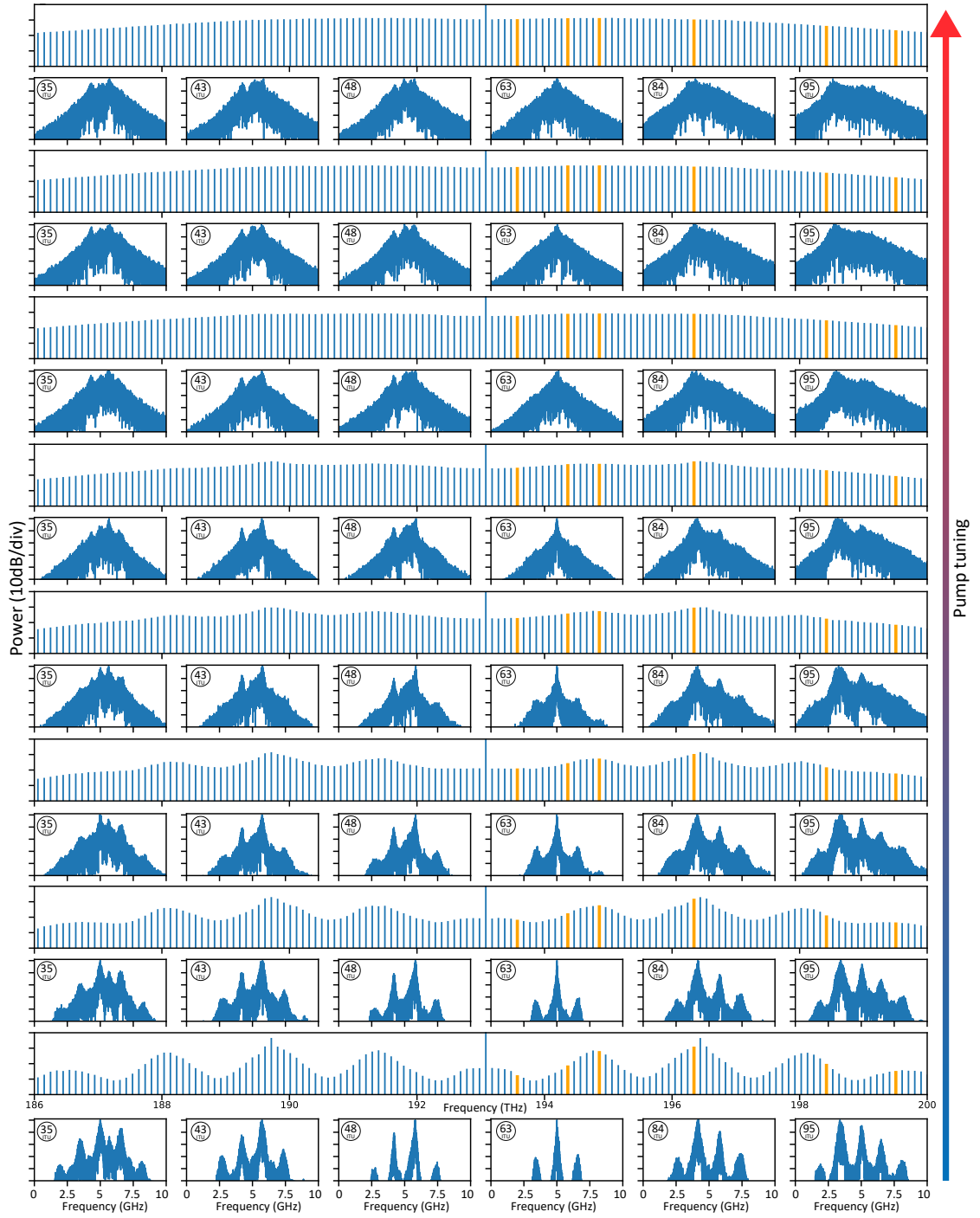


Figure B.3: **Numerical calculations of chaotic MI comb state.** Numerically calculated optical spectra (1st, 3rd, 5th ... row) and heterodyne beatnote power spectral densities (2nd, 4th, 6th, ... row) of selected comb lines (ITU: 35, 43, 48, 63, 84, 95) for different laser cavity detuning (cf. Ext. Data Fig. B.1).

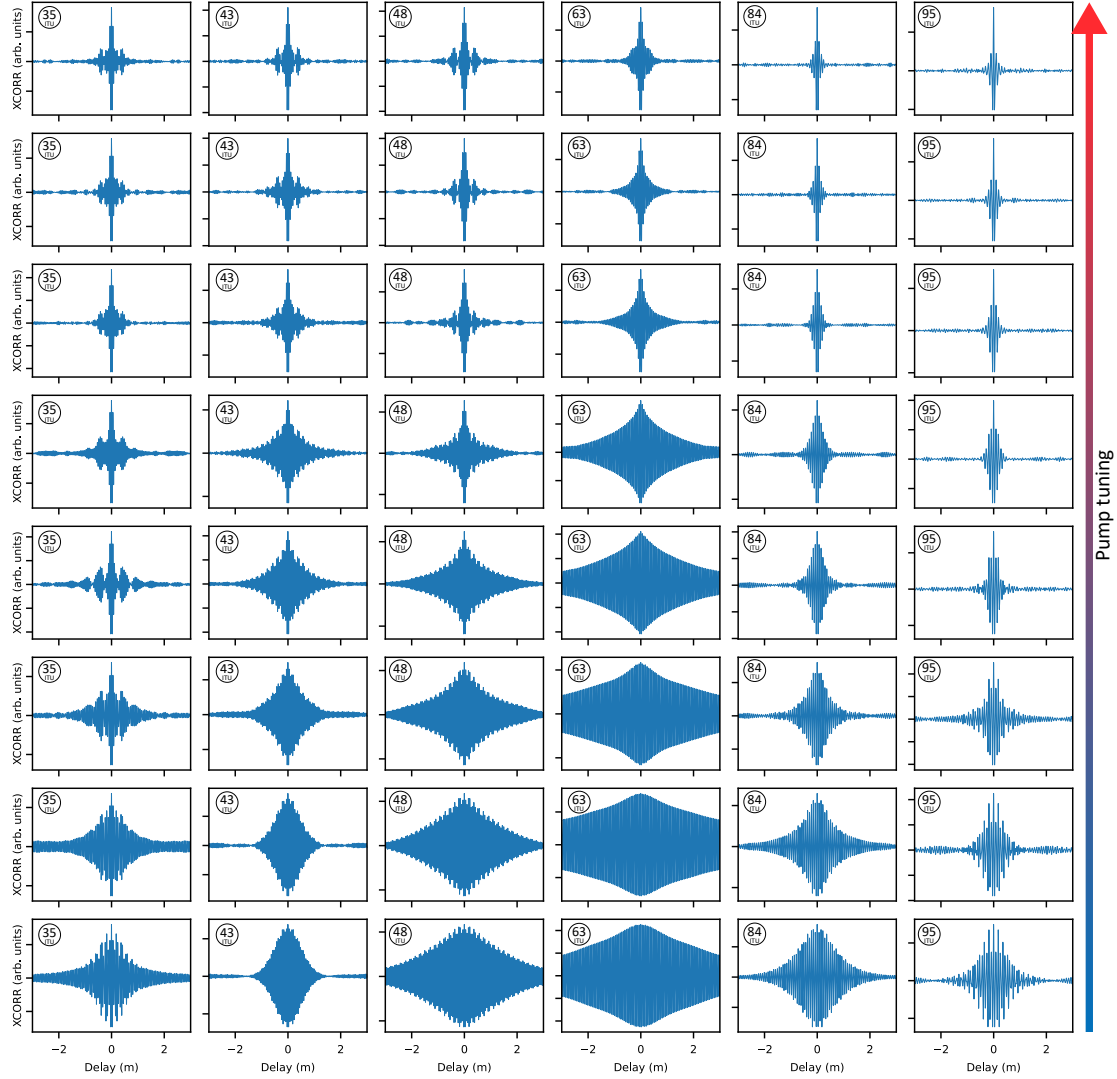


Figure B.4: Numerical calculations of chaotic MI comb state. a) Auto-correlation traces of chaotic MI comb lines shown in Extended Data Fig. B.3 (cf. Ext. Data Fig. B.2).

Numerical investigation of the noise bandwidth

In the previous sections, we showed that the maximal resolution is attained in the presoliton switching zone, which is depicted in Fig. B.6a as the edge of the MI zone. Tuning further into the bistable region of the tilted resonance will switch the resonator into one of the coherent regimes: DKS or CW; therefore, the preferred operating point should be at the end of the monostable branch. If the internal linewidth of the device (κ_0) is fixed, the range resolution can be improved by increasing the coupling κ_{ex} . In order to show it, we considered two identical resonators with different couplings to the bus waveguide: an overcoupled $\kappa_{\text{ex}} = 9\kappa_0$ and a critically coupled $\kappa_{\text{ex}} = \kappa_0$ devices. The corresponding tilted resonances for the input power 0.9 W in Fig. B.6a show that

the overcoupled device has more optical power (i.e. more photons) in the monostable region. Further, we converted the number of photons to Kerr frequency shift and computed noise bandwidth for a set of comb lines in the chaotic state at the end of the MI zone by performing similar numerical simulations as above. In Fig. B.6b we show the dependence of the noise bandwidth on Kerr frequency shift for both devices with increased pump power 1.0 W, 1.1 W,...,2.0 W. Both devices have the same trend of resolution improvement with the pump power, but the overcoupled resonator shows better performance than the critically coupled one. Increasing κ_{ex} decreases the loaded quality factor but provides with more effective photon flux into the cavity. In contrast to the soliton generation, where critically coupled devices provide with larger soliton existence range, the overcoupled resonators in the MI regime have more intracavity power and thus provide with better resolution.

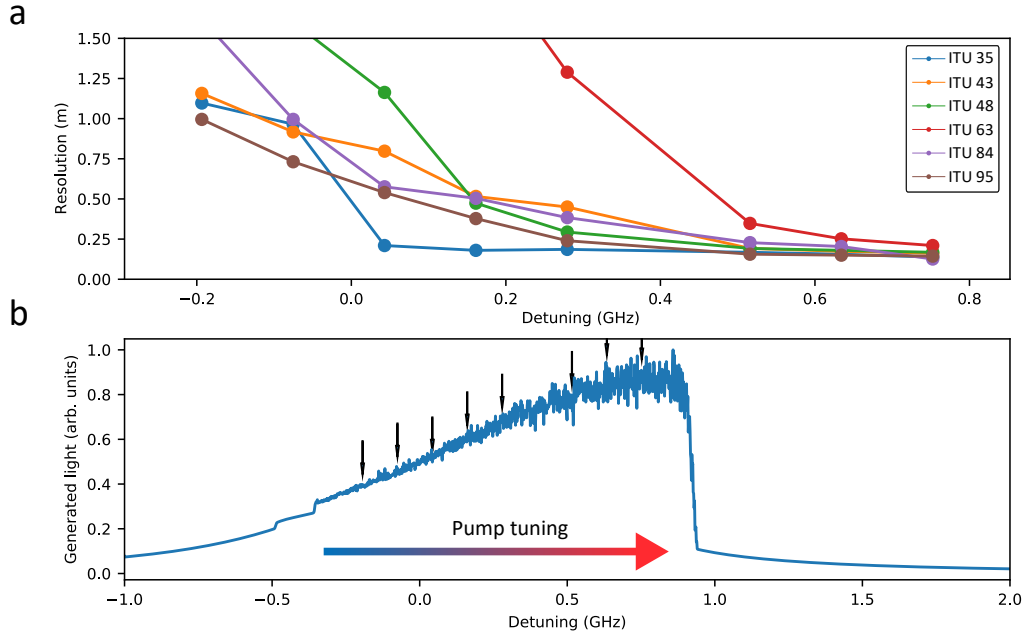


Figure B.5: Numerical calculations of RMCW LiDAR resolution. a) Simulation of range resolution evolution of selected comb lines inferred as full width at half maximum (FWHM) of auto-correlation traces depicted in Extended Data Fig. B.4. (cf. Ext. Data Fig. B.2b). b) Intracavity generated power vs pump detuning. Zero detuning corresponds to the "cold" cavity resonance frequency. Black arrows indicate detuning values used in simulations.

B.3 Direct detection RMCW LiDAR

We note there are two possible implementations of RMCW. Coherent detection employing extra local oscillator for every comb tooth and direct detection requiring highly sensitive photodiodes performing incoherent measurements of the electric field amplitude. While we demonstrated coherent LiDAR based on heterodyne detection, direct detection chaotic microcomb RMCW LiDAR is equally feasible, since MI possess both

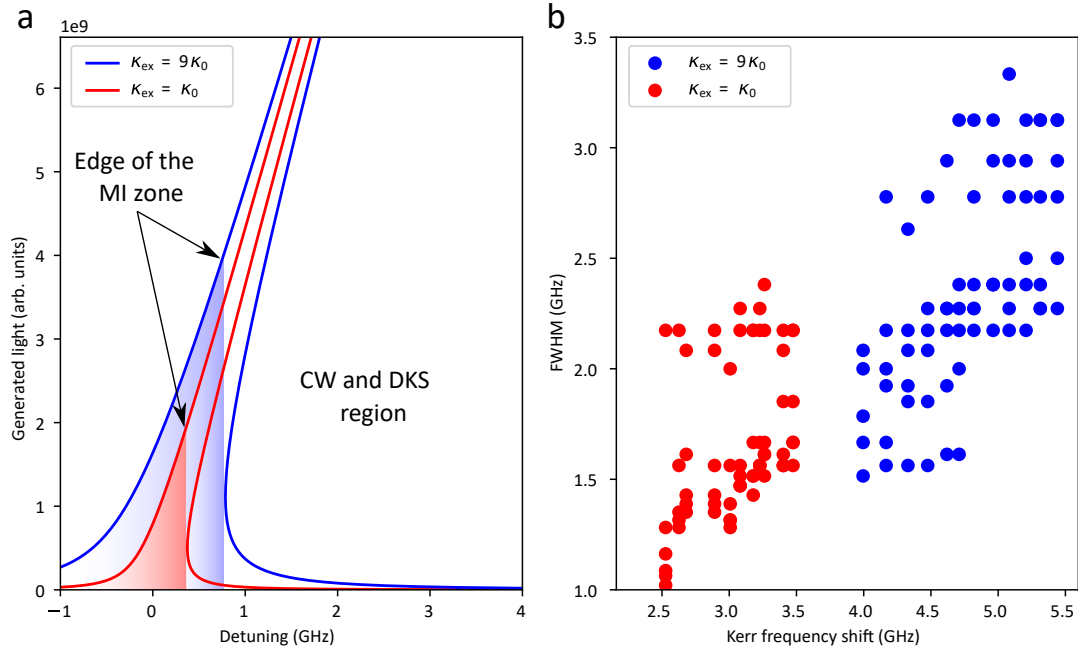


Figure B.6: **Modulation instability noise dependence on microresonator Kerr frequency shift.** a) Tilted resonance for critically coupled $\kappa_{ex} = \kappa_0$ and overcoupled $\kappa_{ex} = 9\kappa_0$ resonators for 0.9 W input power. b) Simulated MI state evolution of characteristic noise bandwidth of selected channels as a function of Kerr frequency shift for increasing pump power and fixed pre-soliton switching detuning (very right black arrow on Extended Data Fig. B.5) for critically and overcoupled cases. FWHM is calculated as the speed of light divided by distance resolution inferred from autocorrelation trace.

amplitude and frequency random-like modulation. Exclusion of local oscillators simplifies the setup (cf. Ext. Data Fig. B.7) and requires sensitive photodetectors instead of coherent receivers .

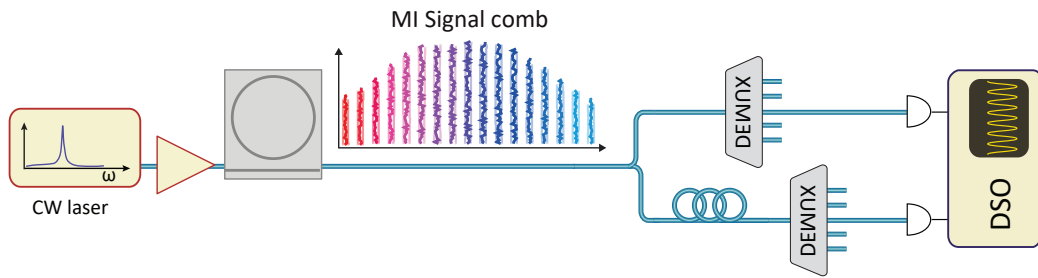


Figure B.7: **Direct detection RMCW LiDAR mock-up setup.** Direct-detection LiDAR setup utilizes only MI comb and does not require coherent receivers since the amplitude of the waveform is measured only.

Baraja is an example of commercial company utilizing pure amplitude modulation CW LiDAR [167]. Given widely used spectral scan approach, chaotic microcombs could be readily applied in the similar setting to remove the necessity for the laser scan and

introduce parallelism due the multitude of the comb lines.

Fig. B.8 depicts fiber delay distance measurement with ~ 1 cm level precision and resolution inferred from cross-correlation traces. Resolution in case of pure amplitude modulation corresponds to the resolution of coherent RMCW LiDAR highlighting similar effective noise bandwidth in amplitude and frequency domains.

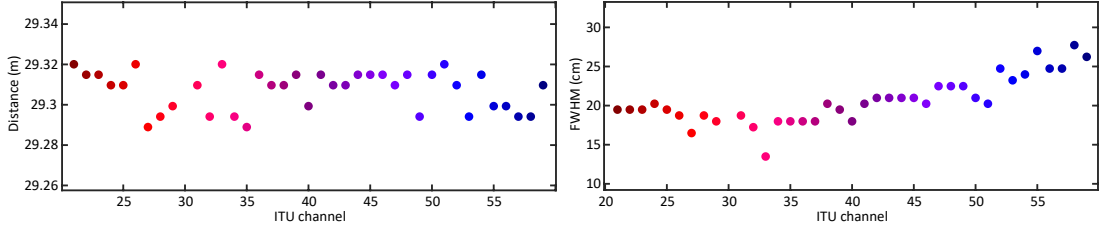


Figure B.8: **Direct detection RMCW LiDAR.** (Left) Fiber delay measurement via direct detection of MI based RMCW LiDAR. (Right) FWHM of cross-correlation traces corresponding to distance resolution of direct detection RMCW LiDAR. The values of channel dependent resolution correspond to the case of coherent RMCW LiDAR where the signals were digitally high-pass filtered with 550 MHz pass frequency.

B.4 Comparison with ASE noise LiDAR

Evidently, one could argue that ASE noise could be used as an optical source for RMCW LiDAR. Indeed ASE noise from erbium doped fiber amplifier (EDFA) is broadband and follows random-like Gaussian statistics. It would have much higher noise bandwidth even after being filtered by DEMUX unit than a chaotic MI comb line resulting in higher resolution. Fig. B.9 demonstrates distance resolution of ASE noise based RMCW LiDAR versus digital band-pass filter bandwidth.

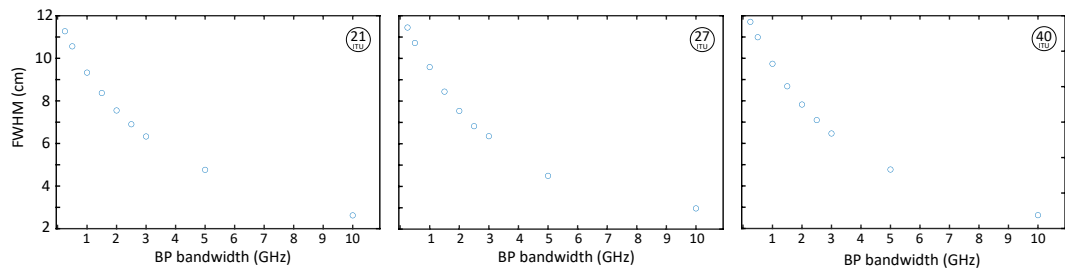


Figure B.9: **ASE based LiDAR.** Broadband amplification spontaneous emission noise from erbium doped fiber amplifier is used to determine achievable distance resolution. Figures depict FWHM or distance resolution versus digital band-pass filter bandwidth for 21, 27, and 40 ITU channels correspondingly.

Here, we give a theoretical estimation of the power requirements for ASE source and MI comb considering application to parallel ranging. To compare power efficiency,

we consider an erbium doped fiber pumped by a 1480 nm laser with power P_0 and a 1550 nm laser pumping a microresonator for MI comb generation with the same power P_0 . For simplicity, we consider our EDFA to have unity quantum conversion efficiency and unity power efficiency. That said, all the pumped power results in ASE noise. We limit the spectral window to 1530 – 1560 nm range (for easy comparison with commercial 192-196 THz DEMUX). We also consider the power spectrum of ASE to be flat and uniform. For MI generation, we consider 3 dB coupling loss for each facet of the chip (6 dB overall) and 20% MI conversion efficiency (as we observed experimentally) and the same FSR. We note that our microresonator was not specifically dispersion engineered to have an optimal flat shape at 1530-1560 nm window. As shown in Fig. 2a in the manuscript, our MI covers 1522-1586 nm band (189 - 197 THz). However, SiN microresonator dispersion engineering allows tailoring the waveguide dispersion by changing the microresonator's height and width to achieve a required dispersion profile [239]. That is why we will consider a dispersion engineered MI comb with a flat spectral band in 1530-1560 nm for optimal comparison. Thus, we will consider the useful MI power to be $(0.5)^2 \times 20\% \times P_0 = 0.05P_0$ (disregarding exponentially decaying comb lines out of the window of interest). To reach the same power efficiency (i.e., the same optical power illuminates the target), the ASE source needs to utilize at least 5% of its bandwidth in 1530-1560 nm window, i.e., $4 \text{ THz} \times 5\% = 200 \text{ GHz}$. For 40 channel ranging, one ASE channel would require $200 \text{ GHz} / 40 = 5 \text{ GHz}$ bandwidth to meet the same power efficiency as MI. In this estimation, we took the upper bound for quantum conversion efficiency (not achievable) for EDFA, while the MI generation power budget can be improved in terms of both coupling loss (integrating laser on a chip [138] and power efficiency (engineering the required dispersion).

However, for coherent ranging applications, not only does the optical power illuminating the target matter but intensity of the beam on the target. And in case of parallel ranging with diffractive optics, the power spectral density translates into intensity on the target. Considering the numbers above, i.e., assuming the same power efficiency for 40 channel ranging, the MI-based heterodyne detection would be 5 times more efficient than ASE heterodyne detection (irrespective of the total ASE bandwidth utilized). Assuming following parameters: 2.5 cm collimator aperture size, 100 m ranging distance, 1550 nm wavelength – results in Fresnel number ≥ 1 , i.e., near field light propagation. In this case, the heterodyne detection efficiency depends on the intensity of the collimated beam on the target [209, 108, 240]. The diffraction grating spreads the multicolor beam across the target. The effective noise bandwidth of MI is 1 GHz, while for the ASE source with the same power efficiency, one channel would require a 5 GHz bandwidth. If we adopt the same schematics as in our experiments, the diffraction grating spreads the beam horizontally. The ASE channels would be spread 5 more times than MI resulting in less intensity on target. The spread is proportional to the channel bandwidth since we use diffractive optics. The drawback of the ASE source, in terms of coherent ranging with optical disperses, spread power spectrum results in a spread beam spot. In fact, if we

use more ASE bandwidth we get more power and more spread, resulting in constant intensity derived from spectral density. If we denote κ_{ASE} and κ_{MI} as power conversion efficiency for ASE and MI from the pump of power P_0 , then the ratio of heterodyne detection efficiency between ASE and MI would be:

$$\frac{FSR}{B_{eff}} \times \frac{\kappa_{MI}}{\kappa_{ASE}} \sim \frac{100GHz}{1GHz} \times \frac{0.05P_0}{P_0} = 5 \quad (B.6)$$

Speaking broadly, utilization of MI allows arbitrary FSR and dispersion, which results in a tailored power spectrum of MI comb. It enables effective redistribution of the pump power densely to particular channels and flexibility to change it on demand. In contrast, the ASE power spectrum is fixed, and the power is distributed sparsely, resulting in the spread on the target after passing through diffractive optics, while coherent ranging requires high intensities on the target.

B.5 SNR, resolution and precision of coherent RMCW LiDAR

In this section we will discuss the SNR, resolution and precision of RMCW LiDAR from an analytical standpoint. To begin with, we would like to draw the readers attention to similarities between conventional FMCW and coherent RMCW ranging techniques. Indeed, as we show below both achieve a distance resolution of $c/2B$, where B stands for the sweep amplitude for FMCW and characteristic frequency noise bandwidth in case of RMCW. Additionally, the equations for measurement precision also share many similarities. Also we note that both approaches yield similar SNR and reach single-photon sensitivity.

SNR

The SNR for shot-noise limited coherent detection with unity quantum efficiency is

$$SNR = \frac{\langle I^2 \rangle}{\langle \Delta I^2 \rangle} = \frac{P^{sig}}{\hbar\omega B_{RF}} \quad (B.7)$$

where B_{RF} stands for the effective noise bandwidth of the Fourier transform window. This level of sensitivity is expected in conventional FMCW approach [240].

The calculation of the SNR for RMCW includes two steps: the coherent detection of signal and reference and their cross-correlation. The latter closely follows the discussion outlined in chapter 8 of [241]. To simplify our derivation we will consider the RMCW signal to be bandwidth-limited white Gaussian noise with a zero mean. We will also consider a simple model for signal x and reference y currents after coherent detection

step as

$$\begin{aligned}
 x(t) &= s(t - \tau_d) + n(t) \\
 y(t) &= s(t) + m(t) \\
 R_{xx}(0) &= R_{ss}(0) + R_{nn}(0) = S + N \\
 R_{yy}(0) &= R_{ss}(0) + R_{mm}(0) = S + M \\
 R_{xy}(\tau) &= R_{ss}(\tau - \tau_d)
 \end{aligned} \tag{B.8}$$

Where $s(t)$ represents the contribution to the current from the initial random signal, $m(t)$ and $n(t)$ are noise terms that appear after photodetection due to the shot noise, thermal noise and other possible noise sources. The SNR of the current y , for example, reads as $\text{SNR}_y = \langle s^2 \rangle / \langle m^2 \rangle = R_{ss}(0) / R_{mm}(0) = S / M$. τ_d is a delay of the signal current with respect to the reference current. All of these terms are mutually uncorrelated. We did not introduce an attenuation coefficient for the $s(t - \tau_d)$ term to keep the clarity and as it will be evidenced later, the ratio of the amplitudes S and M, N matters rather than the absolute value of S . To calculate the SNR of the cross-correlation trace between the signal x and the reference y currents we take the maximum of the cross-correlation function squared and divide by its variance $\text{SNR} = R_{xy}^2(\tau_d) / \text{Var}[R_{xy}(\tau)]$. The denominator term in case of bandwidth-limited white Gaussian noise signals x, y can be estimated as [241, 242]

$$\text{Var}[R_{xy}(\tau)] \approx \frac{1}{2BT} [R_{xx}(0)R_{yy}(0) + R_{xy}^2(\tau)] \tag{B.9}$$

where B is a signal noise bandwidth and T is the time length of x and y and $T \gg \tau_d$. Taking the upper bound for the variance estimate of cross-correlation at $\tau = \tau_d$ we approximate the value of SNR to be

$$\begin{aligned}
 \text{SNR} &\approx R_{xy}^2(\tau_d) / \text{Var}[R_{xy}(\tau_d)] \\
 &= 2BT / [2 + M/S + N/S + (M/S)(N/S)]
 \end{aligned} \tag{B.10}$$

At this point we make two more assumptions. First, the reference current has a much higher SNR than the signal current $(S/M) \gg (S/N)$. It is a reasonable assumption since we can always allocate some amount of signal power straight after generation and send it directly to the detector without any loss, while the target arm will experience free-space optical loss. Second, the SNR of the imaged photocurrent is much less than one $S/N \ll 1$. This is not only a realistic assumption but also a desired property in spread spectrum communications [151] and military applications supporting optical analogue of electronic counter-countermeasures and low probability of intercept [149]. In the FMCW approach the SNR of the imaged photocurrent should be more than one since it corresponds to the beatnote of a single frequency (with a width of resolution bandwidth), however in case of RMCW the spectrum is spread out resulting in much lower SNR at the photodetection stage, while it will be boosted taking cross-correlation.

Under these assumptions we finally get [242, 7]

$$\text{SNR} \approx 2BT \left(\frac{S}{N} \right) \quad (\text{B.11})$$

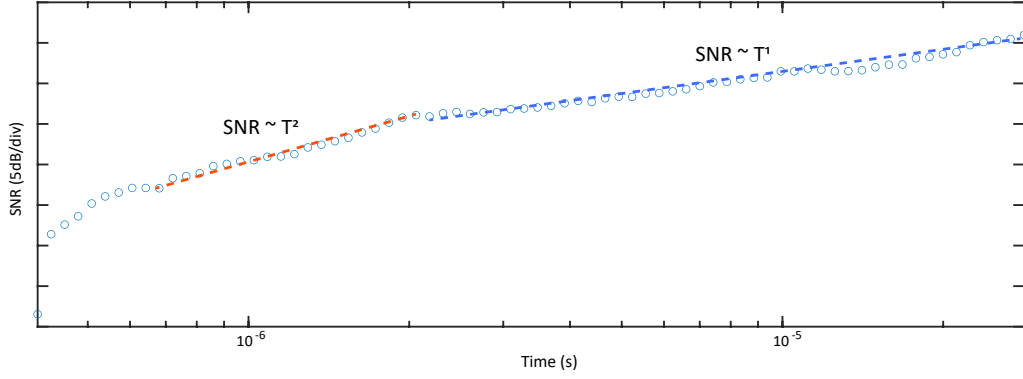


Figure B.10: **SNR of the cross-correlation trace time dependence.** ITU 21 channel SNR versus measurement time dependence for a free-space measurement. Blue dashed line highlights a linear dependence in accordance with formula B.11 for measurement times more than delay time equal to ~ 350 ns.

Effectively, the photocurrent SNR (that is S/N) gets multiplied by time-bandwidth product (cf. Fig. B.10). If one uses a Nyquist sampling rate of $f_s = 2B$ the SNR would read as $\approx f_s T \left(\frac{S}{N} \right)$, where $f_s T$ is simply a number of sampled data points. Further, we will estimate the value of S/N , where S stands for the initial random signal current variance and N is a variance of the photodetection noise, or, equivalently this ratio equals to the ratio of power spectral densities at $f < B$ of signal and noise currents, considering them to be flat. We will assume a shot-noise limited heterodyne detection with unity quantum efficiency. To distinguish SNR at different stages we apply the notation

$$\text{SNR}_{\text{corr}} = 2BT \left(\frac{S}{N} \right) = 2BT * \text{SNR}_{\text{pd}} \quad (\text{B.12})$$

Two random signals one of which is a true signal (target signal) and the other is a random noise have an SNR determined as a ratio of variances of their currents $\text{SNR}_{\text{pd}} = \langle \sigma I_s^2 \rangle / \langle \sigma I_n^2 \rangle$. The variance of the target signal $\sigma I_s^2 \propto 2P^{\text{sig}} P^{\text{LO}}$, while the variance of the noise $\sigma I_n^2 \propto 2\hbar\omega P^{\text{LO}} \Delta\nu_{\text{RBW}}$. The resolution bandwidth $\Delta\nu_{\text{RBW}}$ equals to the sampling rate, since the time-domain variance of the current noise is determined by the number of the shot noise photons collected during the sampling time. The ratio of the variances leads to

$$\text{SNR}_{\text{pd}} = \frac{\langle \sigma I_s^2 \rangle}{\langle \sigma I_n^2 \rangle} = \frac{P^{\text{sig}}}{\hbar\omega f_s} \quad (\text{B.13})$$

Appendix B. Appendix to chapter 5 - Chaotic microcomb based parallel ranging

Substituting eq. B.13 in to eq. B.12 and considering sampling rate to be twice as noise bandwidth $f_s = 2B$, we arrive to eq. B.7, where the resolution bandwidth B_{RF} is inverse of the measurement time T .

In Fig. B.11a,b we show SNR in chess imaging experiment and average SNR per optical channel. Fig. B.12 depicts the same ranging experiment as in Fig. 5.5b but for integration time of $1 \mu\text{s}$, i.e. on average 10dB less SNR per channel, which can be witnessed in detection count.

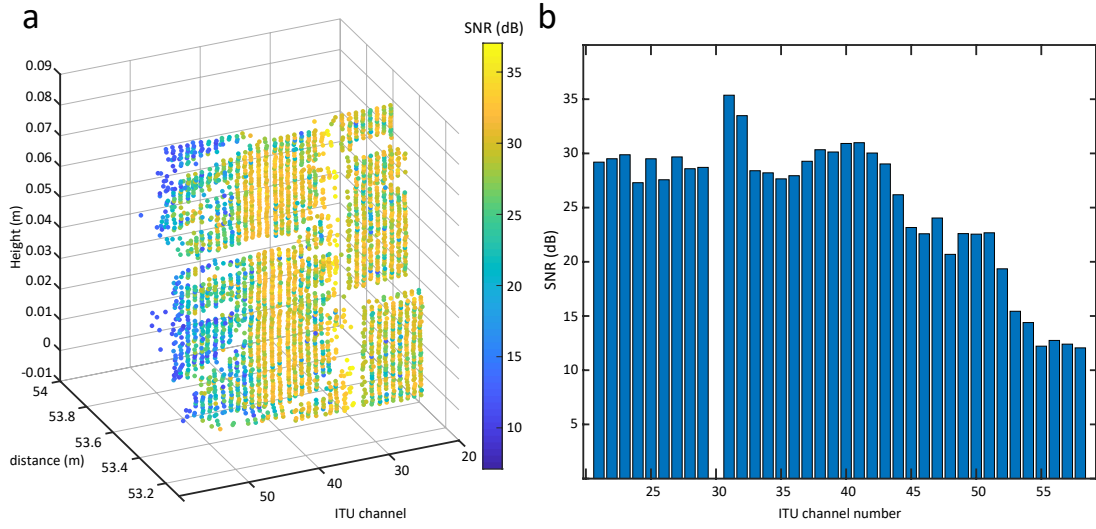


Figure B.11: **SNR in imaging experiment.** a) Imaging scene of chess figurines where the colormap corresponds to the SNR of detected pixels. b) Average SNR per optical channel at 10 μs acquisition time.

Distance measurement resolution

We find it useful to bring analogies between FMCW and RMCW approaches, given they have a lot in common. That is why for our next discussion on resolution and precision we will first derive it for the case of FMCW and then compare it to the results of RMCW. In the context of LiDAR, the term distance resolution usually refers to a longitudinal (or axial) resolution, i.e. the minimum resolvable distance between two reflectors within a single optical path. Recall that the value of the beatnote for a given measured distance in FMCW case with triangular ramp waveform modulation follows $f_b = \tau_d \cdot 2B/T = 2R/c \cdot 2B/T$ [134]. The minimum separation frequency one can resolve is determined by the measurement time, which often is the same as a chirp period T . The value of the beatnote is derived by taking the Fourier transform over the up/down ramp with duration $T/2$ resulting in frequency resolution $2/T$. Then, the distance resolution reads as

$$\Delta R = \frac{cT}{4B} \Delta f_b = \frac{c}{2B} \quad (\text{B.14})$$

In case of RMCW with flat-top power spectrum with finite bandwidth, the resolution can be inferred directly from the auto-correlation function. According to the Wiener-Khinchin theorem, the auto-correlation function is the Fourier transform of the power spectral density of the signal. The Fourier transform of a rectangular function with the width B is a sinc function ($\sin(\pi x)/(\pi x)$) with first zeros at $t = \pm 1/B$. Following the convention, two sinc functions can be resolved if the maximum of the second sinc

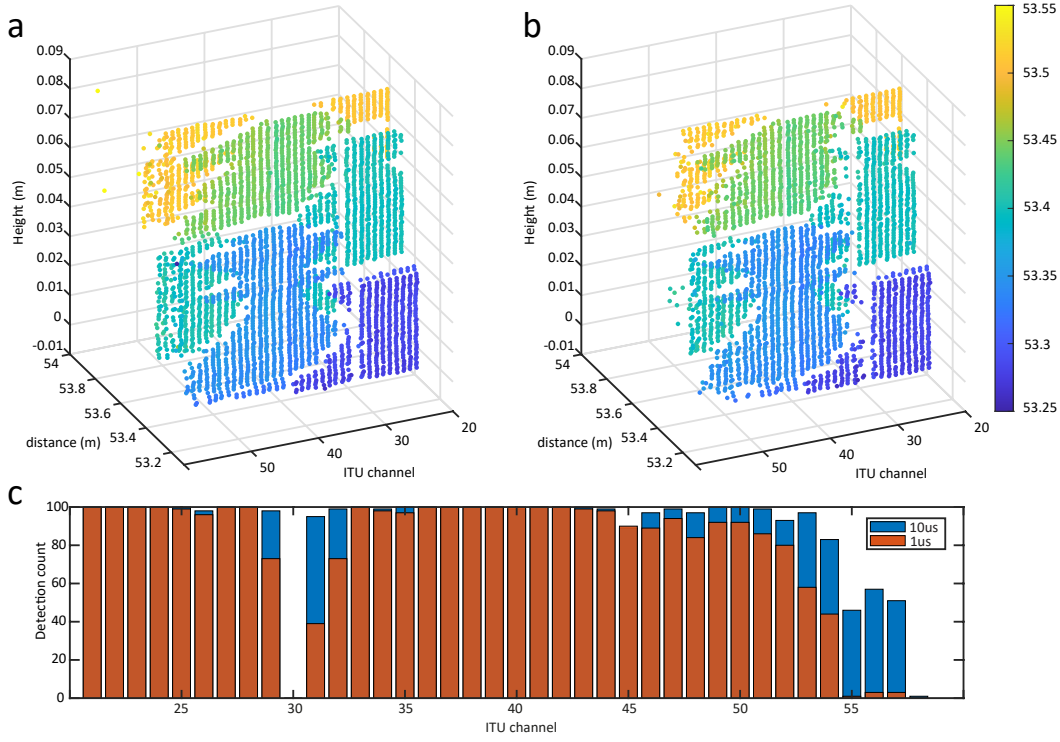


Figure B.12: **Ranging acquisition time variation.** a) Chess imaging with $10 \mu\text{s}$ pixel acquisition time similar to Fig. 5.5b. b) Chess imaging with $1 \mu\text{s}$ pixel acquisition time. Pixels at the figures' edges and corresponding to pump channels have lower detection count. c) Pixel detection count for different acquisition times. In case of not sufficient detection rate RMCW LiDAR can dynamically update its measurement integration time in "real-time" or batch processing.

corresponds to the position of the minimum of the first sinc function, which leads to the following expression for RMCW ranging resolution:

$$\Delta R = \frac{c\Delta T}{2} = \frac{c}{2B} \quad (\text{B.15})$$

In case of a random modulation with a pulse sequence, one assumes the pulse width $1/B$ as a time resolution unit and gets the same equation as B.15 for distance resolution [155, 169].

Distance measurement precision

Mathematically, precision is a standard deviation of the estimated value and the impact of random noise on the estimation. Many LiDAR papers provide precision results without further quantification on SNR, measurement time, sampling rate or number of sampled points, all of which strongly impact the measurement precision. Sometimes it is mentioned that high SNR enables sub-resolution precision or one can see estimates of precision in FMCW case given as $\Delta R/(SNR)$ [243], where ΔR stands for resolution.

Montgomery and O'Donoghue [244] studied a least squares fit problem with a sinusoidal signal in presence of random uncorrelated noise. Analytical formula for precision reads as

$$\sigma_f = \sqrt{\frac{6}{N_s}} \frac{1}{\pi T} \frac{1}{\sqrt{\text{SNR}}} = \sqrt{\frac{6}{f_s}} \frac{1}{\pi \sqrt{\text{SNR}}} T^{-3/2} \quad (\text{B.16})$$

where N_s is a number of sampled points and other definitions are consistent with the previous sections. The same formula was heuristically derived in [245]. Similar result with a $\sqrt{2}$ difference was obtained examining Cramer-Rao lower bound [246]. The estimate for the distance precision can be readily achieved substituting eq. B.16 into eq. B.14

$$\begin{aligned} \sigma_R &= \frac{cT}{4B} \sigma_f = \frac{c}{2B} \sqrt{\frac{6}{N_s}} \frac{1}{2\pi} \frac{1}{\sqrt{\text{SNR}}} \\ &= \sqrt{\frac{6}{N_s}} \frac{1}{2\pi} \frac{\Delta R}{\sqrt{\text{SNR}}} \end{aligned} \quad (\text{B.17})$$

Indeed, the precision improves with a higher SNR, but follows a square root power law. It also improves with a number of samples, which can be reformulated in terms of measurement time, sampling rate or even chirp bandwidth if the latter is linked to the sampling rate.

For RMCW Carter[158] gives a rigorous derivation of the Cramer-Rao lower bound on time delay estimation variance for bandwidth-limited white Gaussian signals with uncorrelated white noise:

$$\sigma_\tau^2 = \frac{3}{8\pi^2} \frac{1 + 2\text{SNR}_{\text{pd}}}{\text{SNR}_{\text{pd}}^2} \frac{1}{B^3 T} \quad (\text{B.18})$$

where SNR_{pd} denotes the SNR ratio of the signal channel after the detection prior to cross-correlation with a reference channel.

In case of a high SNR_{pd} the formula can be simplified and the distance precision reads as:

$$\begin{aligned} \sigma_R &= \frac{c}{2B} \frac{\sqrt{3}}{2\pi} \sqrt{\frac{2}{\text{SNR}_{\text{pd}}}} \frac{1}{BT} \\ &= \sqrt{\frac{12}{N_s}} \frac{1}{2\pi} \frac{\Delta R}{\sqrt{\text{SNR}_{\text{pd}}}} \end{aligned} \quad (\text{B.19})$$

where we have considered sampling rate to be twice as noise bandwidth giving the term N_s and the formula resembling eq. B.17 for FMCW case.

However in case of RMCW LiDAR the returned signal has low SNR, since the signal is

Appendix B. Appendix to chapter 5 - Chaotic microcomb based parallel ranging

spread over the whole bandwidth and noise variance dominates over the signal variance. The low SNR case is discussed in [158, 247]. Assuming $\text{SNR}_{\text{pd}} \ll 1$, eq. B.15 for distance can be written:

$$\sigma_R = \sqrt{\frac{6}{N_s}} \frac{1}{2\pi} \frac{\Delta R}{\text{SNR}_{\text{pd}}} \quad (\text{B.20})$$

where in comparison to eq. B.17 the dependence on electrical current SNR is just inverse but not squared.

C Experimental methods

C.1 IQ modulation/demodulation for coherent telecommunication experiment

In this section, I will describe the process of conducting a coherent telecommunication experiment. Coherent techniques refer to those that utilize the phase of light for data transmission. In the simplest form of binary phase shift keying (BPSK), the phase of the carrier is shifted by π , which results in the same quadrature. However, if the phase is shifted by $\pi/2$, $\pi/4$, or any other fraction, the experiment must be performed using the in-phase and quadrature (IQ) components.

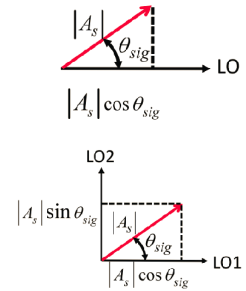


Figure C.1: Homodyne vs IQ detection

The need for the IQ components becomes evident when considering a situation in which only one quadrature, the in-phase component, can be measured. For example, let's say the vector rotates by an angle such that the x-projection is 1/2 (down from the initial value of 1). The precise angle of rotation cannot be determined without knowledge of the quadrature component (cf. Fig. C.1). This is why in coherent telecommunication, one may encounter concepts such as IQ format (also known as quadrature amplitude modulation), IQ modulator, IQ receiver, and others.

At a more general level, the need for a second quadrature arises naturally. Consider an optical (or RF, or any other) carrier $\cos(\omega t)$. This carrier is a basis vector in 2D space, and the second basis vector is $A \sin(\omega t)$, which is orthogonal to the first one. These two vectors represent amplitude and phase, respectively.

This note consists of two parts: IQ modulation and IQ demodulation and processing. The photo of full experimental setup is presented

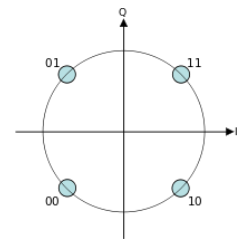


Figure C.2: QPSK format

Appendix C. Experimental methods

in auxiliary materials (below). I will mainly review the experimental steps and details. To cover basics, please refer to [129, 248]

IQ modulation

In order to create a modulated optical waveform, you need a laser, an IQ modulator, and driving electronics (details on setting up the AWG can be found in the "auxiliary materials" section). For simplicity, we will be using QPSK (quadrature phase shift keying) modulation format (refer to Fig. C.2).

The lab has several IQ modulators, mostly sourced from Thorlabs, which can handle bandwidths up to 14 GHz. Typically, a QPSK modulator requires five inputs: two RF drives for the I and Q components, and three DC biases (see Fig. C.3).

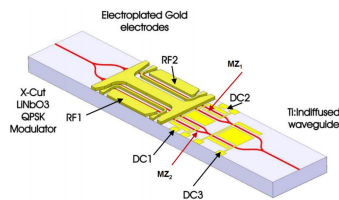


Figure C.3: QPSK modulator

The main bit stream is fed into the I and Q RF arms. These arms should be connected directly to the arbitrary waveform generator (we use the Keysight AWG M8195A in the lab, which has a 25 GHz bandwidth). Setting the DC biases is a bit trickier. The I and Q arms need to be biased to their null points, and the third joint bias should create a 90° phase shift between the I and Q components to make them into quadratures.

A QPSK modulator consists of two nested Mach-Zehnder modulators (MZMs). A null point of an MZM corresponds to zero transmission. However, we should observe how the electric field changes around that point. Fig. C.4 shows both the transfer functions of the field and intensity. If the null point is properly tuned, each arm can be driven with $2V\pi$, resulting in the most efficient modulation (with the highest extinction ratio). For more complex formats like 64 QAM or 256 QAM, you should consider the nonlinearity and use low driving voltages (as low as $\sim 0.1 V\pi$). No matter the driving voltage, the phase shift between 0 and 1 (the lower and upper points for the field) will always be π . So, with a π phase shift for both the I and Q components, all you need to do is rotate them by 90° relative to each other (using the DC bias 3), and the transmitter part is ready.

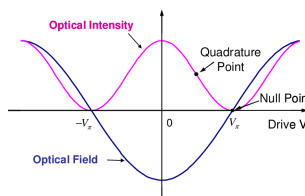


Figure C.4: MZM transfer function

While I have explained the biases that need to be applied, it's not yet clear how to do it. The solution is simple: you need to bias the QPSK modulator to single-sideband (SSB) operation. To achieve this, you need to send an RF sine signal to the I and Q RF arms. If you're using an AWG, select channels 1 and 2 (or 3 and 4) and press the I and Q window next to them. The AWG will automatically apply a 90° phase shift for the Q component for any signal, which is exactly what we need. If you're not

C.1 IQ modulation/demodulation for coherent telecommunication experiment

using an AWG, you need to send an RF sine to I and an RF cosine to Q. If the biases are set up correctly, you should observe a single sideband on the OSA with the carrier and the opposite sideband suppressed. Try to get maximum suppression.

The process of calibration involves several steps:

- To perform a 10 GBaud transmission experiment, the biases should be calibrated with a 10 GHz sine wave.
- RF amplifiers are used immediately after the AWG to drive the I and Q RF arms. When using QPSK, it is advantageous to apply a higher voltage, up to $2V_{\pi}$, however, this may result in extra sidebands due to the nonlinear operation regime. The reason for using RF amplifiers is that the Thorlabs electrodes for the I and Q RF driving and biases share a common base, so the voltage applied to the biases would leak through the I and Q RF arms back to the AWG, causing it to complain. The RF amplifiers have a DC cutoff.
- When using amplifiers, make sure that the power levels are similar, which can be confirmed by checking the voltage on a scope. Fine-tuning can later be done to optimize the SSB.
- Custom voltage boxes from an electronics workshop are used and they can suffer from temperature drift, so it's important to check and re-tune the SSB from time to time if the experiment takes more than 10 minutes. iXBlue has a dedicated device, the iXBlue Mach-Zehnder Modulators Bias Controller, which continuously monitors and tunes the biases to keep them optimal.
- When monitoring signals on an oscilloscope, make sure to calibrate the RF delays of the cables connecting the coherent receiver to the scope. This can be done by detecting the generated SSB signal and observing the I and Q RF signals on the scope's two channels. If the phase shift is not 90 degrees, calibrate the delay by adding extra delay digitally in the scope's channel settings. To ensure proper calibration, redo the process using a 9 or 7 GHz sine wave, but not a 5 GHz wave.
- The Keysight AWG is used for both calibration and IQ data stream and has a simple GUI that allows for selection from all standard waveforms, including data streams with variable modulation formats. The parameters of the applied filters (such as raised cosine) can be selected for later demodulation or other signal tweaking. Information on how to use the GUI can be found in the Lab OneNote or in the hardware folder on the server.

Once all calibration steps are completed, the IQ data stream can be sent.

IQ demodulation

IQ receiver

The structure of the coherent receiver was partially covered in chapter 4. The coherent receiver is a combination of an optical hybrid and two balanced photodetectors [129]. It has two optical inputs, one for the signal and one for the local oscillator (LO), which are combined and split into four optical inputs for the balanced photodiodes. These photodiodes produce the I and Q quadratures that make up the signal of interest, $I + iQ$.

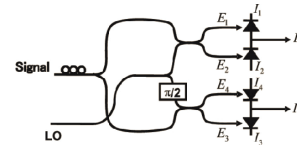


Figure C.5: Coherent receiver

There are two ways to implement a coherent receiver: the homodyne and heterodyne methods. The homodyne method uses the same laser for the signal and the LO, while the heterodyne method uses a different laser. The heterodyne method is more commonly used today and is easier to post-process.

To simplify post-processing, determining which physical detection channels correspond to the I and Q signal quadratures and calibrating the initial delay is helpful. The delay is primarily introduced by differences in the lengths of electrical cables. The calibration of the IQ receiver works similarly to the delay calibration of an IQ modulator described above.

Auxiliary material

The following steps describe how to set up the Keysight AWG. A complete set of documentation can be found at this [link](#).

- Install the Keysight Front Panel and Drivers for the AWG M8195A from the Keysight website. If the provided link is broken, simply search for "AWG M8195A" on the Keysight website.
- Connect the AWG to your PC via LAN connection and launch the front panel. Your PC should recognize the device.
- Use pre-installed waveforms from the front panel GUI, or use IQ tools to generate custom waveforms. The IQ tools can be found in the link provided above.

C.1 IQ modulation/demodulation for coherent telecommunication experiment

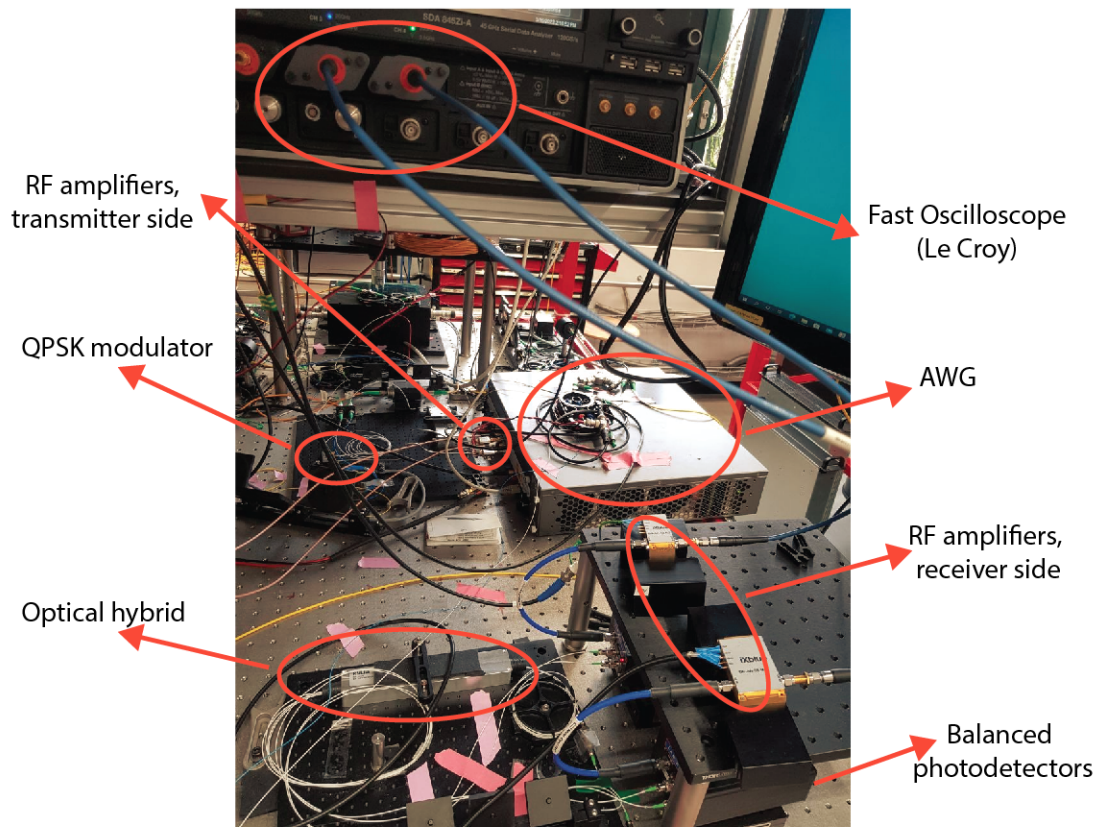


Figure C.6: Experimental setup for IQ modulation and detection

C.2 Post-processing and BER estimation in telecommunication experiment

Binary formats (PSK / ASK).

The conventional method of estimating the bit error rate (BER) involves comparing the bits sent with the bits received. However, when the signal-to-noise ratio (SNR) is high and there are few or no errors, estimating the BER can be challenging.

An alternative approach to estimating the BER is to analyze the statistics of the samples contained in an eye diagram. An eye diagram is a visualization of the signal, where a series of samples are sliced and stacked into a frame. This type of diagram can be obtained using an oscilloscope in persistence mode.

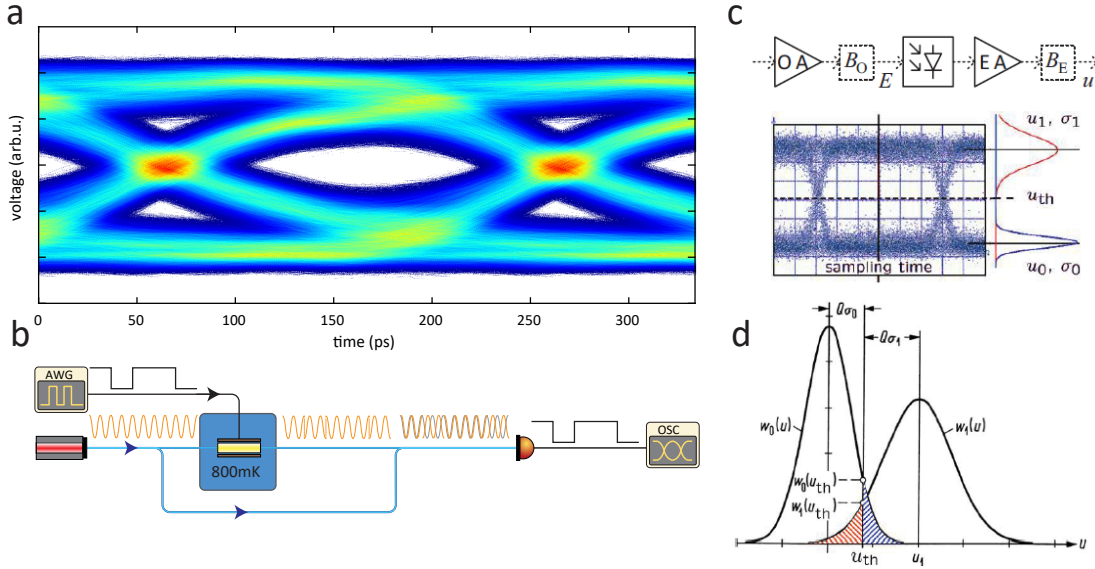


Figure C.7: **Eye diagram in telecommunication experiment in BER calculation** a) Eye diagram obtained in PSK detection experiment. b) Experimental setup employed in Ref. [249] c) BER calculation via statistics of the EYE. d) Error probability distributions. c,d) adapted from [250].

$$\text{BER}_{\text{op}} = \frac{1}{2} \text{erfc} \left(\frac{Q}{\sqrt{2}} \right), Q = \frac{u_1 - u_0}{\sigma_1 + \sigma_0} \approx \sqrt{\gamma},$$

$$u_{\text{th}} = \frac{u_1 \sigma_0 + u_0 \sigma_1}{\sigma_0 + \sigma_1}, \frac{w_1(u_{\text{th,op}})}{\sigma_0} = \frac{w_0(u_{\text{th,op}})}{\sigma_1} \text{ for } \frac{p(1t)}{p(0t)} = \frac{\sigma_1}{\sigma_0}.$$
(C.1)

It appears that for a simple amplitude modulation the BER can be derived analytically (cf. eq. C.1, having several assumptions, of course) through the mean and standard deviation of the detected '1' and '0' levels [250]. Thus, collecting even small dataset with

no errors (for good BER), estimation for BER can be derived. The detection of phase-shift keying, as illustrated in Fig. C.7b, was performed using self-homodyne beating and direct intensity detection.

Higher order formats (QPSK/QAM).

Experiment description

The telecommunication experiment was carried out by the author in Ref. [91]. The frequency comb carriers were encoded with an IQ modulator that was driven by an arbitrary waveform generator (AWG) using a $2^{11} - 1$ pseudo random bit sequence. All of the comb lines were simultaneously QPSK modulated at a rate of 10 GBaud/s and sent through a 1 km optical fiber link. At the receiver stage, every optical channel was individually accessed through a commercial 40-channel WDM unit that covered a range of 192-196 THz. Heterodyne detection was performed using an external laser (local oscillator) on a home-built coherent receiver. The coherent receiver consisted of a 90° optical hybrid and two balanced photodetectors, followed by broadband electrical amplifiers.

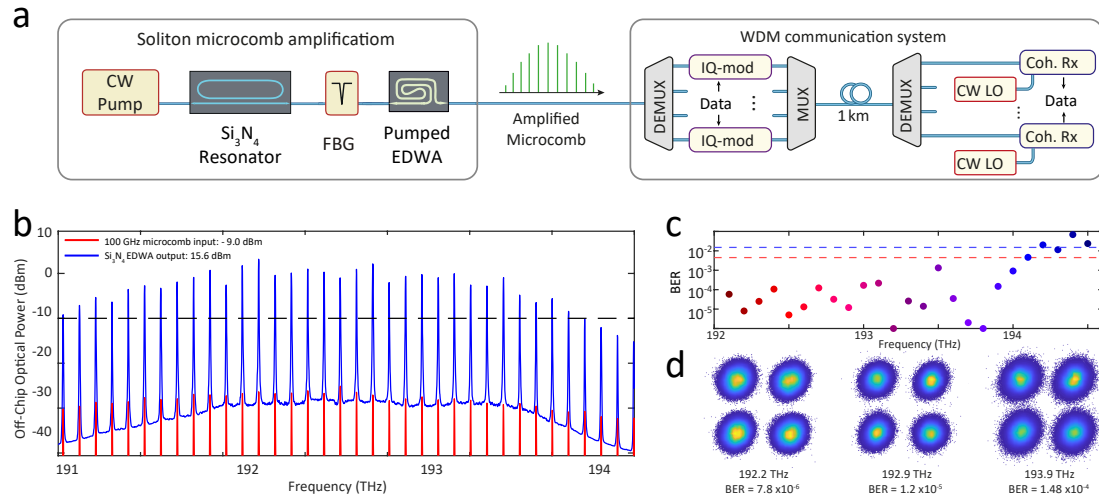


Figure C.8: On-chip amplification of soliton microcombs. a) Experimental setup for soliton amplification, microwave generation and wavelength-division multiplexing optical communication. FBG, fiber Bragg grating; DEMUX, demultiplexer; LO, local oscillator. b) Optical spectra of amplified 100 GHz soliton microcomb and the input. c) Measured Bit Error Ratio (BER). Blue (red) dashed line corresponds to 7%soft-decision (20% hard-decision) forward error correction overhead. d) Reconstructed QPSK constellation diagrams. (Part of the figure was made by the author for [91] and adapted here).

Data traces were recorded by a 40 GSa/s oscilloscope and post-processed offline. For every optical channel, time traces consisting of 4 million samples were recorded to provide sufficient statistical reasoning for the stated BER values in Fig. C.8d [251]. In the experiment, only EDWA was used to amplify the comb, but in a real-world

Appendix C. Experimental methods

telecommunication setting, a number of optical amplifiers would be used to meet the required optical power budget and OSNR, depending on the modulation format, receiver sensitivity, and noises and losses in the link [252].

Post-processing

The following section outlines the process of demodulating the IQ detected data stream for a QPSK signal. The information provided assumes that both quadratures I and Q have been detected using a pre-calibrated coherent receiver setup, as previously described. The steps outlined in this section have been adapted from MatLab's communication toolbox for QPSK transmission and have been implemented in reference [91]. The code can be found on Zenodo and [here](#).

The steps to demodulate the IQ detected data stream are as follows:

- Apply global IQ correction to the data stream, which involves adjusting the amplitude and rotating the constellation. Following steps will do it on a symbol-to-symbol basis (fine adjustment).
- Use a coarse frequency offset compensator (`comm.CoarseFrequencyCompensator`) to shift the beatnote to the baseband. (For the heterodyne detection the beatnote will be offset)
- Apply a raised cosine receiver filter reducing number of samples per symbol from 4 to 2 (`comm.RaisedCosineReceiveFilter`). The data rate was 10 Gbaud, and the sampling frequency was 40 Gs/s (LeCroy SDA) resulting in 4 samples per symbol. The AWG applies raised cosine filter to transmit the analog signal, because it reduces required bandwidth compared to non-return-to-zero signal with only 0 and 1 levels. The same operation should be repeated on the on the receiver side.
- (Optional) Apply global IQ correction again. Following the implementation in [61] it indeed worked better.
- Use fine phase recovery to track the phase from symbol to symbol, which can change by 0, 90, 180, or 270 degrees for QPSK signals.
- Apply symbol timing synchronization to have one sample per symbol using the "Mueller-Muller (decision-directed)" timing error detector method, which has been found to work best. The order of the last two steps can be adjusted based on the algorithm being used.
- Fine-tune various global parameters to achieve the best constellation, as measured by the EMR/EVM metrics described in reference [253].

- Lastly, if the ASK/PSK the BER can be estimated without a direct comparison between transmitted and received bits, in case of higher order formats, such a comparison usually takes place, though similar to SNR terms such as EMR/EVM terms are introduced [253], which are related to BER. If the initial pre-calibration was done right (essentially arranging I and Q in proper order), after post-processing there are 4 different options corresponding to global rotation of the constellation diagram by 0, 90, 180, 270 degrees [254]. In real world scenarios, a specific preamble is used before the data stream, which solves this phase ambiguity by cross-correlation. In case of ref. [91], I performed cross-correlation of the received data-stream with a sent data stream, thus determining the global offset and then calculating the true BER.

The steps outlined above can be found in the MatLab telecommunication toolbox. Additionally, there are several articles that describe the implementation of coherent communication experiments and provide an overview of the steps involved, such as the studies in references [61] and [39].

C.3 Delay line distance measurement via VNA response

In all of the FMCW ranging experiments we utilized a reference MZM for chirp calibration. Thus, we could determine the excursion B knowing the precise distance of the delay. Here, I will describe an easy technique to measure distance delay ΔL via VNA response.

The experimental schematics is outlined in Fig. C.9a. The basic idea is similar to the interferometric measurement with varied delay, but here we sweep the carrier frequency and measure the response.

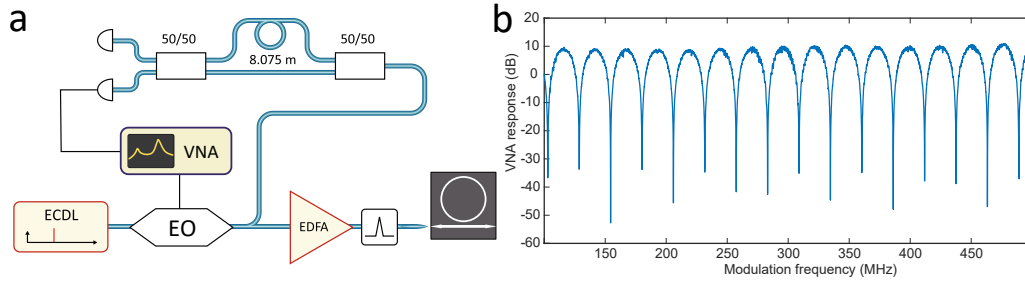


Figure C.9: **Concept of chaotic microcomb based inertia-free ranging.** a) Schematic of experimental setup for VNA response distance measurement. b) VNA response versus modulation frequency.

The interference after the delay line induces the following current

$$I \sim |E \cos(\omega t + \phi_1) + E \cos(\omega t + \phi_2)|^2 = 2(|E|^2 + |E|^2 \cos(\phi_1 - \phi_2)) \quad (\text{C.2})$$

The delay line determines the phase difference $\phi_1 - \phi_2 = k\Delta L$. One can infer the delay by varying the frequency of the carrier ν and recording the fringe pattern (cf Fig. C.9b)

$$I \sim \cos(k\Delta L) = \cos\left(\frac{2\pi n \nu}{c} \Delta L\right) = \cos\left(\frac{2\pi n(\nu_0 + \Delta\nu)}{c} \Delta L\right) = \cos\left(\frac{2\pi n \Delta\nu}{c} \Delta L + \phi_0\right) \quad (\text{C.3})$$

ν_0 stands for the absolute frequency of the optical carrier, $\Delta\nu$ is the optical side-band frequency carrier offset or applied RF modulation frequency. Finally, the delay can be found by fitting the 'sin²' function to the measured VNA response (Fig. C.9b) of the delay line.

Bibliography

- [1] C. Urmson, J. Anhalt, D. Bagnell, C. Baker, R. Bittner, M. N. Clark, J. Dolan, D. Duggins, T. Galatali, C. Geyer, M. Gittleman, S. Harbaugh, M. Hebert, T. M. Howard, S. Kolski, A. Kelly, M. Likhachev, M. McNaughton, N. Miller, K. Peterson, B. Pilnick, R. Rajkumar, P. Rybski, B. Salesky, Y.-W. Seo, S. Singh, J. Snider, A. Stentz, W. Whittaker, Z. Wolkowicki, J. Ziglar, H. Bae, T. Brown, D. Demitrish, B. Litkouhi, J. Nickolaou, V. Sadekar, W. Zhang, J. Struble, M. Taylor, M. Darms, and D. Ferguson, "Autonomous driving in urban environments: Boss and the Urban Challenge," *Journal of Field Robotics*, vol. 25, pp. 425–466, 2008.
- [2] P. Research, "Automotive lidar market size."
- [3] B. Schwarz, "Mapping the world in 3d," *Nature Photonics*, vol. 4, pp. 429–430, 2010.
- [4] H. Bostick, "A carbon dioxide laser radar system," *IEEE Journal of Quantum Electronics*, vol. 3, pp. 232–232, 1967.
- [5] R. I. MacDonald, "Frequency domain optical reflectometer," *Applied Optics*, vol. 20, p. 1840, 1981.
- [6] D. Uttam and B. Culshaw, "Precision time domain reflectometry in optical fiber systems using a frequency modulated continuous wave ranging technique," *Journal of Lightwave Technology*, vol. 3, pp. 971–977, Oct. 1985.
- [7] I. Hwang and C. Lee, "Mutual Interferences of a True-Random LiDAR With Other LiDAR Signals," *IEEE Access*, vol. 8, pp. 124123–124133, 2020.
- [8] J. Petit, B. Stottelaar, M. Feiri, and F. Kargl, "Remote attacks on automated vehicles sensors: Experiments on camera and lidar," *Black Hat Europe*, vol. 11, pp. 1–13, 2015.
- [9] M. Okano and C. Chong, "Swept Source Lidar: simultaneous FMCW ranging and nonmechanical beam steering with a wideband swept source," *Optics Express*, vol. 28, pp. 23898–23915, Aug. 2020.

Bibliography

- [10] P. A. Roos, R. R. Reibel, T. Berg, B. Kaylor, Z. W. Barber, and W. R. Babbitt, "Ultrabroadband optical chirp linearization for precision metrology applications," *Optics Letters*, vol. 34, p. 3692, 2009.
- [11] K. J. Vahala, "Optical microcavities," *Nature*, vol. 424, pp. 839–846, Aug. 2003.
- [12] P. Del'Haye, A. Schliesser, O. Arcizet, T. Wilken, R. Holzwarth, and T. J. Kippenberg, "Optical frequency comb generation from a monolithic microresonator," *Nature*, vol. 450, pp. 1214–1217, Dec. 2007.
- [13] T. Herr, V. Brasch, J. D. Jost, C. Wang, M. Kondratiev, M. L. Gorodetsky, and T. J. Kippenberg, "Temporal solitons in optical microresonators," *Nature Photonics*, vol. 8, pp. 145–152, 2014.
- [14] H. Lee, T. Chen, J. Li, K. Y. Yang, S. Jeon, O. Painter, and K. J. Vahala, "Chemically etched ultrahigh-Q wedge-resonator on a silicon chip," *Nature Photonics*, vol. 6, pp. 369–373, June 2012.
- [15] E. Obrzud, S. Lecomte, and T. Herr, "Temporal solitons in microresonators driven by optical pulses," *Nature Photonics*, vol. 11, pp. 600–607, Sept. 2017.
- [16] D. J. Wilson, K. Schneider, S. Hönl, M. Anderson, Y. Baumgartner, L. Czornomaz, T. J. Kippenberg, and P. Seidler, "Integrated gallium phosphide nonlinear photonics," *Nature Photonics*, vol. 14, pp. 57–62, Jan. 2020.
- [17] B. J. M. Hausmann, I. Bulu, V. Venkataraman, P. Deotare, and M. Lončar, "Diamond nonlinear photonics," *Nature Photonics*, vol. 8, pp. 369–374, May 2014.
- [18] M. Pu, L. Ottaviano, E. Semenova, and K. Yvind, "Efficient frequency comb generation in AlGaAs-on-insulator," *Optica*, vol. 3, pp. 823–826, Aug. 2016.
- [19] V. B. Braginsky, M. L. Gorodetsky, and V. S. Ilchenko, "Quality-factor and nonlinear properties of optical whispering-gallery modes," *Physics Letters A*, vol. 137, pp. 393–397, 1989.
- [20] M. Lipson, "Guiding, modulating, and emitting light on Silicon-challenges and opportunities," *Journal of Lightwave Technology*, vol. 23, pp. 4222–4238, Dec. 2005.
- [21] M. H. P. Pfeiffer, A. Kordts, V. Brasch, M. Zervas, M. Geiselmann, J. D. Jost, and T. J. Kippenberg, "Photonic Damascene process for integrated high-Q microresonator based nonlinear photonics," *Optica*, vol. 3, pp. 20–25, Jan. 2016.
- [22] A. Gondarenko, J. S. Levy, and M. Lipson, "High confinement micron-scale silicon nitride high Q ring resonator," *Optics express*, vol. 17, pp. 11366–11370, 2009.
- [23] M. H. P. Pfeiffer, J. Liu, A. S. Raja, T. Morais, B. Ghadiani, and T. J. Kippenberg, "Ultra-smooth silicon nitride waveguides based on the Damascene reflow process: fabrication and loss origins," *Optica*, vol. 5, pp. 884–892, July 2018.

-
- [24] J. Liu, G. Huang, R. N. Wang, J. He, A. S. Raja, T. Liu, N. J. Engelsen, and T. J. Kippenberg, "High-yield, wafer-scale fabrication of ultralow-loss, dispersion-engineered silicon nitride photonic circuits," *Nature Communications*, vol. 12, p. 2236, Apr. 2021.
- [25] T. Herr, *Solitons and dynamics of frequency comb formation in optical microresonators*. PhD thesis, EPFL, Lausanne, 2013.
- [26] V. Brasch, *Soliton Kerr Frequency Combs Generated in Integrated Photonic Chips*. PhD thesis, EPFL, Lausanne, 2016.
- [27] E. G. A. Lucas, *Physics of Dissipative Kerr Solitons in Optical Microresonators and Application to Frequency Synthesis*. PhD thesis, EPFL, Lausanne, 2019.
- [28] M. Karpov, *Dynamics and Applications of Dissipative Kerr Solitons*. PhD thesis, EPFL, Lausanne, 2020.
- [29] H. Guo, M. Karpov, E. Lucas, A. Kordts, M. Pfeiffer, V. Brasch, G. Lihachev, V. Lobanov, M. Gorodetsky, and T. Kippenberg, "Universal dynamics and deterministic switching of dissipative Kerr solitons in optical microresonators," *Nature Physics*, vol. 13, pp. 94–102, 2017.
- [30] A. Tikan and A. Tuszynski, "PyCORA," Jan. 2023.
- [31] A. M. Turing, "The chemical basis of morphogenesis," *Philosophical Transactions of the Royal Society of London. Series B, Biological Sciences*, vol. 237, pp. 37–72, Aug. 1952.
- [32] C. Godey, I. Balakireva, A. Coillet, and Y. Chembo, "Stability analysis of the spatiotemporal Lugiato-Lefever model for Kerr optical frequency combs in the anomalous and normal dispersion regimes," *Phys. Rev. A*, vol. 89, p. 063814, June 2014.
- [33] A. B. Matsko, W. Liang, A. A. Savchenkov, and L. Maleki, "Chaotic dynamics of frequency combs generated with continuously pumped nonlinear microresonators," *Optics Letters*, vol. 38, pp. 525–527, Feb. 2013.
- [34] L. A. Lugiato and R. Lefever, "Spatial Dissipative Structures in Passive Optical Systems," *Phys. Rev. Lett.*, vol. 58, pp. 2209–2211, May 1987.
- [35] M. Karpov, M. H. P. Pfeiffer, H. Guo, W. Weng, J. Liu, and T. J. Kippenberg, "Dynamics of soliton crystals in optical microresonators," *Nature Physics*, vol. 15, pp. 1071–1077, 2019.
- [36] E. Lucas, H. Guo, J. D. Jost, M. Karpov, and T. J. Kippenberg, "Detuning-dependent properties and dispersion-induced instabilities of temporal dissipative Kerr solitons in optical microresonators," *Physical Review A*, vol. 95, p. 043822, 2017.

- [37] N. Akhmediev, W. Krolikowski, and A. Lowery, "Influence of the Raman-effect on solitons in optical fibers," *Opt. Commun.*, vol. 131, pp. 260 – 266, 1996.
- [38] M. Karpov, H. Guo, A. Kordts, V. Brasch, M. H. P. Pfeiffer, M. Zervas, M. Geiselmann, and T. J. Kippenberg, "Raman Self-Frequency Shift of Dissipative Kerr Solitons in an Optical Microresonator," *Phys. Rev. Lett.*, vol. 116, p. 103902, Mar. 2016.
- [39] P. Marin-Palomo, J. N. Kemal, M. Karpov, A. Kordts, J. Pfeifle, M. H. P. Pfeiffer, P. Trocha, S. Wolf, V. Brasch, M. H. Anderson, R. Rosenberger, K. Vijayan, W. Freude, T. J. Kippenberg, and C. Koos, "Microresonator-based solitons for massively parallel coherent optical communications," *Nature*, vol. 546, pp. 274–279, June 2017.
- [40] M. H. Pfeiffer, J. Liu, M. Geiselmann, and T. J. Kippenberg, "Coupling ideality of integrated planar high-Q microresonators," *Physical Review Applied*, vol. 7, p. 024026, 2017.
- [41] M. H. P. Pfeiffer, C. Herkommer, J. Liu, T. Morais, M. Zervas, M. Geiselmann, and T. J. Kippenberg, "Photonic Damascene Process for Low-Loss, High-Confinement Silicon Nitride Waveguides," *IEEE Journal of Selected Topics in Quantum Electronics*, vol. 24, pp. 1–11, July 2018.
- [42] J. Liu, A. S. Raja, M. Karpov, B. Ghadiani, M. H. P. Pfeiffer, B. Du, N. J. Engelsen, H. Guo, M. Zervas, and T. J. Kippenberg, "Ultralow-power chip-based soliton microcombs for photonic integration," *Optica*, vol. 5, pp. 1347–1353, Oct. 2018.
- [43] J. Liu, A. S. Raja, M. H. P. Pfeiffer, C. Herkommer, H. Guo, M. Zervas, M. Geiselmann, and T. J. Kippenberg, "Double inverse nanotapers for efficient light coupling to integrated photonic devices," *Optics Letters*, vol. 43, pp. 3200–3203, 2018.
- [44] Z. L. Newman, V. Maurice, T. Drake, J. R. Stone, T. C. Briles, D. T. Spencer, C. Fredrick, Q. Li, D. Westly, B. R. Ilic, B. Shen, M.-G. Suh, K. Y. Yang, C. Johnson, D. M. S. Johnson, L. Hollberg, K. J. Vahala, K. Srinivasan, S. A. Diddams, J. Kitching, S. B. Papp, and M. T. Hummon, "Architecture for the photonic integration of an optical atomic clock," *Optica*, vol. 6, pp. 680–685, May 2019.
- [45] T. J. Kippenberg, A. L. Gaeta, M. Lipson, and M. L. Gorodetsky, "Dissipative Kerr solitons in optical microresonators," *Science*, vol. 361, Aug. 2018.
- [46] M.-G. Suh, X. Yi, Y.-H. Lai, S. Leifer, I. S. Grudinin, G. Vasisht, E. C. Martin, M. P. Fitzgerald, G. Doppmann, J. Wang, and others, "Searching for exoplanets using a microresonator astrocomb," *Nature Photonics*, vol. 13, pp. 25–30, 2019.
- [47] P. J. Marchand, J. Riemensberger, J. C. Skehan, J.-J. Ho, M. H. P. Pfeiffer, J. Liu, C. Hauger, T. Lasser, and T. J. Kippenberg, "Soliton microcomb based spectral

- domain optical coherence tomography," *Nature Communications*, vol. 12, p. 427, Jan. 2021.
- [48] W. Liang, D. Eliyahu, V. Ilchenko, A. Savchenkov, A. Matsko, D. Seidel, and L. Maleki, "High spectral purity Kerr frequency comb radio frequency photonic oscillator," *Nature Communications*, vol. 6, pp. 7957–7964, 2015.
- [49] M. Yu, Y. Okawachi, A. G. Griffith, N. Picqué, M. Lipson, and A. L. Gaeta, "Silicon-chip-based mid-infrared dual-comb spectroscopy," *Nature communications*, vol. 9, pp. 1869–1876, 2018.
- [50] C. Bao, M.-G. Suh, and K. Vahala, "Microresonator soliton dual-comb imaging," *Optica*, vol. 6, pp. 1110–1116, Sept. 2019.
- [51] J. Feldmann, N. Youngblood, M. Karpov, H. Gehring, X. Li, M. Stappers, M. Le Gallo, X. Fu, A. Lukashchuk, A. S. Raja, J. Liu, C. D. Wright, A. Sebastian, T. J. Kippenberg, W. H. P. Pernice, and H. Bhaskaran, "Parallel convolutional processing using an integrated photonic tensor core," *Nature*, vol. 589, pp. 52–58, Jan. 2021.
- [52] P. Trocha, M. Karpov, D. Ganin, M. H. P. Pfeiffer, A. Kordts, S. Wolf, J. Krockenberger, P. Marin-Palomo, C. Weimann, S. Randel, W. Freude, T. J. Kippenberg, and C. Koos, "Ultrafast optical ranging using microresonator soliton frequency combs," *Science*, vol. 359, pp. 887–891, Feb. 2018.
- [53] J. Liu, H. Tian, E. Lucas, A. S. Raja, G. Lihachev, R. N. Wang, J. He, T. Liu, M. H. Anderson, W. Weng, S. A. Bhave, and T. J. Kippenberg, "Monolithic piezoelectric control of soliton microcombs," *Nature*, vol. 583, pp. 385–390, July 2020.
- [54] E. Lucas, P. Brochard, R. Bouchand, S. Schilt, T. Südmeyer, and T. J. Kippenberg, "Ultralow-noise photonic microwave synthesis using a soliton microcomb-based transfer oscillator," *Nature Communications*, vol. 11, p. 374, Jan. 2020.
- [55] D. T. Spencer, T. Drake, T. C. Briles, J. Stone, L. C. Sinclair, C. Fredrick, Q. Li, D. Westly, B. R. Ilic, A. Bluestone, and others, "An integrated-photonics optical-frequency synthesizer," *arXiv preprint arXiv:1708.05228*, 2017.
- [56] M.-G. Suh, Q.-F. Yang, K. Y. Yang, X. Yi, and K. J. Vahala, "Microresonator soliton dual-comb spectroscopy," *Science*, vol. 354, pp. 600–603, Nov. 2016.
- [57] I. Coddington, N. Newbury, and W. Swann, "Dual-comb spectroscopy," *Optica*, vol. 3, pp. 414–426, Apr. 2016.
- [58] J. Pfeifle, V. Brasch, M. Lauermaun, Y. Yu, D. Wegner, T. Herr, K. Hartinger, P. Schindler, J. Li, D. Hillerkuss, R. Schmogrow, C. Weimann, R. Holzwarth, W. Freude, J. Leuthold, T. J. Kippenberg, and C. Koos, "Coherent terabit communications with microresonator Kerr frequency combs," *Nat. Photon.*, vol. 8, pp. 375–380, 2014.

- [59] P. Marin-Palomo, P. Marin-Palomo, J. N. Kemal, T. J. Kippenberg, W. Freude, S. Randel, C. Koos, C. Koos, and C. Koos, "Performance of chip-scale optical frequency comb generators in coherent WDM communications," *Optics Express*, vol. 28, pp. 12897–12910, Apr. 2020.
- [60] M. H. Anderson, W. Weng, G. Lihachev, A. Tikan, J. Liu, and T. J. Kippenberg, "Zero dispersion Kerr solitons in optical microresonators," *Nature Communications*, vol. 13, p. 4764, Aug. 2022.
- [61] A. Fulop, M. Mazur, A. Lorences-Riesgo, O. B. Helgason, P.-H. Wang, Y. Xuan, D. E. Leaird, M. Qi, P. A. Andrekson, A. M. Weiner, and V. Torres-Company, "High-order coherent communications using mode-locked dark-pulse Kerr combs from microresonators," *Nature Communications*, vol. 9, p. 1598, Apr. 2018.
- [62] H. Shu, L. Chang, Y. Tao, B. Shen, W. Xie, M. Jin, A. Netherton, Z. Tao, X. Zhang, R. Chen, B. Bai, J. Qin, S. Yu, X. Wang, and J. E. Bowers, "Microcomb-driven silicon photonic systems," *Nature*, vol. 605, pp. 457–463, May 2022.
- [63] A. A. Jorgensen, D. Kong, M. R. Henriksen, F. Klejs, Z. Ye, O. B. Helgason, H. E. Hansen, H. Hu, M. Yankov, S. Forchhammer, P. Andrekson, A. Larsson, M. Karlsson, J. Schroder, Y. Sasaki, K. Aikawa, J. W. Thomsen, T. Morioka, M. Galili, V. Torres-Company, and L. K. Oxenlowe, "Petabit-per-second data transmission using a chip-scale microcomb ring resonator source," *Nature Photonics*, vol. 16, pp. 798–802, Nov. 2022.
- [64] V. Torres-Company and A. M. Weiner, "Optical frequency comb technology for ultra-broadband radio-frequency photonics," *Laser & Photonics Reviews*, vol. 8, pp. 368–393, 2014.
- [65] J. Hu, J. He, J. Liu, A. S. Raja, M. Karpov, A. Lukashchuk, T. J. Kippenberg, and C.-S. Brès, "Reconfigurable radiofrequency filters based on versatile soliton microcombs," *Nature Communications*, vol. 11, p. 4377, Sept. 2020.
- [66] A. Lukashchuk, J. Riemensberger, J. Liu, P. Marin-Palomo, M. Karpov, C. Koos, R. Bouchand, and T. J. Kippenberg, "Photonic-assisted analog-to-digital conversion using integrated soliton microcombs," pp. 280 (4 pp.)–280 (4 pp.), Jan. 2019.
- [67] N. P. O'Malley, K. A. McKinzie, M. S. Alshaykh, J. Liu, D. E. Leaird, T. J. Kippenberg, J. D. McKinney, and A. M. Weiner, "Architecture for integrated RF photonic downconversion of electronic signals," *Optics Letters*, vol. 48, pp. 159–162, Jan. 2023.
- [68] D. Fang, D. Drayss, G. Lihachev, P. Marin-Palomo, H. Peng, C. Füllner, A. Kuzmin, J. Liu, R. Wang, V. Snigirev, A. Lukashchuk, M. Zhang, P. Kharel, J. Witzens,

- C. Scheytt, W. Freude, S. Randel, T. J. Kippenberg, and C. Koos, "320 GHz Analog-to-Digital Converter Exploiting Kerr Soliton Combs and Photonic-Electronic Spectral Stitching," in *2021 European Conference on Optical Communication (ECOC)*, pp. 1–4, Sept. 2021.
- [69] P. Ghelfi, F. Laghezza, F. Scotti, G. Serafino, A. Capria, S. Pinna, D. Onori, C. Porzi, M. Scaffardi, A. Malacarne, and others, "A fully photonics-based coherent radar system," *Nature*, vol. 507, pp. 341–345, 2014.
- [70] X. Ji, X. Yao, A. Klenner, Y. Gan, A. L. Gaeta, C. P. Hendon, and M. Lipson, "Chip-based frequency comb sources for optical coherence tomography," *Optics Express*, vol. 27, pp. 19896–19905, July 2019.
- [71] E. Obrzud, M. Rainer, A. Harutyunyan, M. H. Anderson, J. Liu, M. Geiselmann, B. Chazelas, S. Kundermann, S. Lecomte, M. Cecconi, and others, "A microphotonic astrocomb," *Nature Photonics*, vol. 13, pp. 31–36, 2019.
- [72] C. Demirkiran, F. Eris, G. Wang, J. Elmhurst, N. Moore, N. C. Harris, A. Basumallik, V. J. Reddi, A. Joshi, and D. Bunandar, "An Electro-Photonic System for Accelerating Deep Neural Networks," Dec. 2022.
- [73] Y. Shen, N. C. Harris, S. Skirlo, M. Prabhu, T. Baehr-Jones, M. Hochberg, X. Sun, S. Zhao, H. Larochelle, D. Englund, and M. Soljačić, "Deep learning with coherent nanophotonic circuits," *Nature Photonics*, vol. 11, pp. 441–446, July 2017.
- [74] S. Mittal, G. Moille, K. Srinivasan, Y. K. Chembo, and M. Hafezi, "Topological frequency combs and nested temporal solitons," *Nature Physics*, vol. 17, pp. 1169–1176, Oct. 2021.
- [75] S. K. Ozdemir, S. Rotter, F. Nori, and L. Yang, "Parity–time symmetry and exceptional points in photonics," *Nature Materials*, vol. 18, pp. 783–798, Aug. 2019.
- [76] K. Komagata, A. Tusnin, J. Riemensberger, M. Churaev, H. Guo, A. Tikan, and T. J. Kippenberg, "Dissipative Kerr solitons in a photonic dimer on both sides of exceptional point," *Communications Physics*, vol. 4, pp. 1–13, July 2021.
- [77] A. K. Tusnin, A. M. Tikan, and T. J. Kippenberg, "Nonlinear states and dynamics in a synthetic frequency dimension," *Physical Review A*, vol. 102, p. 023518, Aug. 2020.
- [78] A. Tikan, J. Riemensberger, K. Komagata, S. Hönl, M. Churaev, C. Skehan, H. Guo, R. N. Wang, J. Liu, P. Seidler, and T. J. Kippenberg, "Emergent nonlinear phenomena in a driven dissipative photonic dimer," *Nature Physics*, vol. 17, pp. 604–610, May 2021.
- [79] R. Dandliker, R. Thalmann, and D. Prongué, "Two-wavelength laser interferometry using superheterodyne detection," *Optics Letters*, vol. 13, pp. 339–341, May 1988.

- [80] Y. Salvade, N. Schuhler, S. Leveque, and S. L. Floch, "High-accuracy absolute distance measurement using frequency comb referenced multiwavelength source," *Applied Optics*, vol. 47, pp. 2715–2720, May 2008.
- [81] J. Ye, "Absolute measurement of a long, arbitrary distance to less than an optical fringe," *Optics Letters*, vol. 29, pp. 1153–1155, May 2004.
- [82] I. Coddington, W. C. Swann, L. Nenadovic, and N. R. Newbury, "Rapid and precise absolute distance measurements at long range," *Nature Photonics*, vol. 3, pp. 351–356, June 2009.
- [83] M.-G. Suh and K. J. Vahala, "Soliton microcomb range measurement," *Science*, vol. 359, pp. 884–887, Feb. 2018.
- [84] E. D. Caldwell, L. C. Sinclair, N. R. Newbury, and J.-D. Deschenes, "The time-programmable frequency comb and its use in quantum-limited ranging," *Nature*, pp. 1–7, Oct. 2022.
- [85] N. Pavlov, S. Koptyaev, G. Lihachev, A. S. Voloshin, A. S. Gorodnitskiy, M. Ryabko, S. V. Polonsky, and M. L. Gorodetsky, "Narrow-linewidth lasing and soliton kerr microcombs with ordinary laser diodes," *Nature Photonics*, vol. 12, pp. 694–698, 2018.
- [86] A. S. Voloshin, N. M. Kondratiev, G. V. Lihachev, J. Liu, V. E. Lobanov, N. Y. Dmitriev, W. Weng, T. J. Kippenberg, and I. A. Bilenko, "Dynamics of soliton self-injection locking in optical microresonators," *Nature Communications*, vol. 12, p. 235, Jan. 2021.
- [87] G. Lihachev, J. Riemensberger, W. Weng, J. Liu, H. Tian, A. Siddharth, V. Snigirev, V. Shadymov, A. Voloshin, R. N. Wang, J. He, S. A. Bhave, and T. J. Kippenberg, "Low-noise frequency-agile photonic integrated lasers for coherent ranging," *Nature Communications*, vol. 13, p. 3522, June 2022.
- [88] M. Churaev, R. N. Wang, V. Snigirev, A. Riedhauser, T. Blesin, C. Möhl, M. A. Anderson, A. Siddharth, Y. Popoff, D. Caimi, S. Honl, J. Riemensberger, J. Liu, P. Seidler, and T. J. Kippenberg, "A heterogeneously integrated lithium niobate-on-silicon nitride photonic platform," Sept. 2022.
- [89] Z. Li, R. N. Wang, G. Lihachev, Z. Tan, V. Snigirev, M. Churaev, N. Kuznetsov, A. Siddharth, M. J. Berekhi, J. Riemensberger, and T. J. Kippenberg, "Tightly confining lithium niobate photonic integrated circuits and lasers," Aug. 2022.
- [90] A. Siddharth, T. Wunderer, G. Lihachev, A. S. Voloshin, C. Haller, R. N. Wang, M. Teepe, Z. Yang, J. Liu, J. Riemensberger, N. Grandjean, N. Johnson, and T. J. Kippenberg, "Near ultraviolet photonic integrated lasers based on silicon nitride," *APL Photonics*, vol. 7, p. 046108, Apr. 2022.

-
- [91] Y. Liu, Z. Qiu, X. Ji, A. Lukashchuk, J. He, J. Riemensberger, M. Hafermann, R. N. Wang, J. Liu, C. Ronning, and T. J. Kippenberg, "A photonic integrated circuit-based erbium-doped amplifier," *Science*, vol. 376, pp. 1309–1313, June 2022.
- [92] P. F. Mcmanamon, T. A. Dorschner, D. L. Corkum, L. J. Friedman, D. Hobbs, M. Holz, S. Liberman, H. U. Y. Q. Nguyen, D. P. Resler, R. C. Sharp, and E. A. Watson, "Optical phased array technology," *Proceedings of the IEEE*, vol. 84, pp. 268–298, 1996.
- [93] J. Sun, E. Timurdogan, A. Yaacobi, E. S. Hosseini, and M. R. Watts, "Large-scale nanophotonic phased array," *Nature*, vol. 493, pp. 195–199, Jan. 2013.
- [94] N. Kuse and M. E. Fermann, "Frequency-modulated comb LIDAR," *APL Photonics*, vol. 4, p. 106105, Oct. 2019.
- [95] Y. Chembo and C. Menyuk, "Spatiotemporal Lugiato-Lefever formalism for Kerr-comb generation in whispering-gallery-mode resonators," *Phys. Rev. A*, vol. 87, p. 053852, May 2013.
- [96] X. Yi, Q.-F. Yang, X. Zhang, K. Y. Yang, X. Li, and K. Vahala, "Single-mode dispersive waves and soliton microcomb dynamics," *Nature Communications*, vol. 8, p. 14869, 2017.
- [97] X. Yi, Q.-F. Yang, K. Y. Yang, and K. Vahala, "Active capture and stabilization of temporal solitons in microresonators," *Opt. Lett.*, vol. 41, pp. 2037–2040, May 2016.
- [98] C. Wang, Z. Deng, C. Gu, Y. Liu, D. Luo, Z. Zhu, W. Li, and H. Zeng, "Line-scan spectrum-encoded imaging by dual-comb interferometry," *Optics Letters*, vol. 43, pp. 1606–1609, Apr. 2018.
- [99] X. Zhang, J. Pouls, and M. C. Wu, "Laser frequency sweep linearization by iterative learning pre-distortion for FMCW LiDAR," *Optics Express*, vol. 27, pp. 9965–9974, Apr. 2019.
- [100] I. Grudinin, "Arbitrary optical waveform generation utilizing frequency discriminators," Nov. 2021.
- [101] B. Behroozpour, P. A. M. Sandborn, N. Quack, T.-J. Seok, Y. Matsui, M. C. Wu, and B. E. Boser, "Electronic-Photonic Integrated Circuit for 3D Microimaging," *IEEE Journal of Solid-State Circuits*, vol. 52, pp. 161–172, Jan. 2017.
- [102] T.-J. Ahn and D. Y. Kim, "Analysis of nonlinear frequency sweep in high-speed tunable laser sources using a self-homodyne measurement and Hilbert transformation," *Applied Optics*, vol. 46, pp. 2394–2400, May 2007.
- [103] M. Zhang, B. Buscaino, C. Wang, A. Shams-Ansari, C. Reimer, R. Zhu, J. M. Kahn, and M. Lončar, "Broadband electro-optic frequency comb generation in a lithium niobate microring resonator," *Nature*, vol. 568, pp. 373–377, Apr. 2019.

Bibliography

- [104] M. Karpov, H. Guo, A. Kordts, V. Brasch, M. H. P. Pfeiffer, M. Zervas, M. Geiselmann, and T. J. Kippenberg, "Raman self-frequency shift of dissipative kerr solitons in an optical microresonator," *Physical Review Letters*, vol. 116, pp. 1–5, 2016.
- [105] H. Guo, E. Lucas, M. H. P. Pfeiffer, M. Karpov, M. Anderson, J. Liu, M. Geiselmann, J. D. Jost, and T. J. Kippenberg, "Intermode Breather Solitons in Optical Microresonators," *Phys. Rev. X*, vol. 7, p. 041055, Dec. 2017.
- [106] T. Klein, W. Wieser, L. Reznicek, A. Neubauer, A. Kampik, and R. Huber, "Multi-MHz retinal OCT," *Biomedical Optics Express*, vol. 4, pp. 1890–1908, Oct. 2013.
- [107] A. Martin, D. Dodane, L. Leviandier, D. Dolfi, A. Naughton, P. O'Brien, T. Spuessens, R. Baets, G. Lepage, P. Verheyen, P. D. Heyn, P. Absil, P. Feneyrou, and J. Bourderionnet, "Photonic Integrated Circuit-Based FMCW Coherent LiDAR," *Journal of Lightwave Technology*, vol. 36, pp. 4640–4645, Oct. 2018.
- [108] C. Rogers, A. Y. Piggott, D. J. Thomson, R. F. Wiser, I. E. Opris, S. A. Fortune, A. J. Compston, A. Gondarenko, F. Meng, X. Chen, G. T. Reed, and R. Nicolaescu, "A universal 3D imaging sensor on a silicon photonics platform," *Nature*, vol. 590, pp. 256–261, Feb. 2021.
- [109] X. Zhang, K. Kwon, J. Henriksson, J. Luo, and M. C. Wu, "A large-scale microelectromechanical-systems-based silicon photonics LiDAR," *Nature*, vol. 603, pp. 253–258, Mar. 2022.
- [110] H. Tian, J. Liu, B. Dong, J. C. Skehan, M. Zervas, T. J. Kippenberg, and S. A. Bhave, "Hybrid integrated photonics using bulk acoustic resonators," pp. 1–41, 2019.
- [111] Q. Fang, T.-Y. Liow, J. F. S., K. W. Ang, M. B. Yu, G. Q. Lo, and D.-L. Kwong, "Wdm multi-channel silicon photonic receiver with 320 gbps data transmission capability," *Optics Express*, vol. 18, p. 5106, 2010.
- [112] T. J. Ahn and D. Y. Kim, "Analysis of nonlinear frequency sweep in high-speed tunable laser sources using a self-homodyne measurement and hilbert transformation," *Applied Optics*, vol. 46, p. 2394, 2007.
- [113] M. Piels, J. F. Bauters, M. L. Davenport, M. J. R. Heck, and J. E. Bowers, "Low-loss silicon nitride awg demultiplexer heterogeneously integrated with hybrid iii-v/silicon photodetectors," *Journal of Lightwave Technology*, vol. 32, pp. 817–823, 2014.
- [114] A. J. Metcalf, V. Torres-Company, D. E. Leaird, and A. M. Weiner, "High-power broadly tunable electrooptic frequency comb generator," *IEEE Journal on Selected Topics in Quantum Electronics*, vol. 19, pp. 231–236, 2013.
- [115] R. Qian, K. C. Zhou, J. Zhang, C. Viehland, A.-H. Dhalla, and J. A. Izatt, "Video-rate high-precision time-frequency multiplexed 3D coherent ranging," *Nature Communications*, vol. 13, p. 1476, Mar. 2022.

-
- [116] A. S. Raja, A. S. Voloshin, H. Guo, S. E. Agafonova, J. Liu, A. S. Gorodnitskiy, M. Karpov, N. G. Pavlov, E. Lucas, R. R. Galiev, and others, "Electrically pumped photonic integrated soliton microcomb," *Nature communications*, vol. 10, pp. 680–687, 2019.
- [117] B. Stern, X. Ji, Y. Okawachi, A. L. Gaeta, and M. Lipson, "Battery-operated integrated frequency comb generator," *Nature*, vol. 562, pp. 401–405, 2018.
- [118] C. O. d. Beeck, B. Haq, L. Elsinger, A. Gocalinska, E. Pelucchi, B. Corbett, G. Roelkens, and B. Kuyken, "Heterogeneous III-V on silicon nitride amplifiers and lasers via microtransfer printing," *Optica*, vol. 7, pp. 386–393, May 2020.
- [119] S. Schiller, "Spectrometry with frequency combs," *Optics Letters*, vol. 27, pp. 766–768, May 2002.
- [120] F. Keilmann, C. Gohle, and R. Holzwarth, "Time-domain mid-infrared frequency-comb spectrometer," *Optics Letters*, vol. 29, pp. 1542–1544, July 2004.
- [121] Y.-D. Hsieh, Y. Iyonaga, Y. Sakaguchi, S. Yokoyama, H. Inaba, K. Minoshima, F. Hindle, T. Araki, and T. Yasui, "Spectrally interleaved, comb-mode-resolved spectroscopy using swept dual terahertz combs," *Scientific Reports*, vol. 4, p. 3816, Jan. 2014.
- [122] T. Mizuno, E. Hase, T. Minamikawa, Y. Tokizane, R. Oe, H. Koresawa, H. Yamamoto, and T. Yasui, "Full-field fluorescence lifetime dual-comb microscopy using spectral mapping and frequency multiplexing of dual-comb optical beats," *Science Advances*, vol. 7, p. eabd2102, Jan. 2021.
- [123] E. Hase, T. Minamikawa, T. Mizuno, S. Miyamoto, R. Ichikawa, Y.-D. Hsieh, K. Shibuya, K. Sato, Y. Nakajima, A. Asahara, K. Minoshima, Y. Mizutani, T. Iwata, H. Yamamoto, and T. Yasui, "Scan-less confocal phase imaging based on dual-comb microscopy," *Optica*, vol. 5, p. 634, May 2018.
- [124] F. R. Giorgetta, W. C. Swann, L. C. Sinclair, E. Baumann, I. Coddington, and N. R. Newbury, "Optical two-way time and frequency transfer over free space," *Nature Photonics*, vol. 7, pp. 434–438, 2013.
- [125] H. J. Kim, D. E. Leaird, and A. M. Weiner, "Rapidly tunable dual-comb rf photonic filter for ultrabroadband rf spread spectrum applications," *IEEE Transactions on Microwave Theory and Techniques*, vol. 64, pp. 3351–3362, 2016.
- [126] B. Lomsadze, B. C. Smith, and S. T. Cundiff, "Tri-comb spectroscopy," *Nature Photonics*, vol. 12, pp. 676–680, Nov. 2018.
- [127] T. Ideguchi, S. Holzner, B. Bernhardt, G. Guelachvili, N. Picqué, and T. W. Hänsch, "Coherent raman spectro-imaging with laser frequency combs," *Nature*, vol. 502, pp. 355–358, 2013.

Bibliography

- [128] V. Ataie, D. Esman, B. P.-P. Kuo, N. Alic, and S. Radic, "Subnoise detection of a fast random event," *Science*, vol. 350, pp. 1343–1346, Dec. 2015.
- [129] K. Kikuchi, "Fundamentals of Coherent Optical Fiber Communications," *Journal of Lightwave Technology*, vol. 34, pp. 157–179, Jan. 2016.
- [130] S. Gao, M. O'Sullivan, and R. Hui, "Complex-optical-field lidar system for range and vector velocity measurement," *Optics Express*, vol. 20, pp. 25867–25875, Nov. 2012.
- [131] F. Derr, "Optical QPSK transmission system with novel digital receiver concept," *Electronics Letters*, vol. 27, pp. 2177–2179, Nov. 1991.
- [132] C. R. Doerr, "Silicon photonic integration in telecommunications," *Frontiers in Physics*, vol. 3, 2015.
- [133] H. Isono, "Latest standardization trend for leading edge high-speed optical transceivers," in *Metro and Data Center Optical Networks and Short-Reach Links IV*, vol. 11712, p. 1171209, Mar. 2021.
- [134] D. F. Pierrottet, F. Amzajerdian, L. Petway, B. Barnes, G. Lockard, and M. Rubio, "Linear FMCW Laser Radar for Precision Range and Vector Velocity Measurements," *MRS Online Proceedings Library*, vol. 1076, p. 10760406, Aug. 2008.
- [135] N. Kuse, T. Tetsumoto, G. Navickaite, M. Geiselmann, and M. E. Fermann, "Continuous scanning of a dissipative Kerr-microresonator soliton comb for broadband, high-resolution spectroscopy," *Optics Letters*, vol. 45, pp. 927–930, Feb. 2020.
- [136] J. Riemensberger, A. Lukashchuk, M. Karpov, W. Weng, E. Lucas, J. Liu, and T. J. Kippenberg, "Massively parallel coherent laser ranging using a soliton microcomb," *Nature*, vol. 581, pp. 164–170, May 2020.
- [137] J. Liu, E. Lucas, A. S. Raja, J. He, J. Riemensberger, R. N. Wang, M. Karpov, H. Guo, R. Bouchand, and T. J. Kippenberg, "Photonic microwave generation in the x-and k-band using integrated soliton microcombs," *Nature Photonics*, pp. 1–6, 2020.
- [138] C. Xiang, J. Liu, J. Guo, L. Chang, R. N. Wang, W. Weng, J. Peters, W. Xie, Z. Zhang, J. Riemensberger, J. Selvidge, T. J. Kippenberg, and J. E. Bowers, "Laser soliton microcombs heterogeneously integrated on silicon," *Science*, vol. 373, pp. 99–103, July 2021.
- [139] T. Vallaitis, R. Bonk, J. Guetlein, D. Hillerkuss, J. Li, R. Brenot, F. Lelarge, G. H. Duan, W. Freude, and J. Leuthold, "Quantum dot SOA input power dynamic range improvement for differential-phase encoded signals," *Optics Express*, vol. 18, pp. 6270–6276, Mar. 2010.
- [140] N. R. Newbury, I. Coddington, and W. Swann, "Sensitivity of coherent dual-comb spectroscopy," *Optics express*, vol. 18, pp. 7929–7945, 2010.

- [141] S. H. Strogatz, *Nonlinear Dynamics and Chaos with Student Solutions Manual: With Applications to Physics, Biology, Chemistry, and Engineering, Second Edition*. Sept. 2018.
- [142] H. Haken, "Cooperative phenomena in systems far from thermal equilibrium and in nonphysical systems," *Reviews of Modern Physics*, vol. 47, pp. 67–121, Jan. 1975.
- [143] J. Dudley, G. Genty, and S. Coen, "Supercontinuum generation in photonic crystal fiber," *Rev. Mod. Phys.*, vol. 78, pp. 1135–1184, Oct. 2006.
- [144] K. Otsuka, *Nonlinear Dynamics in Optical Complex Systems*. Apr. 2000.
- [145] P. Grelu, *Nonlinear Optical Cavity Dynamics: From Microresonators to Fiber Lasers*. Dec. 2015.
- [146] T. Herr, K. Hartinger, J. Riemensberger, C. Wang, E. Gavartin, R. Holzwarth, M. L. Gorodetsky, and T. J. Kippenberg, "Universal formation dynamics and noise of Kerr-frequency combs in microresonators," *Nat. Photon.*, vol. 6, pp. 480–487, 2012.
- [147] X. Xue, Y. Xuan, Y. Liu, P.-H. Wang, S. Chen, J. Wang, D. E. Leaird, M. Qi, and A. M. Weiner, "Mode-locked dark pulse Kerr combs in normal-dispersion microresonators," *Nature Photonics*, vol. 9, pp. 594–600, 2015.
- [148] B. M. Horton, "Noise-Modulated Distance Measuring Systems," *Proceedings of the IRE*, 1959.
- [149] L. Guosui, G. Hong, and S. Weimin, "Development of random signal radars," *IEEE Transactions on Aerospace and Electronic Systems*, vol. 35, pp. 770–777, July 1999.
- [150] F.-Y. Lin and J.-M. Liu, "Chaotic lidar," *IEEE Journal of Selected Topics in Quantum Electronics*, vol. 10, pp. 991–997, Sept. 2004.
- [151] D. Esman, V. Ataie, B. P.-P. Kuo, N. Alic, and S. Radic, "Subnoise Signal Detection and Communication," *Journal of Lightwave Technology*, vol. 34, pp. 5214–5219, Nov. 2016.
- [152] G. Chen, Y. Mao, and C. K. Chui, "A symmetric image encryption scheme based on 3D chaotic cat maps," *Chaos, Solitons & Fractals*, vol. 21, pp. 749–761, July 2004.
- [153] A. Uchida, K. Amano, M. Inoue, K. Hirano, S. Naito, H. Someya, I. Oowada, T. Kurashige, M. Shiki, S. Yoshimori, K. Yoshimura, and P. Davis, "Fast physical random bit generation with chaotic semiconductor lasers," *Nature Photonics*, vol. 2, pp. 728–732, Dec. 2008.
- [154] R. Scholtz, "The spread spectrum concept," *IEEE Transactions on Communications*, vol. 25, pp. 748–755, 1977.

Bibliography

- [155] N. Takeuchi, N. Sugimoto, H. Baba, and K. Sakurai, "Random modulation cw lidar," *Applied Optics*, vol. 22, pp. 1382–1386, May 1983.
- [156] S. E. Craig, W. Fishbein, and O. E. Rittenbach, "Continuous-Wave Radar with High Range Resolution and Unambiguous Velocity Determination," *IRE Transactions on Military Electronics*, vol. MIL-6, pp. 153–161, Apr. 1962.
- [157] R. M. Narayanan, Y. Xu, P. D. Hoffmeyer, and J. O. Curtis, "Design, performance, and applications of a coherent ultra-wideband random noise radar," *Optical Engineering*, vol. 37, pp. 1855–1869, June 1998.
- [158] G. Carter, "Coherence and time delay estimation," *Proceedings of the IEEE*, vol. 75, pp. 236–255, Feb. 1987.
- [159] B. Behroozpour, P. A. M. Sandborn, M. C. Wu, and B. E. Boser, "Lidar System Architectures and Circuits," *IEEE Communications Magazine*, vol. 55, pp. 135–142, Oct. 2017.
- [160] M.-C. Amann, "Phase noise limited resolution of coherent LIDAR using widely tunable laser diodes," *Electronics Letters*, vol. 28, pp. 1694–1696, Aug. 1992.
- [161] S. Axelsson, "Noise radar using random phase and frequency modulation," *IEEE Transactions on Geoscience and Remote Sensing*, vol. 42, pp. 2370–2384, Nov. 2004.
- [162] Z. Yang, C. Li, M. Yu, F. Chen, and T. Wu, "Compact 405-nm random-modulation continuous wave lidar for standoff biological warfare detection," *Journal of Applied Remote Sensing*, vol. 9, p. 096042, May 2015.
- [163] R. Matthey and V. Mitev, "Pseudo-random noise-continuous-wave laser radar for surface and cloud measurements," *Optics and Lasers in Engineering*, vol. 43, pp. 557–571, Mar. 2005.
- [164] M. Quatrevalet, X. Ai, A. Perez-Serrano, P. Adamiec, J. Barbero, A. Fix, J. M. G. Tijero, I. Esquivias, J. G. Rarity, and G. Ehret, "Atmospheric CO₂ sensing with a random modulation continuous wave integrated path differential absorption Lidar," *IEEE Journal of Selected Topics in Quantum Electronics*, vol. 23, pp. 157–167, 2016.
- [165] Y. Wang, B. Wang, and A. Wang, "Chaotic correlation optical time domain reflectometer utilizing laser diode," *IEEE Photonics Technology Letters*, vol. 20, pp. 1636–1638, 2008.
- [166] A. Wang, N. Wang, Y. Yang, B. Wang, M. Zhang, and Y. Wang, "Precise fault location in wdm-pn by utilizing wavelength tunable chaotic laser," *Journal of Lightwave Technology*, vol. 30, pp. 3420–3426, 2012.
- [167] C. Pulikkaseril and N. Langdale-Smith, "Next generation LiDAR for a fully autonomous future," *Baraja Whitepaper*, 2020.

- [168] S. C. Crouch, R. R. Reibel, J. Curry, M. Milvich, and K. Rupavatharam, "Method and system for LIDAR detection and doppler correction of optical phase-encoded range detection," Nov. 2019.
- [169] M. Bashkansky, H. R. Burris, E. E. Funk, R. Mahon, and C. I. Moore, "RF phase-coded random-modulation LIDAR," *Optics Communications*, vol. 231, pp. 93–98, Feb. 2004.
- [170] X. Ai, R. Nock, J. G. Rarity, and N. Dahnoun, "High-resolution random-modulation cw lidar," *Applied Optics*, vol. 50, pp. 4478–4488, Aug. 2011.
- [171] K. Myneni, T. A. Barr, B. R. Reed, S. D. Pethel, and N. J. Corron, "High-precision ranging using a chaotic laser pulse train," *Applied Physics Letters*, vol. 78, pp. 1496–1498, Mar. 2001.
- [172] Y.-H. Liao and F.-Y. Lin, "Dynamical characteristics and their applications of semiconductor lasers subject to both optical injection and optical feedback," *Optics express*, vol. 21, pp. 23568–23578, 2013.
- [173] C.-H. Cheng, C.-Y. Chen, J.-D. Chen, D.-K. Pan, K.-T. Ting, and F.-Y. Lin, "3D pulsed chaos lidar system," *Optics Express*, vol. 26, pp. 12230–12241, Apr. 2018.
- [174] H.-L. Ho, J.-D. Chen, C.-A. Yang, C.-C. Liu, C.-T. Lee, Y.-H. Lai, and F.-Y. Lin, "High-speed 3D imaging using a chaos lidar system," *The European Physical Journal Special Topics*, Jan. 2022.
- [175] P. Grelu and N. Akhmediev, "Dissipative solitons for mode-locked lasers," *Nature Photon.*, vol. 6, pp. 84–92, 2012.
- [176] E. Timurdogan, Z. Su, R.-J. Shiue, M. J. Byrd, C. V. Poulton, K. Jabon, C. DeRose, B. R. Moss, E. S. Hosseini, I. Duzevik, M. Whitson, R. P. Millman, D. A. Atlas, and M. R. Watts, "400G Silicon Photonics Integrated Circuit Transceiver Chipsets for CPO, OBO, and Pluggable Modules," in *Optical Fiber Communication Conference (OFC) 2020 (2020)*, paper T3H.2, p. T3H.2, Mar. 2020.
- [177] A. Lukashchuk, J. Riemensberger, M. Karpov, J. Liu, and T. J. Kippenberg, "Dual chirped microcomb based parallel ranging at megapixel-line rates," *Nature Communications*, vol. 13, p. 3280, June 2022.
- [178] L. Wang, L. Chang, N. Volet, M. H. Pfeiffer, M. Zervas, H. Guo, T. J. Kippenberg, and J. E. Bowers, "Frequency comb generation in the green using silicon nitride microresonators," *Laser & Photonics Reviews*, vol. 10, pp. 631–638, 2016.
- [179] C. Bao, L. Zhang, A. Matsko, Y. Yan, Z. Zhao, G. Xie, A. Agarwal, L. Kimerling, J. Michel, L. Maleki, and A. Willner, "Nonlinear conversion efficiency in Kerr frequency comb generation," *Opt. Lett.*, vol. 39, pp. 6126–6129, Nov. 2014.

Bibliography

- [180] S. Coulibaly, M. Taki, A. Bendahmane, G. Millot, B. Kibler, and M. G. Clerc, "Turbulence-Induced Rogue Waves in Kerr Resonators," *Physical Review X*, vol. 9, p. 011054, Mar. 2019.
- [181] B. Boashash, "Estimating and interpreting the instantaneous frequency of a signal. I. Fundamentals," *Proceedings of the IEEE*, vol. 80, pp. 520–538, Apr. 1992.
- [182] F.-Y. Lin, Y.-K. Chao, and T.-C. Wu, "Effective Bandwidths of Broadband Chaotic Signals," *IEEE Journal of Quantum Electronics*, vol. 48, pp. 1010–1014, Aug. 2012.
- [183] N. Akhmediev, J. M. Soto-Crespo, and A. Ankiewicz, "Extreme waves that appear from nowhere: On the nature of rogue waves," *Physics Letters A*, vol. 373, pp. 2137–2145, June 2009.
- [184] J. M. Dudley, F. Dias, M. Erkintalo, and G. Genty, "Instabilities, breathers and rogue waves in optics," *Nature Photon.*, vol. 8, pp. 755–764, 2014.
- [185] S. O. Rice, "Mathematical analysis of random noise," *The Bell System Technical Journal*, vol. 24, pp. 46–156, Jan. 1945.
- [186] "Corning SMF 28 product information," 2019.
- [187] Y. Jiang, S. Karpf, and B. Jalali, "Time-stretch LiDAR as a spectrally scanned time-of-flight ranging camera," *Nature Photonics*, vol. 14, pp. 14–18, Jan. 2020.
- [188] L. M. Pecora and T. L. Carroll, "Synchronization in chaotic systems," *Physical Review Letters*, vol. 64, pp. 821–824, Feb. 1990.
- [189] G. Hu, J. Xiao, J. Yang, F. Xie, and Z. Qu, "Synchronization of spatiotemporal chaos and its applications," *Physical Review E*, vol. 56, pp. 2738–2746, Sept. 1997.
- [190] L. Kocarev, "Chaos-based cryptography: a brief overview," *IEEE Circuits and Systems Magazine*, vol. 1, pp. 6–21, 2001.
- [191] C. V. Poulton, M. J. Byrd, P. Russo, E. Timurdogan, M. Khandaker, D. Vermeulen, and M. R. Watts, "Long-Range LiDAR and Free-Space Data Communication With High-Performance Optical Phased Arrays," *IEEE Journal of Selected Topics in Quantum Electronics*, vol. 25, pp. 1–8, Sept. 2019.
- [192] I. Kim, R. J. Martins, J. Jang, T. Badloe, S. Khadir, H.-Y. Jung, H. Kim, J. Kim, P. Genevet, and J. Rho, "Nanophotonics for light detection and ranging technology," *Nature Nanotechnology*, vol. 16, pp. 508–524, May 2021.
- [193] K. Goda, K. K. Tsia, and B. Jalali, "Serial time-encoded amplified imaging for real-time observation of fast dynamic phenomena," *Nature*, vol. 458, pp. 1145–1149, Apr. 2009.

-
- [194] S. Diddams, L. Hollberg, and V. Mbele, "Molecular fingerprinting with the resolved modes of a femtosecond laser frequency comb," *Nature*, vol. 445, pp. 627–630, Feb. 2007.
- [195] M. Shirasaki, "Large angular dispersion by a virtually imaged phased array and its application to a wavelength demultiplexer," *Optics Letters*, vol. 21, pp. 366–368, Mar. 1996.
- [196] S. Xiao and A. M. Weiner, "2-D wavelength demultiplexer with potential for > 1000 channels in the C-band," *Optics Express*, vol. 12, pp. 2895–2902, June 2004.
- [197] F. Li, F. Willomitzer, M. M. Balaji, P. Rangarajan, and O. Cossairt, "Exploiting Wavelength Diversity for High Resolution Time-of-Flight 3D Imaging," *IEEE Transactions on Pattern Analysis and Machine Intelligence*, vol. 43, pp. 2193–2205, July 2021.
- [198] A. Lukashchuk, J. Riemensberger, A. Tuszynski, J. Liu, and T. Kippenberg, "Chaotic micro-comb based parallel ranging," *Arxiv*, Dec. 2021.
- [199] S. Xiao, A. Weiner, and C. Lin, "A dispersion law for virtually imaged phased-array spectral dispersers based on paraxial wave theory," *IEEE Journal of Quantum Electronics*, vol. 40, pp. 420–426, Apr. 2004.
- [200] V. Brasch, M. Geiselmann, T. Herr, G. Lihachev, M. H. P. Pfeiffer, M. L. Gorodetsky, and T. J. Kippenberg, "Photonic chip-based optical frequency comb using soliton Cherenkov radiation," *Science*, vol. 351, pp. 357–360, 2016.
- [201] Y. Guo, R. Zhao, G. Zhou, L. Lu, A. Stroganov, M. S. Nisar, J. Chen, and L. Zhou, "Thermally Tuned High-Performance III-V/Si₃N₄ External Cavity Laser," *IEEE Photonics Journal*, vol. 13, pp. 1–13, Apr. 2021.
- [202] P. P. Khial, A. D. White, and A. Hajimiri, "Nanophotonic optical gyroscope with reciprocal sensitivity enhancement," *Nature Photonics*, vol. 12, pp. 671–675, Nov. 2018.
- [203] A. D. White, G. H. Ahn, K. V. Gasse, K. Y. Yang, L. Chang, J. E. Bowers, and J. Vučković, "Integrated passive nonlinear optical isolators," *Nature Photonics*, pp. 1–7, Dec. 2022.
- [204] C. V. Poulton, M. J. Byrd, P. Russo, B. Moss, O. Shatrovov, M. Khandaker, and M. R. Watts, "Coherent LiDAR With an 8,192-Element Optical Phased Array and Driving Laser," *IEEE Journal of Selected Topics in Quantum Electronics*, vol. 28, pp. 1–8, Sept. 2022.
- [205] B. J. Isaac, B. Song, S. Pinna, L. A. Coldren, and J. Klamkin, "Indium Phosphide Photonic Integrated Circuit Transceiver for FMCW LiDAR," *IEEE Journal of Selected Topics in Quantum Electronics*, vol. 25, pp. 1–7, Nov. 2019.

Bibliography

- [206] K. Sayyah, R. Sarkissian, P. Patterson, B. Huang, O. Efimov, D. Kim, K. Elliott, L. Yang, and D. Hammon, "Fully Integrated FMCW LiDAR Optical Engine on a Single Silicon Chip," *Journal of Lightwave Technology*, vol. 40, pp. 2763–2772, May 2022.
- [207] A. v. Rees, A. v. Rees, Y. Fan, Y. Fan, D. Geskus, E. J. Klein, R. M. Oldenbeuving, P. J. M. v. d. Slot, P. J. M. v. d. Slot, and K.-J. Boller, "Ring resonator enhanced mode-hop-free wavelength tuning of an integrated extended-cavity laser," *Optics Express*, vol. 28, pp. 5669–5683, Feb. 2020.
- [208] A. Bancora, G. Lihachev, and et al., "Frequency agile photonic integrated external cavity laser," *In preparation*.
- [209] J. Y. Wang, "Heterodyne laser radar-SNR from a diffuse target containing multiple glints," *Applied Optics*, vol. 21, pp. 464–476, Feb. 1982.
- [210] A. Polman, D. C. Jacobson, D. J. Eaglesham, R. C. Kistler, and J. M. Poate, "Optical doping of waveguide materials by MeV Er implantation," *Journal of Applied Physics*, vol. 70, pp. 3778–3784, Oct. 1991.
- [211] M. Pollnau, "Rare-earth-ion-doped channel waveguide lasers on silicon," *IEEE Journal of Selected Topics in Quantum Electronics*, vol. 21, pp. 414–425, 2015.
- [212] J. Lee, K.-R. Lee, B. E. Eovino, J. H. Park, L. Y. Liang, L. Lin, H.-J. Yoo, and J. Yoo, "A 36-channel auto-calibrated front-end asic for a pmut-based miniaturized 3-d ultrasound system," *IEEE Journal of Solid-State Circuits*, vol. 56, pp. 1910–1923, 2021.
- [213] G. Jung, M. W. Rashid, T. M. Carpenter, C. Tekes, D. M. J. Cowell, S. Freear, F. L. Degertekin, and M. Ghovanloo, "Single-chip reduced-wire active catheter system with programmable transmit beamforming and receive time-division multiplexing for intracardiac echocardiography," in *2018 IEEE International Solid - State Circuits Conference - (ISSCC)*, pp. 188–190, 2018.
- [214] K. Sooksood, E. Noorsal, J. Becker, and M. Ortmanns, "A neural stimulator front-end with arbitrary pulse shape, hv compliance and adaptive supply requiring 0.05mm² in 0.35um hvcmos," in *2011 IEEE International Solid-State Circuits Conference*, pp. 306–308, 2011.
- [215] F. A. Dragonas, G. Neretti, P. Sanjeevikumar, and G. Grandi, "High-voltage high-frequency arbitrary waveform multilevel generator for dbd plasma actuators," *IEEE Transactions on Industry Applications*, vol. 51, pp. 3334–3342, 2015.
- [216] D. Thomson, A. Zilkie, J. E. Bowers, T. Komljenovic, G. T. Reed, L. Vivien, D. Marris-Morini, E. Cassan, L. Viot, J.-M. Fédéli, J.-M. Hartmann, J. H. Schmid, D.-X. Xu, F. Boeuf, P. O'Brien, G. Z. Mashanovich, and M. Nedeljkovic, "Roadmap on silicon photonics," *Journal of Optics*, vol. 18, p. 073003, June 2016.

- [217] W. Jin, Q.-F. Yang, L. Chang, B. Shen, H. Wang, M. A. Leal, L. Wu, M. Gao, A. Feshali, M. Paniccia, K. J. Vahala, and J. E. Bowers, "Hertz-linewidth semiconductor lasers using CMOS-ready ultra-high-Q microresonators," *Nature Photonics*, pp. 1–8, Feb. 2021.
- [218] M. Li, L. Chang, L. Wu, J. Staffa, J. Ling, U. A. Javid, S. Xue, Y. He, R. Lopez-rios, T. J. Morin, H. Wang, B. Shen, S. Zeng, L. Zhu, K. J. Vahala, J. E. Bowers, and Q. Lin, "Integrated Pockels laser," *Nature Communications*, vol. 13, p. 5344, Sept. 2022.
- [219] V. Snigirev, A. Riedhauser, G. Lihachev, J. Riemensberger, R. N. Wang, C. Moehl, M. Churaev, A. Siddharth, G. Huang, Y. Popoff, U. Drechsler, D. Caimi, S. Hoenl, J. Liu, P. Seidler, and T. J. Kippenberg, "Ultrafast tunable lasers using lithium niobate integrated photonics," Aug. 2022.
- [220] M. A. Tran, D. Huang, and J. E. Bowers, "Tutorial on narrow linewidth tunable semiconductor lasers using Si/III-V heterogeneous integration," *APL Photonics*, vol. 4, p. 111101, Nov. 2019.
- [221] Y. Zhu and L. Zhu, "Narrow-linewidth, tunable external cavity dual-band diode lasers through InP/GaAs-Si₃N₄ hybrid integration," *Optics Express*, vol. 27, pp. 2354–2362, Feb. 2019.
- [222] M. Blaicher, M. R. Billah, J. Kemal, T. Hoose, P. Marin-Palomo, A. Hofmann, Y. Kutuvantavida, C. Kieninger, P.-I. Dietrich, M. Lauer mann, S. Wolf, U. Troppenz, M. Moehrle, F. Merget, S. Skacel, J. Witzens, S. Randel, W. Freude, and C. Koos, "Hybrid multi-chip assembly of optical communication engines by in situ 3D nano-lithography," *Light: Science & Applications*, vol. 9, pp. 1–11, Apr. 2020.
- [223] O. B. Helgason, M. Girardi, Z. Ye, F. Lei, J. Schroeder, and V. T. Company, "Power-efficient soliton microcombs," *arXiv:2202.09410 [physics]*, Feb. 2022.
- [224] B. Shen, L. Chang, J. Liu, H. Wang, Q.-F. Yang, C. Xiang, R. N. Wang, J. He, T. Liu, W. Xie, J. Guo, D. Kinghorn, L. Wu, Q.-X. Ji, T. J. Kippenberg, K. Vahala, and J. E. Bowers, "Integrated turnkey soliton microcombs," *Nature*, vol. 582, pp. 365–369, June 2020.
- [225] C. Xiang, W. Jin, O. Terra, B. Dong, H. Wang, L. Wu, J. Guo, T. J. Morin, E. Hughes, J. Peters, Q.-X. Ji, A. Feshali, M. Paniccia, K. J. Vahala, and J. E. Bowers, "Three-dimensional integration enables ultra-low-noise, isolator-free Si photonics," Jan. 2023.
- [226] J. H. Xiao, G. Hu, and Z. Qu, "Synchronization of Spatiotemporal Chaos and Its Application to Multichannel Spread-Spectrum Communication," *Physical Review Letters*, vol. 77, pp. 4162–4165, Nov. 1996.

Bibliography

- [227] J. K. Jang, X. Ji, C. Joshi, Y. Okawachi, M. Lipson, and A. L. Gaeta, "Observation of Arnold Tongues in Coupled Soliton Kerr Frequency Combs," *Physical Review Letters*, vol. 123, p. 153901, Oct. 2019.
- [228] T. G. Hodgkinson, R. A. Harmon, and D. W. Smith, "Demodulation of optical DPSK using in-phase and quadrature detection," *Electronics Letters*, vol. 21, pp. 867–868, Sept. 1985.
- [229] A. Davis, M. Pettitt, J. King, and S. Wright, "Phase diversity techniques for coherent optical receivers," *Journal of Lightwave Technology*, vol. 5, pp. 561–572, Apr. 1987.
- [230] S. W. Ellingson, "Correcting I-Q Imbalance in Direct Conversion Receivers," p. 3.
- [231] P. Feneyrou, L. Leviandier, J. Minet, G. Pillet, A. Martin, D. Dolfi, J.-P. Schlotterbeck, P. Rondeau, X. Lacondemine, A. Rieu, and T. Midavaine, "Frequency-modulated multifunction lidar for anemometry, range finding, and velocimetry," 1. Theory and signal processing," *Applied Optics*, vol. 56, pp. 9663–9675, Dec. 2017.
- [232] V. Brasch, M. Geiselmann, M. H. Pfeiffer, and T. J. Kippenberg, "Bringing short-lived dissipative Kerr soliton states in microresonators into a steady state," *Optics Express*, vol. 24, pp. 29312–29320, 2016.
- [233] X. Xie, R. Bouchand, D. Nicolodi, M. Lours, C. Alexandre, and Y. L. Coq, "Phase noise characterization of sub-hertz linewidth lasers via digital cross correlation," *Optics Letters*, vol. 42, pp. 1217–1220, Apr. 2017.
- [234] D. M. Baney, P. Gallion, and R. S. Tucker, "Theory and Measurement Techniques for the Noise Figure of Optical Amplifiers," *Optical Fiber Technology*, vol. 6, pp. 122–154, Apr. 2000.
- [235] A. Zarifi, B. Stiller, M. Merklein, Y. Liu, B. Morrison, A. Casas-Bedoya, G. Ren, T. G. Nguyen, K. Vu, D.-Y. Choi, A. Mitchell, S. J. Madden, and B. J. Eggleton, "On-chip correlation-based Brillouin sensing: design, experiment, and simulation," *JOSA B*, vol. 36, pp. 146–152, Jan. 2019.
- [236] M. Frigo and S. Johnson, "FFTW: an adaptive software architecture for the FFT," in *Proceedings of the 1998 IEEE International Conference on Acoustics, Speech and Signal Processing, ICASSP '98 (Cat. No.98CH36181)*, vol. 3, pp. 1381–1384 vol.3, May 1998.
- [237] G. Agrawal, *Nonlinear Fiber Optics*. Academic Press, 2013.
- [238] W. H. Press, S. A. Teukolsky, W. T. Vetterling, and B. P. Flannery, *Numerical recipes 3rd edition: The art of scientific computing*. 2007.
- [239] Y. Okawachi, M. R. E. Lamont, K. Luke, D. O. Carvalho, M. Yu, M. Lipson, and A. L. Gaeta, "Bandwidth shaping of microresonator-based frequency combs via dispersion engineering," *Optics Letters*, vol. 39, pp. 3535–3538, June 2014.

-
- [240] A. Y. Piggott, "Understanding the physics of coherent LiDAR," *arXiv:2011.05313 [physics]*, Nov. 2020.
- [241] J. S. Bendat and A. G. Piersol, *Random Data: Analysis and Measurement Procedures*. Sept. 2011.
- [242] B. Stec and W. Susek, "Theory and Measurement of Signal-to-Noise Ratio in Continuous-Wave Noise Radar," *Sensors*, vol. 18, p. 1445, May 2018.
- [243] E. Baumann, J.-D. Deschênes, F. R. Giorgetta, W. C. Swann, I. Coddington, and N. R. Newbury, "Speckle phase noise in coherent laser ranging: fundamental precision limitations," *Optics Letters*, vol. 39, pp. 4776–4779, Aug. 2014.
- [244] M. H. Montgomery and D. Odonoghue, "A derivation of the errors for least squares fitting to time series data," *Delta Scuti Star Newsletter*, vol. 13, p. 28, July 1999.
- [245] D. H. Dolan, "Accuracy and precision in photonic Doppler velocimetry," *Review of Scientific Instruments*, vol. 81, p. 053905, May 2010.
- [246] D. Rife and R. Boorstyn, "Single tone parameter estimation from discrete-time observations," *IEEE Transactions on Information Theory*, vol. 20, pp. 591–598, Sept. 1974.
- [247] A. Quazi, "An overview on the time delay estimate in active and passive systems for target localization," *IEEE Transactions on Acoustics, Speech, and Signal Processing*, vol. 29, pp. 527–533, June 1981.
- [248] M. Sotoodeh, Y. Beaulieu, J. Harley, and D. L. McGhan, "Modulator Bias and Optical Power Control of Optical Complex E-Field Modulators," *Journal of Lightwave Technology*, vol. 29, pp. 2235–2248, Aug. 2011.
- [249] A. Youssefi, I. Shomroni, Y. J. Joshi, N. R. Bernier, A. Lukashchuk, P. Uhrich, L. Qiu, and T. J. Kippenberg, "A cryogenic electro-optic interconnect for superconducting devices," *Nature Electronics*, vol. 4, pp. 326–332, May 2021.
- [250] W. Freude, R. Schmogrow, B. Nebendahl, M. Winter, A. Josten, D. Hillerkuss, S. Koenig, J. Meyer, M. Dreschmann, M. Huebner, C. Koos, J. Becker, and J. Leuthold, "Quality metrics for optical signals: Eye diagram, Q-factor, OSNR, EVM and BER," in *2012 14th International Conference on Transparent Optical Networks (ICTON)*, pp. 1–4, July 2012.
- [251] M. Muller, "Total jitter measurement at low probability levels, using optimized BERT scan method," <http://cp.literature.agilent.com/litweb/pdf/5989-2933EN.pdf>.
- [252] R. Hui and M. O'Sullivan, *Fiber Optic Measurement Techniques*. Jan. 2009.

Bibliography

- [253] R. Schmogrow, B. Nebendahl, M. Winter, A. Josten, D. Hillerkuss, S. Koenig, J. Meyer, M. Dreschmann, M. Huebner, C. Koos, J. Becker, W. Freude, and J. Leuthold, "Error Vector Magnitude as a Performance Measure for Advanced Modulation Formats," *IEEE Photonics Technology Letters*, vol. 24, pp. 61–63, Jan. 2012.
- [254] E. Cacciamani and C. Wolejsza, "Phase-Ambiguity Resolution in a Four-Phase PSK Communications System," *IEEE Transactions on Communication Technology*, vol. 19, pp. 1200–1210, Dec. 1971.

Anton Lukashchuk

Address: Avenue d'Echallens 59, Lausanne

Tel: +41 (0)78 641 7570

Email: anton.lukashchuk@gmail.com

Date / Place of birth: 30.03.1993 / Nakhodka, Russia

Nationality: Russian (Switzerland - permit B)

Civil status: Single



Key competencies

LiDAR, integrated photonics, nonlinear optics, frequency combs, optical fiber communication, digital signal processing, simulation, programming.

Education

- Jan 2018 - present** **PhD in Physics, École Polytechnique Fédérale de Lausanne (EPFL)**
Laboratory of Photonics and Quantum Measurements (LPQM), Prof. T.J. Kippenberg.
Design, simulation, characterization, measurement of integrated photonic waveguides and microresonator frequency combs. Setting up LiDAR and fiber-optic communication experiments with frequency combs and integrated lasers.
Two patent applications.
- Sep 2011 - Jun 2017** **BSc and MSc in Applied Physics and Mathematics, Moscow Institute of Physics and Technology.**
BSc thesis – ‘Optimization of collision integral calculation in kinetic Boltzman equation’; GPA = 4.91/5.0, (Diploma with Honors);
MSc thesis – ‘Hybridization of Amplitude and Differential Phase Modulation in Optical Fibers’; GPA = 4.77/5.0, (Diploma with Honors); Double-degree program with **Skolkovo Institute of Science and Technology**.

Other internships and professional experience

- Aug 2017 - Dec 2017** **Trainee, École Polytechnique Fédérale de Lausanne (EPFL), LPQM**
Design and simulation of advanced dispersion engineered photonic waveguides.
- Aug 2016 - Sept 2016** **Internship, TU Darmstadt, Institute for Microwave Engineering and Photonics.**
- Jan 2017 - Feb 2017** Study of phase rectification via optical injection locking for combining amplitude and phase modulation formats in fiber-optic communication experiment.

Key publications / talks

- **Lukashchuk A**, et al. "Chaotic micro-comb based parallel ranging." [arXiv:2112.10241 \(2021\)](https://arxiv.org/abs/2112.10241).
- **Lukashchuk A**, et al. "Dual chirped microcomb based parallel ranging at megapixel-line rates." [Nature Communications 13.1 \(2022\): 1-8](https://doi.org/10.1038/s41586-022-03111-1).
- Riemensberger J, **Lukashchuk A** et al. "Massively parallel coherent laser ranging using a soliton microcomb." [Nature 581.7807 \(2020\): 164-170](https://doi.org/10.1038/s41586-020-02111-1).
- Invited talk at **EPIC Meeting on Photonics** "[Hybrid Integrated Photonics for Coherent LiDAR](#)", ESA, Noordwijk (2022).

Additional qualifications

Languages: Russian (mother tongue), English (working proficiency), French (B1/B2).

IT: MATLAB, Python, COMSOL Multiphysics, Lumerical, Linux.

Awards

- PhD fellowship European Space Agency NPI "Photonic integrated coherent LiDAR engine"
- Best Oral Presentation prize by Nature Photonics at ECIO 2020